DOCTORAL THESIS

Harnessing Quantum Dynamics:
Heat Engines, Negative Temperatures, and Dynamical Spectroscopy

---

Author: Mohit Lal Bera

Supervisor: Prof. Maciej Lewenstein

A thesis submitted in partial fulfillment of the
requirements for the degree of Doctor of Philosophy
in the

Quantum Optics Theory Group

at

ICFO - The Institute of Photonic Sciences

UNIVERSITAT POLITÉCNICA DE CATALUNYA

Abstract

Quantum technology is dependent on our capacity to manipulate and control the quantum characteristics of particles, such as quantum superposition, entanglement, non-classicality, no-locality, and some collective behaviors, etc. So, the advancement of quantum technology intimately relies on the discovery of new quantum phenomena, a better understanding of the microscopic quantum world, and more precise control over quantum dynamics.

In this thesis, our main objective is to utilize different kinds of quantum dynamics as resources. To do so, we investigate thermodynamics, non-equilibrium steady states, and dynamical spectroscopy in order to categorize the dynamics of quantum systems as having either no external drive (self-drive), a weak external drive, or a strong external drive, respectively.

In the first part, we explore the dynamics of quantum heat engines. In that, we consider dynamics that are driven by time-independent Hamiltonian, i.e., without external driving. We show that when a working system non-locally interacts with two baths at different temperatures, the engine can operate in a one-step cycle, yielding Carnot efficiency at maximum power. This advantage is exclusively because non-local operations are more powerful than local ones. To study such engines in a more systematic manner, we develop a resource theory of heat engines. This provides a framework to study quantum engines operating with a working system composed of a finite number of quantum particles and restricted to few observations, i.e., in the one-shot finite-size regime. We also propose an experimentally feasible model of an engine using an atom-cavity system that yields Carnot efficiency at maximum power.

In the second part, we consider open quantum dynamics, where a system weakly interacts with environments. In particular, we study the Lindblad master equation-based dynamics of quantum systems weakly coupled to two thermal baths at different temperatures. In general, these dynamics lead to non-equilibrium steady states. By selectively coupling a quantum system to two different thermal baths, a synthetic thermal bath can be engineered, and the temperature of such a synthetic bath can be made negative. With this, we explore

steady-state quantum thermodynamics with negative temperatures. We show that the zeroth and the Clausius state of the second law remain unaltered in the case of baths with negative temperatures. However, the Kelvin-Planck statement of the second law updates in this case to incorporate the following. (i) There is spontaneous heat flow from a bath with a negative temperature to a bath with a positive temperature. In this sense, the baths with a negative temperature are 'hotter' than the ones with a positive temperature. (ii) There is spontaneous heat flow from a bath with a less negative temperature to a bath with a more negative temperature. We also introduce a continuous heat engine operating between a positive and negative temperature bath. Our analysis shows that the heat-to-work conversion efficiency for such an engine is always unity. We study the thermodynamic implications of our results.

The third part of the thesis explores systems driven by strong external fields. In such circumstances, we encounter transient quantum dynamics, which cannot be described by thermodynamics. This kind of dynamics is utilized for dynamical spectroscopy. Particularly, we have studied high harmonic generation where a strong laser field interacts with matter. By utilizing the high harmonic generation mechanism, we characterize the topological features of solids. Here, we characterized the (a) topological features of the one-dimensional generalized Su-Schrieffer-Heeger chain and one-dimensional extended Fermi-Hubbard chain by exploiting high harmonic spectroscopy, (b) characterization of localization and delocalization phases in the one-dimensional non-interacting quasi-periodic Aubry-Andŕe-Harper model, and (c) characterization of a quantum critical phase in 1-D strongly correlated by high harmonic spectroscopy.

Resume

La tecnología cuántica depende de nuestra capacidad para manipular y controlar las características cuánticas de las partículas, como la superposición cuántica, el entrelazamiento, la no clasicidad, la no localidad y algunos comportamientos colectivos, etc. Por lo tanto, el avance de la tecnología cuántica se basa íntimamente en la descubrimiento de nuevos fenómenos cuánticos, una mejor comprensión del mundo cuántico microscópico y un control más preciso sobre la dinámica cuántica.

En esta tesis, nuestro principal objetivo es utilizar diferentes tipos de dinámica cuántica como recursos. Para hacerlo, investigamos la termodinámica, el estado estacionario sin equilibrio y la espectroscopia dinámica para categorizar la dinámica de los sistemas cuánticos sin impulso externo (autoimpulso), un impulso externo débil o un impulso externo fuerte con impulso cuántico.

En la primera parte, exploramos la dinámica de los motores térmicos cuánticos. Específicamente, consideramos dinámicas que son impulsadas por un hamiltoniano independiente del tiempo, es decir, sin control externo. Mostramos que cuando un sistema en funcionamiento interactúa de forma no local con dos baños a diferentes temperaturas, el motor puede operar en un ciclo de un solo paso, lo que produce la eficiencia de Carnot a máxima potencia. Esta ventaja se debe exclusivamente a que las operaciones no locales son más poderosas que las locales. Para estudiar tales motores de una manera más sistemática, desarrollamos una teoría de los recursos de los motores térmicos. Esto proporciona un marco para estudiar los motores cuánticos que funcionan con un sistema de trabajo compuesto por un número finito de partículas cuánticas y restringido a unas pocas observaciones, es decir, en el régimen de tamaño finito de una sola vez. También proponemos un modelo factible experimentalmente de un motor que utiliza un sistema de cavidad atómica que produce la eficiencia de Carnot a máxima potencia.

En la segunda parte, consideramos la dinámica cuántica abierta, donde un sistema interactúa débilmente con los entornos. En particular, estudiamos la dinámica basada en la ecuación maestra de

Lindblad de sistemas cuánticos débilmente acoplados a dos baños termales a diferentes temperaturas. En general, estas dinámicas conducen a estados estacionarios de no equilibrio. Al acoplar selectivamente un sistema cuántico a dos baños térmicos diferentes, se puede diseñar un baño térmico sintético y la temperatura de dicho baño sintético se puede hacer negativa. Con esto, exploramos la termodinámica cuántica de estado estacionario con temperaturas negativas. Mostramos que el cero y el estado de Clausius de la segunda ley permanecen inalterados en el caso de baños con temperaturas negativas. Sin embargo, el enunciado de Kelvin-Planck de la segunda ley se actualiza en este caso para incorporar lo siguiente. (i) Hay un flujo de calor espontáneo de un baño con temperatura negativa a un baño con temperatura positiva. En este sentido, los baños con temperatura negativa son 'más calientes' que los de temperatura positiva. (ii) Hay un flujo de calor espontáneo de un baño con una temperatura menos negativa a un baño con una temperatura más negativa. También presentamos un motor térmico continuo que opera entre un baño de temperatura positiva y negativa. Nuestro análisis muestra que la eficiencia de conversión de calor a trabajo para tal motor es siempre la unidad. Estudiamos las implicaciones termodinámicas de nuestros resultados.

La tercera parte de la tesis explora los sistemas impulsados por fuertes campos externos. En tales circunstancias, nos encontramos con dinámicas cuánticas transitorias, que no pueden ser descritas por la termodinámica. Este tipo de dinámica se utiliza para la espectroscopia dinámica. En particular, hemos estudiado la generación de altos armónicos donde un fuerte campo láser interactúa con la materia. Utilizando el mecanismo de generación de armónicos altos, caracterizamos las características topológicas de los sólidos. Aquí, caracterizamos (a) las características topológicas de la cadena de Su-Schrieffer-Heeger generalizada unidimensional y la cadena de Fermi-Hubbard extendida unidimensional mediante la explotación de la espectroscopia de armónicos altos, (b) la caracterización de las fases de localización y deslocalización en el modelo de Aubry-André-Harper, una cadena unidimensional cuasi-periódica que no interactúa, y (c) caracterización de una fase crítica cuántica en 1-D fuertemente correlacionada mediante espectroscopia de armónicos altos.

Resum

La tecnologia quàntica depèn de la nostra capacitat per manipular i controlar les característiques quàntiques de les partícules, com ara la superposició quàntica, l'entrellaçament, la no-classicitat, la no-localitat i alguns comportaments col·lectius, etc. Per tant, l'avenç de la tecnologia quàntica es basa íntimament en la descoberta de nous fenòmens quàntics, una millor comprensió del món quàntic microscòpic i un control més precís sobre la dinàmica quàntica.

En aquesta tesi, el nostre principal objectiu és utilitzar diferents tipus de dinàmica quàntica com a recursos. Per fer-ho, investiguem la termodinàmica, l'estat estacionari sense equilibri i l'espectroscòpia dinàmica per categoritzar la dinàmica dels sistemes quàntics sense impuls extern (autoimpuls), amb impuls extern feble o amb impuls extern fort amb impuls quàntic.

A la primera part, explorem la dinàmica dels motors tèrmics quàntics. Específicament, considerem dinàmiques que són impulsades per un hamiltonià independent del temps, és a dir, sense control extern. Mostrem que quan un sistema en funcionament interactua de manera no local amb dos banys a temperatures diferents, el motor pot operar en un cicle d'un sol pas, cosa que produeix l'eficiència de Carnot a màxima potència. Aquest avantatge es deu exclusivament al fet que les operacions no locals són més poderoses que les locals. Per estudiar aquests motors de manera més sistemàtica, desenvolupem una teoria dels recursos dels motors tèrmics. Això proporciona un marc per estudiar els motors quàntics que funcionen amb un sistema de treball compost per un nombre finit de partícules quàntiques i restringit a unes poques observacions, és a dir, en el règim de mida finit duna sola vegada. També proposem un model experimental factible d'un motor que utilitza un sistema de cavitat atòmica que produeix l'eficiència de Carnot a màxima potència.

A la segona part, considerem la dinàmica quàntica oberta, on un sistema interactua feblement amb els entorns. En particular, estudiem la dinàmica basada en l'equació mestra de Lindblad de sistemes quàntics dèbilment acoblats a dos banys termals a temperatures diferents. En general, aquestes dinàmiques condueixen a estats estacionaris de no-equilibri. En acoblar selectivament un sis-

tema quàntic a dos banys tèrmics diferents, es pot dissenyar un bany tèrmic sintètic i la temperatura del bany sintètic es pot fer negativa. Amb això explorem la termodinàmica quàntica d'estat estacionari amb temperatures negatives. Mostrem que el zero i l'estat de Clausius de la segona llei romanen inalterats en el cas de banys amb temperatures negatives. Tot i això, l'enunciat de Kelvin-Planck de la segona llei s'actualitza en aquest cas per incorporar el següent. (i) Hi ha un flux de calor espontània d'un bany amb temperatura negativa a un bany amb temperatura positiva. En aquest sentit, els banys amb temperatura negativa són 'més calents' que els de temperatura positiva. (ii) Hi ha un flux de calor espontània d'un bany amb una temperatura menys negativa a un bany amb una temperatura més negativa. També presentem un motor tèrmic continu que opera entre un bany de temperatura positiva i negativa. La nostra anàlisi mostra que l'eficiència de conversió de calor a treball per a aquest motor és sempre la unitat. Estudiem les implicacions termodinàmiques dels nostres resultats.

La tercera part de la tesi explora els sistemes impulsats per forts camps externs. En aquestes circumstàncies ens trobem amb dinàmiques quàntiques transitòries, que no poden ser descrites per la termodinàmica. Aquest tipus de dinàmica es fa servir per a l'espectroscòpia dinàmica. En particular, hem estudiat la generació d'alts harmònics on un camp làser fort interactua amb la matèria. Utilitzant el mecanisme de generació d'harmò- nics alts, caracteritzem les característiques topològiques dels sòlids. Aquí, caracteritzem (a) les característiques topològiques de la cadena de Su-Schrieffer-Heeger generalitzada unidimensional i la cadena de Fermi-Hubbard estesa unidimensional mitjançant l'explotació de l'espectroscòpia d'harmònics alts, (b) la caracterització de les fases de localització i deslocalització al model d'Aubry-André-Harper, una cadena unidimensional quasiperiòdica que no interactua, i (c) caracterització d'una fase crítica quàntica en 1-D fortament correlacionada mitjançant espectroscòpia d'harmònics alts.

Acknowledgements

First of all, I would like to express my deepest gratitude and thank to my supervisor Prof. Maciej Lewenstein. The genuine sense of liberty that you practice and your outlook toward science and the scientific community will guide me in the future. Thank you very much, Maciek; it has been a privilege to learn under your supervision and to benefit from your extraordinary depth and expertise.

I gratefully acknowledge Utso and Manu, who have always been by me in every crisis. Utso played a very constructive role during 2nd half of my Ph.D. tenure. With infinite patience and affection, he has guided me and developed my confidence. Despite my shortcomings, I have acquired a wide range of knowledge from him in areas as diverse as condensed matter, strong field dynamics, quantum thermodynamics, and various programming languages. I admire Manu's idea-driven approach toward basic science and agglomeration of overall science and philosophy. That motivated me to explore the natural world and human society as a whole. I deeply thank Toby and Ravi for being supportive and for many fruitful discussions.

I also thankfully acknowledge all my collaborators, Sergi, Marlena, Jessica, Tanmoy, Kaustav, Varindar, Toby, Marcin, and Prof. Maciej M. Maska for engaging discussions and making our work enjoyable.

These 4.5 years would have not been the same without Swapan, Debraj, Daniel, Alex, Tymoteusz, Yuma, Miguel-Angel, Albert, Gorka, Pavel, Christos, Joana, Borja, Niccolò, Philipp, Guillem, Anubhav, Sourav, Barbara, Paolo, Angelo, and all the other QOT members, who have filled all the days at ICFO with funny and happy memories. Beyond them, I would also like to thank all the other ICFOnians, including Human resources, who have made my life too easy. I owe a debt of gratitude to the ICFO-Indian community. Thank you very much, Avijit, Santanu, Biswajit, Debranjan, Chaitanya, Sukeert, Aamir, Ipsita, Varun, Vindhiya, Pandian, Parmeshwar, Saurab, Himansu, Rajashree, Rajdeep, Rinu, Kartika, Mitradeep, Gaurav, Suchi and others. I also sincerely appreciate Samyo and Chandan, to whom I could rely on in any situation.

Life in Barcelona was outstanding because of various social activi-

ties, including science-day and informal gatherings with Nimesh, Sri, Sanmukhi, Kunal, Mamtha, Vinod, Purandhar, Momchil, Kaustav, and others. Beyond that crazy gatherings with Mallika, Chandan, Samyo, Ipsita, Aamir, Banhirup, Saptam, and others are simply unforgettable. Additionally, I would like to thank Manjima and my family physician in Barcelona, Dr. Roberto Manzanares Isabel.

Finally, I sincerely thank Mr. Sourav Mukherjee, Mrs. Bharati Mukherjee, my parents, uncles and aunts, beloved brothers, sisters, brothers-in-law, and my dear friends for their motivation and support.

List of publications

Peer-reviewed

1. Mohit Lal Bera and Maciej Lewenstein and Manabendra Nath Bera. "Attaining Carnot efficiency with quantum and nanoscale heat engines" npj Quantum Inf. **7**, 31 (2021).

2. Mohit Lal Bera and Sergi Julià-Farré and Maciej Lewenstein and Manabendra Nath Bera. "Quantum heat engines with Carnot efficiency at maximum power" *Physical Review Research*, vol. 4, no. 1, Phys. Rev. Research **4**, 013157 (2022).

Preprints

3. Mohit Lal Bera, Tanmoy Pandit, Kaustav Chatterjee, Varinder Singh, Maciej Lewenstein, Utso Bhattacharya and Manabendra Nath Bera "Steady-state Quantum Thermodynamics with Synthetic Negative Temperatures", arXiv:2305.01215 (2023).

4. Mohit Lal Bera, Jessica O. de Almeida, Marlena Dziurawiec, Marcin Plodzien, Maciej M. Maska, Maciej Lewenstein, Tobias Grass and Utso Bhattacharya "Topological Phase Detection Through High Harmonic Spectroscopy in Extended Su-Schrieffer-Heeger Chains", arXiv:2305.02025 (2023).

Other works not included in this thesis

5. Nicetu Tibau Vidal, Mohit Lal Bera, Arnau Riera and Maciej Lewenstein and Manabendra Nath Bera "Quantum operations in an information theory for fermions", Phys. Rev. A **104** 032411 (2021).

6. Mohit Lal Bera and Manabendra Nath Bera "Quantum Bayes' Rule Affirms Consistency in Measurement Inferences in Quantum Mechanics", arXiv:2207.08623 (2022).

Scientific Acknowledgements

This thesis would not have been possible without the financial support of QOT group at ICFO from: ERC AdG NOQIA; Ministerio de Ciencia y Innovation Agencia Estatal de Investigaciones (PGC2018-097027-B-I00/10.13039/501100011033, CEX2019-000910-S/10.13039/501100011033, Plan National FIDEUA PID2019-106901GB-I00, FPI, QUANTERA MAQS PCI2019-111828-2, QUANTERA DYNAMITE PCI2022-132919, Proyectos de I+D+I "Retos Colaboración" QUSPIN RTC2019-007196-7); MICIIN with funding from European Union NextGenerationEU(PRTR-C17.I1) and by Generalitat de Catalunya; Fundació Cellex; Fundació Mir-Puig; Generalitat de Catalunya (European Social Fund FEDER and CERCA program, AGAUR Grant No. 2021 SGR 01452, QuantumCAT U16-011424, co-funded by ERDF Operational Program of Catalonia 2014-2020); Barcelona Supercomputing Center MareNostrum (FI-2022-1-0042); EU (PASQuanS2.1, 101113690); EU Horizon 2020 FET-OPEN OPTOlogic (Grant No 899794); EU Horizon Europe Program (Grant Agreement 101080086 - NeQST), National Science Centre, Poland (Symfonia Grant No. 2016/20/W/ST4/00314); ICFO Internal "QuantumGaudi" project; European Union's Horizon 2020 research and innovation program under the Marie-Skłodowska-Curie grant agreement No 101029393 (STREDCH) and No 847648 ("La Caixa" Junior Leaders fellowships ID100010434: LCF/BQ/PI19/11690013,LCF/BQ/PI20 /11760031, LCF/BQ/PR20/11770012,LCF/BQ/PR21/11840013). I personally acknowledge the financial support from MCIN/AEI/10.13039/5011000 11033. Views and opinions expressed are, however, those of the author(s) only and do not necessarily reflect those of the European Union, European Commission, European Climate, Infrastructure and Environment Executive Agency (CINEA), nor any other granting authority. Neither the European Union nor any granting authority can be held responsible for them.

Contents

List of Figures

List of Tables

Chapter 1

Introduction

Quantum devices play important roles in modern technology. These devices rely on the static as well as the dynamical properties of quantum systems. The quantum systems are fundamentally different from the classical ones. In particular, the former allows to have quantum superposition [1–4] and interference [5], non-classicality [6–8], entanglement [9–12], EPR correlations [13], non-locality [14–16], contextuality [17], etc. It is obvious that at every instant of time, during evolution, the microscopic configuration of a quantum system changes at microscopic scales. To control the device made up of quantum systems, one desires to have information about microscopic configuration and knowledge of how the configuration changes over time. Thus one of the major requirements to develop modern technology is to acquire a better understanding of the quantum systems and have precise control over their dynamics [18, 19].

In general, the dynamics of a quantum system vary in different physical situations. Again, by engineering these physical situations, one may selectively induce dynamics in a quantum system. The dynamics we are concerned with are crudely classified into three different categories as follows.

First, when the system is evolved in isolation, it undergoes unitary dynamics. Its state, in that case, changes deterministically and reversibly following Schrödinger equation and Liouville-von Neumann equation [5, 20]. In these situations, the evolution is driven by the system's own time-independent Hamiltonian.

The second category corresponds to an evolution of a system in the presence of a weak interaction with an environment. These dy-

namics are referred to as open quantum system dynamics and are responsible for decoherence, relaxation, or dissipation in a system in general. There are various approaches and techniques to express open quantum dynamics, e.g., Floquet dynamics [21–29], LGKS master equation [30], etc. These evaluations again can be used to engineer various dynamics of interests, for example, Floquet Hamiltonian engineering [21–29]; measurement-induced dynamics, which exploits the probabilistic nature of quantum mechanics measurements to drive system operations [31–34].

The third category is due to the situation, where the evolution of a system is driven by a strong external field. These are also called strongly driven systems. These evolutions are studied in many contexts. The interaction between the high energy photons and atoms or solids introduces the dynamics associated with non-linear spectroscopy, attosecond physics, high harmonic generation, etc [35–41]. By manipulating the Hamiltonian in a controlled manner, one may induce the desired dynamics based on different underlying physical principles [42–47]. Tuning the inter-system interaction allows researchers to control quantum states or state transitions. One may achieve quantum control by applying sequences of pulses [48–51] or by slowly changing the parameters in a quantum system's Hamiltonian to perform tasks like quantum annealing [52–56].

In this thesis, we aim to utilize these dynamics as resources and study quantum thermodynamics in closed and open quantum systems and the transient response of a system observed by using dynamical spectroscopy. In the coming few paragraphs, we want to highlight the three important concepts that illustrate the three different resources we mentioned in the above discussion.

a) *Quantum heat engines:* With the development of quantum mechanics, there have been efforts to study thermodynamics in the quantum regime. The current technology enables us to prepare an ensemble of a finite number of quantum particles in well-defined states. These ensembles can again be brought in interaction with a thermal bath in a controlled manner. Clearly, in this situation, one cannot study thermodynamics with the average thermodynamics quantities, as statistical averaging is not possible for a finite number of particles. Further, due to quantum superposition, the system exhibits quantum uncertainties which may become reasonably large.

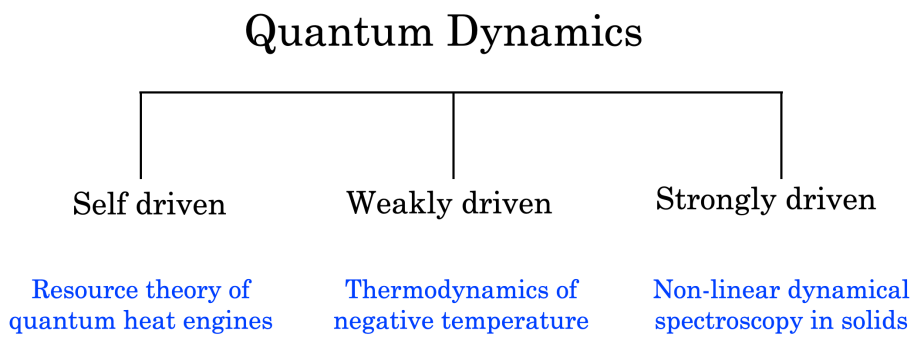

Figure 1.1: The cases of quantum dynamics explored in this thesis.

Also, ergodicity, in general, cannot be applied to the quantum regime. This is because the act of observation at different times introduces disturbance into the system and, thereby, modifies the dynamics from the one which solely occurs due to the interaction with a thermal bath. Thus, these demanded an extension of the traditional notion of thermodynamics and leads to various approaches that are suitable for the understanding of thermodynamics involving quantum particles.

There are various approaches in quantum thermodynamics based on open quantum dynamics, fluctuation theorem, and resource theory [57]. In the first part of the thesis, we shall deal with the resource theoretic approach to the quantum thermodynamics of heat engines. The resource theory is an information-theory based rigorous mathematical framework which was initially developed in the context of entanglement theory. There are two resource theory based approaches in dealing with thermodynamics in the quantum regime: one is based on complete passivity [58–60] and another one is based on athermality [61–67]. The former one relies on asymptotically many (in thermodynamic limit) number of quantum particles in interaction with a thermal bath. The latter, on the other hand, extends thermodynamics in one-shot finite size regime where the number of particles can be finite and restricted to one or finite observations.

The study of quantum thermodynamics exploiting resource theory of athermality finds many interesting observations. For instance, it showed for the first time that thermodynamics in the one-shot finite size regime is fundamentally irreversible [62], and one cannot extract thermodynamic work from energetic coherence. In this regime, one

needs many second laws to determine the state transformations [64]. It also could quantify the one-shot extractable work from a given state and one-shot work cost to prepare a state of a system. Later on these second laws are extended to understand the transformation between states with energetic coherence [65]. However, all these studies are limited to the situation where a finite number of quantum particles interact with a single thermal bath. Here we develop a resource theory of quantum heat engine applicable to one-shot finite-size limit, where a few quantum particles simultaneously interact with two baths or more thermal baths at different temperatures [68]. For that, we first introduce free operations as semi-local thermal operations. These operations are defined to be the operations the quantum systems undergo through the strictly energy and entropy conserving non-local interactions with the baths. Accordingly, we also introduce the resource-free states, in thermodynamic sense, as the semi-thermal states. We show that any state that is not semi-thermal has some thermodynamic potential to perform work and these resources are quantified with the help of α-free entropies which is again expressed in terms of Rènyi relative entropies. With these, we systematically develop the resource theory and show that the thermodynamics of heat engines are fundamentally irreversible in the one-shot finite-size regime. To determine the state transformations, we find that one needs many second laws and derive them in terms of α-free entropies. This also enables us to quantify the one-shot extractable work from a state and the work cost to prepare a state. Beyond this, with the help of this framework, we propose a quantum heat engine that operates in one-step cycle and yields Carnot efficiency at maximum power. That concludes that the power-efficiency trade-off is no more a fundamental constraint in nature [69]. We also introduce a physically realizable model to realize such an engine using quantum optical systems.

b) *Synthetic negative temperature:* In general, there is no way that a quantum system can ever be genuinely isolated from its surrounding. That prompted the development of the idea of the open quantum system [70]. The evolution of closed quantum systems is often characterized by unitary dynamics. However, the system, together with the environment, forms a closed system, but when the dynamics of the system are considered, it is referred to as an open quantum system.

It is not possible to provide a unitary description of the evolution of the system of interest. The time dynamics of an open quantum system can be fully characterized by the Lindblad-Gorini-Kossakowski-Sudarshan (LGKS) form of master equation in the presence of weak coupling with the environment. It is widely used to study quantum optics [71], non-equilibrium statistical mechanics [72], condensed matter physics [73] and quantum information theory [74]. In non-equilibrium steady state scenarios, we see various interesting quantum phenomena [75,76], like macroscopic coherence phenomena [77], non-trivial topology [78], phase transition [33, 79, 80], topological transport [81], entanglement generation [82, 83], optical switching device [84], floquet insulators [85], floquet engineering [86], quantum computation [87, 88].

This thesis considers the cases where a finite-dimensional quantum system weakly interacts with multiple baths at different temperatures and utilizes open quantum dynamics as a resource to attain something that is otherwise not possible. In particular, we study steady-state thermodynamics with negative temperatures. One of the possibilities for quantum systems with bounded energy is that, in a certain situation, it can assume 'negative' temperatures. There the population distribution of a system or bath becomes an inverted Boltzmann distribution. In other words, states with higher energy are populated more than the ones with lower energy. It was first studied by Purcell and Pound in the context of nuclear spin systems [89]. Subsequently, Ramsey made a comprehensive discussion on the thermodynamic of negative temperatures and the inter-relation between negative and positive temperatures [90]. He argued that the Kelvin-Planck statement of the second law should be updated to incorporate that heat flows spontaneously from a bath with a negative temperature to one with a positive temperature.

This raised various fundamental questions on the thermodynamic meaning of negative temperature, see for example [91–94]. Nevertheless, the doubts regarding thermodynamics with negative temperatures are not resolved. Recent theoretical [95, 96] and experimental [97, 98] studies with cold atoms have brought the debate on negative temperatures back again into the spotlight. The works in [99–101] claim that "all previous negative temperature claims and their implications are invalid as they arise from the use of an entropy definition that is inconsistent both mathematically and thermodynam-

ically." Later studies in [102–108] argue that negative temperature is a valid extension of thermodynamics if the temperature is defined using Boltzmann entropy as the measure of entropy.

Apart from these foundational issues, there are studies to use negative temperature baths in constructing thermal devices, such as heat engines, refrigerators, heat pumps, etc. [109–111]. There are also some studies about how the Carnot cycle should be modified in the presence of negative temperatures [112–114]. Some propositions are also made to construct a quantum Otto engine [115, 116] and refrigerators [117] using baths with effective negative temperatures. It is shown that the heat-to-work conversion efficiency of an engine operating between negative and positive temperatures would be greater than the engines operating with positive temperatures [97, 98, 116]. However, much of these models of thermal devices either utilize already existing negative temperature baths without caring how it may be created or effectively prepare one by inverting the populations using some external means.

In this thesis, we outline a method to create a genuine thermal bath with arbitrary temperature, including negative temperature, and study steady-state quantum thermodynamics. The bath is synthesized by letting a quantum system simultaneously interact with two thermal baths at different temperatures without any external driving. With these synthetic baths, we study various laws of steady-state quantum thermodynamics and constructed heat engines. We start with proving the zeroth law and show that whenever two such baths with identical temperature are brought in touch with each other, there is no net heat flow. This, in turn, legitimizes the notion of the temperature of the synthetic bath (namely, the synthetic temperature). In case of two different temperatures, we prove the Kelvin-Planck statement of second law and demonstrate that there is a spontaneous heat flow from the bath with negative temperature to the one with positive temperature. This corroborates with the finding of Ramsey [90], the bath with negative temperature is 'hotter' than that of the ones with positive temperatures. Interestingly, in such cases, the entropy flow is opposite to the direction of heat flow which is again expected for the baths with negative temperatures. We also construct continuous heat engines involving synthetic baths and find that engines operating between positive and negative temperature baths can yield unit engine efficiency.

c) *Dynamical spectroscopy:* We investigated the quantum dynamics of a system in the presence of a strong external drive; the thermodynamic description is not possible here like in previous sections. Here we witness the transient quantum dynamics far from equilibrium. To explore that, we chose strong field physics. There has been a lot of interest across many new strong field phenomena, such as high harmonic generation [118, 119], multiphoton ionization [120], above-threshold ionization [38], nonsequential double ionization [121], attosecond pulse generation [122, 123], coherent EUV emission [124], etc.

The generation of higher-order harmonics is the result of interactions between intense light and material substances, e.g., gas, plasma, solid, or liquid samples. During this non-linear procedure, a strong light is used to illuminate the target, and as a consequence, the sample emits a high harmonic spectrum. Here, strong light refers to the energy of the laser field stronger than the binding field inside materials. The initial evidence of HHG came from the interaction of intense light with plasma [125], and later, from the interaction of strong light with gas [126]. Subsequently, Ferray *et. al.* showed the following interesting features of HHG spectra: as in a perturbative regime, spectral intensity decreases as the harmonic number increases, then decreases while intensity remains approximately constant, creating a plateau that cannot be explained by perturbation theory, and finally abruptly ends at the high harmonic cut-off [127]. This is the mandatory signature of HHG spectra. The Three-step model was then introduced by Corkum as an intuitive explanation of the HHG phenomena, which can provide a vivid and powerful insight into the mechanics of HHG [120]. This semi-classical model describes HHG in a three-step process: Ionization of an atom, acceleration of the released electron in the laser field, and subsequent recombination of the electron with the parent ion, all of which culminate in the emission of a photon with very high energy. In this scenario, electrons and field are considered classical objects, but dynamics follow quantum mechanical principles.

Lewenstein *et al.* provided a more inclusive interpretation of the Three-step model of the HHG, which became known as the Lewenstein model [118]. This model is also considered to be semi-classical due to the fact that it applies quantum mechanical principles to the

atomic degrees of freedom while using classical principles to the description of the field. In fact, both the Tree-step model and Lewenstein belong to the semi-classical domain. However, in comparison to the Three-step model, the Lewenstein model offers a description of the process of high-harmonic production that is both more comprehensive and better in agreement with experimental results. Recently, Lewenstein *et al.* have offered a revised interpretation, one that treats the HHG process as wholly quantum mechanical. [128].

Over the course of the past few decades, research into the HHG processes that occur in atomic and molecular gases has developed into a well-established and highly esteemed subsection of the field of research. To produce HHG in solids that are similarly effective and to adapt it to technology, a firmer grasp of the underlying mechanisms that govern HHG in solids is essential. In addition, the periodic nature of a crystalline solid and the band structure that is associated with it gives rise to a number of sophisticated phenomena, whereas such phenomena do not occur in atoms. Due to the nonparabolic character of the conduction bands, dynamic Bloch oscillations [129, 130], in particular, are accountable for the generation of high harmonics in solids. There is no manifestation of this behavior in atoms. The solids generally are studied in reciprocal space due to the periodic nature of solid crystals. In reciprocal space, the first step is to create an electron-hole pair from the valance band utilizing the strong electric field. Then, due to the absorption of the photon from the field, the electrons migrate to the conduction band. Crystal momentum follows the changing vector potential over time. The motion of carriers in the bands leads to non-perturbative intraband harmonic emission [119, 131]. Interband harmonic radiation is emitted at the same time as a consequence of recombination [132, 133]. There has been a lot of interest in high-harmonic production in solid-state materials such as dielectrics, conductors, and semiconductors [132, 134]. Ghimire *et al.* demonstrated the first experimental evidence of HHG in bulk crystal [119]. In fact, it enables the research of previously unexplored domains of physics and the invention of cutting-edge solid-state spectroscopy and microscopy technologies that study electronic configurations of solids [135, 136].

In recent years it has been found that the electrical conduction in solids is closely related to the topological properties of electronic wave functions of solids. In this thesis, we study the topological char-

acteristics of solids with the tool of HHG spectroscopy. A significant amount of attention and effort has been given to understanding and utilizing topological phases of matter in physics. Diverse systems on a variety of platforms have been designed to exhibit topological features, including such as solid [137–139], photonic [140–160], atomic [161–167], acoustic [168–183], etc.

Topological phases of the matter later emerged to be a new class of phases of materials that don't follow the Landau-Ginzburg paradigm. In contrast with other kinds of matter, topological matter exhibits entirely unique properties. This allows topological matter to protect itself against local perturbations and is consequently resilient against defects and disorder. Thus, the study of topological matter reveals the identification of previously unknown states of matter, such as topological insulators [42, 184–187] and topological superconductors [23, 188–190], each of which have distinctive electrical, optical, and thermal characteristics. One needs a strong field to produce HHG spectroscopy that makes it possible to access bulk modes as well as edge modes. This makes HHG spectroscopy the most efficient technique to characterize different kinds of solids [119, 191–194]. In the last section of the thesis, we investigate time dynamics that are far off from equilibrium and in the transient domain. Intense light interacts with matter and produces HHG. We treat this time dynamics as a resource to characterize various types of topological phases of matter. For the purpose of studying the topological characteristics of solids by HHG spectroscopy, we focus on the following models: the one-dimensional periodic and non-interacting SSH model, the one-dimensional non-interacting and quasi-periodic Aubry-Andŕe-Harper model, and one-dimensional interacting extended Fermi-Hubbard model (EFHM).

Jürß *et al.* introduced a method to distinguish topological and non-topological phases in a 1-D non-interacting SSH model by HHG spectroscopy [195]. But the most crucial question about the method is whether it can distinguish between different types of topological phases. Here we propose a method that can classify different types of topological phases in the SSH chain. To do so, we consider the 1-D chain of the extended SSH model where 1st, as well as 2nd nearest neighbor hopping, are allowed. We use the HHG-spectroscopic technique to distinguish between different types of topological phases with different modes in the 1-D chain of the extended SSH model.

We observe a phase transition between metal and insulators in open boundary conditions. Among the insulators, we can distinguish three different types of insulators: trivial insulators, topological insulators with two zero energy edge modes, and topological insulators with four zero energy edge modes.

In the project with the ESSH model, by utilizing the HHG spectroscopic technique, we observed that electrons in an insulating phase show remarkably different behaviors than electrons in a delocalized metallic phase. This motivates us to study in further detail localized and delocalized phases of matter with the tool of high harmonic spectroscopy. To do so, we consider the one-dimensional non-interacting and quasi-periodic Aubry-Andŕe-Harper model (AAH). Here, for different strengths of modulation, all single-particle states of the system are either fully localized or fully delocalized. Our goal is also to investigate the presence of topological edge states in the AAH model. Another special property of the energy state of the system is exhibited at the transition point between the localized and delocalized phases of the AAH model, that the system shows multi-fractal behavior. Within the purpose of this specific study, we investigate whether or not HHG spectroscopy can characterize the multi-fractal behavior and distinguish between the localized and delocalized phases. So far, we can see clearly from the strength of HHG spectra.

In this study, we also look at the Extended Fermi Hubbard Model (EFHM), which is a model of interacting electrons in 1-D solids. In 1-D, this model displays three unique phases, which are known as the charge density wave (CDW), the Mott insulator (MI), and the bond order wave (BOW), respectively. Each one of them demonstrates properties that are typical of the interacting insulating phases. In addition to this, BOW is capable of exhibiting topological behavior similar to that of the SSH model. In this particular project, we use the HHG spectroscopic technique to distinguish between three interacting insulating phases. Moreover, we study the BOW phase in detail to distinguish the two degenerate ground states with unique topological signatures.

1.1 Short overview of the thesis

This thesis is dedicated to investigating three different types of time dynamics of quantum systems: the system that evolves in the absence of an external drive, the system that is driven by a weak external drive, and the system that is driven by a strong external drive.

Chapter 2 studies those scenarios where the system is driven by self-drive and can approach thermal equilibrium. The thermodynamic description was possible for such a system. Using the information-theoretic tool, we develop a resource theoretic framework for a quantum heat engine. Our framework is able to provide a protocol for a one-step Carnot engine. We show thermodynamical reversibility is possible in the one-shot finite-size quantum regime. Exploiting genuine quantum mechanical properties, our heat engine can attain Carnot efficiency at maximum power in the one-shot finite-size quantum regime. Thus it has been shown that the power-efficiency trade-off is no more a fundamental constraint in nature.

Chapter 3 is dedicated to exploring the time dynamics of steady-state non-equilibrium scenarios. Using the open quantum system approach and Lindblad master equation, we create synthetic baths and study steady-state quantum thermodynamics in the presence of negative temperature. Various thermodynamics laws are derived in the presence of negative temperature and analyse their thermodynamic implications. Exploiting negative temperature baths, we introduce autonomous quantum heat engines and study their thermodynamic properties and efficiency.

In Chapter 4, we investigate the transient time dynamics of the quantum systems. In this particular scenario, an intense laser field illuminates the material, giving rise to higher-order harmonics. Utilizing this, we characterize the topological properties of three different types of systems: the one-dimensional periodic and non-interacting SSH model, the one-dimensional non-interacting quasi-periodic Aubry-Andŕe-Harper model, and the one-dimensional interacting extended Fermi-Hubbard model.

We discuss the future perspective of this thesis work in Chapter 5. Additionally, in Appendix A we provide all the background materials necessary to supplement the results discussed in Chapter 2. The supplementary information regarding the Chapter 3 and Chapter 4, respectively are provided in Appendix B and Appendix C.

Chapter 2

Resource theory of quantum heat engines

Heat engines are the fundamental building blocks of modern technology. These were invented primarily to convert heat into mechanical work. To lay a theoretical framework and to uncover the laws governing the processes in the engines, thermodynamics was empirically developed [196]. Later, it has been founded on statistical mechanics [197]. There, the *zeroth law* establishes the notion of thermodynamic equilibrium. The *first law* ensures the total energy conservation for feasible thermodynamic processes, and thereby restricts the class of operations that are thermodynamically allowed. The *second law* provides the necessary and sufficient conditions for the state transformations under such processes. For example, the Carnot's statement of second law delimits the efficiency of work extraction in a heat engine. The laws find deep implications in the fundamental understanding of nature, and are applicable in areas beyond their initial domain of application, such as in quantum mechanics, relativity, physics of black-holes, etc.

The formulation of standard thermodynamics (STh) based on statistical mechanics assumes that the systems are large and composed of an asymptotically large number of particles ($N \to \infty$) interacting with even larger baths, where the average fluctuation in energy approaches zero. This is termed usually as the *asymptotic regime*. When we perform measurement of thermodynamic quantities we typically get answers corresponding to ensemble average values. There, the ergodic theorem is assumed to be valid: the time averages are actually

equal to the ensemble averages. Therefore, the asymptotic regime is also assumed to allow many simultaneous or repeated measurements on the particles.

However, the standard thermodynamics (STh) cannot be easily extended beyond this asymptotic regime. The situation changes completely for the systems of a finite, but moderate or even small number of quantum particles ($N \ll \infty$). In such cases, from the very beginning, the fluctuations may play a much more important role. The situations may be classified in two regimes: *many-shot finite-size regime* - where repeated measurements (in time) are allowed on a system made up of moderate or a small number of particles, and *one-shot finite-size regime* - where only one-shot measurements are allowed on a system composed of a single or a moderate number of particles. One of the striking features in the one-shot finite-size regime is that the thermodynamics is fundamentally irreversible and needs many second laws to dictate state transformations [198, 199]. Because of that, a heat engine operating in this regime cannot in general achieve reversible transformation. As a consequence, it is not possible to attain the maximum possible heat-to-work conversion efficiency (i.e., the Carnot efficiency) in an engine following the Carnot cycle, unless the system interacting with the baths is made up of an asymptotically large number of particles.

In the last decades, enormous efforts have been put forward to extend thermodynamics to the regimes where a system made up of a finite (typically moderate or small) number of quantum particles interacts with a single thermal bath at fixed temperature [200, 201]. This also includes the situation where one has access to repeated, simultaneous, and one-shot measurements on the particles. It leads to two major approaches to studying quantum thermodynamics. The first, which applies in fact to both the asymptotic regime and the many-shot finite-size regime, is based on fluctuation theorems (FT), exploiting statistical mechanics and open quantum systems dynamics [202–204]. The other one is based on the quantum information theory [64, 198, 205–215]. Among others, the latter leads to a resource theory of quantum systems out of thermal equilibrium, which is commonly termed as the resource theory of quantum thermodynamics (RTQTh) [64, 198, 205]. The RTQTh is applicable to the asymptotic regime, and both many-shot and one-shot finite-size regimes. The RTQTh stands out among the other approaches as it exploits a rig-

orous mathematical framework similar to the resource theory of entanglement, where the latter was developed to characterize the role of entanglement in quantum information processing. There is also another formulation of a resource theory based on complete-passivity (CPTh) [212,213] that generalizes thermodynamics to the situation where system and baths become comparable in size. But, the CPTh is applicable to the asymptotic regime only. These different approaches can be classified in terms of their applications in different regimes, as given in Table 2.1.

Regimes	**Asymptotic** ($N \to \infty$)	**Finite-size** ($N \ll \infty$)
Repeated measurements	STh, CPTh, FT, RTQTh	FT, RTQTh
One-shot measurement	FT, RTQTh	RTQTh

Table 2.1: The table classifies various approaches based on their regime of applications. Here STh, FT, CPTh, and RTQTh represent the standard thermodynamics, the fluctuation theorem, the complete-passivity based resource theory of thermodynamics, and the resource theory of quantum thermodynamics respectively. The N denotes the number of particles in a system interacting with a thermal bath. Note, RTQTh fully characterizes quantum thermodynamics only for the systems that are block-diagonal in the energy eigenbases.

The resource theoretic formulation reveals that thermodynamics in the one-shot finite-size regime is not reversible and one needs many second laws, associated with many free energies, to characterize the transformations among the states that are block-diagonal in energy eigenbases [198, 207]. These second laws have been further studied for more general states having superpositions in energy eigenbases [64,208–210,216]. Interestingly, in [215], it has been shown that by allowing a non-vanishing amount of correlation all these many second laws can be reduced to a single one, based on standard Helmholtz free energy. Recently, the approaches based on fluctuation theory and resource theory have been inter-connected for some cases [217–219]. However, all these investigations are limited to the situations, where the quantum system is interacting with only *one* thermal bath at a fixed temperature. Therefore it is a natural

question to ask whether it is possible to formulate a *resource theory* for heat engines operating in the *one-shot finite-size regime*, where a system composed of few quantum particles is interacting with two or more thermal baths at different temperatures. Apart from some efforts to quantify extractable work and engine efficiency in few special cases, and to study the finite-size effects and the quantum signatures [220–229], there has been no major progress, so far, in formulating a resource theory for quantum heat engines.

The goal of this chapter is to formulate such a resource theory. It is worth mentioning that much of the earlier works, applied to the one-shot finite-size regime, focus on how the a-thermal (non-equilibrium) property of a system can be converted into thermodynamic work, and, for that, one thermal bath is enough. On the contrary, here we develop a resource theory of quantum heat engines to address how, and to what extent, the heat can be converted into work in the one-shot finite-size regime. Therefore, the theory is fundamentally different from the one considered in the earlier works. The new formalism provides the foundation for a novel theoretical understanding of the one-shot conversion of heat into work and the role of inter-system correlations in such processes. At the same time, it opens up new avenues to explore physically realizable quantum heat engines that have higher efficiency and attain Carnot efficiency in the one-shot finite-size regime.

As mentioned, the situation changes drastically once one considers thermodynamics in the presence of more than one thermal bath at different temperatures, which is the case for a heat engine. The first difficulty appears in defining the resource-free states. There does not exist a state that is simultaneously in equilibrium with all the baths. All states have some non-vanishing thermodynamic resources. Furthermore, it is not possible to define the free operations, as the free operations are supposed to map a resource-free state to a resource-free state. Therefore, one cannot formulate a resource theory for heat engines just by merely extending the one formulated for a single bath. Rather, to start with, it requires one to introduce a new class of thermodynamic operations that are allowed in a heat engine, a new form of states as the resource-free states, and to invoke new quantifiers of thermodynamic resources. This leads us to introduce an entirely new resource theory for quantum and nano-scale heat engines, below.

Further, we present quantum and nano-scale heat engines that attain the maximum possible heat-to-work conversion efficiency, i.e., the Carnot efficiency, in the one-shot finite-size regime. To prove our results and to address quantum thermodynamics in the one-shot finite-size regime in general, we formulate a resource theory for quantum heat engines in which a system with few quantum particles interacts with two or multiple thermal baths. With the precise characterization of thermodynamic operations by introducing a first law for engines, we derive the second laws for quantum state transformation in the presence of two or multiple baths at different temperatures by using information-theoretic tools. The newly introduced engine operations are more general in the sense that the system interacts with the baths simultaneously. We term these engine operations as "semi-local thermal operations" (SLTOs). The SLTOs not only enable us to build a Carnot heat engine operates with a one-step cycle but also enhances the work extraction efficiency in the one-shot finite-size regime – in this sense, the SLTOs is more powerful than the ones considered earlier. As revealed by this resource theoretic framework, the state transformations in the quantum engine are fundamentally irreversible in general and must obey many second laws. As an important result of this framework, we design a reversible engine transformation that attains the maximum possible efficiency for work extraction, i.e., the Carnot efficiency. Along with efficiency, power is also a key parameter to characterize a heat engine. If we want to study power and efficiency on the same footing. We encounter the fundamental power efficiency trade-off. An engine that transforms heat to work with maximum power can never achieve Carnot efficiency and vice versa. We address this problem by using a resource theoretic framework. It has been shown that the power efficiency trade-off is no more a fundamental constraint, and one can achieve Carnot efficiency with maximum power simultaneously. These qualities make out heat engine superior to other ones.

2.1 Resource-free operations and states

A typical (Carnot) heat engine is comprised of two heat baths B_1 and B_2 with the inverse temperatures $\beta_1 = 1/T_1$ and $\beta_2 = 1/T_2$ respectively and a working system, as shown in the Figure 2.1. We assume $\beta_1 < \beta_2$ throughout this chapter. The engine operates in a cycle composed of four thermodynamically reversible steps: (C1) First, an isothermal transformation $(\rho, H) \to (\sigma, H)$ in interaction with the bath B_1 at inverse temperature β_1, where the state changes $(\rho \to \sigma)$ without updating the system Hamiltonian H. (C2) Second, an adiabatic transformation $(\sigma, H) \to (\sigma, H')$ without any contact with the baths, where the system's state remains unchanged but the system Hamiltonian modifies to $H \to H'$. (C3) Third, an isothermal transformation $(\sigma, H') \to (\rho, H')$ in interaction with the bath B_2 at inverse temperature β_2, only changing the state. (C4) Finally, an adiabatic transformation $(\rho, H') \to (\rho, H)$ without any interaction with the baths, and updating only the system Hamiltonian $H' \to H$. The steps (C1)-(C4) constitute a cycle and the engine operates repeating the cycle many times. The important point is that, in the steps (C1) and (C2), the working system interacts with one bath at a time.

In our proposed quantum heat engine, we define a new engine operation where a working system (S_{12}) is composed of two non-interacting subsystems S_1 and S_2. The subsystems S_1 and S_2 semi-locally interact with the baths B_1 and B_2 respectively (see Figure 2.2). With this, the number of steps in the Carnot engine is reduced. For instance, consider that the subsystems S_1 and S_2 with the Hamiltonians H_{S_1} and H_{S_2} are in the states ρ and σ respectively. Then the isothermal steps (C1) and (C3) can be combined to one step, as

$$(\rho \otimes \sigma,\ H_{S_1} + H_{S_2}) \to (\sigma \otimes \rho,\ H_{S_1} + H_{S_2}),$$

where $H_{S_1} = H$ and $H_{S_2} = H'$, and $H_{S_1} + H_{S_2} \equiv H_{S_1} \otimes \mathbb{I}_{S_2} + \mathbb{I}_{S_1} \otimes H_{S_2}$. In this step, the subsystems swap their states without changing their Hamiltonian. Further, both the adiabatic steps (C2) and (C4) can be performed in one step as well, that is

$$(\sigma \otimes \rho,\ H_{S_1} + H_{S_2}) \to (\sigma \otimes \rho,\ H'_{S_1} + H'_{S_2}),$$

where $H'_{S_1} = H'$ and $H'_{S_2} = H$. Here the subsystems swap their local Hamiltonians without modifying their states. In fact, the four steps

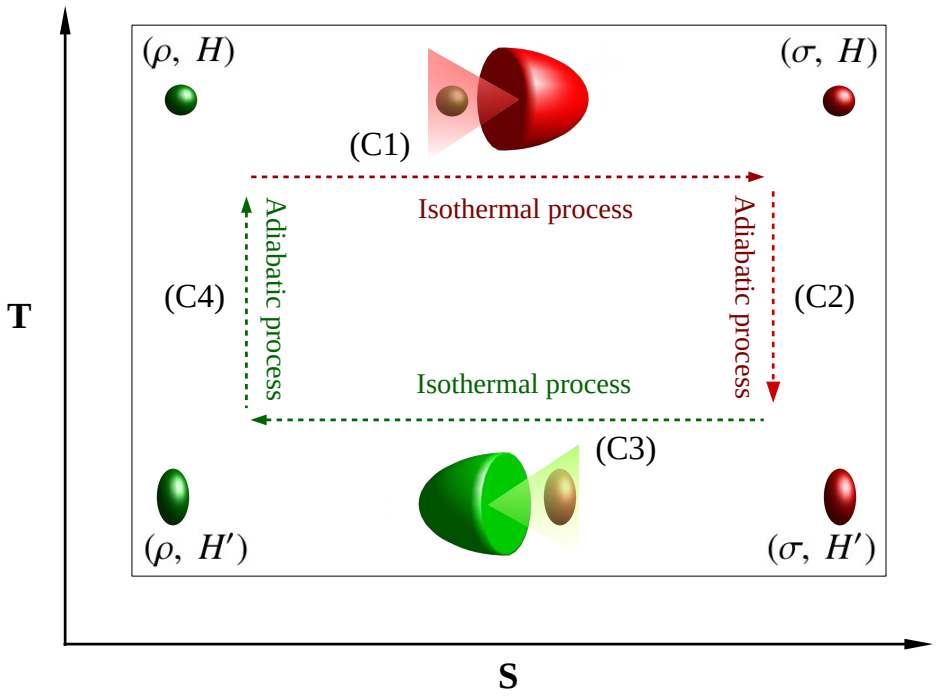

Figure 2.1: **A schematic of the operations in a traditional Carnot heat engine.** The horizontal and vertical axes are the thermodynamic entropy (S) and the temperature (T). The engine is made up of one working system and two heat baths with inverse temperatures $\beta_1 = 1/T_1$ and $\beta_2 = 1/T_2$, where $\beta_1 < \beta_2$. The operations in such an engine involve four distinct steps (C1)-(C4) in each cycle (see text for details). The steps (C1) and (C3) represent the isothermal transformations in interaction with thermal baths, where the state of the working system changes without changing the Hamiltonian (horizontal arrows). The steps (C2) and (C4) represents the adiabatic transformations in isolation from the baths, where the working system updates its Hamiltonian without changing its states (vertical arrows).

in a Carnot heat engine can be further reduced to just one step which enables one to attain maximum possible heat-to-work conversion efficiency, as we shall discuss later.

Semi-local thermal operations: Let us now introduce the general form of thermodynamically allowed (semi-local) operations that a (bipartite) quantum system S_{12} undergoes in a quantum heat engine. The bipartite system S_{12} can be in an arbitrary state. Even, the states may possess strong correlation, e.g., quantum entanglement, shared by the subsystems S_1 and S_2. The only restriction is that the Hamiltonian of the system is non-interacting and has the form $H_{S_{12}} = H_{S_1} + H_{S_2}$, where H_{S_1} and H_{S_2} are the local Hamiltonians of the subsystems S_1 and S_2 respectively. The Hamiltonians of the baths B_1 and B_2 are denoted as H_{B_1} and H_{B_2} respectively.

Definition 1 (Semi-local thermal operations (SLTOs))**.** *In a quantum heat engine, the thermodynamic operations on system S_{12} in a state $\rho_{S_{12}}$ are defined as*

$$\Lambda_{S_{12}}\left(\rho_{S_{12}}\right) = \mathrm{Tr}_{B_1B_2}\left[U(\gamma_{B_1}\otimes\gamma_{B_2}\otimes\rho_{S_{12}})U^\dagger\right], \tag{2.1}$$

with the condition that the global unitary U satisfies the commutation relations

$$\left[U,\ H_{B_1}+H_{S_1}+H_{B_2}+H_{S_2}\right] = 0, \tag{2.2}$$
$$\left[U,\ \beta_1\left(H_{B_1}+H_{S_1}\right)+\beta_2\left(H_{B_2}+H_{S_2}\right)\right] = 0, \tag{2.3}$$

where the thermal states of the baths are denoted by $\gamma_{B_x} = \frac{e^{-\beta_x H_{B_x}}}{\mathrm{Tr}\left[e^{-\beta_x H_{B_x}}\right]}$ for $x = 1, 2$.

The resultant operations on the system S_{12} are semi-local in the sense that, even though the subsystems (S_1 and S_2) "selectively" interact with the baths (B_1 and B_2), the unitary U still allows certain interactions among them with the constraints (2.2) and (2.3). It should be noted that the commutation relations (2.2) and (2.3) together constitute the *first law* for quantum heat engines. It ensures strict conservation of the total energy $E_{12} = E_1 + E_2$ and the total weighted-energy $E_{12}^{\beta_1\beta_2} = \beta_1 E_1 + \beta_2 E_2$ of the baths and the system,

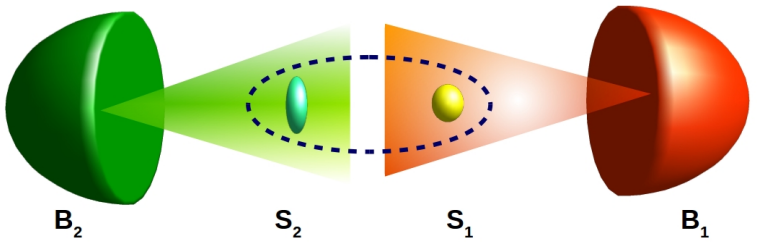

Figure 2.2: **Semi-local thermal operations.** Instead of considering a system undergoing a transformation in the presence and absence of baths once at a time, we generalize the engine operations using a bipartite system S_{12}, with two non-interacting sub-systems S_1 and S_2 and the Hamiltonian $H_{S_{12}} = H_{S_1} + H_{S_2}$. There, the sub-systems S_1 and S_2 are *semi-locally* interacting with the baths B_1 and B_2 at inverse temperature β_1 and β_2 respectively, at the same time. The bath-system composites B_1S_1 and B_2S_2 are allowed to exchange energy through *semi-local thermal operations* (SLTOs), as introduced in Definition 1.

where E_1 and E_2 are the energies of the B_1S_1 and B_2S_2 composites respectively. In other words, the global unitary U respects

$$\Delta E_1 + \Delta E_2 = 0, \tag{2.4}$$
$$\beta_1 \Delta E_1 + \beta_2 \Delta E_2 = 0, \tag{2.5}$$

where ΔE_1 and ΔE_2 are the changes in energy in B_1S_1 and B_2S_2 respectively. The strict energy conservation ensured by the constraint (2.2) (or Eq. (2.4)) is absolutely important to guarantee the proper counting of work involved in a process. The constraint (2.3) (or Eq. (2.5)) brings up the semi-local character of the operation. In particular, for a system S_{12} with the subsystems S_1 and S_2 that are initially in local thermal equilibrium with the baths B_1 and B_2 respectively, the unitary U cannot bring the subsystems away from their local equilibrium even though it is a global operation (see Appendix A.3).

As it will be clear soon, the relation (2.3) or Eq. (2.5) guarantee that no thermodynamic resource (free-entropy) can be created in S_{12} by employing SLTOs if the subsystems S_1 and S_2 are initially in thermal equilibrium with the baths B_1 and B_2 respectively. From the information theory point of view, these constraints also imply that

the global unitary operations that respect the first law conserve the thermodynamic purity.

The SLTOs can be further generalized with an access to a bipartite catalyst C_{12} composed of two non-interacting subsystems C_1 and C_2 and the Hamiltonian $H_{C_{12}} = H_{C_1} + H_{C_2}$. The C_1 is clubbed with the subsystem S_1 to form the composite S_1C_1. Similarly, the C_2 is clubbed with the S_2 to form S_2C_2. Then, the composites S_1C_1 and S_2C_2 interacts with the baths B_1 and B_2 via semi-local thermal operations. Such operations are called *catalytic semi-local thermal operations* (cSLTOs) that satisfy

$$\Lambda_{S_{12}C_{12}}(\rho_{S_{12}} \otimes \rho_{C_{12}}) \to \sigma_{S_{12}} \otimes \rho_{C_{12}}, \tag{2.6}$$

where $\rho_{C_{12}}$ is a state of the catalyst. Note, the catalyst remains unchanged before and after the process. These catalytic operations form a larger set of thermodynamically allowed operations compared to SLTOs and respect all the properties satisfied by the SLTOs. The cSLTOs are the allowed thermodynamic operation in a quantum heat engine and constitute the free operation for the resource theory developed in this article. Several useful properties of these operations are outlined in the Appendix A.4. It is interesting to note that the cSLTOs converge to the (local) thermal operations that are introduced in the resource theory of quantum states beyond thermal equilibrium presented in [64, 198, 205], when both the baths are of the same temperature, i.e., for $\beta_1 = \beta_2$.

Semi-Gibbs states: When the subsystems are locally in thermal equilibrium with the baths they are semi-locally interacting with, the corresponding joint uncorrelated state of the system S_{12} becomes $\gamma_{S_{12}} = \gamma_{S_1} \otimes \gamma_{S_2}$, where $\gamma_{S_x} = e^{-\beta_x H_{S_x}} / Z_x$ with the partition functions $Z_x = \mathrm{Tr}\left[e^{-\beta_x H_{S_x}}\right]$ for $x = 1, 2$. We term these states as the *semi-Gibbs* states, as both the local states are Gibbs states with different temperatures corresponding to the baths. The subsystems may assume arbitrary Hamiltonians. The set of all such semi-Gibbs states is denoted by the set $\mathcal{T}_{S_{12}} \ni \gamma_{S_{12}}$. These states are the resource-free states in the resource theory of heat engines that we develop below.

2.2 Resource quantification and state transformation

With the identification of the resource-free states and the free operation with the semi-Gibbs states and the cSLTOs, respectively, we move on to formulate the resource theory. We introduce a resource quantifier that is related to thermodynamic work. The goal is to characterize the general state transformations under the cSLTOs and quantify the thermodynamic work associated with a process occurring in an engine in the one-shot finite-size regime. A major part of the results we discuss below are restricted to the states $\rho_{S_{12}}$ that are block-diagonal in the energy eigenbases of the system Hamiltonian $H_{S_{12}}$, i.e.,

$$[\rho_{S_{12}}, H_{S_{12}}] = 0. \tag{2.7}$$

The cSLTOs are time-translation symmetric with respect to the time-translation driven by $H_{S_{12}}$, and that is why the cSLTOs monotonically decrease the superpositions between different energy eigenbases (see Appendix A.4). A heat engine operates in an arbitrarily large number of cycles. It is, therefore, safe to assume that an arbitrary state will dephase to its block-diagonal form after some cycles. That is why we mainly focus on the transformations among states that are block-diagonal in the energy eigenbases. Although, we briefly discuss the situation when the states are not block-diagonal (see Appendix A.9).

We define the α-free-entropies as the quantifiers of thermodynamic resource for a system composed of an arbitrary number of quantum particles undergoing a transformation in a quantum heat engine.

Definition 2 (α-free-entropies)**.** *Consider a system S_{12} is in a state $\rho_{S_{12}}$ block-diagonal in the eigenbasis of the Hamiltonian $H_{S_{12}}$. Then the α-free-entropy of $\rho_{S_{12}}$ is expressed, for all $\alpha \in [-\infty, \infty]$, as*

$$S_\alpha(\rho_{S_{12}}, \gamma_{S_1} \otimes \gamma_{S_2}) = D_\alpha\left(\rho_{S_{12}} \parallel \gamma_{S_1} \otimes \gamma_{S_2}\right) - \log Z_1 Z_2, \tag{2.8}$$

where the Rényi α-relative entropy is given by

$$D_\alpha(\rho \parallel \gamma) = \frac{sgn(\alpha)}{\alpha - 1} \log \mathrm{Tr}\left[\rho^\alpha \, \gamma^{1-\alpha}\right].$$

Here the thermal states of the subsystems are $\gamma_{S_x} = \frac{e^{-\beta_i H_{S_x}}}{Z_x}$*, and the partition functions are* $Z_x = \mathrm{Tr}\left[e^{-\beta_x H_{S_x}}\right]$ *for* $x = 1, 2$.

The α-free-entropies quantify the thermodynamic purity present in the state $\rho_{S_{12}}$. It can be checked that the α-free-entropies vanish for the semi-Gibbs states. Thus, as expected, these do not possess a non-zero thermodynamic purity. For $\rho_{S_{12}} = \rho_{S_1} \otimes \rho_{S_2}$, the α-free-entropy is additive as $S_\alpha(\rho_{S_{12}}, \gamma_{S_1} \otimes \gamma_{S_2}) = S_\alpha(\rho_{S_1}, \gamma_{S_1}) + S_\alpha(\rho_{S_2}, \gamma_{S_2})$, where $S_\alpha(\rho_{S_x}, \gamma_{S_x}) = D_\alpha\left(\rho_{S_x} \,\|\, \gamma_{S_x}\right) - \log Z_x$. We recover Helmholtz free-entropy $S_1(\rho_{S_{12}}, \gamma_{S_1} \otimes \gamma_{S_2}) = \beta_1 E_{S_1} + \beta_2 E_{S_2} - S(\rho_{S_{12}})$ for $\alpha \to 1$, where $E_{S_1/S_2} = \mathrm{Tr}\, H_{S_{1/2}} \rho_{S_{12}}$ is the energy of the subsystem and $S(\rho_{S_{12}})$ is the von Neumann entropy. Thus the α-free-entropies are the one-shot generalizations of the Helmholtz free-entropies defined in the context of thermodynamics with multiple conserved charges, where the charges are mutually commuting and fully independent from each other, i.e., the charges live in disjoint Hilbert spaces. With the α-free-entropies, the transformations in a quantum heat engine can be characterized in terms of the second laws.

Many second laws for block-diagonal states: Consider a general transformation, via cSLTO,

$$\left(\rho_{S_{12}}, H_{S_{12}}\right) \to \left(\sigma'_{S_{12}}, H'_{S_{12}}\right), \tag{2.9}$$

where along with the transformation among the block-diagonal states ($\rho_{12} \to \sigma'_{12}$) the initial non-interacting Hamiltonian $H_{S_{12}} = H_{S_1} + H_{S_2}$ of the system S_{12} is updated to $H'_{S_{12}} = H'_{S_1} + H'_{S_2}$. Then the second laws that provide the necessary and sufficient conditions for such transformations are given in the theorem below. This theorem can be proven using similar lines of reasoning as the ones considered in Ref. [64], with additional complexities and technicalities particular to the engine scenario (see Appendix A.6).

Theorem 1 (Second laws for block-diagonal states)**.** *Under cSLTOs, the transformation in Eq.* (2.9) *is possible if, and only if,*

$$S_\alpha\left(\rho_{S_{12}}, \gamma_{S_1} \otimes \gamma_{S_2}\right) \geqslant S_\alpha\left(\sigma'_{S_{12}}, \gamma'_{S_1} \otimes \gamma'_{S_2}\right), \quad \forall \alpha \geqslant 0, \tag{2.10}$$

where $\gamma_{S_x} = \frac{e^{-\beta_x H_{S_x}}}{\mathrm{Tr}\left[e^{-\beta_x H_{S_x}}\right]}$ *and* $\gamma'_{S_x} = \frac{e^{-\beta_x H'_{S_x}}}{\mathrm{Tr}\left[e^{-\beta_i H'_{S_i}}\right]}$*, for* $x = 1, 2$.

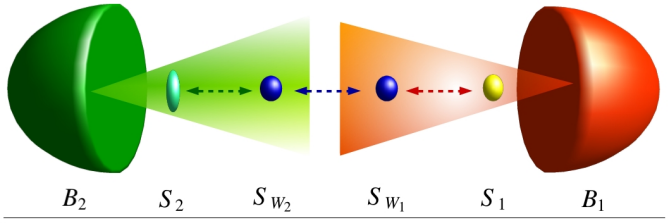

Figure 2.3: **Extraction of free-entropy.** A battery $S_{W_{12}}$ with two non-interacting sub-systems S_{W_1} and S_{W_2} is used to store free-entropy (or work) once extracted. The battery subsystems can be the two-level systems and are restricted to remain in the pure states always. For the protocol to extract free-entropy and work, see text.

Therefore, any transformation among the block-diagonal states under the cSLTOs must respect the above monotonic relation for the α-free-entropies for all α. For the transformation among the states that are not block-diagonal in the eigenbases of $H_{S_{12}}$, the above constitutes only the necessary conditions where the corresponding dephased block-diagonal states have to satisfy (2.10). This necessary condition can be further supplemented with the monotonic decrease of quantum time-translation asymmetry present in the states, as cSLTOs are time translation symmetric operations (Appendix A.9).

Free-entropy distance, work, and fundamental irreversibility: Apart from dictating state transformations, the Theorem 1 delimits the amount of thermodynamic resource, i.e., free-entropy, can be extracted using a state transformation in an engine. It also quantifies the amount of the free-entropy required to be expended to make a transformation possible. Now the free-entropy distance is introduced to quantify the extractable free-entropy or the free-entropy cost in the one-shot finite-size regime, in terms of the works that can be stored in a battery. Here, a battery is an additional quantum system that stores work in the form of pure energy.

Now, a battery $S_{W_{12}}$, with two sub-systems S_{W_1} and S_{W_2} and the non-interacting Hamiltonian $H_{S_{W_{12}}} = H_{S_{W_1}} + H_{S_{W_2}}$ is attached with the system S_{12} to store free-entropy (or work) once extracted, as shown in Figure 2.3. Without loss of generality, the battery subsystems are considered to be two-level systems with the Hamiltonians

$H_{S_{W_1}} = W_1|W_1\rangle\langle W_1|_{S_{W_1}}$ and $H_{S_{W_2}} = W_2|W_2\rangle\langle W_2|_{S_{W_2}}$, and these are restricted to remain in the eigenstates of the Hamiltonians always. The S_{W_1} is tagged with subsystem S_1 and similarly the S_{W_2} is with S_2. The initial battery state is chosen to be the zero-energy state $\rho^i_{S_{W_{12}}} = |0\rangle\langle 0|_{S_{W_1}} \otimes |0\rangle\langle 0|_{S_{W_2}}$. The composites $S_1S_{W_1}$ and $S_2S_{W_2}$ interact with the baths B_1 and B_2 (at different inverse temperatures β_1 and β_2) respectively through semi-local thermal operations, so that the overall transformation is

$$\left(\rho_{S_{12}} \otimes \rho^i_{S_{W_{12}}},\ H_{S_{12}} + H_{S_{W_{12}}}\right) \to \left(\sigma'_{S_{12}} \otimes \rho^f_{S_{W_{12}}},\ H'_{S_{12}} + H_{S_{W_{12}}}\right),$$

where final state of the battery is $\rho^f_{S_{W_{12}}} = |W_1\rangle\langle W_1|_{S_{W_1}} \otimes |W_2\rangle\langle W_2|_{S_{W_2}}$. Note, the battery Hamiltonian remains unchanged in the transformation. The values of W_1 and W_2 depend on the very cSLTO under which the transformation happens. Therefore, it is natural to ask how much a guaranteed amount of free-entropy involved in a transformation. To answer that, we introduce the free-entropy distance in the theorem below. We refer to the Supplemental Information for the proof.

Theorem 2 (Free-entropy distance)**.** *For the transformation in Eq.* (2.9) *via a cSLTO, the free-entropy distance between the initial and final states of the system is given by*

$$\begin{aligned} S_d(\rho_{12} \to \sigma'_{12}) &= \beta_1 W_1 + \beta_2 W_2, \\ &= \inf_{\alpha \geqslant 0} \left[S_\alpha(\rho_{S_{12}}, \gamma_{S_1} \otimes \gamma_{S_2}) - S_\alpha(\sigma'_{S_{12}}, \gamma'_{S_1} \otimes \gamma'_{S_2}) \right]. \end{aligned} \tag{2.11}$$

As we mentioned earlier, the change in thermodynamics purity which is measured in terms of the change in free-entropy is related to work. From this free-entropy distance, the one-shot work can be derived. Consider the transformation given in Eq. (2.9) via a cSLTO. If the initial state possesses larger free-entropy than the final one, i.e., $S_\alpha\left(\rho_{S_{12}}, \gamma_{S_1} \otimes \gamma_{S_2}\right) \geqslant S_\alpha\left(\sigma'_{S_{12}}, \gamma'_{S_1} \otimes \gamma'_{S_2}\right)$ for all $\alpha \geqslant 0$, the transformation can take place spontaneously under cSLTOs. For this forward process, the $S_d(\rho_{12} \to \sigma'_{12}) = \beta_1 W_1^f + \beta_2 W_2^f \geqslant 0$. Then, the guaranteed *one-shot extractable work* from the process is

$$W_{ext} = W_1^f + W_2^f \geqslant 0. \tag{2.12}$$

In the special case where the final state is the semi-Gibbs state $\sigma'_{12} = \gamma_{S_1} \otimes \gamma_{S_2}$ and the subsystem Hamiltonians do not change $H_{S_{12}} = H'_{S_{12}}$, the W_{ext} quantifies the *one-shot distillable work* from the state $\rho_{S_{12}}$.

To perform the reverse transformation $\left(\sigma'_{S_{12}}, H'_{S_{12}}\right) \to (\rho_{S_{12}}, H_{S_{12}})$, the Theorem 2 constrains that the minimum one-shot free-entropy to be supplied to ascertain the transformation is

$$\begin{aligned} S_d(\rho_{12} \leftarrow \sigma'_{12}) &= \beta_1 W_1^b + \beta_2 W_2^b, \\ &= \sup_{\alpha \geqslant 0} \left[S_\alpha(\rho_{S_{12}}, \gamma_{S_1} \otimes \gamma_{S_2}) - S_\alpha(\sigma'_{S_{12}}, \gamma'_{S_1} \otimes \gamma'_{S_2}) \right]. \end{aligned} \tag{2.13}$$

Now, the minimum necessary work required, that is the *one-shot work cost*, to implement the transformation is

$$W_{cost} = W_1^b + W_2^b \geqslant 0. \tag{2.14}$$

For $\sigma'_{12} = \gamma_{S_1} \otimes \gamma_{S_2}$ and $H_{S_{12}} = H'_{S_{12}}$, the W_{cost} represents the *one-shot work of formation* of the state $\rho_{S_{12}}$.

Fundamentally, the thermodynamic reversibility is no longer respected in the one-shot finite-size regime. This irreversibility can be understood from the fact that the free-entropy distance of a forward process is not in general equal to its reverse process, and

$$S_d(\rho_{12} \to \sigma'_{12}) \leqslant S_d(\rho_{12} \leftarrow \sigma'_{12}), \tag{2.15}$$

where the equality holds for a few special cases. As a corollary, the extractable work from the transformation and the work cost to reverse it are not equal and follow the inequality $W_{ext} \leqslant W_{cost}$, where, again, the equality holds only in few cases. However, in the asymptotic limit, i.e., when the working system is composed of an asymptotically large number of particles, the reversibility is recovered as the equality in Eq. (2.15) is achieved on average (see Appendix A.10).

Heat engine exclusively utilizing correlation: It is known that the inter-system correlation can store thermodynamic work potential and can lead to "anomalous" heat flow - a spontaneous heat transfer from a cooler to a warmer body [211]. However, the studies were restricted to the asymptotic regime. Now, we are able to characterize such thermodynamic potential and its role in anomalous heat flow in the

one-shot finite-size regime. For example, consider a system state $\rho_{S_{12}}$ which has non-vanishing correlation shared by the subsystems S_1 and S_2, i.e., $\rho_{S_{12}} \neq \rho_{S_1} \otimes \rho_{S_2}$, where $\rho_{S_1} = \mathrm{Tr}_{S_2}[\rho_{S_{12}}]$ and $\rho_{S_2} = \mathrm{Tr}_{S_1}[\rho_{S_{12}}]$. Now the one-shot free-entropy stored in the correlation is given by

$$S_d(\rho_{S_{12}} \to \rho_{S_1} \otimes \rho_{S_2}) = \beta_1 W_1^c + \beta_2 W_2^c. \tag{2.16}$$

The work store in the correlation is $W_{ext}^c = W_1^c + W_2^c$ and this work can be utilized to drive heat flow from the cold to the hot bath, as it happens in a refrigeration process. Note, the block-diagonal states can possess classical correlations. These states are sufficient to run an engine that repeats its cycle many times. Consequently, one may construct a heat engine that exclusively exploits the (classical) correlation to convert heat into work. For that, one needs an initial correlated bipartite system in the state $\rho_{S_{12}}$ and the final uncorrelated state $\sigma'_{S_{12}} = \rho_{S_1} \otimes \rho_{S_2}$ in each cycle, where $\rho_{S_1/S_2} = \mathrm{Tr}_{S_2/S_1}[\rho_{S_{12}}]$. We must note that only the classical correlations can be accessed and utilized in the one-shot finite-size regime. However, in the asymptotic regime, any form of correlation, including the quantum entanglement, can be accessed to drive a heat engine (see Appendix A.10).

2.3 Quantum heat engines with Carnot efficiency at maximum power

One of the central laws of thermodynamics for heat engines in the classical regime, that is, the second law, imposes a fundamental limit on the maximum heat-to-work conversion efficiency in an engine, given by Carnot efficiency. This efficiency is only achieved when the engine operates in a cycle using reversible transformations, which requires it to run infinitely slowly. As a consequence, the engine's power - work extracted per unit time - becomes close to null. In general, realistic engines operate in finite time to deliver a non-vanishing power, and then, the efficiency is compromised. The trade-off between efficiency and power is studied extensively in the past decades; see, for example, [230–232], in the context of finite-time classical engines.

In general, the laws of thermodynamics cannot be directly applied to the engines that use working fluids made up of few particles. In

that case, the conventional (or statistical) notion of average quantities such as energy or entropy becomes incomplete. The situation becomes further constrained for engines operating in the quantum regime, where the working fluid is composed of few quantum systems and the effects due to quantum fluctuations cannot be ignored. There have been extensive studies to understand thermodynamics in this regime, see for example [64, 198, 201–206, 210–218, 233], and it is revealed that, in general, a quantum system in contact with a thermal bath delivers fluctuating work. Consequently, a quantum engine, where a working fluid sequentially or incoherently interacts with two baths in a cycle in the presence of highly fluctuating input and output energy fluxes, is expected to have fluctuations in both efficiency and power, see for example [69, 222, 224, 226, 234–259]. In fact, finite size heat engines, in general, deliver fluctuating efficiency [222, 237, 239]. It is also true for power for engines operating with finite-time cycle [245, 250]. Apart from that, there are power losses due to energy coherence [244]. Also, there are proposals that smartly exploit energy coherence to increase power, see for example [236, 241, 251]. The overall performance of an engine considering inter-relations between power and efficiency in the presence of quantum fluctuation are studied in [69, 247, 248, 250–256, 260]. In [243], the authors derive the lower and upper bound on maximum efficiency at a given power for the low dissipation heat engines. This bound generalizes the bound on efficiency at maximum power given by [247]. These engines also exhibit universal constraints for efficiency and power [249]. For general cases, a universal trade-off between efficiency and power is introduced in [69]. A trade-off relation based on geometric arguments is derived in [253] for any thermodynamically consistent microdynamics. Further studies based on the geometry of work fluctuation and efficiency are made in [254] for microscopic heat engines.

As in classical engines, it is now commonly believed that yielding maximum power at Carnot efficiency is impossible in a quantum engine. Earlier studies have assumed engines with a working system that interacts with the hot and cold baths at different stages of an engine cycle or with both baths simultaneously but only enabling incoherent heat transfer. Furthermore, the working system is either composed of a statistically large number of particles, or a few particles, allowing a large number of measurements. The role of quantum fluctuations in delimiting efficiency or power or both becomes more

prominent for the quantum engines operating in the one-shot finite-size regime, i.e., engines with a finite number of quantum particles constituting the working system and restricted to one-shot measurements or observations. So far, there are no comprehensive studies on that.

Here we introduce quantum heat engines operating in the one-shot finite-size regime and study the power and efficiency of heat-to-work conversion. We show that these engines can simultaneously attain maximum efficiency, i.e., the Carnot efficiency, and maximum power in the one-shot finite-size regime. Therefore, there is no fundamental trade-off between power and efficiency that an engine has to respect in the quantum regime. Our approach is fundamentally different from the earlier ones in the sense that: (i) the engines are fully quantum as they operate in the one-shot finite-size regime and allow genuine entanglement between the baths and working system, (ii) the working system simultaneously interacts with the hot and cold baths via semi-local thermal operations, and (iii) the engines run in a one-step cycle. The framework relies on the resource theory recently developed to establish the thermodynamic laws in quantum heat engines [261]. The engines deliver maximum power, along with Carnot efficiency, purely because the engines allow a coherent transfer of heat from hot to cold baths by establishing quantum entanglement between the working system and the baths, thereby attaining maximum quantum speed for the reversible state transformation in each engine cycle. Finally, we also introduce a physically realizable quantum heat engine based on a quantum-optical system.

2.3.1 Engine operating in one-step cycle

We consider an engine composed of two baths B_1 and B_2 with corresponding Hamiltonians H_{B_1} and H_{B_2} and inverse temperatures β_1 and β_2 respectively; a bipartite (working) system S_{12} with non-interacting subsystems S_1 and S_2 and described by the Hamiltonian $H_{S_{12}} = H_{S_1} + H_{S_2}$; a bipartite battery $S_{W_{S_{12}}}$ with non-interacting subsystems S_{W_1} and S_{W_2} with the Hamiltonian $H_{S_{W_{12}}} = H_{S_{W_1}} + H_{S_{W_2}}$. Here the battery plays the role of a piston in a traditional engine that takes away work converted from heat. Throughout this work, we assume $\beta_1 < \beta_2$. All systems under consideration have Hamiltonians bounded from below, with the lowest energy equal to zero. The baths

are considerably large compared to the systems, and the degeneracy in their microcanonical ensembles scales exponentially with the change in energy. That means the energies of the working systems and the battery are tiny compared to the baths, while the latter have the highest energies close to infinity. The properties of large baths are outlined in Appendix A.1.

The engine lets the baths interact with the working system and the batteries via a global unitary evolution (U) where the composite $S_1S_{W_1}$ semi-locally interacts with B_1 and $S_2S_{W_2}$ with B_2. As a result, a semi-local thermal operation (SLTO) (Eq. (1)) is implemented on the system-battery composite $S_{12}S_{W_{12}}$.

$$\begin{aligned}\Lambda_{S_{12}S_{W_{12}}}&\left(\rho_{S_{12}}\otimes\rho_{S_{W_{12}}}\right)\\&=\mathrm{Tr}_{B_1B_2}\left[U(\gamma_{B_1}\otimes\gamma_{B_2}\otimes\rho_{S_{12}}\otimes\rho_{S_{W_{12}}})U^\dagger\right],\end{aligned}\tag{2.17}$$

where the global unitary U satisfies

$$\left[U,\ H_{B_1}+H_{S_1}+H_{S_{W_1}}+H_{B_2}+H_{S_2}+H_{S_{W_2}}\right]=0,\tag{2.18}$$

$$\left[U,\ \beta_1\left(H_{B_1}+H_{S_1}+H_{S_{W_1}}\right)+\beta_2\left(H_{B_2}+H_{S_2}+H_{S_{W_2}}\right)\right]=0.\tag{2.19}$$

Here the baths are in the equilibrium states denoted by $\gamma_{B_x}=\frac{e^{-\beta_x H_{B_x}}}{\mathrm{Tr}\left[e^{-\beta_x H_{B_x}}\right]}$ for $x=1,2$, and $\rho_{S_{12}}$ is any state of S_{12}. The $\rho_{S_{W_{12}}}$ is the state of the battery $S_{W_{12}}$, where the subsystems S_{W_1} and S_{W_2} always remain in their energy eigenstates and store or supply energy in the form of work. The commutation relation (2.18) guarantees strict conservation of total energy of baths-system-battery composite. Note, this ensures conservation of all moments of energy and not just the average energy. The relation (2.18), in turn, represents the quantum version of the first law for engines. The relation (2.19) ensures strict weighted energy conservation.

In an engine operating in cycles, the system S_{12} mediates the heat transfer from B_1 to B_2, while a part of that is converted into work and stored in the battery $S_{W_{12}}$. At the end of each cycle, the S_{12} should recover its initial state so it can be reused for the next cycle. But the battery gets excited to a higher energy eigenstate to store work. Interestingly, the engine executes this transformation in a one-step cycle (see Figure 2.4) by implementing semi-local thermal operations

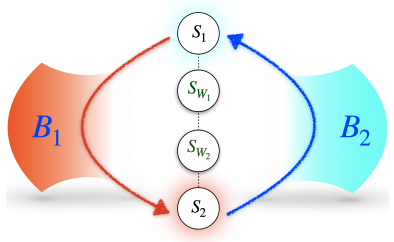

Figure 2.4: **One-step engine cycle.** An engine consists of two baths B_1 and B_2 at inverse temperatures β_1 and β_2 ($\beta_1 < \beta_2$), a working system $S_{12} \equiv S_1 S_2$ and a battery $S_{W_{12}} \equiv S_{W_1} S_{W_2}$. In each one-step engine cycle, the composite $S_1 S_{W_1} - S_{W_2} S_2$ semi-locally interact with the baths $B_1 - B_2$ and undergoes a transformation so that the working sub-systems S_1 and S_2 swaps their states along with Hamiltonians (as indicated by the arrows) and the battery sub-systems update their states. As a result, there is an overall flow of heat from B_1 to B_2 and, in this process, part of that heat is converted into work and stored in $S_{W_1} S_{W_2}$. At the end of each cycle, the state of $S_1 S_2$ becomes identical to its initial state upto a swap operation and is, again, reused in the next cycles. See text for more details.

on $S_{12} S_{W_{12}}$, as

$$\left(\rho_{S_{12}} \otimes \rho^i_{S_{W_{12}}},\ H_{S_{12}} + H_{S_{W_{12}}}\right) \to \left(\sigma'_{S_{12}} \otimes \rho^f_{S_{W_{12}}},\ H'_{S_{12}} + H_{S_{W_{12}}}\right).$$

Consequently, the state of the working system transforms as $\rho_{S_{12}} \to \sigma'_{S_{12}}$ and at the same time the Hamiltonian is modified as $H_{S_{12}} = H_{S_1} + H_{S_2} \to H'_{S_{12}} = H'_{S_1} + H'_{S_2}$. Further, it satisfies the cyclicity conditions $\sigma'_{S_{12}} = U_{S_1 \leftrightarrow S_2}\left(\rho_{S_{12}}\right)$, $H'_{S_1} = H_{S_2}$, and $H'_{S_2} = H_{S_1}$, where the unitary $U_{S_1 \leftrightarrow S_2}$ swaps the states of the subsystems S_1 and S_2. The battery undergoes the transformation $\rho^i_{S_{W_{12}}} \to \rho^f_{S_{W_{12}}}$ without updating its Hamiltonian. To understand how the above transformation executes the (four-step) Carnot cycle in one-step, let us focus on the transformation happening in the system, that is $(\rho_{S_{12}}, H_{S_{12}}) \to (\sigma'_{S_{12}}, H'_{S_{12}})$. For this purpose, we ignore the battery as it only changes states without updating its Hamiltonians and thereby stores or releases work. Consider, $\rho_{S_{12}} = \rho \otimes \sigma$ and $H_{S_{12}} = H + H'$, where H and H' are the Hamiltonians of the subsystems S_1 and S_2

respectively. Then the (one-step) engine operation leads to

$$(\rho \otimes \sigma,\ H + H') \to (\sigma \otimes \rho,\ H' + H). \tag{2.20}$$

This involves two simultaneous sub-transformations. One is $(\rho,\ H) \to (\sigma,\ H')$ via a semi-local interaction with B_1, which can be understood as the combination of an isothermal $(\rho,\ H) \to (\sigma,\ H)$ and then an adiabatic $(\sigma,\ H) \to (\sigma,\ H')$ transformations. The other sub-transformation $(\sigma,\ H') \to (\rho,\ H)$ takes place in semi-local interaction with the bath B_2, which again can be understood as the combination of an isothermal $(\sigma,\ H') \to (\rho,\ H')$ and then an adiabatic $(\rho,\ H') \to (\rho,\ H)$ transformations. Clearly, this mimics the situation of a Carnot engine where one working system initially in (ρ, H) undergoes two isothermal (in interaction with two different baths) and two adiabatic transformations but in one step.

2.3.2 Maximum power with Carnot efficiency

The engines equipped with SLTOs can yield better performance than the traditional heat engines. Not only can the engines execute the Carnot cycle in one step, but they are also superior to conventional heat engines in efficiency and power. Most importantly, these engines can deliver maximum power with Carnot efficiency. Note, to attain maximum power and efficiency simultaneously, the engine has to undergo the fastest possible thermodynamically reversible transformation in each cycle, which we are going to demonstrate below. Without loss of generality, we consider the working subsystems S_1 and S_2 as qubits with the Hamiltonians $H_{S_1} = a|1\rangle\langle 1|_{S_1}$ and $H_{S_2} = a|1\rangle\langle 1|_{S_2}$ respectively having identical energy spacing. We also assume, without loss of generality, that the battery subsystems S_{W_1} and S_{W_2} are qubits with the Hamiltonians $H_{S_{W_1}} = E_{W_1}|1\rangle\langle 1|_{S_{W_1}}$ and $H_{S_{W_2}} = E_{W_2}|1\rangle\langle 1|_{S_{W_2}}$ respectively. The maximum heat-to-work conversion efficiency per (one-step) cycle is attained by implementing a thermodynamically reversible state transformation in $S_1S_2S_{W_1}S_{W_2}$ composite

$$|0,1,0,0\rangle_{S_1S_2S_{W_1}S_{W_2}} \to |1,0,1,1\rangle_{S_1S_2S_{W_1}S_{W_2}}, \tag{2.21}$$

using a semi-local thermal operation [261], where the subsystems S_1 and S_2 swap their states without changing the Hamiltonians, and the

batteries S_{W_1} and S_{W_2} get excited. Here we denote $|i,j,k,l\rangle_{S_1S_2S_{W_1}S_{W_2}} = |i\rangle_{S_1} \otimes |j\rangle_{S_2} \otimes |k\rangle_{S_{W_1}} \otimes |l\rangle_{S_{W_2}}$.

For simplicity, we may consider the working system and the battery to be the parts of single system $S \equiv S_1S_2S_{W_1}S_{W_2}$ with the Hamiltonian $H_S = a_0|0\rangle\langle 0|_S + a_1|1\rangle\langle 1|_S$, where $a_0 = a$ and $a_1 = a + E_{W_1} + E_{W_2}$ with the corresponding energy eigenstates $|0\rangle_S = |0,1,0,0\rangle_{S_1S_2S_{W_1}S_{W_2}}$ and $|1\rangle_S = |1,0,1,1\rangle_{S_1S_2S_{W_1}S_{W_2}}$. Then, the engine becomes compact and has three constituents; hot and cold baths (B_1 and B_2) and a two-level system (S). The engine cycle starts with the initial state $|0\rangle_S$ and ends with the final state $|1\rangle_S$ of S (as shown in Figure 2.5). The corresponding global transformation, leading to this one-step cycle, is

$$\gamma_{B_1} \otimes \gamma_{B_2} \otimes |0\rangle\langle 0|_S \xrightarrow{U} \tau_{B_1B_2} \otimes |1\rangle\langle 1|_S, \tag{2.22}$$

where $\tau_{B_1B_2}$ is final state of the baths. The unitary U strictly conserves energy of B_1B_2S composite and weighted-energy of B_1B_2 composite, i.e.,

$$[U,\ H_{B_1} + H_{B_2} + H_S] = 0, \tag{2.23}$$
$$[U,\ \beta_1 H_{B_1} + \beta_2 H_{B_2}] = 0. \tag{2.24}$$

The commutation relation (2.23) ensures the strict conservation of total energy. The relation (2.24) ensuring strict conservation of entropy is a special case of the general condition (2.19) where the transformation is cyclic. Here the system S remains in the energy eigenstates before and after the cycle without changing its energy and entropy. Because of that, the entropy conservation is guaranteed by the strict weighted-energy conservation of the baths only (See Appendix (A.12) for more details). Note, the semi-local nature of the evolution is clearly understood here as the system S is simultaneously interacting with both the baths via the unitary U.

Now we show that the unitary U, that satisfies relations (2.23) and (2.24), leading to the transformation (2.22) indeed attains Carnot efficiency. Then we consider constructing a driving Hamiltonian, corresponding to the unitary U, that delivers maximum power with Carnot efficiency.

Since the initial (and final) state of S is an energy eigenstate, the global initial state of B_1B_2S can be expressed in the block-diagonal

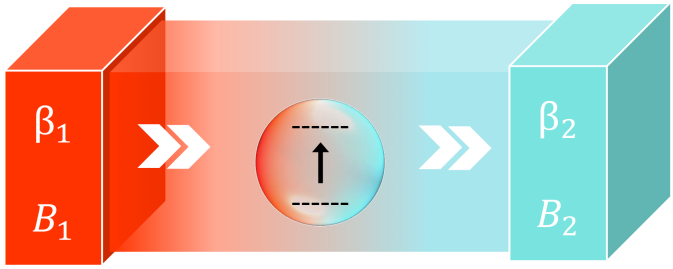

Figure 2.5: **A compact engine.** An engine consists of two baths B_1 and B_2 at inverse temperatures β_1 and β_2 respectively, and a working system S. The system S simultaneously interacts with both the baths via a semi-local thermal operation. The engine operates in a one-step cycle by exciting the system S from lower energy to a higher energy eigenstate. See text for more details.

form with respect to total energies, as

$$\gamma_{B_1} \otimes \gamma_{B_2} \otimes |0\rangle\langle 0|_S = \bigoplus_{E_{B_{12}}+a_0} [\gamma_{B_1} \otimes \gamma_{B_2}]_{E_{B_{12}}} \otimes |0\rangle\langle 0|_S, \tag{2.25}$$

with $E_{B_{12}} = E_{B_1} + E_{B_2}$, where E_{B_1} and E_{B_2} are the energies corresponding to the baths B_1 and B_2 respectively, and

$$[\gamma_{B_1} \otimes \gamma_{B_2}]_{E_{B_{12}}} = p(E_{B_{12}}) \sum_{i=1}^{d_1(E_{B_1})d_2(E_{B_2})} |E_{B_{12}}(i)\rangle\langle E_{B_{12}}(i)|,$$

where $d_1(E_{B_1})$ and $d_2(E_{B_2})$ represent the degeneracies corresponding to the bath energies E_{B_1} and E_{B_2} respectively and $p(E_{B_{12}}) = e^{-\beta_1 E_{B_1} - \beta_2 E_{B_2}} / Z_{B_1} Z_{B_2}$. A strictly total energy conserving unitary also takes a block-diagonal form, $U = \bigoplus_{E_{B_{12}}+a_0} U_{E_{B_{12}}+a_0}$, where the unitary $U_{E_{B_{12}}+a_0}$ operates only on the block with the total energy $E_{B_{12}} + a_0$ and implements a transformation

$$[\gamma_{B_1} \otimes \gamma_{B_2}]_{E_{B_{12}}} \otimes |0\rangle\langle 0|_S \to [\tau_{B_1 B_2}]_{E'_{B_{12}}} \otimes |1\rangle\langle 1|_S, \tag{2.26}$$

where $E'_{B_{12}} = E'_{B_1} + E'_{B_2}$. Note, $E_{B_{12}} + a_0 = E'_{B_{12}} + a_1$ as required by the total energy conservation. The strict conservation of total weighted-energy of the baths ensures

$$\beta_1(E'_{B_1} - E_{B_1}) + \beta_2(E'_{B_2} - E_{B_2}) = \beta_1 Q_1 + \beta_2 Q_2 = 0, \tag{2.27}$$

where Q_1 and Q_2 are the heat flow out of the baths B_1 and B_2 respectively. The Eq. (2.27) is nothing but the Clausius equality. This in turn, ensures the thermodynamic reversibility of the state transformation. Note, this condition also implies $d_1(E_{B_1})d_2(E_{B_2}) = d_1(E'_{B_1})d_2(E'_{B_2})$, where $d_1(E'_{B_1})$ and $d_2(E'_{B_2})$ are degeneracies in the energies corresponding to E'_{B_1} and E'_{B_2} of the baths B_1 and B_2 respectively (see Appendix A.1 for more details). It is an essential requirement for a unitary transformation where the rank and the spectra of the (unnormalized) state of each total energy block remain unchanged.

Similar transformations, as in Eq. (2.26), also take place in all other total energy blocks due to the evolution by the unitary U. As a result, the desired state transformation, given in Eq. (2.22), is achieved and thereby completes the one-step engine cycle. The extracted work per cycle is given by $W_{ext} = a_1 - a_0 = Q_1 + Q_2$ as a consequence of strict conservation of total energy. Hence, the heat-to-work conversion efficiency becomes maximum in the one-shot finite-size regime, given by

$$\eta = \frac{W_{ext}}{Q_1} = 1 - \frac{\beta_1}{\beta_2}, \tag{2.28}$$

which is the Carnot efficiency, as expected for any reversible engine cycle.

Let us demonstrate how the global unitary U can be implemented using an interaction Hamiltonian

$$H_{in} = \hbar g \bigoplus_{E_{B_{12}}+a_0} \sum_{i=1}^{d_1(E_{B_1})d_2(E_{B_2})} |E'_{B_{12}}(i), 1\rangle\langle E_{B_{12}}(i), 0|_{B_1B_2S} + h.c.,$$

where, again, $|E_{B_{12}}(i)\rangle \equiv |E_{B_1}(i), E_{B_2}(i)\rangle$ and $|E'_{B_{12}}(i)\rangle \equiv |E'_{B_1}(i), E'_{B_2}(i)\rangle$, and g is the coupling constant. The global unitary is then $U(t) = e^{-itH_{in}/\hbar}$ for any time t. Under this unitary, an initial state $|E_{B_1}(i), E_{B_2}(i), 0\rangle_{B_1B_2S}$ in the total energy block evolves to $|\psi(t)\rangle = U(t)|E_{B_1}(i), E_{B_2}(i), 0\rangle_{B_1B_2S}$ at time t, where

$$\begin{aligned} |\psi(t)\rangle = \cos(gt)\ &|E_{B_1}(i),\ E_{B_2}(i),\ 0\rangle_{B_1B_2S} \\ &- i\sin(gt)\ |E'_{B_1}(i),\ E'_{B_2}(i),\ 1\rangle_{B_1B_2S}, \end{aligned} \tag{2.29}$$

which is a genuinely entangled state of B_1, B_2, and S for $gt \neq z\pi/2$ with $z \in \mathbb{Z}$. The desired final state is attained at time $\tau = \pi/(2g)$,

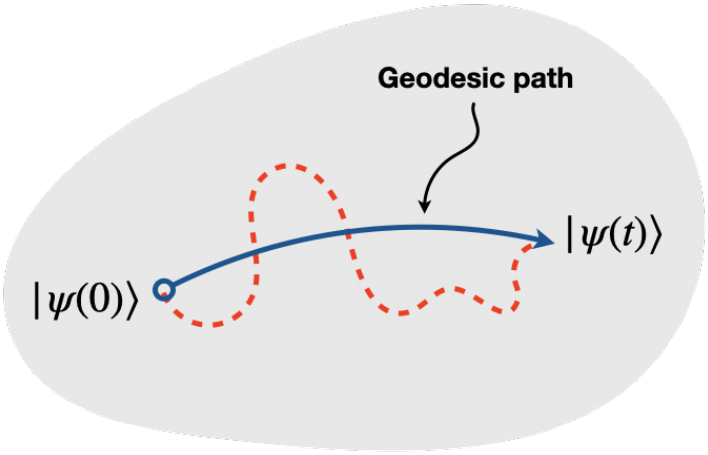

Figure 2.6: **Geodesic trajectory of evolution.** Evolution of states on a quantum state space (the gray area). An initial state $|\psi(0)\rangle$ at time $t = 0$ is evolved to $|\psi(t)\rangle$ at time $t = t$. There are infinitely many paths connecting the states. One with the shortest path is called the geodesic path (solid (blue) line). Any other path (dotted (red) line) is longer than the geodesic one.

where all the constitutes become uncorrelated from each other. It is important to highlight that the above engine evolution enables a coherent heat transfer from B_1 to B_2, which happens due to entanglement in the intermediate time and is fundamentally different from conventional engines. Similar evolution takes place in every total energy block, and the overall transformation (2.22) is attained at time τ. With this, the engine extracts W_{ext} work in τ time. Thus, the power delivered by the engine, i.e., work extraction per unit time, is

$$P = \frac{W_{ext}}{\tau} = \frac{2gW_{ext}}{\pi}. \tag{2.30}$$

Contrary to the traditional understanding, the reversible (one-step) engine cycle via semi-local thermal operation requires finite time. Not only that, as we argue below, the interaction Hamiltonian H_{in} drives the evolution with the maximum attainable speed to result in the shortest possible transformation time. The speed of evolution is defined by the distance traversed by a system per unit time in its quantum state space [262]. For pure states, the distance is measured using Fubini-Study metric, given by $s = \frac{1}{2}(1 - |\langle\psi|\phi\rangle|^2)$ for any two

states $|\psi\rangle$ and $|\phi\rangle$. The speed of evolution of the state $|\psi(t)\rangle$ is

$$v = \frac{ds}{dt} = \frac{\Delta H_{in}}{\hbar} = g, \tag{2.31}$$

where $ds = \frac{1}{2}(1 - |\langle\psi(t)|\psi(t+dt)\rangle|^2)$ and energy uncertainty $\Delta H_{in} = \sqrt{\langle\psi(t)|H_{in}^2|\psi(t)\rangle - \langle\psi(t)|H_{in}|\psi(t)\rangle^2}$. Note, the speed of evolution v is same for every total energy block and, hence, for the overall transformation. The uncertainty ΔH_{in} is independent of time and has the maximum possible value, equals to $\hbar g$ for any driving Hamiltonian bounded by the operator norm $\hbar g$. Furthermore, the interaction Hamiltonian H_{in} drives the evolution following a geodesic trajectory [262] connecting the initial and the final states which represents the shortest path (see Figure 2.6). The evolution following shortest path with maximum speed results in the minimum time required to complete the transformation in the one-step engine cycle. As a consequence, the power P in Eq. (2.30) is the maximum possible one. Note, quantum effects such as entanglement are believed to degrade the performance of engines. But, on the contrary, here we find that the engines operating with semi-local thermal operations can exploit entanglement to deliver maximum power with Carnot efficiency.

2.4 A quantum optics based heat engine

Here we discuss a physically realizable quantum heat engine transferring maximum power with Carnot efficiency following the theoretical framework presented above. We propose an engine composed of two thermal cavities and a three-level working system (see Figure 2.7). The bath B_1 is a single-mode optical cavity with a Hamiltonian $H_{B_1} = \hbar\omega_1 a_1^\dagger a_1 = \sum_n n\omega_1 |n\rangle\langle n|_{B_1}$, at inverse temperature β_1. Here $a_1^\dagger$ and a_1 are the creation and annihilation operators of the mode in B_1 respectively, ω_1 represents the mode frequency, and n and $|n\rangle$ are the number of excitation and the corresponding number state. Similarly, the bath B_2 at inverse temperature β_2 is another optical cavity with a Hamiltonian $H_{B_2} = \hbar\omega_2 a_2^\dagger a_2 = \sum_m m\omega_2 |m\rangle\langle m|_{B_2}$. The system S is a three-level atom (in Λ-configuration) with the Hamiltonian $H_S = \sum_{i=1}^3 E_i |i\rangle\langle i|_S$ with $E_1 = 0$. The overall Hamiltonian of the baths and the system composite is then $H_0 = H_{B_1} + H_{B_2} + H_S$.

A semi-local thermal operation, leading to a one-step cycle, is implemented by introducing an intensity-dependent coupling between the bath modes and the atom by the interaction Hamiltonian

$$H_I = f_1(N_1)+f_2(N_2) + \hbar g_1\theta_1(N_1)(a_1\sigma_{31} + h.c.) + \hbar g_2\theta_2(N_2)(a_2\sigma_{32} + h.c.), \tag{2.32}$$

with the number operator $N_k = a_k^\dagger a_k$ corresponds to the bath B_k for $k = 1, 2$, and $\sigma_{ij} = |i\rangle\langle j|_S$ $(i \neq j)$ is the transition operator from $|j\rangle_S$ to $|i\rangle_S$ for $i, j = 1, 2, 3$. The $f_1(N_1)$ and $f_2(N_2)$ are some intensity-dependent potentials in the cavity fields. The state $|3\rangle_S$ is coupled with $|1\rangle_S$ and $|2\rangle_S$ via intensity-dependent dipole-couplings $g_1\theta(N_1)$ and $g_2\theta(N_2)$ respectively, where $\theta(N_1)$ and $\theta(N_2)$ are some functions of the number operators, and g_1 and g_2 are some constants. There is no direct coupling between $|1\rangle_S$ and $|2\rangle_S$. The technical details of how the interaction Hamiltonian (2.32) may be realized are described in Appendix A.13.

With the choice of (identical) detuning $\Delta = (E_3 - E_k)/\hbar - \omega_k$ and the couplings

$$\frac{g_k^2}{\Delta}\theta_k^2(N_k) = f_k(N_k) = \frac{g_k^2}{\Delta}N_k^{-1}, \tag{2.33}$$

for $k = 1,\ 2$. The above formula should be fulfilled possibly exactly for large values of N_k, especially if we work at relatively high temperatures. It has to be regularized, obviously, for $N_k = 0$ to avoid the singularity. Nevertheless, with these choices, the three-level problem can be exactly reduced to a two-level problem irrespective of whether the detuning Δ is small or large, similar to what is shown in [263–265]. Then, the corresponding two-level Hamiltonian becomes $H_S' = \frac{1}{2}\hbar\omega_0(|2\rangle\langle 2| - |1\rangle\langle 1|)$, and the interaction Hamiltonian, after rotating-wave approximation, transforms to

$$H_I' = \hbar g(A_1 A_2^\dagger\sigma_{12} + A_1^\dagger A_2\sigma_{21}), \tag{2.34}$$

where $A_k = a_k N_k^{-1/2}$ and $g = g_1 g_2/\Delta$ is the effective Rabi frequency. Here $\omega_0 \approx \omega_1 - \omega_2$, i.e., the pump mode with ω_1 and Stokes mode with ω_2 are in two-mode resonance with the states $|1\rangle_S$ and $|2\rangle_S$. The ω_1 and ω_2 are chosen so that $\beta_1\omega_1 = \beta_2\omega_2$. Then, the unitary $U(t) = \exp[-itH_I'/\hbar]$ generated by H_I' strictly conserves total energy of baths and system, and total weighted-energy of the baths

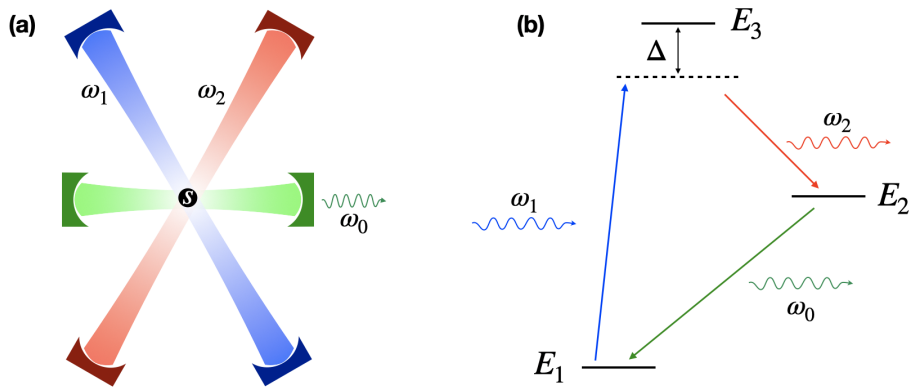

Figure 2.7: **An optical-cavity based quantum heat engine.** (a) A three-level quantum system S (i.e., working system) is placed in three overlapping optical cavities. Thermal cavities with frequencies ω_1 and ω_2 at inverse temperatures β_1 and β_2 ($\beta_1 < \beta_2$) represent the baths B_1 and B_2 respectively. The cavity with frequency ω_0 is in resonance with the transition between the ground state and the first excited state of the system. (b) The three-level system S simultaneously interacts with baths B_1 and B_2 via two-mode amplitude-dependent coupling. In each engine cycle, it absorbs a photon with energy $\hbar\omega_1$ from B_1 and emits a photon with $\hbar\omega_2$ energy to the bath B_2 and excites itself from energy E_1 to E_2. The system then emits a photon with energy $\hbar\omega_0$ via stimulated emission in a cavity (green) in resonance with the transition. See text for more details.

alone, as $[U(t),\ H'_S + H_{B_1} + H_{B_2}] = 0$ and $[U(t),\ \beta_1 H_{B_1} + \beta_2 H_{B_2}] = 0$ respectively for all time t.

The initial state of the composite B_1B_2S can now be expressed in blocks classified by (n, m), as

$$\gamma_{B_1} \otimes \gamma_{B_2} \otimes |1\rangle\langle 1|_S = \bigoplus_{n,m} p_{nm}\ |n, m, 1\rangle\langle n, m, 1|_{B_1B_2S},$$

with $p_{nm} = \exp[-\beta_1 n E_{B_1} - \beta_2 m E_{B_2}]/Z_{B_1}Z_{B_2}$, where Z_{B_1} and Z_{B_2} are the partition functions of the baths B_1 and B_2 respectively. Due to the constraints on strict total energy conservation, the $U(t)$ operates on each block (n, m) independently. For a block (n, m), the initial state $|n, m, 1\rangle_{B_1B_2S}$ evolves to $|\phi(t)\rangle = U(t)|n, m, 1\rangle_{B_1B_2S}$ at some time

t, and it is given by

$$|\phi(t)\rangle = \cos(gt)\ |n, m, 1\rangle_{B_1B_2S} - i\sin(gt)\ |n-1, m+1, 2\rangle_{B_1B_2S}, \tag{2.35}$$

which is an entangle state. This is true for all blocks (n, m), except the blocks $(0, m)$. Note, the time taken to evolve the initial state to the desired final states are same for all blocks except $(0,\ m)$, and that is $\tau = \pi/(2g)$. As a consequence, the joint initial state of B_1B_2S evolves to $\rho^f_{B_1B_2S} = U(t)(\gamma_{B_1} \otimes \gamma_{B_2} \otimes |0\rangle\langle 0|_S)U(t)^\dagger$, and at time $\tau = \pi/(2g)$, the final state of the system S becomes,

$$\rho^f_S = \mathrm{Tr}_{B_1B_2}\, \rho^f_{B_1B_2S} = \frac{1}{Z_{B_1}}|1\rangle\langle 1|_S + \left(1 - \frac{1}{Z_{B_1}}\right)|2\rangle\langle 2|_S \to |2\rangle\langle 2|_S$$

for $Z_{B_1} \to \infty$, which is true for low inverse temperature β_1 of bath B_1, or $|B_1| \to \infty$. In each cycle, the system S undergoes the transformation $|1\rangle_S \to |2\rangle_S$ and thereby extracts $\hbar\omega_0$ amount of work with the Carnot efficiency $\eta = 1 - \beta_1/\beta_2$. The transformation takes place with the maximum quantum speed following a geodesic trajectory and the time requires for that is $\tau = \pi/(2g)$. Hence, the cycle delivers maximum power $P = 2g\hbar\omega_0/\pi$. The work is extracted in the form of photons at ω_0 by placing the atom in a resonant cavity and letting the stimulated emission $|2\rangle_S \to |1\rangle_S$ (see Fig. 2.7).

It is worth mentioning that there have been several propositions of quantum heat engines based on optical cavity or bosonic baths earlier, for example in [266,267], where a quantum system interacts with two bosonic thermal baths at different temperatures. However, in contrast to the engines considered above, these engines only allow incoherent heat transfer from hot to cold baths. They do not guarantee strict conservation of total energy in order to characterize the energetics correctly. Because of that, they cannot deliver maximum power with Carnot efficiency.

2.5 Summary

In this work, we have developed a resource theory of quantum heat engines to systematically study thermodynamics in the presence of two or more baths in the finite-size one-shot regime. We stress that

the earlier works focus on how the a-thermal (or out-of-equilibrium) properties of a system transform into thermodynamic work and do not consider the conversion of heat into work. For such considerations, one thermal bath is sufficient. On the contrary, the resource theory developed for quantum heat engines, with two or more thermal baths, is the only framework to systematically address how and to what extent the heat can be converted into work in the quantum heat engines operating in the one-shot finite-size regime.

We have proceeded with the precise characterizations of thermodynamic operations, i.e., the semi-local thermal operations, by introducing the first law for engines, where the system simultaneously interacts with both the baths. In addition to strict total energy conservation, the first law also ensures a strict weighted-energy conservation. Then, we have defined semi-Gibbs states as resource-free states and free-entropies as the measure of thermodynamic resource applicable in the one-shot finite-size regime. With this, we have formulated the second laws for state transformations in a quantum engine. Our formulation reveals that the state transformations in a quantum engine are irreversible, in general, and are dictated by many second laws.

For finite-time classical engines, it is known that the maximum power at maximum heat-to-work conversion efficiency is impossible [230]. For quantum engines, where the working systems interacting with the baths are quantum mechanical, the situation is quite different because the quantum uncertainties present in the system further delimit the extractable work in each cycle. For finite-time quantum heat engines considered earlier, there are various trade-off relations between power and efficiency [69, 253], and both of these quantities cannot be maximized simultaneously.

The quantum engines considered here can deliver maximum power with maximum efficiency and are fundamentally different from conventional ones studied earlier. Firstly, the engine operates in the one-shot finite-size regime, where the working system is genuinely quantum in the sense that it is made up of a small number of quantum particles (i.e., of finite-size) and allows one or few observations or measurements (i.e., one-shot measurement). Secondly, the working system interacts with both hot and cold baths simultaneously via a semi-local thermal operation. These operations are powerful compared to the operations in traditional engines as they

can implement a one-step engine cycle and create entanglement between the baths and the working system. Because of that, it enables a coherent flow of heat from hot to cold bath via the working system and results in maximum power with maximum efficiency. With this, our results have demonstrated that there, in principle, does not exist a fundamental trade-off relation between power and efficiency. We have also put forward an experimentally feasible quantum heat engine operating in the one-shot finite-size regime with a three-level atom as a working system and two thermal optical cavities as the baths. We have explicitly introduced an intensity-dependent interaction between the atom and cavities that executes the one-step engine cycle yielding maximum power at Carnot efficiency.

In summary:

- We have introduced a a concrete mathematical framework leading to a resource theory and a novel theoretical understanding of quantum and nano-scale heat engine, and, in particular, many second laws to dictate state transformation, conversion of heat into work in quantum heat engines operating in the one-shot finite-size regime, and the role of inter-system correlations in such processes.

- We have explored quantum heat engine that converts heat into work by exclusively utilizing inter-system correlations.

- We have introduced quantum heat engines that operate via one-step cycles in the one-shot finite-size regime and enable a coherent heat transfer from hot to cold baths by establishing genuine quantum entanglement between the working system and the baths.

- We have demonstrated that there is no fundamental trade-off relation between power and efficiency.

- We have shown a general protocol with which a quantum heat engine can deliver maximum power with Carnot efficiency in the one-shot finite-size regime.

- We have proposed a physically realizable model of such a quantum heat engine based on an atom-cavity system.

Chapter 3

Steady-state quantum thermodynamics with synthetic negative temperatures

Thermodynamics constitutes a fundamental building block of the modern understanding of nature. With the advent of quantum mechanics, there have been numerous efforts to extend the framework to systems composed of a finite or large number of quantum particles while each particle has a discrete energy spectrum and the states are in a superposition of different energy levels, see for example [201]. One of the possibilities for quantum systems with bounded energy is that, in certain situations, they can assume 'negative' temperatures. This arises when the population distribution of a system or bath becomes an inverted Boltzmann distribution, i.e., states with higher energy are populated more than the ones with lower energy. It was first pointed out by Purcell and Pound in the context of nuclear spin systems [89]. Subsequently, Ramsey comprehensively discussed the thermodynamic implications of such negative temperatures and the inter-relation between negative and positive temperatures [90]. He advocates for an amendment to the Kelvin-Planck statement of the second law to incorporate that heat flows spontaneously from a bath with a negative temperature to one with a positive temperature. In this sense, the negative temperature is 'hotter' than a positive temperature.

Initially, Schöpf raised some foundational questions regarding the dynamics of negative temperature [91]. He claimed that it is impossi-

ble to transform a thermodynamic system adiabatically: from a positive finite temperature to the positive infinite temperature, then from there to a negative infinite (Boltzmann) temperature, and then subsequently to a negative finite (Boltzmann) temperature [91]. Tykodi and Tremblay [92–94] disagreed and showed that the arguments used by Schöpf are thermodynamically inconsistent as these violate the second law of thermodynamics. Nevertheless, the debates on thermodynamics with negative temperatures are not settled. Recent theoretical [95, 96] and experimental [97, 98] studies with cold atoms have brought the debate on negative temperatures back again into the spotlight. The works in [99–101] claim that "all previous negative temperature claims and their implications are invalid as they arise from the use of an entropy definition that is inconsistent both mathematically and thermodynamically." Another study in [268] states that thermodynamic equilibrium at negative temperatures would be unstable but can be used for work storage or battery. Several researchers have come forward and systematically explained that identification of the thermodynamic entropy exclusively with the volume entropy proposed by Gibbs is the root of all doubts [102–106], and it is inconsistent with the postulates of thermodynamics [107, 108]. Using Boltzmann entropy as the thermodynamic entropy, they argue that negative temperature is a valid extension of thermodynamics.

Apart from these foundational issues, there are questions on whether a negative temperature bath can be used to construct thermal devices, such as heat engines, refrigerators, heat pumps, etc. Initially, a study on Carnot engines was made by Geusic, et al. [109] and, later on, by Landsberg and Nakagomi [110, 111] in this context. There are also some studies about how the Carnot cycle should be modified in the presence of negative temperatures [112–114]. Further, some propositions are made to construct a quantum Otto engine [115, 116, 269] and refrigerators [117] using a bath with effective negative temperature. It is shown that the heat-to-work conversion efficiency of an engine operating between negative and positive temperatures would be greater than unity [97, 98, 116]. However, much of these models of thermal devices either utilize already existing negative temperature baths without caring how it may be created or effectively prepare one by inverting the populations using some external means.

In this work, we outline how to create a thermal bath with arbi-

trary temperature, including negative temperature, and study steady-state quantum thermodynamics. The bath is synthesized by letting a quantum system interact simultaneously with two thermal baths at different positive temperatures without external driving. We study various laws of steady-state quantum thermodynamics with these synthetic baths and construct continuous heat engines. We start by proving the zeroth law and show that there is no net heat flow whenever two such baths with identical temperatures are brought in contact with each other. This, in turn, legitimizes the notion of the temperature of a synthetic bath (namely, the synthetic temperature). In the case of two different temperatures, we prove the Kelvin-Planck statement of the second law and demonstrate that there is a spontaneous heat flow from a bath with a negative temperature to one with a positive temperature. This corroborates with the finding of Ramsey [90] - baths with negative temperatures are 'hotter' than the ones with positive temperatures. Interestingly, in such cases, the entropy flow is opposite to the direction of heat flow which is again expected for the baths with negative temperatures. We also construct Carnot engines involving synthetic baths and find that engines operating between positive and negative temperature baths can yield unit engine efficiency. This leads us to question the physical meaning of heat flow in the presence of a bath with negative temperatures. With a systematic analysis, we show that the heat associated with a bath with a negative temperature is equivalent to work but with a negative entropy flow.

3.1 Synthetic baths and negative temperatures

In general, naturally occurring thermal equilibrium results in non-negative temperatures. Only in certain situations, as discussed earlier, can the temperatures be negative. Below, we introduce a method through which a bath with an arbitrary temperature can be synthesized. The temperatures of these synthetic baths can assume arbitrary values, including negative ones.

The method utilizes a qutrit system, a hot bath (H) with inverse temperature β_H, and a cold bath (C) at inverse temperature β_C. The energy levels of the qutrit are denoted by $|1\rangle$, $|2\rangle$, $|3\rangle$, with the corresponding Hamiltonian $H = (E_H - E_C)\,|2\rangle\langle 2| + E_H\,|3\rangle\langle 3|$. As shown

in Fig. 3.1, the hot (cold) bath weakly interacts with the levels $|1\rangle$ and $|3\rangle$ (levels $|2\rangle$ and $|3\rangle$). As convention, we consider $\beta_H < \beta_C$, Planck constant $\hbar = 1$, and the Boltzmann constant $k_B = 1$ throughout this project. The levels $|1\rangle$ and $|2\rangle$ are not directly coupled. However, they are indirectly linked through the level $|3\rangle$. When the couplings between the qutrit and the baths are weak and satisfy the Markov condition, the overall dynamics is expressed in terms of the Lindblad or Lindblad-Gorini-Kossakowski-Sudarshan (LGKS) form of master equation [70]

$$\dot{\rho} = \mathcal{L}_U(\rho) + \mathcal{L}_H(\rho) + \mathcal{L}_C(\rho). \tag{3.1}$$

Here ρ represents the density matrix corresponding to a state of the qutrit. The first term on the right-hand side of Eq. (3.1) $\mathcal{L}_U(\rho) = i\,[\rho, H]$ takes care of the unitary part of the evolution due to the system Hamiltonian H. The second and third terms, with the Lindblad super-operators (LSOs) $\mathcal{L}_H(\cdot)$ and $\mathcal{L}_C(\cdot)$, represent the contributions due to the dissipative part of the evolution induced by the hot and cold thermal baths, respectively. The LSOs are expressed (for $X = H,\ C$) as

$$\begin{aligned}\mathcal{L}_X(\rho) = \Gamma_X(N_X+1)\left(A_X\rho A_X^\dagger - 1/2\,\{A_X^\dagger A_X, \rho\}\right) \\ + \Gamma_X N_X\left(A_X^\dagger\rho A_X - 1/2\,\{A_X A_X^\dagger, \rho\}\right),\end{aligned} \tag{3.2}$$

where $A_H = |1\rangle\langle 3|$, $A_C = |2\rangle\langle 3|$, anti-commutator $\{Y, Z\} = YZ + ZY$, and $N_X = 1/(e^{\beta_X E_X} - 1)$. The coefficient Γ_X is the Weiskopf-Wigner decay constant. The overall dynamics leads to heat exchange between the baths and the system. The heat fluxes are quantified as $\dot{Q}_X = \mathrm{Tr}[\mathcal{L}_X(\rho)\ H]$ due to interaction with the bath X [270–272]. Heat flux $\dot{Q}_X > 0$ implies that heat is flowing into the qutrit system from the bath with inverse temperature β_X.

This dynamics always leads to a steady state, say σ, which is diagonal in the energy eigenstates. The the populations $\{p_i\}$ of the states $\{|i\rangle\}$ satisfy

$$\frac{p_1}{p_3} = e^{\beta_H E_H}, \text{ and } \frac{p_2}{p_3} = e^{\beta_C E_C}.$$

The populations corresponding to states $|1\rangle$ and $|3\rangle$ attain thermal equilibrium with the hot bath, and similarly, the populations of $|2\rangle$

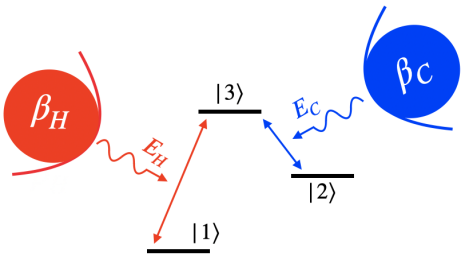

Figure 3.1: A synthetic bath is created using two baths with different temperatures and letting them interact with a qutrit system. In particular, the hot bath (H) with inverse temperature β_H is weakly coupled to the energy eigenstates $|1\rangle$ and $|3\rangle$. The cold bath (C) with inverse temperature β_C weakly interacts with the energy eigenstates $|2\rangle$ and $|3\rangle$. As a result, the populations of the states $|1\rangle$ and $|2\rangle$ reach an equilibrium corresponding to a synthetic temperature β_S. By tuning the temperature of the baths and the energy spacing between the states, an arbitrary synthetic temperature can be obtained, including negative temperatures. See text for more details.

and $|3\rangle$ attain thermal equilibrium with the cold bath. In fact, the dynamics drives the overall system to reach thermal equilibrium, albeit in interactions with two baths at different temperatures. This is justified because the heat flux and entropy production vanish, i.e., $\dot{Q}_X = 0$ for $X = H, C$ and $-\beta_H \dot{Q}_H - \beta_C \dot{Q}_C = 0$ respectively. As the entire system is in thermodynamic equilibrium, so as the populations of the states $|1\rangle$ and $|2\rangle$.

In general, if one introduces an interaction between the levels $|1\rangle$ and $|2\rangle$, be it time-dependent or time-independent, the heat and entropy fluxes become non-zero [271, 272] and the corresponding populations change. But once the interaction is switched off, the populations revert to their equilibrium values. This is as if the levels $|1\rangle$ and $|2\rangle$, or the subspace spanned by these two levels, are interacting with a synthetic bath at inverse temperature β_S, defined as

$$\beta_S = \frac{1}{E_S} \ln\left(\frac{p_1}{p_2}\right) = \frac{1}{E_S} \ln\left(\frac{p_1}{p_3}\,\frac{p_3}{p_2}\right) = \frac{\beta_H E_H - \beta_C E_C}{E_S}, \tag{3.3}$$

where $E_S = E_H - E_C$. We note that a Lindblad super-operator (LSO) cannot be given exclusively for the equilibration dynamics due to the

synthetic bath. However, as we discuss in the later sections, this is a legitimate thermal bath. We call β_S the 'synthetic' inverse temperature because it can be tuned to assume arbitrary values, including negative values, by changing the energy-level spacings and the β_H and β_C. In literature, there are debates on whether the temperature of a system can be continuously changed from a positive to a negative equilibrium temperature [268]. However, in this setup, the inverse temperature of the synthetic bath can be tuned continuously, e.g., from $\beta_S > 0$ to $\beta_S < 0$, including $\beta_S = 0$ (infinite temperature).

3.2 Thermodynamics with synthetic baths

To study thermodynamics with synthetic temperatures, we consider two different qutrit systems L and R with the corresponding Hamiltonians $H_X = (E_{XH} - E_{XC})\ |2\rangle\langle 2| + E_{XH}\ |3\rangle\langle 3|$, with $X = L, R$. We assume $E_{XH} - E_{XC} = E_S$ for both systems, i.e., the energy spacing between $|1\rangle$ and $|2\rangle$ for both L and R are same. For brevity, we denote $H_L \equiv H_L \otimes \mathbb{I}$ and $H_R \equiv \mathbb{I} \otimes H_R$. Each system couples to a hot and a cold bath with inverse temperatures β_H and β_C respectively (see Fig. 3.2) and reaches an equilibrium state. Without an interaction in between, the equilibrium state of the composite LR becomes

$$\rho_L \otimes \rho_R = \sum_{m,n=1}^{3} p_m q_n\ \ |m\ n\rangle\langle m\ n|, \tag{3.4}$$

where $p_1/p_3 = e^{\beta_H E_{LH}}$, $p_2/p_3 = e^{\beta_C E_{LC}}$, $q_1/q_3 = e^{\beta_H E_{RH}}$, and $q_2/q_3 = e^{\beta_C E_{RC}}$. The population ratio between the degenerate energy states $|21\rangle$ and $|12\rangle$ is

$$p_1 q_2 / p_2 q_1 = e^{(\beta_{LS} - \beta_{RS}) E_S}, \tag{3.5}$$

where β_{LS} and β_{RS} are the synthetic temperatures corresponding to qutrit L and R respectively.

An interaction is introduced that only couples subspace spanned by the energy levels belonging to $|1\rangle$ and $|2\rangle$ in each qutrit, ensuring an energy exchange between L and R only through these subspaces. The most general interaction Hamiltonian that drives an energy exchange between these subspaces is given by

$$H_{in} = (\lambda + i\,\gamma)\ |12\rangle\langle 21| + (\lambda - i\,\gamma)\ |21\rangle\langle 12|, \tag{3.6}$$

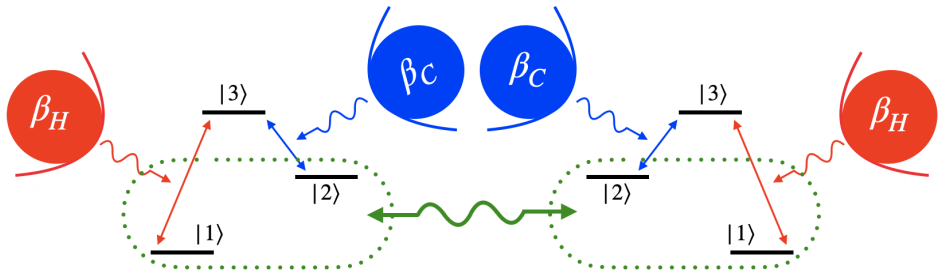

Figure 3.2: Two synthetic baths are engineered with the help of a hot and a cold bath at inverse temperatures β_H and β_C, respectively. Each synthetic bath is created by letting the baths weakly interact with one qutrit, as shown in Fig. 3.1. Different synthetic temperatures are engineered by tuning energy spacings between the states $|1\rangle$, $|2\rangle$, and $|3\rangle$. In addition, an interaction is introduced between the synthetic baths to study the heat and entropy flow. See text for more details.

where $\lambda, \gamma \in \mathbb{R}$. This interaction also strictly conserves energy, as $[H_{in}, H_L + H_R] = 0$. The overall dynamics of LR is expressed as

$$\dot{\rho}_{LR} = i\ [\rho_{LR}, H_T] + \mathcal{L}_L(\rho_{LR}) + \mathcal{L}_R(\rho_{LR}), \tag{3.7}$$

where $H_T = H_L + H_R + H_{in}$, $\mathcal{L}_L(\cdot) = \mathcal{L}_{LH}(\cdot) + \mathcal{L}_{LC}(\cdot)$, and $\mathcal{L}_R(\cdot) = \mathcal{L}_{RH}(\cdot) + \mathcal{L}_{RC}(\cdot)$. Here, $\mathcal{L}_{XH}(\cdot)$ and $\mathcal{L}_{XC}(\cdot)$ are the LSOs taking into account the dissipative part of the dynamics due to the coupling with hot and cold baths, respectively, with the qutrit X. Under this dynamics, the composite system LR reaches a steady state, say σ_{LR}. Then, the heat flux and the entropy flux, respectively, are

$$\dot{Q}_X = \mathrm{Tr}[\mathcal{L}_X(\sigma_{LR})\ H_X], \qquad \dot{S}_X = \beta_{XS}\dot{Q}_X, \tag{3.8}$$

with $X = L, R$, and $\dot{Q}_X = \dot{Q}_{XH} + \dot{Q}_{XC}$.

In absence of any interaction between the L and R, the steady (or equilibrium) state is $\sigma_{LR} = \rho_L \otimes \rho_R$ (see Eq. (3.4)). Then, the heat flux from L is $\dot{Q}_L = 0$, as $\dot{Q}_{LH} = \dot{Q}_{LC} = 0$. However in presence of interaction via H_{in}, the steady state becomes $\sigma_{LR} \neq \rho_L \otimes \rho_R$, and then the $\dot{Q}_L = \dot{Q}_{LH} + \dot{Q}_{LC} \neq 0$. This means that there is heat flux through the subspace spanned by $\{|1\rangle, |2\rangle\}$ of L, which we may consider as the heat flux due to the synthetic bath associated with L. By convention, $\dot{Q}_L > 0$ implies a heat flux from the synthetic bath to

L, which is then passed to R. With these tools at hand, we now set out to explore steady-state quantum thermodynamics with synthetic temperatures. Note that the first law is always respected at steady state as $\dot{Q}_L + \dot{Q}_R = 0$. Thus, our emphasis would be on studying the zeroth and second laws.

Zeroth law - In thermodynamics, the zeroth law interlinks the notion of temperature with equilibrium. It states that if two systems are in thermal equilibrium, they must have the same temperature and vice versa. Again, thermal equilibrium implies that when two systems are in contact, there is no net flux in any thermodynamic quantities (such as heat and entropy) between systems. In such situations, the overall entropy production also vanishes. Below we show that, in the two-qutrit scenario discussed above, there is no net flux of any thermodynamic quantity whenever the synthetic temperatures are identical for both qutrits.

Recall the setup we consider in Fig. 3.2. Without any interaction, the steady state of LR is $\rho_L \otimes \rho_R$, which is diagonal in the energy eigenstates (see Eq. (3.4)). With same synthetic inverse temperatures $\beta_{LS} = \beta_{RS}$, the populations of the states $|12\rangle$ and $|21\rangle$ satisfy $p_1 q_2 = p_2 q_1$ (see Eq. (3.5)). It means, the matrix corresponding to the state $\rho_L \otimes \rho_R$ in the subspace spanned by $\{|12\rangle,\ |21\rangle\}$ is proportional to an identity operator. Now an interaction between L and R introduced by H_{in}, as in Eq. (3.6). It is easily seen that $[H_{in}, \rho_L \otimes \rho_R] = 0$ for $\beta_{LS} = \beta_{RS}$. Thus, even after the interaction is switched on, the steady state remains unaltered, i.e., $\sigma_{LS} = \rho_L \otimes \rho_R$ and $\dot{\sigma}_{LR} = 0$. Hence, there is no exchange of heat and entropy between L and R, as $\dot{Q}_X = \dot{S}_X = 0$ for $X = L, R$. This implies that the synthetic baths are in thermal equilibrium whenever the synthetic temperatures are identical, irrespective of whether the temperatures are positive or negative. A numerical analysis also confirms this. See Fig. 3.3(a).

Second law - For $\beta_{LS} \neq \beta_{RS}$, heat and entropy flow is possible from one qutrit to the other. However, the flow cannot be arbitrary. The second law dictates the physically allowed processes given that zeroth and first laws are respected. There are various statements of the second law. Below, we analyze the Kelvin-Planck statement to deal with the directionality of heat flow and the Clausius statement regarding entropy production.

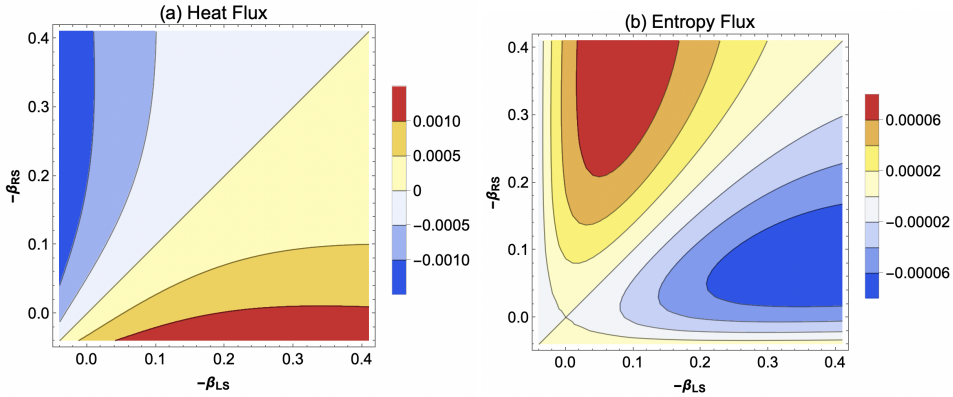

Figure 3.3: The figures represent heat and entropy fluxes, $\dot{Q}_L$ and $\dot{S}_L$, respectively, through the qutrit L. The numerical calculation is carried out with the parameters: $\Gamma_H = \Gamma_C = 0.001$, $\beta_H = 0.05$, $\beta_C = 1$, $\lambda = 1$, $\gamma = 0$, $E_S = 9.5$. The different synthetic inverse temperatures are obtained by tuning the energy E_H of $|3\rangle$ for the qutrits L and R. (a) The density plot represents the Kelvin-Planck statement of the second law in terms of the heat flux through L, i.e., $\dot{Q}_L$. The plot shows no heat flux for $\beta_{LS} = \beta_{RS}$. This corroborates with the zeroth law. However, there is a positive (negative) heat flux $\dot{Q}_L$, i.e., heat flows from L to R (from R to L), whenever $-\beta_{LS} > -\beta_{RS}$ ($-\beta_{LS} < -\beta_{RS}$) implying bath with β_{LS} (β_{RS}) is hotter than β_{RS} (β_{LS}). Clearly, a bath with a negative temperature is always 'hotter' than any bath with a positive temperature. (b) The density plot represents the variation of entropy flux $\dot{S}_L$ for different synthetic temperatures. As seen from the plot, for $\beta_{LS} = \beta_{RS}$, $\dot{S}_L = 0$. For $\beta_{LS} > 0$ and $\beta_{RS} > 0$, the direction of entropy flux is same with the heat flux as expected for the baths with positive temperatures. However, the direction of heat flow is opposite to the direction of entropy flow, in general, for baths with negative inverse temperatures. See text for details.

Let us consider the case for which $-\beta_{LS} > -\beta_{RS}$. When there is no interaction between the qutrits, the equilibrium state of the composite LS is $\rho_L \otimes \rho_R$. The state is expressed in the block-diagonal form as

$$\rho_L \otimes \rho_R = \Pi_0 \rho_L \otimes \rho_R \Pi_0 + \Pi_1 \rho_L \otimes \rho_R \Pi_1,$$

where $\Pi_0 = |12\rangle\langle 12| + |21\rangle\langle 21|$ and $\Pi_1 = \mathbb{I} - \Pi_0$. The populations corresponding to the energy eigenstates $|12\rangle$ and $|21\rangle$ satisfy $p_1 q_2 < p_2 q_1$ (see Eq. (3.5)).

Now let us disconnect the thermal baths and introduce an interaction driven by H_{in}. This, or the total Hamiltonian H_T, evolves the composite and induces a rotation onto the subspace spanned by $|12\rangle$ and $|21\rangle$ only. At the same time, the other part of the density matrix remains unchanged. As a result, there appear off-diagonal elements in this subspace. Say, the state of LR after any evolution becomes

$$\begin{aligned}\rho'_{LR} = a\,|12\rangle\langle 12| + b\,|12\rangle\langle 21| + c\,|21\rangle\langle 12| + d\,|21\rangle\langle 21| \\ + \Pi_1 \rho_L \otimes \rho_R \Pi_1.\end{aligned}$$

The unitary nature of the evolution in the subspace $|12\rangle$ and $|21\rangle$ guarantees that $a > p_1 q_2$ and $d < p_2 q_1$. For this reason and as the off-diagonal elements do not contribute to the populations of the reduced state of L, i.e., $\rho'_L = \mathrm{Tr}_R\, \rho'_{LR}$, we find $p'_1 = \langle 1|\rho'_L|1\rangle > p_1$ and $p'_2 = \langle 2|\rho'_L|2\rangle < p_2$. Similarly, for the reduced state of $\rho'_R = \mathrm{Tr}_L\, \rho'_{LR}$, the modified populations becomes $q'_1 = \langle 1|\rho'_R|1\rangle < q_1$ and $q'_2 = \langle 2|\rho'_R|2\rangle > q_2$. Note, the populations corresponding to level $|3\rangle$ for both L and R remain unchanged, i.e., $\langle 3|\rho'_L|3\rangle = p_3$ and $\langle 3|\rho'_R|3\rangle = q_3$. Clearly, the qutrit L loses some energy. As the evolution respects strict energy conservation, the qutrit R gains the same amount of energy. Thus, any evolution due to H_{in} ensures that there is an energy flow from L to R for $-\beta_{LS} > -\beta_{RS}$. After this modification, if L is now exposed to its baths, the dissipative dynamics due to $\mathcal{L}_L(\cdot)$ forces the qutrit to restore its equilibrium state, $p'_1 \to p_1$ and $p'_2 \to p_2$. This, in turn, increases the energy of L by absorbing some heat from the hot and cold baths or, equivalently, from the synthetic bath. Similarly, if R is exposed to its baths, some of its energy is released to its synthetic bath in the form of heat and thereby attains its equilibrium. Note in this process, to reach the equilibrium, the populations of $|3\rangle$ do not remain constant throughout in both L and R.

From the above arguments, we see that the unitary evolution with the interaction between L and R drives the composite out of equilibrium leading to a spontaneous heat flow from L to R for $-\beta_{LS} > -\beta_{RS}$. At the same time, the dissipative evolution due to thermal interactions with the baths tries to restore the composite back to the initial equilibrium state $(\rho_L \otimes \rho_R)$ by pumping some heat into L and absorbing some heat from R. When both unitary and dissipative evolutions occur simultaneously, as in Eq. (3.7), the opposing tendencies balance each other and result in a steady state, say σ_{LR}. This steady state is again block-diagonal in total energy eigenstates and has off-diagonal elements in the eigenstates $|12\rangle$ and $|21\rangle$. Nevertheless, the steady-state dynamics generate a heat flux from L to R,

$$\dot{Q}_L = \mathrm{Tr}[\mathcal{L}_L(\sigma_{LR})\, H_L] = \mathrm{Tr}[\mathcal{L}_L(\sigma_L)\, H_L] > 0, \tag{3.9}$$

and $\dot{Q}_R = -\dot{Q}_L$. The expression of $\dot{Q}_L$ can be given analytically, and it has complicated dependencies with all the parameters. Rather, a numerical analysis is more illuminating; we have done so in Fig. 3.3(a). Again for $-\beta_{LS} < -\beta_{RS}$, we find that $\dot{Q}_L < 0$. This means that there is a spontaneous heat flow from R to L.

In thermodynamics, the Kelvin-Planck statement of the second law states that heat can only flow from a hot bath to a cold bath when no external work is performed. As we see above for $-\beta_{LS} > -\beta_{RS}$, there is a heat flow from L to R. This means that: (1) baths with negative inverse temperatures are 'hotter' than the baths with positive inverse temperatures; (2) baths with larger negative inverse temperatures are 'hotter' than those with smaller negative inverse temperatures. This is in conformation with the findings of Ramsey [90]. However, one important point to be noted here is that although there is a heat flow from a negative to a positive temperature bath, the entropy flow is the opposite. This is indeed a signature of a bath having a negative temperature.

The Clausius statement, another formulation of the second law, states that the overall entropy production is always positive in a thermodynamical process. For steady-state thermodynamics with synthetic baths, the overall entropy production is given by

$$\Sigma = \dot{S}_{LR} - \beta_{LS}\dot{Q}_L - \beta_{RS}\dot{Q}_R, \tag{3.10}$$

where $\dot{S}_{LR} = \partial S_{LR}/\partial t$ is the rate of change in von Neumann entropy $S_{LR} = -\operatorname{Tr}[\sigma_{LR} \log \sigma_{LR}]$, and β_{LS} (β_{RS}) is the synthetic inverse temperature of L (R) and $\dot{Q}_L$ ($\dot{Q}_R$) is the heat flux from L (R). Note at steady state, the $\partial S_{LR}/\partial t = 0$ and $\Sigma = (\beta_{RS} - \beta_{LS})\, \dot{Q}_L$, as $\dot{Q}_L = -\dot{Q}_R$. For $-\beta_{LS} > -\beta_{RS}$, the heat flux from L is positive, $\dot{Q}_L > 0$. Consequently, $\Sigma > 0$. Similarly, $\dot{Q}_L < 0$ for $-\beta_{LS} < -\beta_{RS}$, and thus $\Sigma > 0$. For $\beta_{LS} = \beta_{RS}$, we have $\Sigma = 0$. Thus, the Clausius inequality in the differential form is

$$\Sigma \geq 0,$$

and it is always satisfied as long as the Kelvin-Planck statement is respected.

At steady state, the entropy production rate is positive, $\Sigma \geq 0$. This is mainly due to the dissipative interaction between the baths and the system. However, one may find out an entropy flow through the system LR, as

$$\dot{S}_X = -\operatorname{Tr}[\mathcal{L}_X(\sigma_{LR}) \log \sigma_{LR}],$$

for $X = L, R$ (see Appendix B.1). At steady state, $\dot{S}_L + \dot{S}_R = 0$ as the state does not evolve over time. $\dot{S}_L > 0$ implies that there is an entropy flux from bath with inverse temperature β_{LS} to R via L, and similarly for $\dot{S}_R > 0$. In general, for a bath with positive temperature, an outflow of heat is associated to a decrease in entropy. One striking feature we must note here is that, although there is a spontaneous heat flow from a bath with negative temperature to a bath with positive temperature, the entropy flow is just opposite to that (see Fig. 3.3(b)). This is also true when both baths are of negative temperatures. For a bath with negative temperature, an outflow of heat is associated with an increase in entropy of the bath. Thus, a bath with negative temperature in general acts as an entropy sink.

3.3 Quantum heat engines with a bath at negative temperature

Now we discuss heat engines operating with a bath at synthetic temperatures, particularly at negative temperatures. A device acting as a heat engine aims to transform heat into work. A generic heat

engine consists of three primary parts: two separate heat baths with different temperatures and a working system. It operates by absorbing heat from the hot bath. The working system transforms part of this heat into work, dumping the rest into the cold bath. The model of a quantum heat engine (QHE) we are concerned with utilizes a synthetic bath with negative temperature and a heat bath with positive temperature (as depicted in Fig. 3.4). The working system is composed of a qutrit (L) and a qubit (W). The synthetic bath with inverse temperature β_{LS} is created using two baths at different temperatures β_H and β_C and letting these weakly interact with L, similar to the one considered in Fig. 3.1. The Hamiltonian of L is given by $H_L = (E_H - E_C)|2\rangle\langle 2| + E_H|3\rangle\langle 3|$. The qubit W is weakly coupled to a bath at inverse temperature $\beta_W \geq 0$, and its Hamiltonian is $H_W = E_W|2\rangle\langle 2|$, where $E_W = E_H - E_C$. To operate the device as a heat engine, a time-dependent interaction is introduced between L and W driven by the interaction Hamiltonian

$$H_{in}^E(t) = \delta\,(|11\rangle\langle 22|\;\, e^{i\omega t} + |22\rangle\langle 11|\, e^{-i\omega t}). \tag{3.11}$$

The total Hamiltonian is then $H_T^E = H_0 + H_{in}^E(t)$, where $H_0 = H_L + H_W$. The overall dynamics will never lead to a steady state for a time-dependent interaction. However, for a periodic time dependence, there is a rotating frame in which the interaction becomes time-independent. For instance, to move from the laboratory frame to a rotating frame to we may introduce a rotation, given by the unitary $U = \exp[iH_R t]$ which satisfies $[H_R, H_0] = 0$. For a suitable H_R, the interaction becomes time-independent, i.e., $V_{in} = UH_{in}^E(t)U^\dagger$. In this rotating frame, the overall dynamics comprising the unitary and the dissipative evolution is given by (see Appendix B.1)

$$\dot{\rho}_{LW}^R = i[\rho_{LW}^R, \bar{H}_T^E] + \mathcal{L}_L(\rho_{LW}^R) + \mathcal{L}_W(\rho_{LW}^R), \tag{3.12}$$

for a state ρ_{LW}, with $\rho_{LW}^R = U\rho_{LW}U^\dagger$ and $\bar{H}_T^E = H_0 - H_R + V_{in}$. Note the LSOs remain unchanged in the rotating frame. Now that the time-dependence in the Hamiltonian is lifted, the dynamics attains a steady state σ_{LW}^R in the rotating frame.

With this, the heat flux, entropy flux, and the power in the laboratory frame are quantified as (see Appendix B.1)

$$\dot{Q}_X = \mathrm{Tr}\,[\mathcal{L}_X(\sigma_{LW}^R)\; H_0],\;\; \dot{S}_X = -\,\mathrm{Tr}[\mathcal{L}_X(\rho_{LW}^R)\log\sigma_{LW}^R],$$
$$\text{and}\;\; P = i\,\mathrm{Tr}\,[\sigma_{LW}^R\,[V_{in}, H_0]]. \tag{3.13}$$

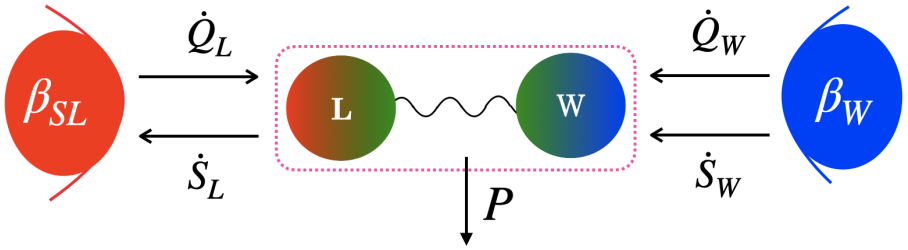

Figure 3.4: A schematic of a quantum heat engine operating with two baths; one with negative inverse temperature β_{SL} and the other with positive temperature β_W. The negative temperature is synthesized by weakly coupling a qutrit L with a hot and a cold bath, as discussed in Fig. 3.1. This is as if the energy levels $|1\rangle$ and $|2\rangle$ are coupled to a synthetic bath at inverse temperature β_{SL}. A qubit W is weakly coupled to the bath with β_W. In the engine, L and W are coupled through a time-dependent interaction as in Eq. (3.11). The arrows represent the direction of heat ($\dot{Q}_X$) and entropy ($\dot{S}_X$) fluxes for $X = L, W$, and P represents the power of the engine. See text for more details.

for $X = L, W$, and $[A, B] = AB - BA$. Here $\dot{Q}_X$ and $\dot{S}_X$ represent the heat and entropy fluxes through system X respectively, and P represents the power. The condition $\dot{Q}_L + \dot{Q}_W + P = 0$ is always satisfied as required by the first law [273, 274] and at steady state, $\dot{S}_L + \dot{S}_W = 0$. For any negative inverse temperature $\beta_{LS} < 0$, we have, as confirmed by numerical analysis, $\dot{Q}_L > 0$, $\dot{Q}_W > 0$, and $P < 0$. This means the device draws heat from both the synthetic bath and the bath with inverse temperature β_W. For traditional engines, the efficiency is calculated as the ratio of work extracted and the heat absorbed by the engine from the hot bath. Here, the heat is absorbed from both baths. For each bath, the corresponding engine efficiency may be defined as

$$\eta_L = \frac{-P}{\dot{Q}_L}, \text{ and } \eta_W = \frac{-P}{\dot{Q}_W}.$$

It can be easily checked that $\eta_L > 1$ and $\eta_W > 1$. Thus, the efficiency exceeds unity for an engine operating between baths with positive and negative temperatures. This is what is also claimed in literature [109]. We, however, find this conclusion incomplete. The heat-to-

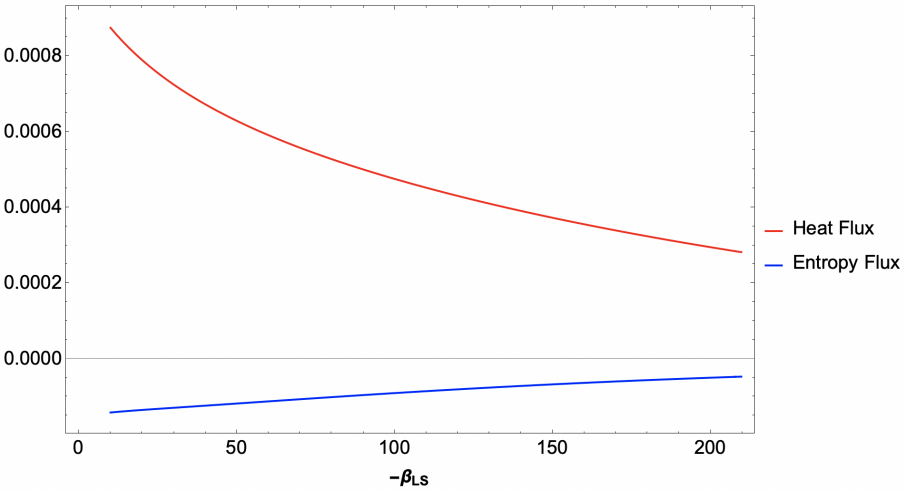

Figure 3.5: The plot represents a change in heat flux ($\dot{Q}_L$) and entropy flux ($\dot{S}_L$) through L in the engine with respect to β_{SL}. The calculation is done with the parameters: $\beta_H = 0.01$, $\beta_W = 0.1$, $\beta_C = 10$, $\delta = 5$, $\omega = 1$, and $E_S = 5$. As clearly seen, $\dot{Q}_L > 0$ and $\dot{S}_L < 0$ for all $\beta_{SL} < 0$. See text for more details.

work conversion efficiency should always be defined with respect to the total amount of heat entering the engine and the amount of work produced out of that. In that sense, the total heat flux entering the engine is $\dot{Q}_L + \dot{Q}_W$, and this entire heat is converted into work. As a result, we find

$$\eta = \frac{-P}{\dot{Q}_L + \dot{Q}_W} = 1,$$

i.e., the engine efficiency becomes unity. Thus, the efficiency of an engine can never exceed unity in any circumstance as long as the first law, i.e., the overall energy conservation, is respected.

This is, nevertheless, different from what we see in traditional heat engines. It raises a question on the physical meaning of the heat released or absorbed by a bath with a negative temperature. By definition, heat is a form of energy that is always associated with a change in the entropy of the corresponding bath. Heat flow, thus, occurs with an entropy flow. The work, on the other hand, is a pure form of energy and is not associated with any flow of entropy. In traditional engines operating with baths at positive temperatures,

the direction of heat flow and the direction of entropy flow is the same. That is how a bath gets cooled down when it releases some heat. For a bath with a negative temperature, this is not true (see Fig. 3.3(b)). There the bath's entropy increases as it releases heat. For the engine we have considered above, the direction of heat flux $\dot{Q}_L > 0$ is opposite to the direction of entropy flux $\dot{S}_L < 0$ in L which is coupled to the negative bath (see Fig. 3.5). While for W, coupled to positive temperature bath, the direction of heat flux $\dot{Q}_W > 0$ is the same as the direction of entropy flux $\dot{S}_W > 0$. In fact, while heat is entering the engine from both baths, there is an entropy flow from the bath with inverse temperature β_W to the bath with β_{SL} where the latter acts as an entropy sink.

In order to understand the thermodynamic nature of this heat, let us make a closer inspection of the process that is happening on L and W alone in the rotating frame. To create a synthetic bath with negative temperature, L interacts with hot and cold baths with inverse temperatures β_H and β_C. The corresponding heat fluxes are $\dot{Q}_{LH} = \mathrm{Tr}[\mathcal{L}_{LH}(\sigma^R_{LW})\ H_L]$ and $\dot{Q}_{LC} = \mathrm{Tr}[\mathcal{L}_{LC}(\sigma^R_{LW})\ H_L]$. Recall that $\mathcal{L}_L(\cdot) = \mathcal{L}_{LH}(\cdot) + \mathcal{L}_{LC}(\cdot)$. We can also quantify the power as $P_L = i\,\mathrm{Tr}[\sigma_{LW}\ [V_{in}, H_L]]$ which is produced in L. For the interaction V_{in}, we always find $\dot{Q}_{LH} > 0$, $\dot{Q}_{LC} < 0$, and $P_L > 0$. For W, the heat flux and power can be similarly calculated, and they are $\dot{Q}_W > 0$ and $P_W < 0$. At steady state, we have

$$\begin{aligned}
&\dot{Q}_{LH} + \dot{Q}_{LC} + P_L = 0,\\
&\dot{Q}_W + P_W = 0,\\
&P = P_L + P_W.
\end{aligned}$$

Note $\dot{Q}_L = \dot{Q}_{LH} + \dot{Q}_{LC}$ and $\dot{Q}_L = -P_L$. This may imply that the heat flux from the synthetic bath is quantitatively equal to the power extracted from L. But, as mentioned above, this cannot be just power, as power is not associated with any entropy flux. Here, instead, we see an entropy flux opposite to the power extracted (heat flux) in L. This leads us to conclude that heat from a bath with a negative temperature is thermodynamic work but with negative entropy.

3.4 Conclusion

In this work, we have studied steady-state quantum thermodynamics with negative temperatures. For that, we have engineered synthetic baths by utilizing two baths at different positive temperatures and letting them weakly interact with qutrit systems in a particular fashion. These synthetic baths can assume arbitrary temperatures, including negative ones. These baths with negative temperatures are exploited to study steady-state thermodynamics. We have explored the thermodynamic laws, particularly the zeroth and second laws. We have shown that whenever two synthetic baths with identical temperatures are brought in contact, there is no heat flow in between. This, in turn, legitimizes the notion of temperatures in synthetic baths. On the other hand, for non-identical temperatures, there is a heat flow. Further, heat always flows spontaneously from a bath with a negative temperature to a positive one. This implies that a bath with a negative temperature is 'hotter' than a bath with a positive temperature. Further, there is a heat flow from a bath with a less negative temperature to a bath with a more negative temperature. We have then studied the Clausius statement of the second law in case of negative temperatures and found that there is always non-negative entropy production in the steady-state thermal processes. Then, we have introduced a heat engine model that operates between two baths, one with negative temperature and the other with positive temperature. Unlike traditional engines, these engines always yield unit heat-to-work conversion efficiency. A systematic analysis has revealed that the heat flow from a bath with a negative temperature is equivalent to an injection of work into the working system by an equal amount. This is exactly the reason why these engines yield unit efficiency.

Finally, we conclude that:

- A thermal bath with a negative temperature can be synthesized with two baths with different positive temperatures.
- In steady-state thermodynamics with negative temperatures, the zeroth law and the Clausius statement of the second law remain unchanged. However, the Kelvin-Plack statement is to be appended to incorporate that there is a spontaneous heat

flow from a bath with a negative temperature to a bath with a positive temperature and from a bath with smaller negative temperature to a bath with a larger negative temperature.

- A continuous heat engine can be constructed using baths with negative and positive temperatures. In such engines, the heat-to-work conversion efficiency is always unity. This is maximum for any device that respects first law, i.e., conservation of total energy.
- On the fundamental level, the thermodynamic nature of heat from a bath with a positive temperature is qualitatively different from the one with a negative temperature. For the former, heat flows in the same direction as entropy flow. For the latter, heat flows in the opposite direction of entropy flow. Further, heat from a bath with a negative temperature is thermodynamic work but with negative entropy.

Chapter 4

Dynamical spectroscopy

In this chapter, we explore the transient quantum dynamics as a potential resource. We consider such a scenario of transient quantum dynamics like High Harmonic Generation (HHG), which is a consequence of the interaction between materials and a strong laser field. Such HHG processes can divulge crucial system details that can be investigated. In the following part, we discuss in detail the mechanisms of HHG in atoms (Sec. 4.1) and then solids (Sec. 4.2) which is the main focus of this chapter. Finally, we shall see how HHG can be utilized for dynamical spectroscopy to characterize different solids.

4.1 HHG in Atomic systems

When a photon with appropriate energy is incident upon an atom, it can interact with an electron in the atom and excite it to a higher energy state as in Fig. 4.1. In order for the atom to be excited, the energy of the photon must be the same as the difference in energy between two specific energy levels.

In general such a scenario, a dimensionless parameter is defined to compare the different energy scales involved in the problem. Such a parameter was introduced by Leonid Veniaminovich Keldysh, which is known as the Keldysh parameter λ.

$$\lambda = \sqrt{\frac{I_p}{2U_p}} \tag{4.1}$$

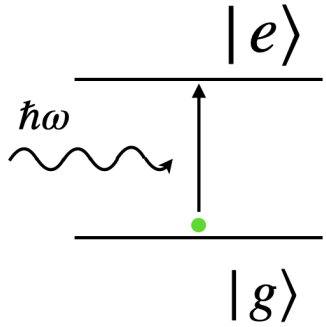

Figure 4.1: Single-photon absorption: The ground state ($|g\rangle$) atom has become excited ($|e\rangle$) due to the absorption of a photon of energy $\hbar\omega$.

where I_p and U_p are the ionization energy and the ponderomotive energy, respectively. The ponderomotive energy is expressed,

$$U_p = \frac{e^2 E_0^2}{4m\omega_o^2} \tag{4.2}$$

Depending on the effective value of λ, we encounter different process as follow:

Multiphoton Ionization (MPI) $(\lambda \gg 1)$: In this scenario, the energy of the incident photon is off-resonant with the energy gap. Nevertheless, electrons might be excited by multiphoton absorption. Then the emission process will eventually lead to the electron returning to its ground state. As a consequence, a high-energy photon is released as in Fig. 4.2. This procedure is often carried out in a laser field, where the high intensity of the laser field permits the atom or molecule to absorb a large number of photons in a relatively short period of time. Because MPI is a non-linear process, it follows that the ionization rate will swiftly increase in proportion to the laser intensity.

Tunnel Ionization $(\lambda \ll 1)$: Tunnel ionization takes place when the strength of the electric field is sufficient to overcome the binding energy of the electrons in the atom or molecule, causing the electrons to tunnel through the potential barrier and become ionized as in Fig. 4.3. This process takes place when the electric field is strong enough to overcome the binding energy of the electrons and the process is known as ”strong field ionization”. The tunnel ionization

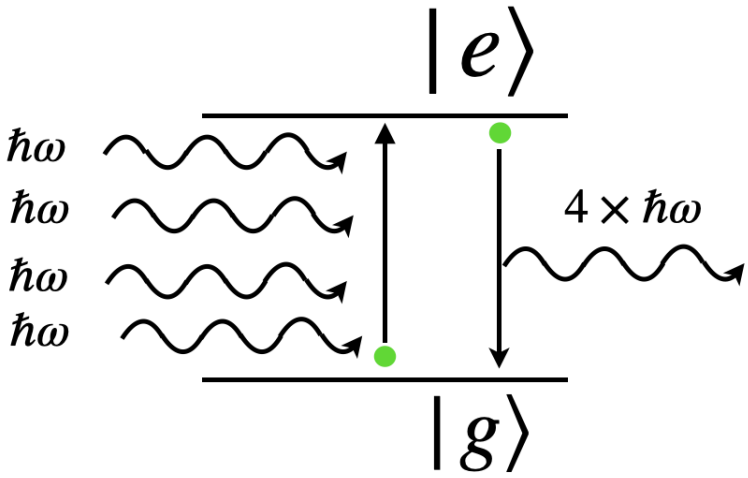

Figure 4.2: Multiphoton ionization: In this scenario, the energy of the incoming photon is not in resonance with the energy gap between two levels, an electron may jump to a higher energy level by absorbing a series of photons.

process leads to the development of a highly charged ion, then the electron moves in the laser field, and when the laser field turns, the electron then can subsequently recombine with the ion that it was derived from to generate higher harmonics. In this extremely nonlinear optical process, low-energy photons are converted into one soft x-ray photon. This multi-photon process paves the way to exploring the frontiers of physics on the order of one quintillionth (10^{-18}) of a second and generates the notion of ultrafast measurements.

The high harmonic generation (HHG) was encountered by experimentalists [125, 126]. Later on, Ferray *et al.* [127] phenomenologically described the characteristics of HHG spectra, which are as follows: At first, the intensity of spectra decreases as the harmonic number increases, as in a perturbative regime; then, the harmonic number further increases the intensity remains approximately constant over a broad region, creating a plateau that cannot be explained by perturbation theory; and finally, the plateau ends abruptly at a point called the high harmonic cut-off. This is the signature characteristic of HHG spectra.

There are a couple of theoretical models that attempt to give intuition about the microscopic picture of HHG. Corkum introduced a three-step model to explain HHG, which has become popular as Simple-man's model [120]. In this semi-classical model, the movement of electrons in the laser field is described as a classical phenomenon, even though tunneling and recombination are described as quantum phenomena. The simple man model predicted: In HHG, the electrons that are liberated by tunnel ionization are accelerated back toward the ionized atoms or molecules by the laser field, and when they recombine with the ion, they emit photons with energies that are many times higher than the frequency of the original laser pulse. The other model was introduced by Lewenstein *et al.*, which is famous as the Lewenstein model [118]. This model actually modified Simple-man's model, where they use the strong field approximation technique and consider the electric field as a classical field and electrons as quantum particles. Recently Lewenstein *et al.* have further provided a completely quantum mechanical description of HHG [128].

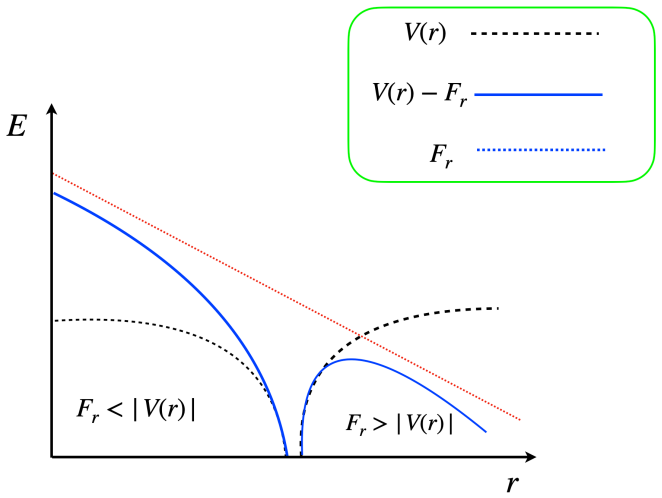

Figure 4.3: Schematic view of tunnel ionization of the atomic system, here $V(r)$ and F_r are the binding energy of electrons and the external electric field, respectively.

After this, we discuss exclusively about HHG in solids, leaving atoms and molecules behind.

4.2 HHG in solids

The energy difference between electrons in solids is more complicated than in the two-level atomic systems. The electrons in solids lie within a band structure and the electron crystal momentum plays a role in the interaction between light and matter in solids. When light is absorbed by a material, it has the possibility to excite an electron, bringing it from a lower energy state to a higher one and forming an electron-hole pair as a result of the transition. The probability of this happening depends on the energy and the polarization of the incident light and the density of states in the band structure at the energy level of the electron. Even when light interacts with a solid, it can also transfer momentum to the electrons, driving them to accelerate to higher momentum values within the band of energy levels. This acceleration may lead to the transition from the valence band to the conduction band as well. This process is known as optical or photon-induced acceleration, and it can be used to manipulate the electronic properties of solids. However, this process is very reliant on the band structure of the material and the properties of incident light. In the scenario of light emission, it displays richer dynamics due to the different electronic structures of solids. The crystal momentum of the electron, on the other hand, determines the probability of it being excited to a certain energy level. This is determined by the symmetry of the crystal lattice as well as the characteristics of the excited states.

The realization of HHG in solids would occur through two mechanisms [134, 275, 276]: interband polarization and intra-band current. This shares many similarities with the three-step approach that is often employed to explain HHG in atomic substances [133, 277–279]. However, there are also significant dissimilarities with the atomic three-step model. In the solid phase, the cutoff frequency of HHG varies linearly with the strength of the electric field [133, 280]. In the gas phase, however, the cutoff frequency varies linearly with the intensity of the driving electric field [120, 281]. After an electron has been ionized in a gas, it accelerates through the gas by driving field.

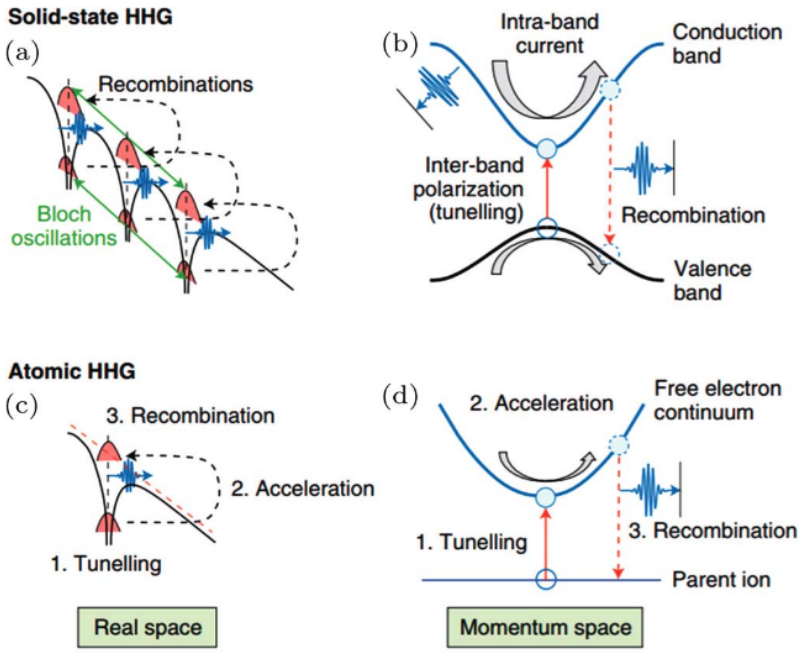

Figure 4.4: **HHG mechanism in solids and atoms, [276].**

However, the band structure of a solid prevents the free acceleration of electrons.

The two mechanisms of HHG in solid have been discussed below.

4.2.1 The intra-band mechanism

After the electrons are driven by the electric field from a partially filled valance band to a partially filled conduction band, then the intra-band mechanism kicks in. Due to the strong electric field, the electron is driven anharmonically in the conduction band, and the hole is driven anharmonically in the valance band. The strongly anharmonic motion of the electrons (and holes) results in an anharmonic current that governs HHG in solids. Since the currents that are responsible for the emission of light are confined inside distinct band—that is, the holes are in the valence band, and the electrons are in the conduction band (Fig. 4.4; [276])—this process is referred to as the intra-band mechanism [119, 282].

Electron's motion under intra-band mechanism: We calculate the

group velocity of the electron's wave packet, which itself is composed of a superposition of several Bloch waves with different values of crystal momentum k. The dispersion relation of band structure is denoted as $\mathbb{E}(k)$, and the group velocity would be [283],

$$v_g = \frac{1}{\hbar}\frac{d\mathbb{E}(k)}{dk} \tag{4.3}$$

The electrons traverse through an electric field with strength $\mathscr{E}$ for the duration $dt \to 0$, then the change in energy would be

$$d\mathbb{E} = -e\,\mathscr{E}\,v_g\,dt \tag{4.4}$$

using Eq. (4.3) and Eq. (4.4) we can write,

$$\hbar\frac{dk}{dt} = -e\,\mathscr{E} \tag{4.5}$$

It implies that changes in the crystal momentum of Bloch electrons are due to the external electric field $\mathscr{E}$. We can define the acceleration of a Bloch electron as,

$$\mathfrak{a} = \frac{1}{\hbar}\frac{d}{dt}\frac{d\mathbb{E}(k)}{dk} = \frac{1}{\hbar}\frac{d^2\mathbb{E}(k)}{d^2k}\frac{dk}{dt} = -\frac{1}{\hbar^2}\frac{d^2\mathbb{E}(k)}{d^2k}\,e\,\mathscr{E} \tag{4.6}$$

The above equation expresses the equation of the motion of moving particles in the crystal. The term, $[\frac{d^2\mathbb{E}(k)}{d^2k}]^{-1}$ is referred as the effective mass of moving particles in a crystal.

The intra-band current: The intra-band current is the consequence of the anharmonicity of the motion of electrons and holes within their respective bands [119]. We assume a particular scenario where the electrons and holes are created by the external field, and the electrons are already migrated to the conduction band. The same electric field also drives the electron and hole in their respective band. In this situation, the equation of motion of electrons is expressed by Eq. (4.5). Now, we apply an oscillatory electric field with frequency ω_0 under a constant envelope,

$$\mathscr{E}(t) = \mathscr{E}_0\cos(\omega_0\,t) \tag{4.7}$$

According to Eq. (4.5) we can write:

$$\frac{dk}{dt} = -\mathscr{E}_0 \cos(\omega_0 t) \tag{4.8}$$

$$k(t) = -\frac{\mathscr{E}_0}{\omega_0} sin(\omega_0 t) \tag{4.9}$$

here we assume $\hbar = e = [\frac{d^2\mathbb{E}(k)}{d^2k}]^{-1} = 1$.
One can expand Eq. (4.8) and can write

$$\mathbb{E}(k) = \sum_{r=0}^{\infty} h_r \cos(rka) \tag{4.10}$$

here, a is the lattice constant, and h_r is another constant that is associated with the band structure of the crystal.

Now we use Eq. (4.10) and Eq. (4.8) to get the the group velocity,

$$\begin{aligned} v_g = \frac{d\mathbb{E}(k)}{dk} &= -\sum_{r=1}^{r_{max}} (r\ a\ h_r\ ) \sin(r\ a\ k(t)) \\ &= -\sum_{r=1}^{r_{max}} (r\ a\ h_r\ )\ \sin\left(-r\ a\frac{\mathscr{E}_0}{\omega_0}\sin(\omega_0 t)\right) \\ &= \sum_{r=1}^{r_{max}} (r\ a\ h_r\ )\ \sum_n J_{2n-1}\left(r\ a\frac{\mathscr{E}_0}{\omega_0}\right)\ \sin((2n-1)\omega_0 t) \end{aligned} \tag{4.11}$$

here we use Jacobi-Anger expansion in the form of the Bessel function J_n of first kind of order n, $\sin(a\sin x) = \sum_{n=-\infty}^{\infty} J_n(a)\sin(nx)$.
The equation for current would be derived from the expression of group velocity in Eq. (4.11)

$$\mathcal{I}_{\text{intra}}(t) = -\frac{2e}{(2\pi)^3}\int_{BZ} v_g(k\ t)\ f_G(k\ t)\ d^3k \tag{4.12}$$

$f_G(k\ t)$ is the time-dependent distribution function of the wave packet. So, one can calculate the high harmonic I_{HHG} from the time derivative of of the current.

$$I_{HHG}(t) \propto \left|\frac{\partial\mathcal{I}_{\text{intra}}(t)}{\partial t}\right|^2 \xrightarrow{FFT} I_{HHG}(\omega) \propto \left|\omega\widetilde{\mathcal{I}}_{\text{intra}}(\omega)\right|^2 \tag{4.13}$$

However, for simplicity, we assume that a wave packet is localized at a particular k.

$$\mathcal{I}_{\text{intra}}(t) \propto v_g(t) \tag{4.14}$$

Then, one can easily calculate I_{HHG} directly from the group velocity.

$$I_{HHG}(t) \propto \left|\frac{\partial v_g(t)}{\partial t}\right|^2 \xrightarrow{FFT} I_{HHG}(\omega) \propto \left|\omega \widetilde{V}_G(\omega)\right|^2 \tag{4.15}$$

Applying Eq. (4.11) to Eq. (4.15) we can calculate higher-order harmonics

$$I_{HHG,(2n-1)}(\omega) \propto \left|N\omega_0 \sum_{r=1}^{r_max} (r\ a\ h_r) J_{2n-1}\left(\frac{r\ a\ \mathscr{E}_0}{\omega_0}\right)\right|^2 \tag{4.16}$$

where $n \in \mathbb{N} > 0$ and we use the

$$FT\{\sin\left((2n-1)\omega_0\ t\right)\} \propto \delta(\omega - (2n-1)\omega_0)$$

Eq. (4.16) indicates that only the odd-integer $(2n-1)$ harmonics are emitted. Also, the Bloch frequency is often introduced,

$$\omega_B = \frac{ea\mathscr{E}_0}{\hbar} = a\ \mathscr{E}_0 \tag{4.17}$$

where, $\hbar = e = 1$.
However, Eq. (4.16) would be modified by Bloch frequency,

$$I_{HHG,(2n-1)}(\omega) \propto \left|N\omega_0 \sum_{r=1}^{r_max} (r\ a\ h_r) J_{2n-1}\left(\frac{r\ \omega_B}{\omega_0}\right)\right|^2 \tag{4.18}$$

The intraband picture predicts a cutoff frequency of the order if the electron (or hole) is confined to a single cosine-shaped conduction (or valence) band,

$$N_{\text{cutoff}} = \frac{\omega_B}{\omega_0}. \tag{4.19}$$

All in all, we see from the analysis that Bloch oscillation plays a crucial role in generating intra-band current in solids.

Role of Bloch oscillation: Bloch oscillation describes the oscillation of a particle (e.g., an electron) confined in a periodic potential when a constant force is operating on it. When an electric field accelerates an electron, the particle encounters a periodic potential as it traverses through a crystal lattice. Bloch oscillation is the result of this potential, which causes the velocity of the electron to oscillate back and forth and produce the oscillation. Bloch oscillation has been shown to have a substantial consequence for high harmonic generation in solid-state materials [130, 132, 284]. In particular, it can contribute to the intra-band current in HHG, which is the current that flows within the conduction band of the material. Let us consider that a periodic band is partially filled with electrons, and a constant electric field $-\mathscr{E}$ is acting on the band. According Eq. (4.5)

$$\frac{dk(t)}{dt} = \mathscr{E} \quad \Rightarrow \quad k(t) = \mathscr{E}.t \tag{4.20}$$

Again, we assume a cosine brand structure $\mathbb{E}(k) = 2 - \cos(ka)$, the group velocity would be,

$$\frac{d\mathbb{E}(k)}{dk} = a \sin(ka) = a \sin(\mathscr{E}.t.a) = \sin(\omega_B.t) \tag{4.21}$$

the expression of ω_B has been given in Eq. (4.17).
Eq. (4.21) implies that the group velocity with Bloch frequency ω_B results in the acceleration within the bands. The group velocity in the Bloch oscillation flips signs ($t = \frac{\pi}{\omega_B}$), which is also worth noting. Another important point is if the driving field is not adequately powerful and changes sign before the electron reaches the Brillouin zone boundary, no Bloch oscillations can occur because the electrons never reach the Brillouin zone boundary. This can be understood with a simple example, considering that electrons start at $k = 0$ and the electric field is expressed in Eq. (4.7). We have $k(t) = -\frac{\mathscr{E}_0}{\omega_0} \sin \omega_0 t$ from Eq. (4.9). The Bloch oscillation can occur if the amplitude of $k = \frac{\mathscr{E}_0}{\omega_0}$ is greater or equal to the Brillouin zone edge $\frac{\pi}{a}$,

$$\frac{\mathscr{E}_0}{\omega_0} \geq \frac{\pi}{a} \Rightarrow \omega_B \geq \pi\omega_0 \tag{4.22}$$

Next, we discuss the second mechanism of HHG in solids.

4.2.2 The interband mechanism

The interband mechanism refers to the process by which electrons are migrated from the valence band to the conduction band due to the absorption of high-energy photons. This process generates polarization within the material. The polarization arises from the separation in the opposite direction of the electron and hole charge carriers in real space due to the electric field of the incident light. However, in $k-$space, the electron and hole charge carriers move in the same direction. In real space, though, the electrons and the holes are driven in opposite directions by the field, causing a dipole moment to be created. Thus, the change in dipole moment causes the change in polarization inside the material, resulting in a current generation. Due to the external electric field, the charge carrier electrons and holes accelerate, which ultimately finally recombine and result in the emission of light. This polarization current is often referred to as interband current. That can be obtained directly from polarization $P(t)$,

$$\mathcal{I}_{\text{inter}}(t) = \frac{\partial P(t)}{\partial t} \tag{4.23}$$

The calculation for the associated radiation spectrum is the modulus square of the Fourier transform of the time derivative of the current. This is equivalent to taking the Fourier transform of the dipole acceleration.

$$\begin{aligned}
\mathcal{R}_{\text{inter}}(\omega) &= \left| FT\left\{ \frac{\partial}{\partial t}\mathcal{I}_{\text{inter}}(t) \right\} \right|^2 \\
&= \left| FT\left\{ \frac{\partial^2}{\partial^2 t}P(t) \right\} \right|^2 \\
&\propto \left| \omega^2 \widetilde{P}(\omega) \right|^2
\end{aligned} \tag{4.24}$$

here we take the Fourier transform of the time derivative, which is proportional to $i\omega$. On summing the contribution from intra-band and interband mechanisms, the resultant harmonics can be obtained

as

$$\begin{aligned}\mathcal{R}(\omega) &= \left| FT\left\{ \frac{\partial}{\partial t}\mathcal{I}_{\text{intra}}(t) + \frac{\partial}{\partial t}\mathcal{I}_{\text{inter}}(t) \right\} \right|^2 \\ &= \left| FT\left\{ \frac{\partial}{\partial t}\mathcal{I}_{\text{intra}}(t) + \frac{\partial^2}{\partial^2 t}P(t) \right\} \right|^2 \\ &\propto \left| i\omega\widetilde{\mathcal{I}}_{\text{intra}}(\omega) + \omega^2\widetilde{P}(\omega) \right|^2 \end{aligned} \tag{4.25}$$

Thus, the interplay between intra-band and interband action is one of the essential processes that generate HHG in solids. Hence, we have two processes that, in theory, are able to explain how high-harmonic light might be generated from a solid. The obvious issue that has to be asked is which of these two mechanisms is prominent for the generation of high-order harmonics in solids. The last decade has seen a great deal of debate on these issues, but no clear resolution has emerged.

However, the incorporation of HHG into solids has the potential to transform a broad number of disciplines, spanning from fundamental studies of light-matter interactions to applied research in materials science, quantum technologies, and surface science [285]. It facilitated a new way to understand physical phenomena beyond linear response regimes such as:
a) Ultrafast imaging: HHG can be used to capture images of dynamic processes on ultrafast timescales, providing insights into the behavior of materials and biological systems. For example, researchers have used HHG to image the motion of electrons in graphene, providing new insights into the electronic properties of this material [35, 286, 287].
b) Ultrafast electronics: HHG can be used to generate high-frequency signals for use in ultrafast communication and computing technologies. For example, one can use HHG to generate terahertz radiation, which has potential applications in high-speed wireless communication and sensing [129, 288, 289].
c) Attosecond physics: HHG can be used to generate extremely short bursts of light, known as attosecond pulses, which are useful for studying ultrafast processes on the timescale of electronic motion.

For example, researchers have used HHG to study the dynamics of electronic motion in atoms and molecules, providing insights into fundamental processes in quantum physics [38, 39, 290–292].
d) Ultrafast spectroscopy: We can utilize HHG to study the properties of materials on extremely short timescales, providing insights into the behavior of electrons and the dynamics of chemical reactions. For example, HHG has been used to study the behavior of electrons in topological insulators, which have potential applications in quantum computing [293–298].

Beyond these, there are several applications of HHG, such as Nonlinear optics, ultra-fast magnetism [299–301], quantum materials [302–305] and more [306–308].

Here, we employ HHG spectroscopy to investigate three distinct properties of solids: topological features in the generalized non-interacting SSH chain; the distinction between localized and delocalized phases in the non-interacting Aubry-André-Harper model; and the topological phase in the 1-dimensional strongly correlated extended Fermi Hubbard model. In recent years, the field of condensed matter physics has seen an increasing interest in the study of topological phases of matter. These phases are characterized by non-local and non-perturbative properties that are protected by topological invariants, which are robust against perturbations and imperfections. The discovery of topological insulators [185, 309] and topological superconductors [137, 310] has led to the exploration of a wide range of topological phases in different materials, including cold atoms [311] and photonic [312–314] systems. The study of these systems is not only of fundamental interest, but also has potential applications in various fields, such as quantum computing [315–318], spintronics [319], and magnetometry [320].

In the following section, we explore the topological feature of the 1-D Extended Su- Schrieffer-Heeger chains.

4.3 Detection of topological phase in extended Su-Schrieffer-Heeger chains

The Su-Schrieffer-Heeger (SSH) model is one of the simplest models that exhibit non-trivial topological properties. It is a one-dimensional model originally introduced to describe the electronic properties of

polyacetylene [321, 322], a linear polymer of carbon and hydrogen atoms. The model is described by a tight-binding Hamiltonian representing hopping of electrons between adjacent sites, with two different parameters, representing alternating single and double bonds. The SSH model exhibits two different phases, characterized by the number of edge states that appear in the band gap at a zero-energy. In the trivial phase, there are no zero-energy states, while in the topological phase, there are two such states that appear at the open ends of the system. Various extensions of the SSH model have been explored, including longer-range tunneling terms that describe the hopping between second nearest neighbors [318, 323]. An appropriately extended SSH model may exhibit additional topological phases, such as a phase characterized by four edge states.

High harmonic spectroscopy in condensed matter is a burgeoning field in strong-field attosecond science that has the potential to uncover the structural and dynamical properties of materials [291, 324]. High harmonic generation (HHG) is a nonlinear optical process that occurs when an intense laser field interacts with a material, producing high-order harmonics of the incident frequency. In recent years, the connection between strong-field attosecond science and the topological condensed matter has started to be explored theoretically [325–333] and experimentally [334, 335]. In the context of the SSH model, theoretical studies have shown that high-harmonic spectroscopy can be used to detect topological properties [326, 327]. In particular, the high-harmonic spectra of the SSH model exhibit characteristic features that allow to distinguish between trivial and non-trivial topological phases, and to identify the topological edge states. Nevertheless, it remains unclear whether two different non-trivial topological phases, with various non-zero number of edge states, can also be identified using HHG.

To address this issue, in this work, we consider the extended version of the SSH model which includes second neighbor electronic hopping as studied in Ref. [336]. This model exhibits topological phases with zero, two, and four-edge states. We propose a method to distinguish between these phases using high-harmonic spectroscopy. Our method is based on the analysis of the non-linear polarization of the material, which reveals characteristic signatures of the topological phases. We show that our method can provide a clear distinction between materials with two and four edge states, and can be used to

identify and control the topological properties of other topological materials. Our method could have significant implications for the study of topological phases in condensed matter and could aid in the development of new technologies.

4.3.1 The extended Su-Schrieffer-Heeger model

The Su-Schrieffer-Heeger (SSH) model [321,337] is a theoretical model used in solid-state physics to describe the electronic properties of one-dimensional crystalline systems. The model considers a chain of alternating atoms in sublattices A and B in a two site unit cell [327]. The electrons hop inside the unit cell (intra cell) and between nearest neighbor unit cells (inter cells) with different hopping amplitudes. The model is thus characterized by a parameter called the dimerization parameter, which represents the difference in the hopping strengths between the intra and intercellular bonds. When the intercellular dimerisation is stronger than the intracellular one, it exhibits a nontrivial topological phase with a bulk gap, and supports the presence of topologically protected edge states at the boundary of the chain. This allows the SSH model to be a prototypical model of a 1D topological insulator. The topological nature of the SSH model is due to the presence of a chiral symmetry which is a discrete symmetry that anti-commutes with the SSH Hamiltonian and shows that the model is invariant under the exchange of its two sublattices. It also ensures that for every positive energy of the system there exists a negative energy with the same magnitude. Interestingly, the energies are also symmetrical under swap of the dimerisations, and the dispersion relation is identical and gapped everywhere (insulator), except when the dimerisation is zero where it is gapless (metal). However, the system has distinct properties under swap of the dimerisation as the eigenvectors differ significantly. In fact, when the Berry curvature of the eigenvectors in quasi-momentum space is integrated over the entire Brillouin zone, one finds different topological invariants called Chern numbers. This shows that the two insulating phases are topologically distinct. The presence of different topological sectors implies the impossibility of crossing from an insulating phase to another without undergoing a topological phase transition which involves the closing of the bulk gap (i.e. the metallic phase where the winding number is ill-defined) of the system. This is why when

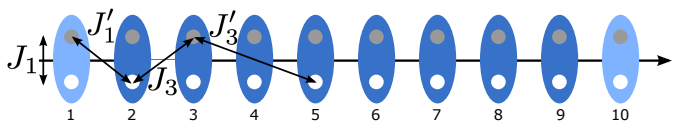

Figure 4.5: Schematic representation of the one-dimensional ESSH model described by the Hamiltonian (Eq. (4.27)): Each blue ellipse represents a unit cell containing two sites: A-type sites drawn below, and B-type sites drawn above. To keep chiral symmetry in tact, we only include hopping processes between A-type and B-type sites, including intracell hopping, J_1, hoppings between neighboring cells,J_1' and J_3, as well as hopping between next-to-nearest cells, J_3'.

the system with a non-zero bulk topological invariant is put under an open boundary condition, there appears a zero energy (edge) mode within the bulk gap of the system, sharply localised at the boundary separating a topologically non-trivial region (insulator) from a topologically trivial one. The non-interacting tight-binding model used in this study does not consider electron-electron interactions. As a result, it is possible to obtain precise analytical results for both the band structure and the winding number, making it a representative example of a 1D topological insulator [309]. The SSH model has so far been experimentally realized in various systems: cold atoms [338], photonic lattices [161, 339], and mechanical systems [340]. The topological phase diagram of the standard SSH can be extended to include phases with higher values of topological invariants, if not restricted to only nearest neighbor electronic hopping. Allowing for a longer range of hopping, such as, hopping between second neighbor sites, generates a model which we denote as an extended Su-Schrieffer-Heeger (ESSH) model, extensively studied in Ref. [323]. However, hoppings only between the different sublattices are included to preserve the chiral symmetry of the model, which in turn keeps the topology intact. More specifically, in this work, we study the Hamiltonian of the 1D ESSH model:

$$\begin{aligned}\mathcal{H} = J_1 \sum_{n=1}^{N} (\hat{c}_{n,A}^{\dagger}\, \hat{c}_{n,B} + h.c.) + J_1' \sum_{n=1}^{N} (\hat{c}_{n,B}^{\dagger}\, \hat{c}_{n+1,A} + h.c.) \\ + J_3 \sum_{n=1}^{N} (\hat{c}_{n,A}^{\dagger}\, \hat{c}_{n+1,B} + h.c.) + J_3' \sum_{n=1}^{N} (\hat{c}_{n,B}^{\dagger}\, \hat{c}_{n+2,A} + h.c.)\end{aligned} \tag{4.26}$$

where N is the number of cells, in a chain of $M = 2N$ sites in the chain. In the second quantized notation, $\hat{c}^{\dagger}_{n,s}$ ($c_{n,s}$) is the electron creation (annihilation) operator at unit cell n with sublattices $s = A, B$. The first term represents intracellular electron hopping with strength J_1, the second represents the nearest neighbor intercellular hopping between B at cell n and A at cell $n+1$, the third is nearest neighbour hopping between A at cell n and B at cell $n+1$ whereas the fourth term captures the next nearest neighbour hopping between B at cell n and A at cell $n+2$ (see Fig. 4.5). In the first quantized notation, the Hamiltonian in real space can be written as

$$\begin{aligned}\mathcal{H} =& J_1 \left(\sum_{n=1}^{N} |n, A\rangle\langle n, B| + h.c \right) \\ &+ J_1' \left(\sum_{n=1}^{N} |n, B\rangle\langle n+1, A| + h.c \right) \\ &+ J_3 \left(\sum_{n=1}^{N} |n, A\rangle\langle n+1, B| + h.c \right) \\ &+ J_3' \left(\sum_{n=1}^{N} |n, B\rangle\langle n+2, A| + h.c \right).\end{aligned} \tag{4.27}$$

As in the standard SSH model, the extended SSH model Hamiltonian also preserves the three discrete symmetries: chiral, particle-hole and time-reversal and is classified under the BDI topological class with its topological invariant (the winding number) belonging to the set of integers $\mathbb{Z}$. On an open boundary, the ESSH can host different numbers of edge modes: zero, two or four edge modes, depending on the absolute value of its bulk winding number being zero, one or two. In contrast the standard SSH model, possess only two possibilities – zero or two edge modes on the ends of the open chain.

It is straightforward to calculate the winding number by writing down the Hamiltonian in Eq. (4.27) in momentum representation, which can be obtained by replacing,

$$\begin{aligned}|n, A\rangle &= \sum_k e^{-ikx_{nA}} |k, A\rangle, \\ |n, B\rangle &= \sum_k e^{-ik'x_{nB}} |k', B\rangle,\end{aligned} \tag{4.28}$$

where $|k, s\rangle$ is the quasi-momentum ket with momentum k and sublattice index $s = A, B$ and using periodic boundary conditions. With this, the Hamiltonian in Eq. (4.27) reduces to,

$$\mathcal{H} = \sum_k \left(|k, A\rangle, |k, B\rangle\right) \left[h_x(k)\sigma_x + h_y(k)\sigma_y\right] \begin{pmatrix} \langle k, A| \\ \langle k, B| \end{pmatrix}, \tag{4.29}$$

where

$$\begin{aligned} h_x(k) &= J_1 + J_1' \cos ka + J_3 \cos ka + J_3' \cos 2ka \\ h_y(k) &= J_1' \sin ka - J_3 \sin ka + J_3' \sin 2ka \end{aligned} \tag{4.30}$$

Due to the presence of discrete translational invariance in the system, it reduces to two-level systems in the sublattice basis for each quasi-momentum mode k and can therefore be easily written down in terms of Pauli matrices σ_x and σ_y. Further, this decomposition into the Pauli basis allows us to compute the winding number using h_x and h_y,

$$\mathcal{W} = \frac{1}{2\pi} \int_{BZ} \frac{h_x \partial_k h_y - h_y \partial_k h_x}{h_x^2 + h_y^2} \mathrm{d}k \tag{4.31}$$

The winding number for this model can have values $\mathcal{W} = -1, 0, 1, 2$, which through the bulk-boundary correspondence directly yields the number of edge modes the system possesses in an open boundary condition as two times its absolute value $2|\mathcal{W}|$. From the energy spectrum plotted in Fig. 4.10, one can see the band gap structure, the different number of zero energy modes or edge modes and the winding number for the two most interesting cases when the system (a) has winding number one and thus one pair of edge modes (b) has two pairs of edge modes with winding number two. Fixing the value of the parameters $J_1 = J_1' = 1$, one can vary the other two parameters J_3 and J_3' and calculate the winding number to obtain a phase diagram showing different possible phases in the ESSH system as has been illustrated in Fig. 4.7.

4.3.2 Incident laser field

In this section, we study the coupling of the 1D ESSH model to a linearly polarised electric field from a laser. The laser wavelength is assumed to be much larger than the length of the system and as

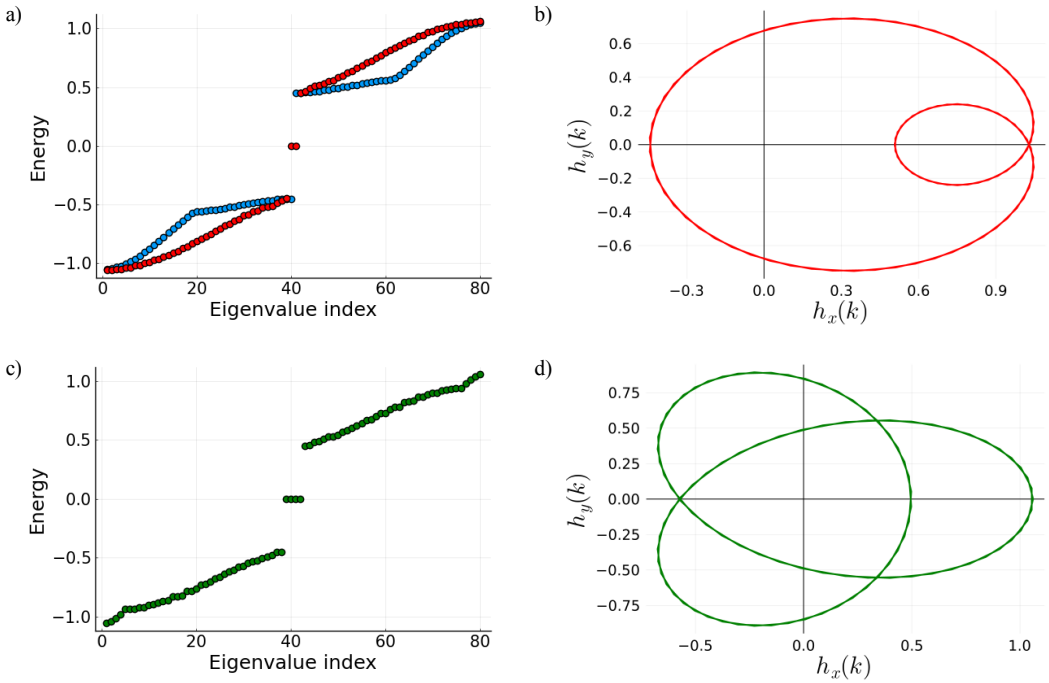

Figure 4.6: Energy eigenvalues with 80 sites (in a.u.), showing zero (a,blue), two (a,red) and four (c,green) zero-energy states with different fixed parameters values of the Hamiltonian (Eq. (4.27)). The figures on the right show the parametric plot of $h_x(k)$ and $h_y(k)$ as defined in Eq. (4.29), with two (b) and four (d) zero-energy states.

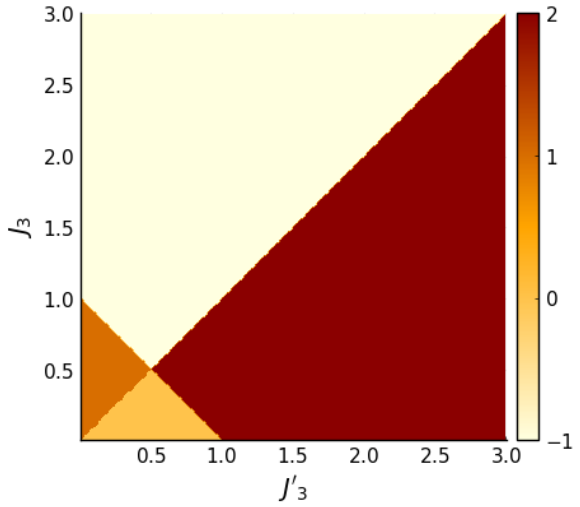

Figure 4.7: Topological phase diagram of the Hamiltonian (Eq.(4.29)) showing various values of the winding number for fixed $J_1 = J'_1$ varying J_3 and J'_3 (in units of J_1), calculated as in Eq.(4.31).

such the coupling to the laser field is well captured within the dipole approximation. The laser vector potential and electric field are:

$$\vec{A}(t) = A(t)\hat{x}, \quad \vec{E}(t) = -\partial_t \vec{A}(t). \tag{4.32}$$

where $\hat{x}$ is the direction along the length of the chain parallel to the laser polarization. The way how the light couples to the matter depends on the geometry of the system. For instance, in the velocity gauge, the light-matter coupling provides the hopping elements with Peierls' phases $\vec{A} \cdot (\vec{r}_{n,s} - \vec{r}_{n',s'})$. For concreteness, we assume that $\vec{A} \cdot (\vec{r}_{n,s} - \vec{r}_{n',s'}) \propto n - n'$. Hence, intracell hopping remains unaffected by the light, i.e. $\vec{A} \cdot (\vec{r}_{n,A} - \vec{r}_{n,B}) = 0$, whereas hopping between neighboring cells acquires a phase $A(t)$, and hopping between next-to-nearest cells a phase $2A(t)$. Accordingly, we have

$$\begin{aligned} J_1(t) &= J_1 & J'_1(t) &= J'_1 e^{iaA(t)} \\ J_3(t) &= J_3 e^{iaA(t)} & J'_3(t) &= J'_3 e^{2iaA(t)}. \end{aligned} \tag{4.33}$$

The eigenstates of the $N \times N$-dimensional ESSH Hamiltonian (4.26) are obtained by exact diagonalization in a real space single particle basis. The $N/2$ lowest energy states (occupied by N electrons, assuming spin degeneracy) are time evolved within the whole laser

pulse duration consisting of 5 cycles ($n_c = 5$). Assuming atomic units ($\hbar = |e| = m_e = 4\pi\epsilon_0 = 1$), the incident laser field has the shape

$$A(t) = A_0 \sin^2\left(\frac{\omega t}{2n_c}\right)\sin(\omega t) \qquad 0 < t < \frac{2\pi n_c}{\omega}. \tag{4.34}$$

The frequency is set to $\omega = 0.03$ (corresponding to $\lambda \simeq 1.5\mu m$), and the vector potential amplitude is $A_0 = 0.5$ (corresponding to a laser intensity $\simeq 20 \times 10^{10}\,\mathrm{Wcm}^{-2}$) throughout this work. The results discussed in this project are qualitatively independent of the details of the laser pulse as long as the incident laser frequency is small compared to the band gap in the insulating phases and the peak strength of the laser is large enough to generate high harmonics.

The time-dependent wavefunction was calculated using the Crank-Nicolson approximation for the time-dependent Hamiltonian

$$|\Psi(t)\rangle = \exp[-i\,\mathcal{H}(t)\delta t]|\Psi(0)\rangle \sim \frac{1 - i\,\mathcal{H}\left(\frac{t}{2}\right)\delta t/2}{1 + i\,\mathcal{H}\left(\frac{t}{2}\right)\delta t/2}|\Psi(0)\rangle, \tag{4.35}$$

solved in individual infinitesimal δt time-steps.

4.3.3 High-harmonic generation

Our primary goal is to estimate the high harmonic spectrum of the ESSH system. Within the semi-classical approach, for uncorrelated emitters, the spectrum of the radiated light is proportional to the absolute square of the Fourier transform of the dipole acceleration [341–343].

$$P(\omega) = \left|\mathrm{FFT}\left[W_B \ddot{X}(t)\right]\right|^2 \tag{4.36}$$

where here we used W_B as the Blackman window function and $\ddot{X}(t)$ is the acceleration or the double time derivative of the time dependent position operator. To calculate the time-dependent expectation value of the position operator we time-evolve all occupied eigenstates b. The time-evolved single-particle wavefunction $\Psi_b(t)$ is then used to compute

$$X(t) = \sum_{b=1}^{N/2}\sum_{j=1}^{N}\sum_{s=A,B}\Psi_b^{j,s*}(t)x_{j,s}\Psi_b^{j,s}(t), \tag{4.37}$$

where $\Psi_b^{j,s}(t)$ is the amplitude of the time-evolved wavefunction on site s of cell j, and the position $x_{j,s}$ is given by

$$x_{j,A} = x_{j,B} = (j-1) - \frac{(a-M)}{4} \tag{4.38}$$

where j is the position of each cell with two sites A and B, as shown in Fig. 4.5. Essentially, the time-evolved average position of all electrons in different (initial) filled eigenstates are summed to obtain the total position of the electron cloud.

In the next Section, we analyze and compare the time-dependent position and the harmonic response of the system at three different parameter points, corresponding to three different phases as illustrated in Fig. 4.10: (a) Phase P_0, represented by the parameter point $J_1 = 0.651$, $J_1' = 0.207$, $J_3 = 0.038$, and $J_3' = 0.156$. From the energy spectrum presented in Fig. 4.10a (blue), we observe the energy band gap of 0.9 (in atomic units) and the winding number of $\mathcal{W} = 0$ corresponding to the trivial insulator phase. (b) Phase P_1, represented by the point $J_1 = 0.51$, $J_1' = 0.42$, $J_3 = 0.056$, and $J_3' = -0.479$. It is illustrated in Fig. 4.10a (red), exhibiting the presence of two zero-energy states that indicate the edge states, in agreement with the winding number $\mathcal{W} = 1$. (c) Phase P_2, represented by $J_1 = 0.059$, $J_1' = 0.021$, $J_3 = 0.26$, and $J_3' = 0.7209$. For this phase, we observe in Fig 4.10b the presence of four zero-energy states, representing the edge modes with $\mathcal{W} = 2$. The parameter choices have been made such that the system has the same band gap and bandwidth in all three phases, allowing for a clear comparison of the results amongst all three phases. We also look at the phase transition point M, which is a metal with the parameters $J_1 = 0.51$, $J_1' = 0.42$, $J_3 = 1$, and $J_3' = 0.91$. The overall goal is to observe whether, through the time-dependent position operator and the harmonic spectra, one can identify certain signatures, which will enable a clear distinction between P_0, P_1, P_2, and M.

4.3.4 Discussions

We first look at the expectation value of the total position operator of the ESSH model as a function of time, as is illustrated in Fig. 4.8 for the three different phases P_0, P_1 and P_2. The position operator has the similar periodicity in all the phases as that of the incident laser beam (Eq. (4.34)) but there is a clear difference in the maximum amplitude

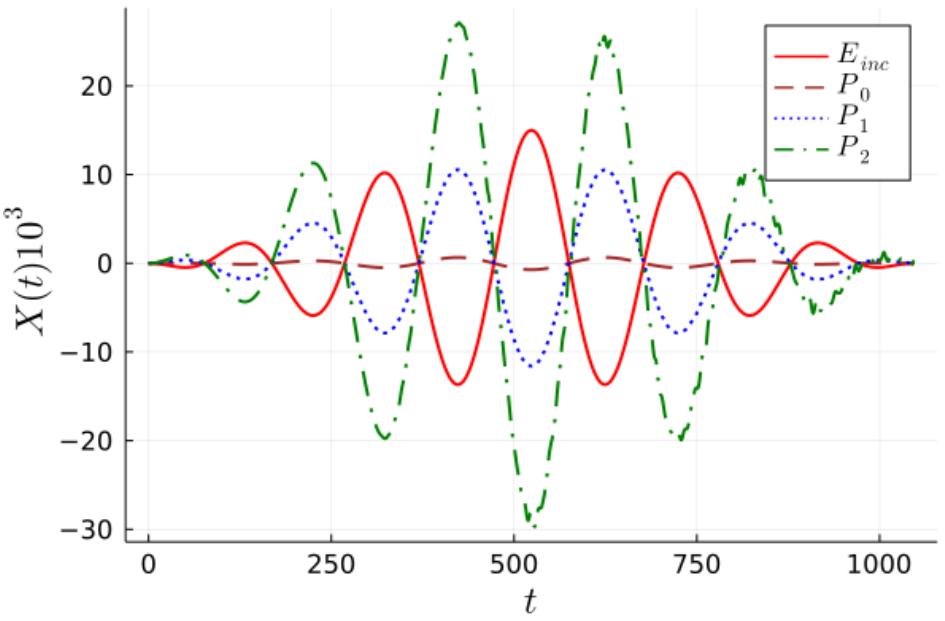

Figure 4.8: Incident electric field (red, solid line) and the expected value of the position operator (Eq.(4.37)) as a function of time, for different topological phases P_0, P_1 and P_2.

for the three phases. Apparently, the change in the average electronic position is the lowest in the topologically trivial insulating phase P_0 and can be attributed to the overall localised nature of the electronic cloud for a half-filled insulator. The presence of edge modes makes the system slightly more metallic and hence the displacement is more in phases (P_1, P_2) with more edge modes in the system. This becomes more apparent as one studies the harmonic spectra of the system.

In Fig. 4.9, we plot the logarithm of the absolute power spectra of the harmonic spectra versus the harmonic order (integer multiple of the incident driving frequency). The harmonic spectra for P_0, P_1 and P_2 show a plateau at high energies beyond the bandgap of the system. The plateau mainly arises from interference between electronic trajectories undergoing interband transitions. A cut-off is also observed at similar harmonic order for all the three curves as it is primarily determined by the bandwidth (energy difference between highest and lowest eigenenergy) of the system, which limits the maximum energy that the electrons can attain during evolution. However the harmonic

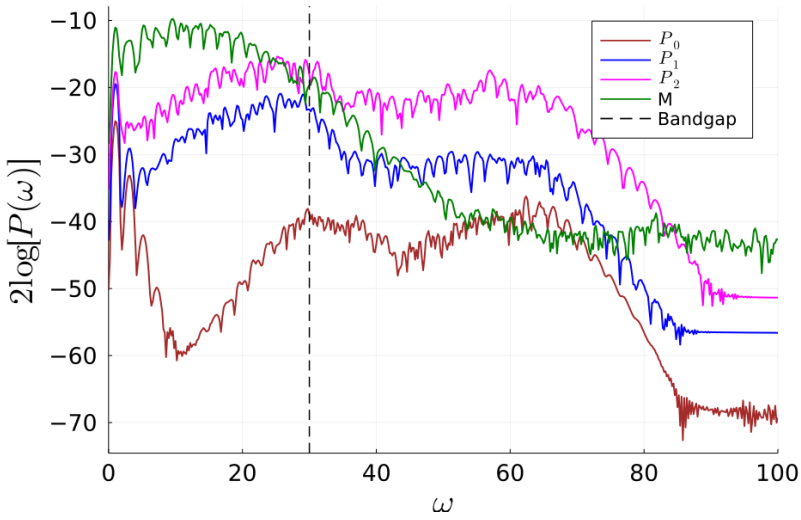

Figure 4.9: The emitted high-harmonic spectra for the phases: metallic, topologically trivial P_0 and two different topologically non-trivial P_1 (with two edge modes) and P_2 (with four edge modes). M indicates the metal phase. The vertical line corresponds to the value of the bandgap (in the units of the incident laser frequency).

response below the band gap is different for P_0 and P_1, P_2 phases. This region, which in usual semiconductors is mostly dominated by intra-band contributions, has a dip for P_0. However, in phases P_1 and P_2, we observe no dip below the bad gap. This happens because there are mid band gap states available for electronic transition due to the presence of edge modes in these phases. These appear as clear signals in the harmonic spectra as now transitions between the filled bulk bands to the mid gap edge states are possible. In contrast, the P_0 phase is a trivial insulator with a bulk gap and no mid gap states, and thus the bulk states can only contribute to the harmonic spectra beyond the band gap. Consequently, there appears a dip in signal below the band gap for such a phase. This feature that allows to distinguish between the high harmonic spectra of topologically trivial and non-trivial phases was also observed in the previous studies of the HHG in the SSH model [326, 327]. Moreover, it has been studied in topological superconductors and the topological nature of the edge modes has been confirmed by showing that it is robust under local perturbations via the HHG [333].

However interestingly, it is not easy to distinguish between the two topological phases based on the harmonic spectra itself, as the overall amplitude difference in the time dependent position being polynomial does not appear as a big difference in the harmonic spectra, which is plotted in a logarithmic scale and it depends on the specific values of the hopping parameters chosen for these two phases. Despite this, by analyzing the contributions of both bulk and edge states to the high-harmonics and using the harmonic spectra of the trivial insulating phase P_0 and the metallic phase transition point M as two extreme reference limits to test for metallicity, we can elaborate below, how precise control over the electronic filling in the ESSH chain allows us to clearly distinguish between all the different topological phases based solely on the HHG spectra.

We assume an ESSH chain away from half-filling where the number of electrons in the chain is ν less than $N/2$. Then the expectation value of the position operator is given by,

$$X(t,\nu) = \sum_{b=1}^{N/2-\nu} \sum_{j=1}^{N} \sum_{s=A,B} \Psi_b^{j,s*}(t) x_{j,s} \Psi_b^{j,s}(t), \tag{4.39}$$

As a consequence, varying the ESSH chain filling, *i.e.* changing the value of $\nu = \{0,1,2,3,4\}$ affects the HHG spectra (Eq. (4.36)) of phases P_0, P_1 and P_2 as shown in Fig. 4.10.

We first focus on phase P_0 (see Fig. 4.10a) and compare the HHG spectra for various fillings against the one at exactly half-filling (yellow). It can clearly be observed that for values of filling till $N/2-1$, the HHG spectra is almost identical no matter the filling. In fact, away from half filling the spectra in fact has no dips as it has at half-filling. This is because even slightly away from half filling the system is no longer an insulator and there is a small number of states available (depending on the filling) for transition within the bulk states below the band gap, producing significant HHG spectra from intra-band dynamics within this partially filled valence band. This HHG spectra resembles that of a metal as can be seen via comparison with the green curve in Fig. 4.9. The order of magnitude difference (in logarithmic scale) between the spectra at half filling and the one away shows how sensitive a probe the HHG spectra is to the filling of the system that produces metallicity and that do not.

This sensitivity acts as a means to quantitatively distinguish the presence of the number of edge modes in phases P_1 (see Fig. 4.10b)

and P_2 (see Fig. 4.10c). By varying the filling of the system with parameters from the P_1 (P_2) phase we see that the system shows metallic HHG spectra till $N/2-2$ ($N/2-3$) states are filled, then suddenly it shows a dip as the bulk of the system becomes insulating when $N/2-1$ ($N/2-2$) states are filled. Thus by continuously monitoring the filling, it is possible to count how many states ahead of half-filling does the system show a transition from metallic behavior to an insulating one. This difference in the number of states gives the number of pairs of edge modes in the system.

The dip in the harmonic power spectra at the filling where the transition from bulk metallic to bulk insulating behavior happens, can be quantitatively determined by summing the inverse of the squared value of power spectra below half the bandgap for every value of ν as,

$$S_p(\nu) = \sum_{w=0}^{\Delta E/2} \frac{1}{P(\omega,\nu)^2}, \tag{4.40}$$

where ΔE is the bulk band gap energy of the system (edge modes excluded). The sum is taken over half the band gap as expectedly the sharp change only affects the harmonic modes below the band gap in the harmonic spectra.

The transition shows up in this quantity $S_p(\nu)$ as a sharp jump with at least ten orders of magnitude difference. In phase P_0 the transition occurs between the completely filled, $\nu = 0$, to $\nu = 1$, where $S_p(0) \sim 10S_p(1)$ saying that the number of pairs of edge modes in the system is zero. In phase P_1, the transition takes place between $\nu = 1$ to $\nu = 2$, where $S_p(0) \sim S_p(1) \sim 10S_p(2)$ and the system then possesses just one pair of edge modes. In phase P_2 the transition is from $\nu = 2$ to $\nu = 3$, which changes $S_p(\nu)$ as $S_p(0) \sim S_p(1) \sim S_p(2) \sim 10S_p(3)$ correctly indicating that there are two pairs of edge modes in the system. We show an illustrative plot of this behavior in Fig. 4.11.

4.3.5 Conclusions

In summary, in this work we allow for second nearest neighbor hopping in addition to the nearest neighbor hopping already present in the standard SSH model with hopping terms within a sublattice being forbidden. This creates the ESSH model with the chiral sym-

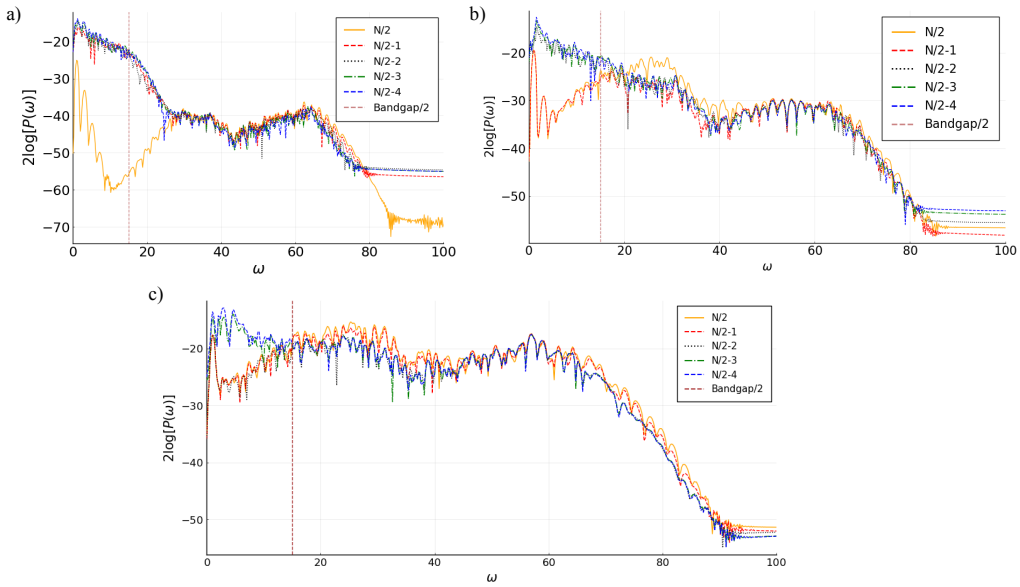

Figure 4.10: High-harmonic spectra for different phases. a) Phase P_0 (zero edge modes). b) Phase P_1 (two edge modes). c) Phase P_2 (four edge modes). Different colors correspond to various fillings of the system. The vertical line indicates half of the value of the bandgap (in the units of the incident laser frequency).

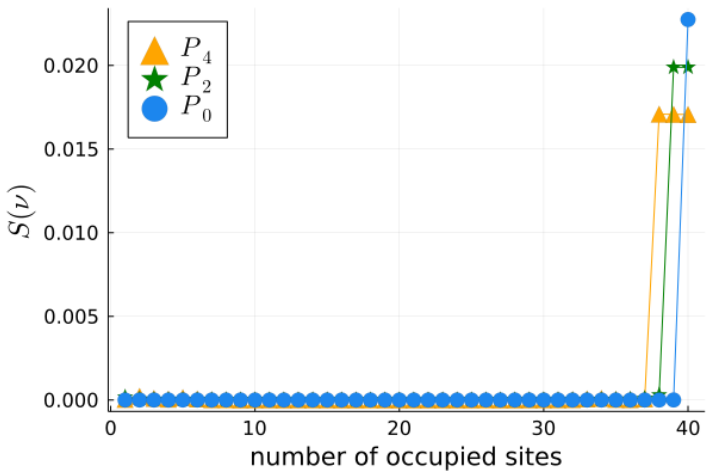

Figure 4.11: $S_p(\nu)$ versus filling for different phases P_0, P_2 and P_4. It shows a peak when all the states in the bulk are filled and the edge states start to be filled. One state in the peak represents zero edge modes or Phase P_0, two states in the peak represents two edge modes or Phase P_2 and three states in the peak represents four edge modes or Phase P_4.

metry in the SSH model being preserved. However, this expands the topological phase diagram of the SSH model to now include new topological phases with higher winding numbers. Such a system under open boundary condition posses three insulating phases with zero, two, and four edge modes at each ends of the chain.

We shine a five-cycle ultrafast laser pulse with strong intensities and below the bulk band gap frequencies parallel to the length of the ESSH chain and calculate the emitted harmonic spectra in response to this illumination. The harmonic spectra in the linear scale show that the overall response of the system below the band gap is different for its three phases; the amplitude being higher when the system has more edge modes. However although the distinction is clearly visible between the HHG spectra from the trivially insulating versus the topological ones, the distinction between the two topological phases is hard to perceive in the logarithmic scale. Therefore, we do a careful analysis of the HHG spectra as a function of filling to show that the HHG spectra is very sensitive to the change from bulk insulating behavior to a bulk metallic behavior, as filling is continuously varied.

Therefore, tracking where the bulk insulating behavior sets in, as a function of filling, we manage to count off the number of pairs of edge states in the system. We have also proposed a quantity that can sharply detect this transition.

Our work concentrates on the study of an idealized model, which features different topological phases. Our goal was to investigate whether and how HHG is suited to differentiate between these phases. Of course, the next step will be to consider analog phases occurring in real materials. It is clear that brings in additional challenges: In the present work, we have not included the effect of scattering between electrons, or electron-phonon and other defects. A phenomenological way of taking such effects into account is by including a dephasing time in the analysis [344]. In fact, that can help to produce a cleaner spectrum by removing longer trajectories that contribute to the HHG spectra. We leave this as an outlook. Also the role of many-body electron-electron interaction has been assumed to be negligible and has not been considered in this work and is beyond the scope of the current project.

In summery:

- The Su-Schrieffer-Heeger (SSH) chain is a one-dimensional model used to understand topological insulators, primarily using nearest neighbor electronic hopping.

- High-harmonic generation, a sophisticated technique, is instrumental in detecting the different topological phases in a material.

- High-harmonic spectroscopy of the SSH chain can discern between trivial and non-trivial topological phases; this refers to differentiating between zero and two topological edge states in the chain.

- The extended SSH model incorporates not only the nearest neighbor interactions, but also the next-nearest neighbors hopping. In this model, topological phases arise due to zero, two, and four zero-energy edge states.

- Despite the complexities of the extended SSH model, high-harmonic spectroscopy is only able to differentiate between

trivial and non-trivial topological phases, which restricts the ability to quantify the number of edge states in the model.

- We demonstrate that high-harmonic spectroscopy can serve as a sensitive tool for discriminating topological phases in systems with more than two topological phases.
- We propose a practical scheme that enables precise quantification of the number of edge modes in each topological phase. This is accomplished by adjusting the electronic filling in the chain.

4.4 Aubry-André-Harper (AAH) model (ongoing)

Quantum localization is a very interesting field of research, where the Aubry-André-Harper model serves as the paradigmatic model which can exhibit quantum localization [345]. The AAH model offers a simple but informative framework for understanding the interplay between quasiperiodicity, localization, and metal-insulator transitions in one-dimensional systems. The critical points of the AAH model feature critical spectra with fractal structure, which are distinguished by having multifractal eigenstates. This multifractality reflects the non-trivial spatial distribution of wave functions, which have a self-similar structure at different length scales. AAH model has been realized in the photonic, acoustic, ultracold atomic systems [138, 169, 346–348]. The Hamiltonian of AAH model is given as follows:

$$H = J\sum_{j}\left(c_j^{\dagger}c_{j+1} + c_{j+1}^{\dagger}c_j\right) + \sum_{j} 2V\cos\left(2\pi\beta j\right)c_j^{\dagger}c_j, \tag{4.41}$$

here, $\beta = \frac{1+\sqrt{5}}{2}$ is the golden ratio, and V and J are the incommensurate potential strength and the hopping amplitude between adjacent sites, respectively. $c_j^{\dagger}(c_j)$ is the creation (annihilation) operator for an electron at the site j. The Hamiltonian of the AAH model exhibits localization phase transition at $V = J$ ($V < J$ is the delocalized phase and $V > J$ – localized phase).

4.4.1 Localization

AAH Hamiltonian exhibits a localization transition at $V = J$ where every single particle's eigenstate is simultaneously localized at a finite detuning strength. We consider an eigenstate $|\chi_j(x)\rangle$ is localized at x_0, if for every $\kappa > 0$ one can find a distance $d > 0$ such that.

$$|\Phi_j(x_0 \pm d)|^2 < \kappa \tag{4.42}$$

This implies the probability of a particle with the eigenstate $|\chi_j(x)\rangle$ far from the center x_0 is zero. But in the center x_0, the eigenstate is highly localized. This can be expressed as:

$$|\chi_j(x, x_0)\rangle = f(x, x_0)\, e^{-\frac{|x-x_0|}{\delta}} \tag{4.43}$$

where, $f(x, x_0)$ and δ are an arbitrary function and localization length, respectively. The localization length of all eigenstates can be written as:

$$\delta = \log\left(\frac{V}{J}\right) \tag{4.44}$$

4.4.2 Delocalization

The AAH model exhibits a delocalized or extended phase when the ratio of the incommensurate potential strength (V) to the hopping amplitude between adjacent sites (J) is less than 1(i.e.$V/J < 1$). Under these conditions, the particles exhibit metallic behavior, resulting in strong electrical conductivity. The localization length, a measure of the spatial extent of a particle's wavefunction, is inversely proportional to the degree of delocalization. In a delocalized phase, the localization length is relatively large, indicating that the particles have a greater probability of occupying different sites within the system. Understanding the interplay between localization length and delocalization in the AAH model provides valuable insights into the electronic properties and transport phenomena of quasiperiodic materials.

4.4.3 Inverse participation ratio (IPR)

The Inverse Participation Ratio (IPR) is a useful quantity to characterize the localization properties of quantum states in the Aubry-André-

Harper (AAH) model. IPR quantifies the degree of localization or delocalization of the wavefunction by measuring the weight distribution across the lattice sites. For a given eigenstate ψ_n with components $\psi_n(j)$ at the lattice site j, the IPR can be expressed as:

$$\mathrm{IPR}_n = \sum_j |\psi_n(j)|^4 \tag{4.45}$$

In this expression, the IPR ranges from $1/N$ (for a fully delocalized state, where N is the total number of lattice sites) to 1 (for a completely localized state). For the AAH model, the IPR provides insights into the transition between the localized and delocalized regimes governed by the ratio V/J. A larger IPR value signifies a more localized state, whereas a smaller IPR value indicates a more delocalized or extended state.

4.4.4 Initial result

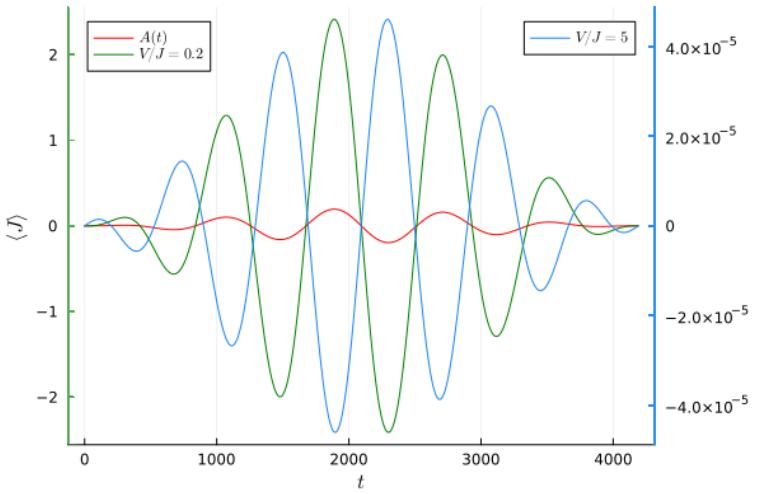

Figure 4.12: Total current: The value of current (green) for $V/J = 0.2$ is 10^5 time larger than the current (blue) for $V/J = 5$ (right axis).

We perform calculations of HHG with the same laser pulse as in SSH model,

$$A(t) = A_0 \sin^2\left(\frac{\omega t}{2n_{cyc}}\right) \sin(\omega t), \tag{4.46}$$

where $A_0 = 0.2$, $\omega = 0.0075$, $n_{cyc} = 5$. We include the laser-matter interaction via the time-dependent Peierls phase: $t_0 \rightarrow t_0 e^{ia_0 eA(t)}$. We consider periodic boundary conditions, and then the coupling between particles, and the laser field is described in the velocity gauge, $c_j^\dagger c_{j+1} \rightarrow e^{-iA(t)} c_j^\dagger c_{j+1}$. The harmonic spectra are obtained from the current operator,

$$I(t) = iJ \left(e^{-iA(t)} c_j^\dagger c_{j+1} - e^{iA(t)} c_{j+1}^\dagger c_j \right), \tag{4.47}$$

as $P(\omega) \propto |FT(\dot{I})|^2$, where FT is a Fourier transform with window function. One can distinguish between localized and delocalized phases from total current in Fig. 4.12, where the ration of $\frac{I_{V/J=0.2}}{I_{V/J=5}} \sim 10^5$ immediately indicates that the current response the system or, subsequently, HHG of the system that can distinguish localized and delocalized phase.

Now we are trying to calculate the multifractal properties at the transition point from HHG spectra itself. This offers a unique chance to investigate multi-fractal phases through the utilization of high-harmonic generation spectra. This represents a significant advancement, given the considerable difficulty associated with observing such phenomena through conventional transportation mechanisms.

4.5 Extended Fermi Hubbard Model (EFHM) (ongoing)

Su-Schrieffer-Heeger (SSH) kind of phases can also occur in interacting fermionic chains [349]. Extended Fermi Hubbard Model (EFHM) is a model which hosts a particular phase which is called the Bond Order Wave (BOW) phase, which arises from the competition between on-site and nearest neighbor interaction in the model [350–354]. Such BOW phases are topological in nature and belong to the same topological class as the SSH model that we discussed earlier. For this particular purpose, we consider the 1-D EFHM to synthesize interacting SSH dynamics. The Hamiltonian of EFHM can be expressed as:

$$\begin{aligned} H = &-J\sum_{i}(c^{\dagger}_{i\sigma}c_{i+1,\sigma} + c^{\dagger}_{i+1,\sigma}c_{i\sigma}) \\ &+ U\sum_{i} n_{i,\uparrow}n_{i,\downarrow} + V\sum_{i} n_i n_{i+1} \end{aligned} \tag{4.48}$$

The hopping amplitude J describes the strength of the electron's motion between neighboring lattice sites. U parameterizes the Hubbard interaction strength in the same lattice site. V accounts for the strength of interaction between the nearest neighbor lattice site. $c^{\dagger}_{i\,\sigma}$ $(c_{i\,\sigma})$ is the creation (annihilation) operators for a fermion with spin σ at site i. $n_{i,\uparrow}(n_{i,\downarrow})$ is the number operator for the up (down) spin electron at site i. $n_i = n_{i,\uparrow} + n_{i,\downarrow}$ is the total electron number operator at site i. EFHM exhibits three insulating phases: Mott insulator (MI), Charge density wave (CDW), and Bond order wave (BOW).

When the onside interaction U is much greater than the nearest neighbor repulsion V and also the hopping strength J, the system lies in the insulating phase which in this case is the MI phase. The CDW phase, another insulating phase with spontaneously broken lattice translational symmetry, appears due to the dominance of repulsion strength between the nearest neighbor sites over onsite interaction U and the hopping strength J of the system.

MI phase has dominant spin density wave correlations and, as

such, is captured by the spin density wave (SDW) structure factor:

$$S_{SDW} \equiv \frac{1}{L}\sum_{lr} e^{iqr}\langle s_l^z s_{l+r}^z\rangle \tag{4.49}$$

here, L is the length of lattice, s_l^z is the spin operator at l site. q is momentum and r is the distance between the adjacent sites. The CDW phase can be characterized by calculating the CDW structure factor:

$$S_{CDW} \equiv \frac{1}{L}\sum_{ij} e^{iqr}(\langle n_i n_{i+j}\rangle - \langle n_i\rangle\langle n_{i+j}\rangle) \tag{4.50}$$

The BOW phase can be characterized by the BOW operator:

$$B_{i,i+1} \equiv \sum_{\sigma}(c_{i,\sigma}^{\dagger}\, c_{i+1,\sigma} + c_{i+1,\sigma}^{\dagger}\, c_{i,\sigma}) \tag{4.51}$$

In the BOW phase, the order is based on the charges along the bond that connect two sites along the chain. In the bond order phase, two kinds of ground states are possible: trivial and topological.

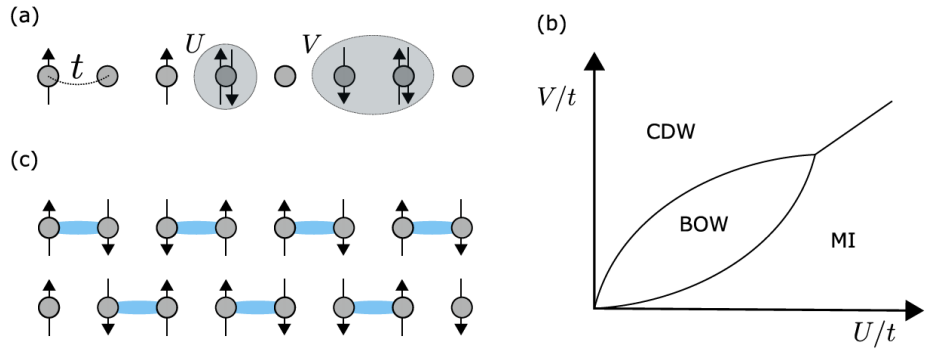

Figure 4.13: Schematic of different phases occur in EFHM: (a) Three phases. (b) The phase diagram in the U-V plane. The BOW phase appears for moderate interactions between the MI and the CDW phase at the transition point. (c) Sketch of the spontaneous dimerization in the BOW phases. The upper chain corresponds to the trivial case, while the lower chain is topologically nontrivial; Figure courtesy [349].

Now we study the Hamilton in Eq. (4.48) in the presence of an intense laser field to see if HHG spectroscopy can act as a successful

tool in distinguishing between the different insulating phases of the system, especially whether it can capture if there are any topological phases as seen the BOW phase in the system. The Hamiltonian becomes time-dependent due to the electric field:

$$H'(t) = -J \sum_{\sigma,j=1} \left(e^{-i\Phi(t)} c^{\dagger}_{j,\sigma} c_{j+1,\sigma} + e^{i\Phi(t)} c^{\dagger}_{j+1,\sigma} c_{j,\sigma} \right) + U \sum_i n_{i,\uparrow} n_{i,\downarrow} + V \sum_i n_i n_{i+1}. \tag{4.52}$$

where the laser electric field $F(t) = -\frac{dA(t)}{dt}$ enters through the time-dependent Peierls phase (Φ), $eaF(t) = -\frac{d\Phi(t)}{dt}$, a, J and $A(t)$ are the lattice constant, hopping strength and the field vector potential respectively. We further study the current in relation to other time-dependent correlators of the system to look for signatures of different phases of the system in the current and, subsequently, the HHG spectra from the current operator.

4.5.1 Initial result

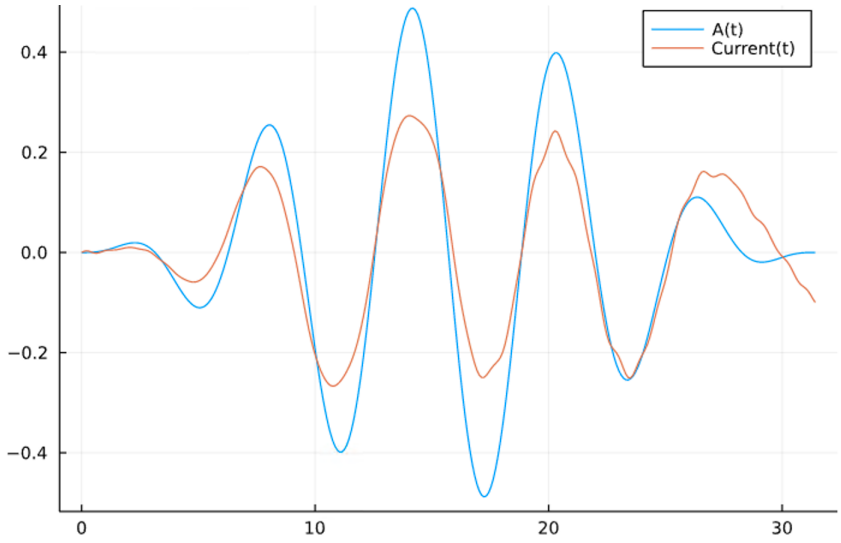

Figure 4.14: Amplitude Vs time; time-dependent vector potential of incident light pulse, and output current pulse are indicated by blue and red color, respectively, at $N = 4, J = 0.5, V = 1.1, U = 0.8$

We perform calculations of HHG with the same laser pulse as in EFHM,

$$A(t) = A_0 \sin^2\left(\frac{\omega t}{2n_{cyc}}\right)\sin(\omega t), \tag{4.53}$$

where $A_0 = 0.2$, $\omega = 0.0075$, $n_{cyc} = 5$.
The harmonic spectra in Fig. 4.14 are obtained from the current operator,

$$J(t) = -ieat_0 \sum_{\sigma}\sum_{j=1}\left(e^{-i\Phi(t)}c^{\dagger}_{j,\sigma}c_{j+1,\sigma} - h.c.\right). \tag{4.54}$$

The data obtained using the DMRG method (Appendix C) matches very well with one obtained from the exact diagonalization method for small system sizes. Further, explore with the DMRG method for more sites in order to characterize the different insulating phases of the EFHM at half-filling using the HHG spectroscopy method.

Chapter 5

Future perspective

This thesis explores the role of quantum dynamics in various regimes and have exploited them to study thermodynamics and spectroscopy. In particular, the first regime is the self-driven dynamics of isolated system, and it is used to study thermodynamics of quantum heat engines. The second regime is concerned with open quantum dynamics where a system is weakly coupled with a thermal environment. In particular, here we have used dynamics based on Lindblad semigroup approach to explore thermodynamics with negative temperatures. The third regime considers driven dynamics where a system is driven by a strong external field. We utilize theses dynamics to explore high harmonic spectroscopy of solids.

Resource theory QHE

Using the self-driven dynamics of isolated system, we have developed a resource theory of heat engines which lays a framework to address thermodynamics in the one-shot finite-size limit. There a working system interacts with a thermal bath through a time-independent interaction Hamiltonians while strictly conserving energy and weighted energy. This dynamics in general drive a working system towards equilibrium. In particular we have found that with the help of these powerful thermal operations, which enables quantum entanglement between the working system and the baths, an engine can operate in a one-step cycle and yield Carnot efficiency at maximum power. We have also introduced an experimentally

feasible model for such an engine based atom-cavity systems. An immediate next step would be to (1) explore construction of a model of a heat engine that exclusively utilizes the correlations between the working systems, (2) extend the resource theory of heat engines to the case with multiple conserved quantities, (3) construct thermo-electric devices with high efficiency and power, etc.

Synthetic negative temperature

Using open quantum dynamics based on Lindblad master equation, we have studied steady-state thermodynamics with baths at negative temperatures. We have also constructed a continuous heat engine operating between a positive and negative bath and have shown that such engines can yield maximum efficiency. An immediate extension of this work can be to (1) explore experimentally realizable model for such engines, (2) studying thermodynamics uncertainty relations for baths at negative temperatures, etc.

HHG spectroscopy

We characterize topological features solids by HHG spectroscopic technique where the transient dynamics has been utilized as the resources. There are currently two projects that are being worked on. This work may be extended further as follows. (1) One can explore the localized phase and delocalized phases of the 1-D quasi-periodic AAH model. (2) One can differentiate between the distinct phases of the strongly correlated 1-D EFHM.

The strongly correlated systems in more than 1-D systems are the natural progression for these initiatives [38, 280, 292]. For example, Cuprates [297] has been investigated using HHG spectroscopy; however, other strongly correlated systems, such as multi-layer graphene, have not been subjected to an investigation of this kind. It is possible that such systems may shed light on many intriguing details.

Not much research has been conducted on HHG in presence of strong interactions, strong disorder, and quasi-periodicity. This path has potential for us, and we would want to investigate it more in the future.

HHG can also be used not only to identify different phases of matter, either strongly correlated or not, but HHG can also be utilized for studying different kinds of quasi-particles. One study has shown how HHG can exploit to detect the simple, non-Abelian anyon such as Majorana fermions [333]. But other classes of non-abelian anyon or exotic particles have not yet been detected via traditional transport-based methods. This is the reason why we want to weaponize the HHG spectroscopic technique so that we can determine whether or not we are able to detect Abelian and non-Abelian phases of matter with unusual quasi-particles such as fractionalized quasi-particle quantum spin liquid and so on.

Appendix A

Appendix: Thermal baths and system-bath composites

The goal of this section is to characterize the Hilbert spaces of considerably large bath(s) at certain temperature(s), small systems that are in and away from thermal equilibrium, and their composites.

A.1 Some useful properties of baths

There are several useful properties of a considerably large bath, compared to the systems they interact with. A bath is considered to be always in thermal equilibrium at a fixed temperature, even after it interacts with a system. Therefore it has to be reasonably large so that it almost does not change after the interaction and remain in equilibrium. So, a bath being large is an important assumption.

All the systems we consider have Hamiltonians bounded from below, i.e., the lowest energy is zero. Consider a bath B_x the Hamiltonian H_{B_x} which has the largest energy is $E_{B_x}^{max} \to \infty$. The heat bath always remains in a Gibbs state $\gamma_{B_x} = \frac{e^{-\beta H_{B_x}}}{\mathrm{Tr}\,[e^{-\beta H_{B_x}}]}$ with inverse temperature β_x. Now say there two baths B_1 and B_2 with the Hamiltonians H_{B_1} and H_{B_2} and the inverse temperatures β_1 and β_2. The joint thermal state of the baths is expressed as

$$\gamma_{B_{12}} = \gamma_{B_1} \otimes \gamma_{B_2}. \tag{A.1}$$

There exists a set of energies $\mathcal{E}_{B_{12}}$ in which the baths jointly live with high probability. Mathematically, for the projector $P_{\mathcal{E}_{B_{12}}}$ that spans

over the space with a set of the total energies $\mathcal{E}_{B_{12}}$, this is expressed as

$$\mathrm{Tr}\left[P_{\mathcal{E}_{B_{12}}}\gamma_{B_{12}}\right] \geqslant 1-\delta, \tag{A.2}$$

where $\delta > 0$. Given this, the bath satisfies the following properties (cf. [198]):

- The energy $E_{B_{12}} \in \mathcal{E}_{B_{12}}$ is peaked around a mean value as $E_{B_{12}} \in \left\{\langle E_{B_{12}}\rangle - O(\sqrt{E_{B_{12}}}), \ldots, \langle E_{B_{12}}\rangle + O(\sqrt{E_{B_{12}}})\right\}$.
- The degeneracies $g_B(E_{B_{12}})$ in the energies $E_{B_{12}} = E_{B_1} + E_{B_2} \in \mathcal{E}_{B_{12}}$ scale exponentially with E_{B_1} and E_{B_1}, i.e., $g_B(E_{B_{12}}) \geqslant e^{xE_{B_1}+yE_{B_2}}$, where $x,\ y$ are constants. Here E_{B_1} and E_{B_2} are the energies of the baths B_1 and B_2 respectively.
- Consider any pair of three energies $(E_{B_1}, E_{S_1}, E'_{S_1})$ and $(E_{B_2}, E_{S_2}, E'_{S_2})$, so that $E_{B_{12}} = E_{B_1} + E_{B_2} \in \mathcal{E}_{B_{12}}$, $E_{S_1} \ll E_{B_1}$, and $E'_{S_1} \ll E_{B_1}$, and similarly $E_{S_2} \ll E_{B_2}$, and $E'_{S_2} \ll E_{B_2}$. Then there exists a $E'_{B_{12}} = E'_{B_1} + E'_{B_2} \in \mathcal{E}_{B_{12}}$ so that $E_{B_1} + E_{S_1} = E'_{B_1} + E'_{S_1}$ and $E_{B_2} + E_{S_2} = E'_{B_2} + E'_{S_2}$.
- For an energy $E_{B_{12}} \in \mathcal{E}_{B_{12}}$, the degeneracies satisfy $g_B(E_{B_{12}} + E_{S_1} + E_{S_2}) \approx g_B(E_{B_{12}})e^{\beta_1 E_{S_1}+\beta_2 E_{S_2}}$.

These properties are instrumental in understanding the thermodynamics of quantum and nano-scale systems interacting with large baths.

A.2 Two baths and two (sub-)systems

Without loss of generality, we consider a bipartite system S_{12} with two subsystems, S_1 and S_2, that are *semi-locally* interacting with two baths B_1 and B_2 respectively where the baths are with the inverse temperatures β_1 and β_2. We skip the discussion on the notion of "semi-local" here. We elaborate on it later to characterize the thermodynamics operations that are applicable in a quantum heat engine.

Say, the two considerably large baths B_1 and B_2 are with Hamiltonians H_{B_1} and H_{B_2} respectively. Further, the small systems S_1 and S_2 are the subsystems of a bipartite system S_{12} with the Hilbert space

Figure A.1: A schematic of a situation where system S_1 is (semi-locally) interacting with the bath B_1, and the system S_2 is semi-locally interacting with the bath B_2. Temperatures of the baths are $T_1 = \frac{1}{\beta_1}$ and $T_2 = \frac{1}{\beta_2}$.

$\mathcal{H}_{S_{12}} = \mathcal{H}_{S_1} \otimes \mathcal{H}_{S_2}$. The system S_{12} possesses a non-interacting Hamiltonian $H_{S_{12}} = H_{S_1} + H_{S_2}$. We denote E_{B_x} and E_{S_x} as the energies of the bath B_x and the subsystem S_x respectively. The bath Hamiltonians $H_{B_{1/2}}$ are bounded from below and could have $E^{\max}_{B_{1/2}} \to \infty$. The system Hamiltonians $H_{S_{1/2}}$ are also bounded from below and satisfy $E^{\max}_{S_{1/2}} \ll E^{\max}_{B_{1/2}}$. We consider here non-degenerate system Hamiltonians $H_{S_{1/2}}$. Extension to degenerate cases can be done easily.

The underlying joint Hilbert space corresponding to the S_{12}, B_1, and B_2 is now $\mathcal{H}_{B_1} \otimes \mathcal{H}_{B_2} \otimes \mathcal{H}_{S_1} \otimes \mathcal{H}_{S_2}$. Here we assume the systems to interact as in Supplementary Figure A.1. It can be expressed as the Kronecker sums of constant total energy sub-spaces, i.e.,

$$\begin{aligned} &\mathcal{H}_{B_1} \otimes \mathcal{H}_{B_2} \otimes \mathcal{H}_{S_1} \otimes \mathcal{H}_{S_2} \\ &= \bigoplus_{E_1+E_2} \left(\bigoplus_{E_{S_1}+E_{S_2}} \mathcal{H}_{B_1}^{E_1-E_{S_1}} \otimes \mathcal{H}_{B_2}^{E_2-E_{S_2}} \otimes \mathcal{H}_{S_1}^{E_{S_1}} \otimes \mathcal{H}_{S_2}^{E_{S_2}} \right), \end{aligned} \tag{A.3}$$

where the total energies are given by $E_1 + E_2$, and $E_1 = E_{B_1} + E_{S_1}$ and $E_2 = E_{B_2} + E_{S_2}$ are the energies corresponding to the composites B_1S_1 and B_2S_2 respectively. The total energies are the eigenvalues of the total Hamiltonian

$$H_{B_1B_2S_{12}} = H_{B_1} + H_{S_1} + H_{B_2} + H_{S_2}. \tag{A.4}$$

It is important to notice that there are many combinations E_1 and E_2 for which $E_1 + E_2$ is identical. Consequently, any system-baths joint state can be written in terms of fixed total energy blocks. A system-baths state $\gamma_{B_1} \otimes \gamma_{B_2} \otimes \rho_{S_{12}}$, which is diagonal in the energy

eigenbases, can be expressed as

$$\begin{aligned}\gamma_{B_1}\otimes\gamma_{B_2}\otimes\rho_{S_{12}} &= \sum_{E_1+E_2} P_{E_1+E_2}\left(\gamma_{B_1}\otimes\gamma_{B_2}\otimes\rho_{S_{12}}\right)P_{E_1+E_2}\\ &= \sum_{E_1+E_2} p_{E_1+E_2}\,\rho^{B_1B_2S_{12}}_{E_1+E_2},\end{aligned} \tag{A.5}$$

where $P_{E_1+E_2}$s are the projectors with total energy E_1+E_2 and $p_{E_1+E_2} = \mathrm{Tr}\left[P_{E_1+E_2}\left(\gamma_{B_1}\otimes\gamma_{B_2}\otimes\rho_{S_{12}}\right)\right]$ are the probabilities. Note, for a given value $E_1+E_2=X$, the projector is expressed as $P_{E_1+E_2} = \sum_{E_1^i,E_2^j} P_{E_1^i}\otimes P_{E_2^j}$ for $E_1^i+E_2^j = X$.

Say the set of energies $\mathcal{E}_{12} = \mathcal{E}_1+\mathcal{E}_2$ in which the baths B_1 and B_2 jointly live with high probability and satisfy the properties mentioned for Eq. (A.2). Then, for $E_1\in\mathcal{E}_1$ and $E_2\in\mathcal{E}_2$, the normalized joint state $\rho^{E_1+E_2}_{B_1B_2S_{12}}$ after the projection with the projector $P_{E_1+E_2}$ is

$$\begin{aligned}\rho^{B_1B_2S_{12}}_{E_1+E_2} &= \frac{1}{p_{E_1+E_2}}P_{E_1+E_2}\left(\gamma_{B_1}\otimes\gamma_{B_2}\otimes\rho_{S_{12}}\right)P_{E_1+E_2},\\ &\approx \bigoplus_{E_{S_1}+E_{S_2}} \eta^{B_1B_2}_{E_1-E_{S_1}+E_2-E_{S_2}}\otimes P_{E_{S_1}+E_{S_2}}(\rho_{S_{12}})P_{E_{S_1}+E_{S_2}},\end{aligned} \tag{A.6}$$

where $P_{E_{S_1}+E_{S_2}}$ are the projectors on the system (S_{12}) space spanning over the block given by the energy $E_{S_1}+E_{S_2}$, and

$$\eta^{B_1B_2}_{E_1-E_{S_1}+E_2-E_{S_2}} = \eta^{B_1}_{E_1-E_{S_1}}\otimes\eta^{B_2}_{E_2-E_{S_2}} = \frac{\mathbb{I}^{B_1}_{E_1-E_{S_1}}}{g_{B_1}(E_1)e^{-\beta_1E_{S_1}}}\otimes\frac{\mathbb{I}^{B_2}_{E_2-E_{S_2}}}{g_{B_2}(E_2)e^{-\beta_2E_{S_2}}}. \tag{A.7}$$

With these minimum implements in hand, we move on to characterize semi-local thermal operations below.

A.3 Semi-local thermal operations

Let us now introduce the general form of thermodynamically allowed (semi-local) operations that a (bipartite) quantum system S_{12} undergoes in a quantum heat engine, where the bipartite system S_{12} can be in an arbitrary state. Even, the states may possess strong correlation, e.g., quantum entanglement, shared by the subsystems S_1 and S_2.

Definition 3 (Semi-local thermal operations (SLTOs)). *In a quantum heat engine, the thermodynamic operations on system S_{12} in a state $\rho_{S_{12}}$ are defined as*

$$\Lambda_{S_{12}}\left(\rho_{S_{12}}\right) = \mathrm{Tr}_{B_1B_2}\left[U(\gamma_{B_1}\otimes\gamma_{B_2}\otimes\rho_{S_{12}})U^\dagger\right], \tag{A.8}$$

with the condition that the global unitary U satisfies the commutation relations

$$\left[U,\ H_{B_1}+H_{S_1}+H_{B_2}+H_{S_2}\right]=0, \tag{A.9}$$
$$\left[U,\ \beta_1\left(H_{B_1}+H_{S_1}\right)+\beta_2\left(H_{B_2}+H_{S_2}\right)\right]=0, \tag{A.10}$$

where the thermal states of the baths are denoted by $\gamma_{B_x}=\frac{e^{-\beta_x H_{B_x}}}{\mathrm{Tr}\left[e^{-\beta_x H_{B_x}}\right]}$ for $x=1,2$.

The resultant operations on the system S_{12} are semi-local in the sense that, even though the subsystems (S_1 and S_2) "selectively" interact with the baths (B_1 and B_2), the unitary U still allows certain interactions among them with the constraints (A.9) and (A.10). It should be noted that the commutation relations (A.9) and (A.10) together constitute the first law for quantum heat engines. The relation (A.9) guarantees strict conservation of the total energy $E_{12}=E_1+E_2$, where E_1 and E_2 are the energies of the B_1S_1 and B_2S_2 composites respectively. In addition, the relation (A.10) ensures strict conservation of the total weighted-energy $E_{12}^{\beta_1\beta_2}=\beta_1E_1+\beta_2E_2$, and it signifies that any change in (one-shot) entropy of B_1S_1, due to an exchange of energy between B_1S_1 and B_2S_2, must be compensated by a counter change in (one-shot) entropy of B_2S_2. It is interesting to note that the SLTOs converge to the (local) thermal operations that are introduced in the resource theory of quantum states beyond thermal equilibrium presented in [64, 198, 205], when both the baths are of the same temperature, i.e., for $\beta_1=\beta_2$. Several useful properties of SLTOs are outlined in the Method.

The SLTOs can be further generalized with an access to a bipartite catalyst C_{12} composed of two non-interacting subsystems C_1 and C_2 and the Hamiltonian $H_{C_{12}}=H_{C_1}+H_{C_2}$. The C_1 is clubbed with the subsystem S_1 to form the composite S_1C_1. Similarly, the C_2 is clubbed with the S_2 to form S_2C_2. Then, the composites S_1C_1 and S_2C_2 interacts with the baths B_1 and B_2 via semi-local thermal operations. Such

operations are called catalytic semi-local thermal operations (cSLTOs) that satisfy

$$\Lambda_{S_{12}C_{12}}(\rho_{S_{12}} \otimes \rho_{C_{12}}) \to \sigma_{S_{12}} \otimes \rho_{C_{12}}, \tag{A.11}$$

where $\rho_{C_{12}}$ is a state of the catalyst. Note, the catalyst remains unchanged before and after the process. These catalytic operations form a larger set of thermodynamically allowed operations compared to SLTOs and respect all the properties satisfied by the SLTOs. The cSLTOs are the allowed thermodynamic operation in a quantum heat engine and constitute the free operation for the resource theory developed to prove the results presented in this article (see Supplementary Information).

When the subsystems are locally in thermal equilibrium with the baths they are semi-locally interacting with, the joint uncorrelated state of the system S_{12} becomes $\gamma_{S_{12}} = \gamma_{S_1} \otimes \gamma_{S_2}$, where $\gamma_{S_x} = e^{-\beta_x H_{S_x}}/Z_x$ with the partition functions $Z_x = \mathrm{Tr}\left[e^{-\beta_x H_{S_x}}\right]$ for $x = 1, 2$. We term these states as the semi-Gibbs states. The set of all such semi-Gibbs states is denoted by the set $\mathcal{T}_{S_{12}} \ni \gamma_{S_{12}}$. The SLTOs map the set $\mathcal{T}_{S_{12}}$ onto itself. The SLTOs and the semi-Gibbs states are the precursors of a resource theory of heat engines that we develop in the Supplementary Information.

A.4 Characterization of semi-local thermal operations

Recall the Stinespring dilation of the SLTOs given in the main text,

$$\Lambda_{S_{12}}\left(\rho_{S_{12}}\right) = \mathrm{Tr}_{B_1B_2}\left[U(\gamma_{B_1} \otimes \gamma_{B_2} \otimes \rho_{S_{12}})U^\dagger\right], \tag{A.12}$$

where the global unitary U satisfies the commutation relations (R1) $[U,\ H_{B_1} + H_{B_1} + H_{B_2} + H_{S_2}] = 0$,
and (R2) $\left[U,\ \beta_1\left(H_{S_1} + H_{B_1}\right) + \beta_2\left(H_{S_1} + H_{B_1}\right)\right] = 0$. The H_{S_x} and H_{B_x} are the Hamiltonians of the subsystem S_x and the bath B_x respectively for $x = 1, 2$. The thermal states of the baths are denoted by $\gamma_{B_x} = \frac{e^{-\beta_x H_{B_x}}}{\mathrm{Tr}\left[e^{-\beta_x H_{B_x}}\right]}$.

The unitary U strictly conserves both the total energy and the total weighted-energy, as guaranteed by the commutation relations

(R1) and (R2). It can be expressed in terms of the total energy blocks, as

$$U = \sum_{E_1+E_2} P_{E_1+E_2}\,(U)\,P_{E_1+E_2} = \bigoplus_{E_1+E_2} U_{E_1+E_2}, \tag{A.13}$$

where $P_{E_1+E_2}$ is the projector spanning the sub-space with total energy E_1+E_2. The global unitary U cannot transfer populations among the blocks with different total energies. The $U_{E_1+E_2}$ cannot be arbitrary. Within a block given by the fixed total energy E_1+E_2, the $U_{E_1+E_2}$ can implement population transfer among the states that have identical total weighted-energy $\beta_1 E_1+\beta_2 E_2$.

For a system state $\rho_{S_{12}}$, the $U_{E_1+E_2}$ operates on the total energy block given by the normalized state system-baths composite $\rho^{B_1B_2S_{12}}_{E_1+E_2}$, defined in the earlier section, that is

$$\begin{aligned}\rho^{B_1B_2S_{12}}_{E_1+E_2} &= \frac{1}{p_{E_1+E_2}} P_{E_1+E_2}\left(\gamma_{B_1}\otimes\gamma_{B_2}\otimes\rho_{S_{12}}\right)P_{E_1+E_2},\\ &\approx \bigoplus_{E_1+E_2}\frac{\mathbb{I}^{B_1}_{E_1-E_{S_1}}}{g_{B_1}(E_1)e^{-\beta_1 E_{S_1}}}\otimes\frac{\mathbb{I}^{B_2}_{E_2-E_{S_2}}}{g_{B_2}(E_2)e^{-\beta_2 E_{S_2}}}\\ &\otimes P_{E_{S_1}+E_{S_2}}(\rho_{S_{12}})P_{E_{S_1}+E_{S_2}},\end{aligned} \tag{A.14}$$

as discussed in Section A.2. The E_1 and E_2 are the energies correspond to the composites B_1S_1 and B_2S_2. Recall, there are many combinations of E_1 and E_2 that led to same value of total energy E_1+E_2 and total weighted-energy $\beta_1E_1+\beta_2E_2$.

A.4.1 SLTOs are those that preserve semi-Gibbs states, and vice versa

From the definition of SLTOs itself, it is clear that these operations preserve semi-Gibbs states. Let us consider the microscopic picture. Say the initial system state is in the semi-Gibbs state, given by

$$\rho_{S_{12}} = \gamma_{S_1}\otimes\gamma_{S_2} = \sum_i \frac{e^{-\beta_1 E_i^{S_1}}}{Z_{S_1}}|E_i^{S_1}\rangle\langle E_i^{S_1}|\otimes\sum_j\frac{e^{-\beta_2 E_j^{S_2}}}{Z_{S_2}}|E_j^{S_2}\rangle\langle E_j^{S_2}|, \tag{A.15}$$

where $|E_i^{S_1}\rangle$ are the energy eigenstates of the Hamiltonian $H_{S_1} = \sum_i E_i^{S_1} |E_i^{S_1}\rangle\langle E_i^{S_1}|$ of the subsystem S_1, and the $|E_j^{S_2}\rangle$ are the energy eigenstates of the Hamiltonian $H_{S_2} = \sum_j E_j^{S_2} |E_j^{S_2}\rangle\langle E_j^{S_2}|$ of the subsystem S_2. The Z_{S_1} and Z_{S_2} are the partition functions. For each block with the total energy $E_1 + E_2$, the bath-system composite state, as discussed in Section A.2, is

$$\begin{aligned}
&\rho_{E_1+E_2}^{B_1B_2S_{12}} \\
&= \bigoplus_{E_i^{S_1}+E_j^{S_2}} \frac{\mathbb{I}}{g_{B_1}(E_1)e^{-\beta_1 E_i^{S_1}}} \otimes \frac{\mathbb{I}}{g_{B_2}(E_2)e^{-\beta_2 E_j^{S_2}}} \otimes \\
&\left(\frac{e^{-\beta_1 E_i^{S_1}}}{Z_{S_1}} |E_i^{S_1}\rangle\langle E_i^{S_1}| \otimes \frac{e^{-\beta_2 E_j^{S_2}}}{Z_{S_2}} |E_j^{S_2}\rangle\langle E_j^{S_2}| \right) \\
&= \frac{\mathbb{I}}{g_{B_1}(E_1)Z_{S_1}} \otimes \frac{\mathbb{I}}{g_{B_2}(E_2)Z_{S_2}}.
\end{aligned} \tag{A.16}$$

Clearly, the application of a unitary (with the form (A.13)) on the joint system-bath composite that strictly conserves both the total energy and the total weighted-energy will not change the maximally mixed state (A.16) in every total energy block. Therefore, a semi-Gibbs state will not change upon the application of an SLTO.

Now we consider the reverse statement that is if a semi-Gibbs state preserving operation can be implemented using an SLTO, placed in the Corollary below.

Corollary 3 (Semi-Gibbs preservation of semi-local thermal operations)**.** *Consider two non-interacting sub-systems S_1 and S_2, of a bipartite system S_{12}, that are semi-locally interacting with the baths B_1 and B_2, at inverse temperatures β_1 and β_2, respectively. Then the semi-local thermal operations are the ones that satisfy the semi-Gibbs preservation condition,*

$$\Lambda_{S_{12}}\left(\gamma_{S_1} \otimes \gamma_{S_2}\right) = \gamma'_{S_1} \otimes \gamma'_{S_2} \in \mathcal{T}_{S_{12}}, \quad \forall\, \gamma_{S_1} \otimes \gamma_{S_2} \in \mathcal{T}_{S_{12}}. \tag{A.17}$$

Proof. Let us just consider the situation where the Hamiltonians of the sub-systems do not change, i.e., the situation where $\Lambda_{S_{12}}\left(\gamma_{S_1} \otimes \gamma_{S_2}\right) = \gamma_{S_1} \otimes \gamma_{S_2}$. Extension to the general cases can be simply followed.

Below we show that the semi-Gibbs preserving operations are precisely the semi-local thermal operations when they are applied on

the block-diagonal states, i.e., $[\rho_{S_{12}},\ H_{S_{12}}] = 0$. Let us consider that the Hamiltonian of the system S_{12},

$$H_{S_{12}} = H_{S_1} + H_{S_2}, \tag{A.18}$$

is non-degenerate in system energy. The bath-system composite $(B_1B_2S_{12})$ in the total energy blocks $E_1 + E_2$ is expressed in Eq. (A.5). We restrict ourselves within one total energy block $E_1 + E_2$. We show that, with the help of just permutation between bases, any arbitrary operation can be performed that preserves the corresponding *semi-Gibbs* state within the total energy block. Once done with this, it will be easy to check that such an operation can be implemented in every other total energy blocks. Note, the total energy $E_1 + E_2 \in \mathcal{E}_{12}$ (see Section A.2).

Within a block of total energy $E_1 + E_2$, there are sub-blocks corresponding to the system energies $E_i^{S_1} + E_j^{S_2}$.The permutations among the eigenbases respecting strict conservation of total energy and total weighted-energy will result in transfer of eigenbases among the sub-blocks defined by $E_i^{S_1} + E_j^{S_2}$ (the energy of the system). Each sub-block also constitutes a degenerate subspace with the dimension $g_{B_1}(E_1)e^{-\beta_1 E_i^{S_1}} g_{B_2}(E_2)e^{-\beta_2 E_j^{S_2}}$ (see Section A.2). All the eigenvalues of the system-bath composite in this sub-block become equal to

$$\frac{p(E_i^{S_1} + E_j^{S_2})}{g_{B_1}(E_1)e^{-\beta_1 E_i^{S_1}} g_{B_2}(E_2)e^{-\beta_2 E_j^{S_2}}}, \tag{A.19}$$

after normalization, where $p(E_i^{S_1} + E_j^{S_2}) = \mathrm{Tr}\,[P_{E_i^{S_1}+E_j^{S_2}}\ \rho_{S_{12}}]$. For the notational simplicity, let us denote $p(E_i^{S_1} + E_j^{S_2}) \to p_{ij}$, where i (and j) stands for the energy levels $E_i^{S_1}$ in system S_1 (and $E_j^{S_2}$ in system S_2), and $g_{B_1}(E_1)e^{-\beta_1 E_i^{S_1}} \to d_i$ and $g_{B_2}(E_2)e^{-\beta_2 E_j^{S_2}} \to d_j$.

Now, we can introduce permutations among the states that preserves total energy as well as the total weighted-energy. Then, the 'transition current' between system energy sub-blocks is denoted by $t_{ij\to mn}$, which is equal to the number of eigenstates that are transferred from the ij-th sub-block (corresponding to the system energy $E_i^{S_1} + E_j^{S_2}$) to mn-th sub-block (corresponding to the system energy

$E_m^{S_1} + E_n^{S_2}$). The transition current satisfies

$$\sum_{ij} t_{ij\to mn} = d_m d_n, \tag{A.20}$$

$$\sum_{mn} t_{ij\to mn} = d_i d_j. \tag{A.21}$$

The permutations will lead to a modification in the probability distribution in the system part $\{p_{ij}\} \to \{q_{mn}\}$. The new probability distribution can be written in terms of the transition currents, satisfying (A.20) and (A.21), becomes

$$q_{mn} = \sum_{ij} t_{ij\to mn} \frac{p_{ij}}{d_i d_j} = \sum_{ij} s_{ij\to mn}\, p_{ij}, \tag{A.22}$$

where $s_{ij\to mn} = \frac{t_{ij\to mn}}{d_i d_j}$ is the probability of the transition $ij \to mn$. The transition matrix $\{s_{ij\to mn}\}$ transforms a normalized probability distribution to another normalized probability distribution, as it satisfies the stochastic condition $\sum_{mn} s_{ij\to mn} = 1, \ \forall ij$. Along with the relation $\frac{d_i d_j}{d_m d_n} = \frac{e^{-\beta_1 E_i^{S_1} - \beta_2 E_i^{S_2}}}{e^{-\beta_1 E_m^{S_1} - \beta_2 E_n^{S_2}}}$, the stochastic condition implies that all transformations satisfying the constraints (A.20) and (A.21) guarantee the preservation of the semi-Gibbs state $\gamma_{S_1} \otimes \gamma_{S_2}$. With this, we prove that in a given total energy block, all possible operations that strictly conserve both the total energy and the total weighted-energy are semi-Gibbs preserving operations.

Note, for a given arbitrary semi-Gibbs preserving transformation on the system S_{12} in a block-diagonal state $\rho_{S_{12}}$, a permutation among the system energy sub-blocks within a fixed total energy and total weighted-energy block, can be performed to result in the desired transformation. The resultant operation in the block strictly conserves total energy as well as total weighted-energy. Further for every such block, there exists permutation operations that lead to the same transformation on the system S_{12} part. The combination of all these individual transformations, that are performed in different blocks leads to the implementation of the semi-Gibbs preserving operation on the initial state of the system S_{12}.

It is clear from above that all semi-Gibbs preserving transformations can be performed with the help of permutations within each block having fixed total energy and total weighted-energy. These

operations are unitary and strictly conserve the total energy as well as the total weighted-energy. Hence, these are nothing but the semi-local thermal operations. Therefore, an arbitrary semi-Gibbs preserving operation applied on system in a block-diagonal state can be simulated using semi-local thermal operation. □

We shall re-consider this semi-Gibbs preserving property to characterize the state transformations under SLTOs in Section A.6.1, and in the context of majorization in the Theorem 9.

A.4.2 Catalytic semi-local thermal operations (cSLTOs)

The SLTOs can be further generalized with an access to a bipartite catalyst C_{12} composed of two non-interacting subsystems C_1 and C_2 and the Hamiltonian $H_{C_{12}} = H_{C_1} + H_{C_2}$. The C_1 is clubbed with the subsystem S_1 to form the composite S_1C_1. Similarly, the C_2 is clubbed with the S_2 to form S_2C_2. Then, the composites S_1C_1 and S_2C_2 interacts with the baths B_1 and B_2 via semi-local thermal operations. Such operations are called *catalytic semi-local thermal operations* (cSLTOs) that satisfy

$$\Lambda_{S_{12}C_{12}}(\rho_{S_{12}} \otimes \rho_{C_{12}}) \to \sigma_{S_{12}} \otimes \rho_{C_{12}}, \tag{A.23}$$

where $\rho_{C_{12}}$ is a state of the catalyst. Note, the catalyst remains unchanged before and after the process. These catalytic operations form a larger set of thermodynamically allowed operations compared to SLTOs and respect all the properties satisfied by the SLTOs. The cSLTOs are the allowed thermodynamic operation in a quantum heat engine and constitute the free operation for the resource theory developed in this article. Several useful properties of these operations are outlined in the Appendix A.4. It is interesting to note that the cSLTOs converge to the (local) thermal operations that are introduced in the resource theory of quantum states beyond thermal equilibrium presented in [64, 198, 205], when both the baths are of the same temperature, i.e., for $\beta_1 = \beta_2$.

A.4.3 SLTOs are time-translation symmetric operations

It is interesting to note that the SLTOs, as well as the cSLTOs, are time-translation symmetric operations with respect to the time evolution

generated by the Hamiltonian $H_{S_{12}} = H_{S_1} + H_{S_2}$. In other words, if there is a time translation of the system driven by unitary $V(t) = e^{-itH_{S_{12}}/\hbar}$ for any given time t, then

$$V(t)\left[\Lambda_{S_{12}}(\rho_{S_{12}})\right]V^{\dagger}(t) = \Lambda_{S_{12}}\left[V(t)(\rho_{S_{12}})V^{\dagger}(t)\right], \tag{A.24}$$

i.e., the order of the time translation operations and the SLTO commute. Because of this symmetric property, the SLTOs monotonically decrease the superpositions between different eigenbases of $H_{S_{12}}$ or, in other words, among the energy eigenbases. Note the SLTOs are also time-translation symmetric with respect to the system's weighted-Hamiltonian $H_{S_{12}}^{\beta_1\beta_2} = \beta_1 H_{S_1} + \beta_2 H_{S_2}$, since $[H_{S_{12}}^{\beta_1\beta_2}, H_{S_{12}}] = 0$.

The Eq. (A.24) further implies that the SLTOs commute with the dephasing operations in the eigenbases of the Hamiltonian of the system $H_{S_{12}} = \sum_{i,j}(E_i^{S_1} + E_j^{S_2})|ij\rangle\langle ij|$, i.e.,

$$\Lambda_{S_{12}} \circ P_{S_{12}}(\rho_{S_{12}}) = P_{S_{12}} \circ \Lambda_{S_{12}}(\rho_{S_{12}}), \tag{A.25}$$

where $P_{S_{12}}(\rho_{S_{12}}) = \sum_{ij}\langle ij|\rho_{S_{12}}|ij\rangle\,|ij\rangle\langle ij|$ is the dephasing operation. Note the dephasing operation can be achieved by time averaging time-translated state for a long enough time T,

$$P_{S_{12}}(\rho_{S_{12}}) = \frac{1}{T}\int_0^T V(t)\,(\rho_{S_{12}})\,V(t)dt. \tag{A.26}$$

The Eq. (A.25) signifies that the diagonal elements in the eigenbases of $H_{S_{12}}$, i.e., $P_{S_{12}}(\rho_{S_{12}})$, evolve independently of the off-diagonal elements. Further, the amount of asymmetry present in a state due to the superposition between different energy eigenbases monotonically decreases under the SLTOs. We use these properties to understand the free-entropy locking in superpositions and to add more conditions to supplement the second laws for state transformations below.

A.5 Information theoretic notations and technical tools

In this section, we shall briefly outline the notations and tools that will be used to derive the conditions of state transformation under SLTOs. The interested readers are referred to [64,198] for more details.

A.5.1 Rényi α-entropies

Given an k-dimensional probability distribution $p = \{p_i\}_{i=1}^k$, the Rényi α-entropies are defined as

$$H_\alpha(p) = \frac{\mathrm{sgn}(\alpha)}{1-\alpha} \log \sum_{i=1}^k p_i^\alpha, \ \ \forall \alpha \in \mathcal{R} \setminus \{0,1\}, \tag{A.27}$$

where $\mathrm{sgn}(\alpha) = 1$ for $\alpha \geqslant 0$ and $\mathrm{sgn}(\alpha) = -1$ for $\alpha < 0$. For $\alpha \in \{-\infty, 0, 1, \infty\}$, the H_αs can be computed using limits, and they are

$$\begin{aligned} H_{-\infty}(p) = \log p_{\min}, \quad H_0(p) = \log \mathrm{rank}(p), \\ H_1(p) = -\sum_{i=1}^k p_i \log p_i, \ \text{ and } \ H_\infty(p) = -\log p_{\max}. \end{aligned} \tag{A.28}$$

The $\mathrm{rank}(p)$ means the number of non-zero elements in p, and $p_{\min}$ and $p_{\max}$ are the elements with smallest and largest values in p.

These Rényi entropies can also be defined for arbitrary quantum state ρ, where the $\{p_i\}$ would be the eigenvalues of the density matrix ρ. Note, at $\alpha \to 1$, the $H_1(\rho) = -\mathrm{Tr}\,\rho \log \rho$ becomes the von Neumann entropy of the state ρ.

A.5.2 Rényi α-relative entropies

For any two k-dimensional probability distributions $p = \{p_i\}_{i=1}^k$ and $q = \{q_i\}_{i=1}^k$, the Rényi α-relative entropies are defined as

$$D_\alpha(p \parallel q) = \frac{\mathrm{sgn}(\alpha)}{\alpha - 1} \log \sum_{i=1}^k p_i^\alpha q_i^{1-\alpha}, \quad \forall \alpha \in [-\infty, \infty]. \tag{A.29}$$

For the cases $\alpha \in \{-\infty, 0, 1, \infty\}$, the D_αs are calculated using limits, as

$$D_\infty(p \parallel q) = \lim_{\alpha \to \infty} D_\alpha(p \parallel q) = \log \max_i \frac{p_i}{q_i}, \tag{A.30}$$

$$D_{-\infty}(p \parallel q) = \lim_{\alpha \to -\infty} D_\alpha(p \parallel q) = D_\infty(q \parallel p), \tag{A.31}$$

$$D_0(p \parallel q) = \lim_{\alpha \to 0+} D_\alpha(p \parallel q) = -\log \sum_{i: p_i \neq 0}^k q_i, \tag{A.32}$$

$$D_1(p \parallel q) = \lim_{\alpha \to 1} D_\alpha(p \parallel q) = \sum_i p_i (\log p_i - \log q_i). \tag{A.33}$$

Here we use the conventions that $\frac{0}{0} = 0$ and $\frac{x}{0} = \infty$ for $x > 0$. The Rényi α-relative entropies satisfy many interesting properties, and we shall mention few useful ones below. These entropies monotonically decrease under stochastic maps Λ, i.e.,

$$D_\alpha(p \parallel q) \geqslant D_\alpha(\Lambda(p) \parallel \Lambda(q)), \quad \forall \alpha \in [-\infty, \infty]. \tag{A.34}$$

The inequalities are also known as the data-processing inequality. Another important property is that, for $\alpha \in [0, \infty]$,

$$D_\alpha(p \parallel q) \leqslant D_\delta(p \parallel q), \text{ for } \alpha \leqslant \delta. \tag{A.35}$$

For a k-dimensional probability distribution $\{q_i\}_{i=1}^k$ with $0 < q_i < 1$ and $\forall q_i \in \mathbb{Q}$, there exist a set of natural numbers $\{d_i\}_{i=1}^k$ such that $\sum_i d_i = N$ and $q_i = \frac{d_i}{N}$. Then a fine-grained, N-dimensional uniform probability can be written as

$$\Gamma(q) = \left\{ \underbrace{\frac{q_1}{d_1}, \ldots, \frac{q_1}{d_1}}_{d_1}, \ldots, \underbrace{\frac{q_k}{d_k}, \ldots, \frac{q_k}{d_k}}_{d_k} \right\} = \left\{ \underbrace{\frac{1}{N}, \ldots, \frac{1}{N}}_{N} \right\}. \tag{A.36}$$

Similarly, any other probability distribution $\{p_i\}_{i=1}^k$ can be fine grained to

$$\Gamma(p) = \left\{ \underbrace{\frac{p_1}{d_1}, \ldots, \frac{p_1}{d_1}}_{d_1}, \ldots, \underbrace{\frac{p_k}{d_k}, \ldots, \frac{p_k}{d_k}}_{d_k} \right\}. \tag{A.37}$$

Then, for $\alpha \in [-\infty, \infty]$, the Rényi α-relative entropies are related to the Rényi α-entropies as

$$D_\alpha\left(p|q\right) = D_\alpha\left(\Gamma(p)|\Gamma(q)\right) = \operatorname{sgn}(\alpha) \log N - H_\alpha(p). \tag{A.38}$$

For the situations where $q_i \notin \mathbb{Q}$, we can relate the Rényi α-relative entropies with the Rényi α-entropies using the following Lemma.

Lemma 4 (Ref. [64]). *Consider a non-increasingly ordered, k-dimensional probability distribution $q = \{q_i\}_{i=1}^k$ with $\forall q_i > 0$, and q_is may possibly assume irrational values. Then, for any $\epsilon > 0$, there exists a probability distribution q_ϵ such that*

(i) $\| q - q_\epsilon \| < \epsilon$,

(ii) Each probability in q_ϵ *is rational so that* $q_\epsilon = \left\{\frac{d_i}{N}\right\}_{i=1}^{k}$, *where* $\forall d_i \in \mathbb{N}$ *and* $\sum_{i=1}^{k} d_i = N$.

(iii) There exists a stochastic channel Λ *such that* $\Lambda(q) = q_\epsilon$, *and for any arbitrary probability distribution* r, *the channel satisfies* $\| r - \Lambda(r) \| \leqslant O\left(\sqrt{\epsilon}\right)$.

The Rényi α-relative entropies can be extended to two arbitrary quantum states ρ and σ. For this work, we shall restrict to the cases where $[\rho, \sigma] = 0$, and $\text{supp}[\rho] \subseteq \text{supp}[\sigma]$. Then the Rényi α-relative entropies are defined as

$$D_\alpha(\rho \parallel \sigma) = \frac{\text{sgn}(\alpha)}{\alpha - 1} \log \text{Tr}\left[\rho^\alpha \sigma^{1-\alpha}\right], \quad \forall \alpha \in [-\infty, \infty]. \tag{A.39}$$

For $\alpha \to 0$, it becomes the min-relative entropy,

$$D_{\min}(\rho \parallel \sigma) = D_0(\rho \parallel \sigma) = -\log \text{Tr}\left[\Pi_\rho \sigma\right], \tag{A.40}$$

where Π_ρ is the projector onto the support of the state ρ. For the $\alpha \to 1$, it reduces to the von Neumann relative entropy as

$$D_1(\rho \parallel \sigma) = \text{Tr}\left[\rho(\log \rho - \log \sigma\right]. \tag{A.41}$$

For the case $\alpha \to \infty$, it results in the max-entropy given by

$$D_{\max}(\rho \parallel \sigma) = D_\infty(\rho \parallel \sigma) = \log \min\{\lambda : \rho \leqslant \lambda\sigma\}. \tag{A.42}$$

The Rényi α-relative entropies are known to satisfy the monotonicity relation under completely positive maps, for $\alpha \in [0, 2]$,

$$D_\alpha(\rho \parallel \sigma) \geqslant D_\alpha(\Lambda(\rho) \parallel \Lambda(\sigma)). \tag{A.43}$$

For other values of α, validity of the monotonicity is still an open question.

A.5.3 Majorization and catalytic majorization (trumping)

The majorization relations are useful to introduce partial orders between arbitrary probability distributions [355]. For any two probability distributions $p = \{p_i\}_{i=1}^k$ and $p' = \{p'_i\}_{i=1}^k$, we say that p

majorizes p', i.e., $p \succcurlyeq p'$, if for all $l = 1, \ldots, k$,

$$\sum_{i=1}^{l} p_i^{\downarrow} \geqslant \sum_{i=1}^{l} p_i'^{\downarrow} \quad \text{and} \quad \sum_{i=1}^{k} p_i^{\downarrow} = \sum_{i=1}^{k} p_i'^{\downarrow} = 1, \tag{A.44}$$

where the $p^{\downarrow}$ is obtained by rearranging p in the non-increasing order so that $p_1^{\downarrow} \geqslant p_2^{\downarrow} \geqslant \ldots \geqslant p_k^{\downarrow}$, and similarly we obtain $p'^{\downarrow}$ by rearranging p'. When two probability distributions are partial ordered through a majorization relation, these satisfy the following properties:
(i) Two probability distributions p and p' satisfy a majorization relation, $p \succcurlyeq p'$ if and only if there exist a channel Λ such that $p' = \Lambda(p)$ and Λ satisfies $\Lambda(\eta) = \eta$, where η is the uniform distribution. The channels Λ are called bi-stochastic channels, and these can be implemented using random unitary operations.
(ii) If two probability distributions p and p' satisfy a majorization relation, $p \succcurlyeq p'$, then

$$f(p) \leqslant f(p'), \tag{A.45}$$

where f are all Schur-concave functions. Note, the Rényi α-entropies H_αs are Schur-concave functions for $\alpha \in [-\infty, \infty]$.

Let us now discuss catalytic majorization or trumping. There are situations where p and p' cannot be partially ordered in terms of majorization, but in presence of an additional probability distribution x, it satisfies $p \otimes x \succcurlyeq p' \otimes x$. This is termed as "$p$ trumps p'" or $p \succcurlyeq_T p'$. For two given probability distribution it is often very difficult to find the additional probability distribution x to check if the former are related through trumping. However, if the two probability distributions satisfy following two Lemmas, then one could ensure the existence of at least one x.

Lemma 5 (Ref. [64]). *Let us consider two probability distributions p and p' that do not contain any element equal to zero. Then, p trumps p', i.e., $p \succcurlyeq_T p'$ if, and only if, the Rényi α-entropies satisfy*

$$H_\alpha(p) \leqslant H_\alpha(p'), \quad \forall \alpha \in (-\infty, \infty). \tag{A.46}$$

Obviously, there are situations where the p and p' are not of full-ranks (i.e., with all non-zero elements). In this situation, the Lemma below holds.

Lemma 6 (Ref. [64]). *Let us consider two arbitrary probability distributions p and p'. Then the following are equivalent:*
(i) For an arbitrary $\epsilon > 0$, there exists a full rank probability distribution p'_ϵ such that $\| p' - p'_\epsilon \| \leqslant \epsilon$ and p trumps p'_ϵ (i.e., $p \succcurlyeq_T p'_\epsilon$). (ii) The inequalities are satisfied, $H_\alpha(p) \leqslant H_\alpha(p'), \quad \forall \alpha \in (-\infty, \infty)$.

The notion of majorization and trumping can also be extended to quantum states, say between ρ and ρ'. Then, the majorization relation $\rho \succcurlyeq \rho'$ implies the relations (A.44) where the $p^\downarrow$ and $p'^\downarrow$ are the non-increasingly ordered eigenvalues of ρ and ρ' respectively.

A.5.4 d-majorization and catalytic d-majorization

Not only for two probability distributions, but the majorization-like partial ordering can also be drawn between two pairs of probability distributions. Consider two pairs of probability distributions (p, q) and (p', q'). The (p, q) d-majorizes (p', q') if and only if

$$\sum_i q_i f\left(\frac{p_i}{q_i}\right) \leqslant \sum_i q'_i f\left(\frac{p'_i}{q'_i}\right), \tag{A.47}$$

for any arbitrary concave function f. This d-majorization based preordering is then denoted as $d(p|q) \succcurlyeq d(p'|q')$. Given this definition of d-majorization, we present the following Lemma.

Lemma 7 (Ref. [64]). *Let us consider four probability distributions p, p', q, and q'. Then the following statements are equivalent: (i) The pair (p, q) d-majorizes the pair (p', q'), i.e., $d(p|q) \succcurlyeq d(p'|q')$. (ii) There exists a stochastic channel Λ that satisfies $\Lambda(p) = p'$ and $\Lambda(q) = q'$.*

A catalytic d-majorization can also be introduced as in the following.

Lemma 8 (Ref. [64]). *For two pairs of probability distributions, (p, q) and (p', q') with the constraints that q and q' are of full rank, the following conditions are equivalent:*

(i) The Rényi α-relative entropies satisfy $D_\alpha(p \parallel q) \geqslant D_\alpha(p' \parallel q')$, $\forall \alpha \in [-\infty, \infty]$.

(ii) For $\epsilon > 0$, there exists full-rank probability distributions r, s, and p'_ϵ, and a stochastic channel Λ such that

(a) $\Lambda(p \otimes r) = p'_\epsilon \otimes r$,
(b) $\Lambda(q \otimes s) = q' \otimes s$, *moreover* s *can be a uniform distribution* η *onto the support of* r,
(c) $\| p' - p'_\epsilon \| \leqslant \epsilon$.

We shall use this Lemma for the derivations of the second laws for the state transformations under cSLTOs.

A.6 Second laws for transformations between states block-diagonal in energy eigenbases

In this section, we present the necessary and sufficient conditions for state transformations, i.e., the second laws of state transformations, under (catalytic) semi-local thermal operations. All the necessary and sufficient conditions derived here are based on the assumption that the initial states are block-diagonal in the energy eigenbases of the system. However, the conditions still apply to initial non-block-diagonal states, but only as necessary conditions.

We start with a bipartite system S_{12}, with non-interacting Hamiltonian $H_{S_{12}} = H_{S_1} + H_{S_2}$, and the initial state $\rho_{S_{12}}$. The subsystem S_1 (S_2) is semi-locally interacting with a bath B_1 (B_2) at inverse temperature β_1 (β_2). After a transformation, the final state of the system becomes $\sigma_{S_{12}}$. At this stage, we assume that the system Hamiltonian remains unchanged before and after the transformation. Our goal is to find necessary and sufficient conditions with which we can ascertain that the transformation

$$(\rho_{S_{12}}, H_{S_{12}}) \to (\sigma_{S_{12}}, H_{S_{12}}) \tag{A.48}$$

is possible via a semi-local thermal operation Λ, and vice versa.

A.6.1 State transformation in absence of a catalyst

Suppose, we do not have access to a catalyst. Following the discussion made in Sections A.2 and A.4, we rewrite the initial system-bath

composite as

$$\gamma_{B_1} \otimes \gamma_{B_2} \otimes \rho_{S_{12}} = \sum_{E_{12}} P_{E_{12}} \left(\gamma_{B_1} \otimes \gamma_{B_2} \otimes \rho_{S_{12}}\right) P_{E_{12}} = \sum_{E_{12}} p_{E_{12}} \, \rho_{E_{12}}^{B_1 B_2 S_{12}}. \tag{A.49}$$

Here $E_{12} = E_1 + E_2$ the total energy and the projector $P_{E_{12}}$ spans the system-bath joint space with the same value of total energy E_{12}. The probabilities $p_{E_{12}} = \mathrm{Tr}\left[P_{E_{12}}(\gamma_{B_1} \otimes \gamma_{B_2} \otimes \rho_{S_{12}})\right]$. Now for $E_1, E_{B_1} \in \mathcal{E}_1$ and $E_2, E_{B_2} \in \mathcal{E}_2$, the normalized state of the bath-system composites, in a block of total energy $E_{12} = E_1 + E_2$, is given by

$$\begin{aligned} \rho_{E_{12}}^{B_1 B_2 S_{12}} &= \bigoplus_{E_{S_{12}}} \frac{\mathbb{I}}{g_{B_1}(E_1) e^{-\beta_1 E_{S_1}}} \otimes \frac{\mathbb{I}}{g_{B_2}(E_2) e^{-\beta_2 E_{S_2}}} \otimes P_{E_{S_{12}}}(\rho_{S_{12}}) P_{E_{S_{12}}} \\ &= \bigoplus_{E_{S_{12}}} \eta_{E_1 - E_{S_1}}^{B_1} \otimes \eta_{E_2 - E_{S_2}}^{B_2} \otimes P_{E_{S_{12}}}(\rho_{S_{12}}) P_{E_{S_{12}}}, \end{aligned} \tag{A.50}$$

where $E_{S_{12}} = E_{S_1} + E_{S_2}$ is the system energy and $P_{E_{S_{12}}}$ is the projector correspond to the system energy $E_{S_{12}}$. Similarly, the final joint state of the bath and the system composite can be expressed as

$$\gamma_{B_1} \otimes \gamma_{B_2} \otimes \sigma_{S_{12}} = \sum_{E_{12}} P_{E_{12}} \left(\gamma_{B_1} \otimes \gamma_{B_2} \otimes \sigma_{S_{12}}\right) P_{E_{12}} = \sum_{E_{12}} q_{E_{12}} \, \sigma_{E_{12}}^{B_1 B_2 S_{12}}, \tag{A.51}$$

where $q_{E_{12}} = \mathrm{Tr}\left[P_{E_{12}}(\gamma_{B_1} \otimes \gamma_{B_2} \otimes \sigma_{S_{12}})\right]$. For a total energy $E_{12} = E_1 + E_2$ block, the normalized state becomes

$$\sigma_{E_{12}}^{B_1 B_2 S_{12}} = \bigoplus_{E_{S_{12}}} \eta_{E_1 - E_{S_1}}^{B_1} \otimes \eta_{E_2 - E_{S_2}}^{B_2} \otimes P_{E_{S_{12}}}(\sigma_{S_{12}}) P_{E_{S_{12}}}. \tag{A.52}$$

With these structures of the initial and final states of the system-bath composites, we put forward the necessary and sufficient conditions for the transformations of block-diagonal states under semi-local thermal operations.

Majorization condition

The conditions are derived in terms of majorization (see Section A.5.3) in the following theorem.

Theorem 9 (Majorization condition for state transformations)**.** *Consider two states $\rho_{S_{12}}$ and $\sigma_{S_{12}}$ that are block-diagonal in the eigenbases of the Hamiltonian of the system $H_{S_{12}} = H_{S_1} + H_{S_2}$. Then the transformation $(\rho_{S_{12}}, H_{S_{12}}) \to (\sigma_{S_{12}}, H_{S_{12}})$ by means of semi-local thermal operation is possible if, and only if, the initial and final states of the system-bath composites satisfy the majorization relation*

$$\bigoplus_{E_{S_1}+E_{S_2}} \eta^{B_1}_{E_1-E_{S_1}} \otimes \eta^{B_2}_{E_2-E_{S_2}} \otimes P_{E_{S_{12}}}(\rho_{S_{12}}) P_{E_{S_{12}}} \succcurlyeq \bigoplus_{E_{S_1}+E_{S_2}} \eta^{B_1}_{E_1-E_{S_1}} \otimes \eta^{B_2}_{E_2-E_{S_2}} \otimes P_{E_{S_{12}}}(\sigma_{S_{12}}) P_{E_{S_{12}}} \tag{A.53}$$

for large enough E_1 and E_2.

Moreover, for the cases where the initial system state is not block-diagonal in the eigenbases of $H_{S_{12}}$, the necessary condition for the transformation $(\rho'_{S_{12}}, H_{S_{12}}) \to (\sigma'_{S_{12}}, H_{S_{12}})$ is

$$\bigoplus_{E_{S_1}+E_{S_2}} \eta^{B_1}_{E_1-E_{S_1}} \otimes \eta^{B_2}_{E_2-E_{S_2}} \otimes P_{E_{S_{12}}}(\rho'_{S_{12}}) P_{E_{S_{12}}} \succcurlyeq \bigoplus_{E_{S_1}+E_{S_2}} \eta^{B_1}_{E_1-E_{S_1}} \otimes \eta^{B_2}_{E_2-E_{S_2}} \otimes P_{E_{S_{12}}}(\sigma'_{S_{12}}) P_{E_{S_{12}}}. \tag{A.54}$$

Proof. For the system-bath composite state in a block with fixed total energy $E_{12} = E_1 + E_2$, the allowed operations are any unitary operations that also strictly conserve total weighted-energy $E_{12}^{\beta_1\beta_2} = \beta_1 E_1 + \beta_2 E_2$. Because, such a unitary operation does not alter the total energy as well as the total weighted-energy of the block. However, as we shall show below, we not only can apply all such unitary operations but also implement random unitary operations as long as population remain in this fixed total energy and total weighted-energy block. Note these are the only possible operations that are allowed on the systems-baths joint space as they strictly conserve the total energy and total weighted-energy.

We start with the first part of the theorem and prove it using a protocol involving the following steps, where the initial state of the system-bath composite is with total energy E_{12} and total weighted-energy $E_{12}^{\beta_1\beta_2}$:

(i) *Implementing random unitary operations:* We assume that the E_1 and the E_2, corresponding to the block with energy E_{12}, are reasonably large. This in turn implies that the dimension of the maximally

mixed state $\eta^{B_1}_{E_1-E_{S_1}} \otimes \eta^{B_2}_{E_2-E_{S_2}}$ is exponentially large. Therefore we can divide the state in two normalized sub-parts, as

$$\eta^{B_1}_{E_1-E_{S_1}} \otimes \eta^{B_2}_{E_2-E_{S_2}} = \left(\eta^{B_1}_{E_1''} \otimes \eta^{B_2}_{E_2''}\right) \otimes \left(\eta^{B_1}_{E_1'-E_{S_1}} \otimes \eta^{B_2}_{E_2'-E_{S_2}}\right) \quad \text{(A.55)}$$

where $E_1 = E_1'' + E_1'$ and $E_2 = E_2'' + E_2'$, and each of the sub-parts are in maximally mixed states with exponentially large dimensions. We further assume that $\eta^{B_1}_{E_1-E_{S_1}} \otimes \eta^{B_2}_{E_2-E_{S_2}}$ is so large that it hardly differ from $\eta^{B_1}_{E_1'-E_{S_1}} \otimes \eta^{B_2}_{E_2'-E_{S_2}}$. The initial state of the system-bath composite with total energy E_{12}, is then

$$\left(\eta^{B_1}_{E_1''} \otimes \eta^{B_2}_{E_2''}\right) \otimes \left(\bigoplus_{E_{S_{12}}} \eta^{B_1}_{E_1'-E_{S_1}} \otimes \eta^{B_2}_{E_2'-E_{S_2}} \otimes P_{E_{S_{12}}}(\rho_{S_{12}}) P_{E_{S_{12}}}\right). \quad \text{(A.56)}$$

Now, the state $\eta^{B_1}_{E_1''} \otimes \eta^{B_2}_{E_2''}$ can be used as a control state to implement random unitary operations (i.e., a unital channel) on the rest of the system-bath composite, by using a global unitary on the entire system-bath composite that strictly conserves both total energy and total weighted-energy. Lets say, we implement such a global unitary $U_{E_1+E_2}$ (see Eq. (A.13)) so that the resultant system state becomes $\sigma_{S_{12}}$ after tracing out the baths. Note the joint state of the system-bath composite can still have correlations among them.

(ii) *Destroying unwanted correlations in the system-bath composite state:* Now, we can destroy the unnecessary correlations that may possibly present between the sub-systems and baths after step (i). That is done by a "twirling" operation which is itself a random unitary operation within the total energy block. For each system state with the energy $E_{S_{12}} = E_{S_1} + E_{S_2}$, we apply twirling operation on the bath part B_1B_2 while applying identity operation on the system part, such that the transformed final system-bath state becomes classically correlated as

$$\bigoplus_{E_{S_1}+E_{S_2}} \eta^{B_1}_{E_1-E_{S_1}} \otimes \eta^{B_2}_{E_2-E_{S_2}} \otimes P_{E_{S_{12}}}(\sigma_{S_{12}}) P_{E_{S_{12}}}. \quad \text{(A.57)}$$

Both the operations applied in steps (i) and (ii) are random unitary operations that respect strict conservation of total energy and

total weighted-energy, and these are the precursors of semi-local thermal operations in the joint space of systems and baths (see Section A.4). Further, if two states are related through random unitary operations, then the states satisfy pre-ordering by a majorization relation, and this is a necessary and sufficient condition. Consequently, the transformation is possible if and only if the initial system-bath state majorizes the final one, within a block of total energy E_{12}. Now since baths are considerably large in energy compared to the systems, we can implement the random unitary operations in the other blocks, similar to the steps (i) and (ii), such that the reduced system state becomes exactly the same. As a result, we do not need to check the majorization relation for every block with fixed total total energy. Therefore, the transition $(\rho_{S_{12}}, H_{S_{12}}) \to (\sigma_{S_{12}}, H_{S_{12}})$ is possible if, and only if, the majorization relation (A.53) is satisfied. With this, we complete the proof of the first part.

For the second part, we recall that the reduced operations on the system part, as the result of global unitary operations on the systems-baths composite, respect time-translation symmetry with respect to time translation by the Hamiltonian of the system $H_{S_{12}}$ (see main text). The block-diagonal elements (also known as the 'zero' mode elements) of the system density matrix ($\rho'_{S_{12}}$) with respect to the eigenbases of $H_{S_{12}}$ evolve independently of the off-diagonal elements ('non-zero' modes) under this time-translation symmetric operations. For any transformation connecting the initial state ($\rho'_{S_{12}}$) to a final state ($\sigma'_{S_{12}}$), it is necessary that the corresponding block-diagonal states must satisfy the majorization relation (A.54). This relation cannot provide the sufficient condition as it does not encode information related to the non-block-diagonal elements. □

So far, we have derived the necessary and sufficient condition for transformations between block-diagonal states under semi-local thermal operations. However, the condition requires us a take into account both the system and the bath parameters simultaneously, which is not always practical.

Thermo-majorization condition

Here we aim to derive necessary and sufficient conditions that exclusively depend on the system parameters, based on thermo-majorization.

Consider two quantum states $\rho_{S_{12}}$ and $\sigma_{S_{12}}$, block-diagonal in the eigenbases of the Hamiltonian $H_{S_{12}} = H_{S_1} + H_{S_2}$, with the probabilities $\{p_{ij}\}$ and $\{q_{ij}\}$ respectively. Here the Hamiltonian of the system is written as $H_{12} = \sum_{ij}(E_i^{S_1} + E_j^{S_2})|ij\rangle\langle ij|$, the probabilities are given by $p_{ij} = \langle ij|\rho_{S_{12}}|ij\rangle$ and $q_{ij} = \langle ij|\sigma_{S_{12}}|ij\rangle$. A pre-ordering is done by a non-increasing ordering of the quantities $\{p_{ij}\, e^{(\beta_1 E_i^{S_1} + \beta_2 E_j^{S_2})}\}$ and relabeled, so that

$$\begin{aligned} p_{11}\, e^{(\beta_1 E_1^{S_1} + \beta_2 E_1^{S_2})} \geqslant p_{12}\, e^{(\beta_1 E_1^{S_1} + \beta_2 E_2^{S_2})} \geqslant & p_{21}\, e^{(\beta_1 E_2^{S_1} + \beta_2 E_1^{S_2})} \\ & \geqslant p_{22}\, e^{(\beta_1 E_2^{S_1} + \beta_2 E_2^{S_2})} \geqslant \ldots. \end{aligned} \tag{A.58}$$

This determines the sequence in $\{p_{ij}\}$, which may or may not satisfy a non-decreasing order. We denote the set of the ordered probability distribution as $\{p_{ij}^{\downarrow}\}$, where $p_{11}^{\downarrow}$ is the p_{ij} corresponding to the largest $p_{ij}\, e^{(\beta_1 E_i^{S_1} + \beta_2 E_j^{S_2})}$ value and so on. A similar pre-ordering is also done for $\{q_{ij}\} \to \{q_{ij}^{\downarrow}\}$. Now we construct a Lorentz curve with the points corresponding to the pairs

$$\begin{aligned} &\{(x, y)\} = \\ &\{(0,\ 0), \\ &(p_{11},\ e^{-(\beta_1 E_1^{S_1} + \beta_2 E_1^{S_2})}), \\ &(p_{11} + p_{12},\ e^{-(\beta_1 E_1^{S_1} + \beta_2 E_1^{S_2})} + e^{-(\beta_1 E_1^{S_1} + \beta_2 E_2^{S_2})}), \\ &(p_{11} + p_{12} + p_{21},\ e^{-(\beta_1 E_1^{S_1} + \beta_2 E_1^{S_2})} + e^{-(\beta_1 E_1^{S_1} + \beta_2 E_2^{S_2})} + e^{-(\beta_1 E_2^{S_1} + \beta_2 E_1^{S_2})}), \\ &\quad \vdots \\ &(1,\ Z_1 Z_2)\} \end{aligned}$$

Plotting these points gives a function $f_p(x)$ corresponding to the state $\rho_{S_{12}}$. A similar function is also derived for $\{q_{ij}\}$, and that is $f_q(x)$ for $\sigma_{S_{12}}$.

Theorem 10 (Thermo-majorization condition for state transformations)**.** *A transition $(\rho_{S_{12}}, H_{S_{12}}) \to (\sigma_{S_{12}}, H_{S_{12}})$ can occur under semi-local thermal operation if, and only if, the spectra of $\rho_{S_{12}}$ thermo-majorizes the spectra of $\sigma_{S_{12}}$, i.e.,*

$$f_p(x) \geqslant f_q(x), \ \ \forall x \in [0, Z_1 Z_2]. \tag{A.59}$$

In this sub-section, the derived necessary and sufficient conditions based on majorization are very handy. This is in the sense that they are easy to check, in particular, the one based on thermo-majorization. However, as we have mentioned in Section A.5, there are probability distribution that do not satisfy majorization relation as such, but can still possess a majorization based pre-ordering by having access to another probability distribution as a catalyst. It is not easy to check whether there exists a probability distribution which can act as a catalyst in order satisfy a majorization relation. We can still find necessary and sufficient condition(s) based on Reńyi relative entropies to ensure their existence, which we shall consider in the next sub-section.

A.6.2 Catalytic state transformation

Before we propose the necessary and sufficient conditions for the transformation under catalytic semi-local thermal operations, let us introduce the definition of α-free-entropy (S_α) in terms of the Rényi α-relative entropy (D_α).

α-free-entropies

Consider a state $\rho_{S_{12}}$ of a bipartite system S_{12} with Hamiltonian $H_{S_{12}} = H_{S_1} + H_{S_2}$, where the sub-system S_1 (S_2) is semi-locally interacting with the bath B_1 (B_2) at inverse temperature β_1 (β_2). Also, the state $\rho_{S_{12}}$ is block-diagonal in the eigenbases of the Hamiltonian $H_{S_{12}}$. Then, the Rényi α-relative entropy between the system state and its corresponding semi-Gibbs state, for $\alpha \in [-\infty, \infty]$, is given by

$$D_\alpha(\rho_{S_{12}} \parallel \gamma_{S_1} \otimes \gamma_{S_2}) = \frac{\mathrm{sgn}(\alpha)}{\alpha - 1} \log \mathrm{Tr}\left[(\rho_{S_{12}})^\alpha \, (\gamma_{S_1} \otimes \gamma_{S_2})^{1-\alpha}\right], \tag{A.60}$$

where the thermal states are $\gamma_{S_i} = \frac{e^{-\beta_i H_{S_i}}}{Z_i}$, with $Z_i = \mathrm{Tr}\left[e^{-\beta_i H_{S_i}}\right]$ and $i = 1, 2$. Now the α-free-entropy of the state $\rho_{S_{12}}$ is defined as

$$S_\alpha(\rho_{S_{12}}, \gamma_{S_1} \otimes \gamma_{S_2}) = D_\alpha\left(\rho_{S_{12}} \parallel \gamma_{S_1} \otimes \gamma_{S_2}\right) - \log Z_1 Z_2, \quad \forall \alpha \in [-\infty, \infty]. \tag{A.61}$$

The name 'free-entropy' is justified by fact that it quantifies the work potential stored in a system in terms of entropy, which we shall discuss in the Section A.7. For $\alpha \to 1$, the S_α reduces to the Helmholtz free-entropy as

$$S_1(\rho_{S_{12}}, \gamma_{S_1} \otimes \gamma_{S_2}) = \beta_1 E_{S_1} + \beta_2 E_{S_2} - S(\rho_{S_{12}}), \tag{A.62}$$

where $S(\rho_{S_{12}}) = -\mathrm{Tr}\,\rho_{S_{12}} \ln \rho_{S_{12}}$ is the von Neumann entropy and $E_{S_x} = \mathrm{Tr}\,[\rho_{S_x} H_{S_x}]$ is the average energy of the sub-system S_x, with $x = 1, 2$. For the cases where the state $\rho_{S_{12}}$ is uncorrelated, $\rho_{12} = \rho_{S_1} \otimes \rho_{S_2}$, the α-free-entropy becomes additive $S_\alpha(\rho_{S_{12}}, \gamma_1 \otimes \gamma_2) = S_\alpha(\rho_{S_1}, \gamma_1) + S_\alpha(\rho_{S_2}, \gamma_2)$.

Second laws in terms of α-free-entropies

Now with the notion of α-free-entropy, we go on to propose the necessary and sufficient conditions for catalytic semi-local thermal operation, in the following theorem.

Theorem 11. *Consider two states $\rho_{S_{12}}$ and $\sigma_{S_{12}}$ that are block-diagonal in the eigenbases of a system Hamiltonian $H_{S_{12}} = H_{S_1} + H_{S_2}$. Then, a transformation $(\rho_{S_{12}}, H_{S_{12}}) \to (\sigma_{S_{12}}, H_{S_{12}})$ is possible under semi-local thermal operation if, and only if, for all $\alpha \in (-\infty, \infty)$,*

$$S_\alpha(\rho_{S_{12}}, \gamma_{S_1} \otimes \gamma_{S_2}) \geqslant S_\alpha(\sigma_{S_{12}}, \gamma_{S_1} \otimes \gamma_{S_2}). \tag{A.63}$$

Remark: *The condition for $\alpha = -\infty, \infty$ can be included by continuity.*

Proof. Since the initial and final states are block-diagonal in the energy eigenbases, the theorem above can be proved using catalytic d-majorization shown in the Lemma 8. Replacing the probability distributions, in Lemma 8, with the eigenvalues of the states block-diagonal in energy, as

$p \to \rho_{S_{12}}$; initial state of the system,
$p' \to \sigma_{S_{12}}$; final state of the system,
$q = q' \to \gamma_{S_1} \otimes \gamma_{S_2}$; semi-Gibbs state of the system,
$r \to \rho_{C_{12}}$; a catalyst
$s \to \gamma_{C_1} \otimes \gamma_{C_2}$; semi-Gibbs state of the catalyst.

Note, if we consider that the Hamiltonian of the catalyst $H_{C_{12}} = H_{C_1} + H_{C_2}$ is trivial (i.e., $H_{C_{12}} = \mathbb{I}$), then

$$s = \gamma_{C_1} \otimes \gamma_{C_2} \to \eta; \text{ a uniform distribution.}$$

Let us first assume that the catalyst possesses a trivial Hamiltonian $H_{C_{12}} = \mathbb{I}$ and the conditions (A.63) are satisfied. The latter, in terms of Rényi α-relative entropy, means

$$D_\alpha(\rho_{S_{12}} \parallel \gamma_{S_1} \otimes \gamma_{S_2}) \geqslant D_\alpha(\sigma_{S_{12}} \parallel \gamma_{S_1} \otimes \gamma_{S_2}), \ \ \forall \alpha \in (-\infty, \infty). \tag{A.64}$$

Then, as the Lemma 8 implies, there exists a catalyst $\rho_{C_{12}}$ and a channel Λ that (i) preserves the semi-Gibbas state $\gamma_{S_1} \otimes \gamma_{S_2} \otimes \gamma_{C_1} \otimes \gamma_{C_2}$, as

$$\Lambda\left(\gamma_{S_1} \otimes \gamma_{S_2} \otimes \gamma_{C_1} \otimes \gamma_{C_2}\right) = \gamma_{S_1} \otimes \gamma_{S_2} \otimes \gamma_{C_1} \otimes \gamma_{C_2}, \tag{A.65}$$

and (ii) transforms the initial state as

$$\Lambda\left(\rho_{S_{12}} \otimes \rho_{C_{12}}\right) = \rho^o_{S_{12}} \otimes \rho_{C_{12}}, \tag{A.66}$$

where $\parallel \rho^o_{S_{12}} - \sigma_{S_{12}} \parallel \leqslant \epsilon$. As the operations that preserve semi-Gibbs states are also semi-local thermal operations (see Corollary 3), it implies that such a transformation using catalytic semi-local thermal transformation is possible.

Let us consider the converse now. Suppose there is a catalytic semi-local thermal channel Λ that transforms

$$\Lambda\left(\rho_{S_{12}} \otimes \rho_{C_{12}}\right) = \rho^o_{S_{12}} \otimes \rho_{C_{12}}, \tag{A.67}$$

where $\parallel \rho^o_{S_{12}} - \sigma_{S_{12}} \parallel \leqslant \epsilon$. Then the Lemma 8 implies that the conditions (A.64) are satisfied. This completes the proof. □

For block-diagonal input state of a system, a block-diagonal catalyst is enough

Note, for a block-diagonal input state of a system, a block-diagonal catalyst is enough. This can be seen from the fact that the semi-local thermal operations are time-translation symmetric with respect to the Hamiltonian of the systems $H_{S_{12}}$ (see main text). This is also

true in the presence of catalysts. Therefore, the catalytic semi-local thermal operations are time-translation symmetric with respect to the joint Hamiltonian of the system and the catalyst, $H_{S_{12}} + H_{C_{12}}$. Mathematically, for the catalytic semi-local thermal transformation $\rho_{S_{12}} \otimes \rho_{C_{12}} \to \Lambda(\rho_{S_{12}} \otimes \rho_{C_{12}}) = \sigma_{S_{12}} \otimes \rho_{C_{12}}$, it means

$$\begin{aligned} \Lambda\big(e^{-it(H_{S_{12}}+H_{C_{12}})}\, \rho_{S_{12}} \otimes \rho_{C_{12}}\, e^{it(H_{S_{12}}+H_{C_{12}})}\big) \\ = e^{-it(H_{S_{12}}+H_{C_{12}})}\, \Lambda\left(\rho_{S_{12}} \otimes \rho_{C_{12}}\right)\, e^{it(H_{S_{12}}+H_{C_{12}})}. \end{aligned} \tag{A.68}$$

Due to this time-translation symmetry, the block diagonal elements of the $S_{12}C_{12}$ composite evolve fully independently of the off-diagonal elements. Further, these block-diagonal elements can be expressed as the tensor-products of block-diagonal elements arising from the system S_{12} and the catalyst C_{12} corresponding to the energy eigenbases of their own Hamiltonians. For an initial state $\rho_{S_{12}}$ block-diagonal in energy bases, the block-diagonal part of the catalyst state only participates during the transformation. Therefore, a catalyst in a state block-diagonal in its energy eigenbases is enough.

Avoiding negative α

The second laws for the transformations between system states, that are block-diagonal in energy, are based on the conditions (A.63) for $\alpha \in [-\infty, \infty]$. However, we can get rid of the negative α in the conditions by borrowing an ancillary system in a pure state. The only condition is that, after the transformation, we return it with good fidelity. Even a two-qubit system in a pure state is enough to lift all the conditions involving negative α.

Theorem 12. *Consider two states $\rho_{S_{12}}$ and $\sigma_{S_{12}}$ that are block-diagonal in the energy eigenbases, with the associated Hamiltonian $H_{S_{12}} = H_{S_1} + H_{S_2}$. Additionally, we are allowed to borrow a two-qubit system A_{12} with a trivial Hamiltonian and in a pure state $|0\rangle\langle 0|_{A_1} \otimes |0\rangle\langle 0|_{A_2}$, and then return it with a good fidelity. Then a transformation $(\rho_{S_{12}}, H_{S_{12}}) \to (\sigma_{S_{12}}, H_{S_{12}})$ is possible under semi-local thermal operation if, and only if,*

$$S_\alpha(\rho_{S_{12}}, \gamma_{S_1} \otimes \gamma_{S_2}) \geqslant S_\alpha(\sigma_{S_{12}}, \gamma_{S_1} \otimes \gamma_{S_2}), \quad \forall\, \alpha \geqslant 0. \tag{A.69}$$

Proof. Let us first assume that the transformation

$$\rho_{S_{12}} \otimes |0\rangle\langle 0|_{A_1} \otimes |0\rangle\langle 0|_{A_2} \to \sigma_{S_{12}} \otimes |0\rangle\langle 0|_{A_1} \otimes |0\rangle\langle 0|_{A_2} \tag{A.70}$$

is possible by means of a catalytic semi-local thermal operation. Then, using Theorem 11 and noticing that the Rényi α-relative entropies (D_α) are finite for the state $|0\rangle\langle 0|_{A_1} \otimes |0\rangle\langle 0|_{A_2}$ only for $\alpha \geqslant 0$, we have

$$\begin{aligned} &D_\alpha(\rho_{S_{12}} \otimes |0\rangle\langle 0|_{A_1} \otimes |0\rangle\langle 0|_{A_2} \,\|\, \gamma_{S_1} \otimes \gamma_{S_2} \otimes \gamma_{A_1} \otimes \gamma_{A_2}) \\ &\quad \geqslant D_\alpha(\sigma_{S_{12}} \otimes |0\rangle\langle 0|_{A_1} \otimes |0\rangle\langle 0|_{A_2} \,\|\, \gamma_{S_1} \otimes \gamma_{S_2} \otimes \gamma_{A_1} \otimes \gamma_{A_2}), \end{aligned} \tag{A.71}$$

for all $\alpha \geqslant 0$. Moreover, $D_\alpha(\rho_{S_{12}} \otimes |0\rangle\langle 0|_{A_1} \otimes |0\rangle\langle 0|_{A_2} \,\|\, \gamma_{S_1} \otimes \gamma_{S_2} \otimes \gamma_{A_1} \otimes \gamma_{A_2}) = D_\alpha(\rho_{S_{12}} \,\|\, \gamma_{S_1} \otimes \gamma_{S_2}) + D_\alpha(|0\rangle\langle 0|_{A_1} \otimes |0\rangle\langle 0|_{A_2} \,\|\, \gamma_{A_1} \otimes \gamma_{A_2})$. Thus the conditions (A.71), in turn, imply the conditions (A.69).

Conversely, let us consider that the conditions (A.69) (as well as the conditions (A.71)) are satisfied. As we have indicated earlier, the D_αs become infinite with $|0\rangle\langle 0|_{A_1} \otimes |0\rangle\langle 0|_{A_2}$ for $\alpha < 0$. However, we may allow that the final state of the ancillary system A_{12} is returned in the full-rank state but arbitrarily close to the original state. Then the left-hand side of (A.71) remains infinite but the right-hand side becomes finite. Thus, we are led to

$$D_\alpha(\rho_{S_{12}} \,\|\, \gamma_{S_1} \otimes \gamma_{S_2}) \geqslant D_\alpha(\sigma_{S_{12}} \,\|\, \gamma_{S_1} \otimes \gamma_{S_2}), \quad \forall \alpha \in \mathbb{R}. \tag{A.72}$$

Now by Theorem 11, we say that the state $\rho_{S_{12}} \otimes |0\rangle\langle 0|_{A_1} \otimes |0\rangle\langle 0|_{A_2}$ can be transformed arbitrarily close to the state $\sigma_{S_{12}} \otimes |0\rangle\langle 0|_{A_1} \otimes |0\rangle\langle 0|_{A_2}$. □

A.6.3 State transformation with time dependent Hamiltonians

So far we have restricted ourselves to the cases where the system Hamiltonian remains unchanged before and after the transformations. However, in real situations, this restriction is not often respected. To include all these scenarios, we consider the cases where such changes in Hamiltonians are allowed.

Consider a situation where the non-interacting Hamiltonian $H_{S_{12}} = H_{S_1} + H_{S_2}$ of the system S_{12} changes to $H'_{S_{12}} = H'_{S_1} + H'_{S_2}$, along with the state transformation $\rho_{12} \to \sigma'_{12}$. Here the $(')$ indicates the state with modified Hamiltonian. Such a change in the Hamiltonian often happens due to some time dependencies of the joint Hamiltonian. Then the second laws that incorporate such situations are given in the theorem below.

Theorem 13 (Second law for block-diagonal states)**.** *Under a catalytic semi-local thermal operation, a transformation* $(\rho_{S_{12}}, H_{S_{12}}) \longrightarrow \left(\sigma'_{S_{12}}, H'_{S_{12}}\right)$ *that leads to changes both in system states and the non-interacting system Hamiltonians is possible if, and only if,*

$$S_\alpha\left(\rho_{S_{12}}, \gamma_{S_1} \otimes \gamma_{S_2}\right) \geqslant S_\alpha\left(\sigma'_{S_{12}}, \gamma'_{S_1} \otimes \gamma'_{S_2}\right), \quad \forall \alpha \geqslant 0, \tag{A.73}$$

where $\gamma_{S_i} = \frac{e^{-\beta_i H_{S_i}}}{\mathrm{Tr}\left[e^{-\beta_i H_{S_i}}\right]}$ *and* $\gamma'_{S_i} = \frac{e^{-\beta_i H'_{S_i}}}{\mathrm{Tr}\left[e^{-\beta_i H'_{S_i}}\right]}$*, for* $i = 1, 2$*.*

Proof. Let us assume the total Hamiltonian of the universe is time-independent. Any change happening in the system Hamiltonian can then be understood due to the presence of a clock system X. The joint Hamiltonian of the system and clock system is given by

$$\sum_{t=t_i}^{t_f} H(t) \otimes |t\rangle\langle t|_X, \tag{A.74}$$

where $|t\rangle_X$ are some orthonormal basis. Then a change in Hamiltonian $H(t_i) \to H(t_f)$, along with a transformation in the system state $\rho \to \sigma$, is equivalent to the change in a joint clock-system state as

$$\rho(t_i) \otimes |t_i\rangle\langle t_i|_X \longrightarrow \sigma(t_f) \otimes |t_f\rangle\langle t_f|_X. \tag{A.75}$$

We exploit this argument to change the joint non-interacting Hamiltonian of the system, so that

$$H_{S_{12}} = H_{S_1} + H_{S_2} \longrightarrow H'_{S_{12}} = H'_{S_1} + H'_{S_2}. \tag{A.76}$$

We consider a bipartite clock system X_{12} that is responsible for the change in Hamiltonian of the system S_{12}. Since the transition does not depend on the intermediate times, we simply assume the initial state to be $|t_i\rangle_{X_{1/2}} = |0\rangle_{X_{1/2}}$ and the final state to be $|t_f\rangle_{X_{1/2}} = |1\rangle_{X_{1/2}}$. Therefore, the time-independent joint Hamiltonian of the system and the clock can be written as

$$\begin{aligned} H_{S_{12}X_{12}} = &\left(H_{S_1} \otimes |0\rangle\langle 0|_{X_1} + H'_{S_1} \otimes |1\rangle\langle 1|_{X_1}\right) \\ &+ \left(H_{S_2} \otimes |0\rangle\langle 0|_{X_2} + H'_{S_2} \otimes |1\rangle\langle 1|_{X_2}\right) = H_{S_1X_1} + H_{S_2X_2}. \end{aligned} \tag{A.77}$$

Here X_{12} plays the role of a switch and it controls the Hamiltonian on the system by choosing its state $|ij\rangle\langle ij|_{X_{12}} = |i\rangle\langle i|_{X_1} \otimes |j\rangle\langle j|_{X_2}$. For examples, when the switch X_{12} is in the state $|00\rangle\langle 00|_{X_{12}}$, it implements the Hamiltonian $H_{S_{12}}$ on the system S_{12}. On the other hand, when the switch is in the state $|11\rangle\langle 11|_{X_{12}}$, it switches the system Hamiltonian to $H'_{S_{12}}$. Now consider a catalytic semi-local thermal operation that leads to the transformation

$$\left(\rho_{S_{12}}, H_{S_{12}}\right) \longrightarrow \left(\sigma'_{S_{12}}, H'_{S_{12}}\right). \tag{A.78}$$

This is equivalent to the transformation between the joint system-switch states block-diagonal in energy, and with the fixed Hamiltonian $H_{S_{12}X_{12}}$,

$$\left(\rho_{S_{12}} \otimes |00\rangle\langle 00|_{X_{12}}, H_{S_{12}X_{12}}\right) \longrightarrow \left(\sigma'_{S_{12}} \otimes |11\rangle\langle 11|_{X_{12}}, H_{S_{12}X_{12}}\right) \tag{A.79}$$

under a catalytic semi-local thermal operation applied jointly on the system and the clock. Now following the Theorem 12, we cast the necessary and sufficient conditions for the transformation, as

$$\begin{aligned} &S_\alpha\left(\rho_{S_{12}} \otimes |00\rangle\langle 00|_{X_{12}}, \gamma_{S_1X_1} \otimes \gamma_{S_2X_2}\right) \\ &\quad \geqslant S_\alpha\left(\sigma'_{S_{12}} \otimes |11\rangle\langle 11|_{X_{12}}, \gamma_{S_1X_1} \otimes \gamma_{S_2X_2}\right), \quad \forall \alpha \geqslant 0, \end{aligned} \tag{A.80}$$

where $\gamma_{S_iX_i} = \frac{e^{-\beta_i H_{S_iX_i}}}{\mathrm{Tr}\left[e^{-\beta_i H_{S_iX_i}}\right]}$, for $i = 1, 2$, are the thermal states correspond to the Hamiltonians $H_{S_iX_i}$ and inverse temperatures β_i. Moreover, we notice that

$$\begin{aligned} &S_\alpha\left(\rho_{S_{12}} \otimes |00\rangle\langle 00|_{X_{12}}, \gamma_{S_1X_1} \otimes \gamma_{S_2X_2}\right) \\ &\quad - S_\alpha\left(\sigma'_{S_{12}} \otimes |11\rangle\langle 11|_{X_{12}}, \gamma_{S_1X_1} \otimes \gamma_{S_2X_2}\right) = S_\alpha\left(\rho_{S_{12}}, \gamma_{S_1} \otimes \gamma_{S_2}\right). \end{aligned} \tag{A.81}$$

As a result, the necessary and sufficient conditions for the transformation reduce to

$$S_\alpha\left(\rho_{S_{12}}, \gamma_{S_1} \otimes \gamma_{S_2}\right) \geqslant S_\alpha\left(\sigma'_{S_{12}}, \gamma'_{S_1} \otimes \gamma'_{S_2}\right), \quad \forall \alpha \geqslant 0. \tag{A.82}$$

□

A.7 Free-entropy distance, thermodynamic work and fundamentally irreversibility

In this section, we relate α-free-entropies, introduced in the previous section, with thermodynamic works. A formal connection and equivalence between work and purity have been established in [64, 198]. Here we briefly outline the approach presented in [198]. A thermalization or work extraction process leads an arbitrary system-bath state to a more mixed (or less pure) system-bath state for a given block with fixed total energy. These processes are nothing but randomization (noisy) processes and extensively studied in context purity resource theory [356]. However, there is a subtlety we encounter here, compared to purity resource theory. Nevertheless, one may claim that the thermodynamics is nothing but a purity resource theory constrained by the temperature of the bath and the Hamiltonian of the system [64, 198, 205].

Consider a bipartite system S_{12}, with initial non-interacting Hamiltonian $H_{S_{12}} = H_{S_1} + H_{S_2}$, in an initial state $\rho_{S_{12}}$. After a catalytic semi-local thermal operation, the state and the Hamiltonian for the system are changed to $\sigma'_{S_{12}}$ and $H'_{S_{12}} = H'_{S_1} + H'_{S_2}$ respectively, i.e.,

$$\left(\rho_{S_{12}}, H_{S_{12}}\right) \longrightarrow \left(\sigma'_{S_{12}}, H'_{S_{12}}\right). \tag{A.83}$$

For this transformation we may need a catalyst C_{12}, with the Hamiltonian $H_{C_{12}} = H_{C_1} + H_{C_2}$. However, for simplicity, we consider the catalyst as a part of the system.

Our aim is to exploit this transformation to extract free-entropy and thermodynamic work. For that, we also introduce a battery that stores or expends work. We may think that the bipartite battery $S_{W_{12}}$ is composed of sub-systems S_{W_1} and S_{W_2} with the Hamiltonian $H_{S_{W_{12}}} = H_{S_{W_1}} + H_{S_{W_2}}$, where the two-level Hamiltonians are $H_{S_{W_1}} = W_1|W_1\rangle\langle W_1|$ and $H_{S_{W_2}} = W_2|W_2\rangle\langle W_2|$. The battery sub-system S_{W_1} (S_{W_2}) is semi-locally interacting with the bath B_1 (B_2). Note, these two battery sub-systems can in principle exchange energy, i.e., work, as this operation is allowed by the catalytic semi-local thermal processes. When the battery sub-systems are thermalized to the temperatures of B_1 and B_2, the corresponding semi-Gibbs state becomes $\gamma_{S_{W_1}} \otimes \gamma_{S_{W_2}}$,

where

$$\gamma_{S_{W_i}} = \frac{1}{1+e^{-\beta_i W_i}} \left(|0\rangle\langle 0| + e^{-\beta_i W_i} |1\rangle\langle 1| \right), \tag{A.84}$$

with $i = 1, 2$, and β_i is the inverse temperature of the bath B_i. Now, let us consider the transformation of the system and the battery together

$$\begin{aligned} &\left(\rho_{S_{12}} \otimes |00\rangle\langle 00|_{S_{W_{12}}}, H_{S_{12}} + H_{S_{W_{12}}} \right) \to \\ &\quad \left(\sigma'_{S_{12}} \otimes |00\rangle\langle 00|_{S_{W_{12}}}, H'_{S_{12}} + H_{S_{W_{12}}} \right), \end{aligned} \tag{A.85}$$

where we denote $|W_1 W_2\rangle\langle W_1 W_2|_{S_{W_{12}}} = |W_1\rangle\langle W_1|_{S_{W_1}} \otimes |W_2\rangle\langle W_2|_{S_{W_2}}$. Then second laws, i.e., Theorem 13, ensure the conditions

$$\begin{aligned} &S_\alpha(\rho_{S_{12}} \otimes |00\rangle\langle 00|_{S_{W_{12}}},\ \gamma_{S_1} \otimes \gamma_{S_2} \otimes \gamma_{S_{W_1}} \otimes \gamma_{S_{W_2}}) \\ &\quad \geqslant S_\alpha(\sigma'_{S_{12}} \otimes |W_1 W_2\rangle\langle W_1 W_2|_{S_{W_{12}}},\ \gamma'_{S_1} \otimes \gamma'_{S_2} \otimes \gamma_{S_{W_1}} \otimes \gamma_{S_{W_2}}) \end{aligned} \tag{A.86}$$

to be satisfied for all $\alpha \geqslant 0$. Given the initial, the final and the thermal states of the battery, we can derive the bound on the α-free-entropy stored in the battery, as

$$S_\alpha(\rho_{S_{12}}, \gamma_{S_1} \otimes \gamma_{S_2}) - S_\alpha(\sigma'_{S_{12}}, \gamma'_{S_1} \otimes \gamma'_{S_2}) \geqslant \beta_1 W_1 + \beta_2 W_2, \tag{A.87}$$

where W_1 (W_2) is amount of work stored in the battery sub-system via the transformation in its state $|0\rangle\langle 0|_{W_1} \to |W_1\rangle\langle W_1|_{W_1}$ ($|0\rangle\langle 0|_{W_2} \to |W_2\rangle\langle W_2|_{W_2}$). Due to total energy and total-weighted energy conservation of the global process on the system-battery-baths composite, the battery $S_{W_{12}}$ can only increase its energy. This implies

$$W_1 + W_2 \geqslant 0. \tag{A.88}$$

However, note that the quantities W_1 and W_2 depend on the cSLTO that executes the transformation. Therefore, it is important to quantify the guaranteed amount of free-entropy or the works involved in a state transformation irrespective to the operations that execute it. This quantification is done in terms of the free-entropy distance, given below.

Theorem 14 (Free-entropy distance). *For a catalytic semi-local thermal operation, leading to a transition* $\left(\rho_{S_{12}}, H_{S_{12}}\right) \longrightarrow \left(\sigma'_{S_{12}}, H'_{S_{12}}\right)$*, the free-entropy distance between the initial and final block-diagonal states is given by*

$$\begin{aligned} S_d\left(\rho_{12} \to \sigma'_{12}\right) &= \inf_{\alpha \geqslant 0} \left[S_\alpha(\rho_{S_{12}}, \gamma_{S_1} \otimes \gamma_{S_2}) - S_\alpha(\sigma'_{S_{12}}, \gamma'_{S_1} \otimes \gamma'_{S_2}) \right] \\ &= \beta_1 W_1 + \beta_2 W_2 \geqslant 0. \end{aligned} \tag{A.89}$$

Note, the guaranteed extracted work is $W^{ext} = W_1 + W_2$. The Theorem 14 leads to several interesting results. Now in terms of the free-entropy distance, we can quantify these quantities, as in the following.

Corollary 15 (Extractable free-entropy and free-entropy cost). *For a transformation between the block-diagonal states,* $\left(\rho_{S_{12}}, H_{S_{12}}\right) \longrightarrow \left(\sigma'_{S_{12}}, H'_{S_{12}}\right)$*, under catalytic semi-local thermal operations, the extractable free-entropy* S_{ext}*, and the free-entropy cost* S_{cost} *for the reverse the process, are given by*

$$\begin{aligned} &S_{ext}\left(\rho_{12} \to \sigma'_{12}\right) \\ &= \inf_{\alpha \geqslant 0} \left[S_\alpha(\rho_{S_{12}}, \gamma_{S_1} \otimes \gamma_{S_2}) - S_\alpha(\sigma'_{S_{12}}, \gamma'_{S_1} \otimes \gamma'_{S_2}) \right] = S_d\left(\rho_{12} \to \sigma'_{12}\right), \\ &S_{cost}\left(\sigma'_{12} \to \rho_{12}\right) = -\sup_{\alpha \geqslant 0} \left[S_\alpha(\rho_{S_{12}}, \gamma_{S_1} \otimes \gamma_{S_2}) - S_\alpha(\sigma'_{S_{12}}, \gamma'_{S_1} \otimes \gamma'_{S_2}) \right]. \end{aligned} \tag{A.90}$$

It is clear that the free-entropy that we can extract from the process is in general lower than the free-entropy to be expended to reverse the process. To see this, let us consider the transformation (A.83) and assume $S_{ext}(\rho_{S_{12}} \to \sigma'_{S_{12}}) > 0$. Then,

$$S_{ext}(\rho_{S_{12}} \to \sigma'_{S_{12}}) \leqslant - S_{cost}(\sigma'_{S_{12}} \to \rho_{S_{12}}). \tag{A.91}$$

Therefore, thermodynamics in this regime is fundamentally irreversible, analogous to the cases with single bath [198]. With the help of free-entropy distance, we are also able to compute the distillable free-entropy and free-entropy of formation for a state.

In the situation where the $\sigma_{S_{12}} = \gamma_{S_1} \otimes \gamma_{S_2}$ and the system Hamiltonian does not change, the Corollary 15 leads us to quantify distillable free-entropy S_{dist} for the process $\rho_{S_{12}} \to \gamma_{S_1} \otimes \gamma_{S_2}$, and the free-entropy of formation S_{form} for the process $\gamma_{S_1} \otimes \gamma_{S_2} \to \rho_{S_{12}}$, as

$$\begin{aligned} S_{dist}(\rho_{S_{12}}) &= D_0\left(\rho_{S_{12}} \parallel \gamma_{S_1} \otimes \gamma_{S_2}\right) \\ &= -\log \mathrm{Tr}\left(\Pi_{\rho_{S_{12}}} \gamma_{S_1} \otimes \gamma_{S_2}\right), \end{aligned} \tag{A.92}$$

$$\begin{aligned} S_{form}(\rho_{S_{12}}) &= D_\infty\left(\rho_{S_{12}} \parallel \gamma_{S_1} \otimes \gamma_{S_2}\right) \\ &= \log \min\left\{\lambda : \rho_{S_{12}} \leqslant \lambda(\gamma_{S_1} \otimes \gamma_{S_2})\right\}. \end{aligned} \tag{A.93}$$

A.8 Superposition and free-entropy locking

The cSLTOs are time translation symmetric with respect to the system Hamiltonian $H_{S_{12}}$. Consider a quantum state $\rho_{S_{12}}$ that has superposition in the eigenbases of $H_{S_{12}}^{\beta_1\beta_2}$. Then the state can be expressed as

$$\rho_{S_{12}} = \rho^d_{S_{12}} + \rho^o_{S_{12}}, \tag{A.94}$$

where $\rho^d_{S_{12}}$ is the block-diagonal part of the state and $\rho^o_{S_{12}}$ is the off-diagonal part of the state when it is expressed in the energy eigenbases of the system. The off-diagonal part $\rho^o_{S_{12}}$ evolve independently of the block-diagonal part $\rho^d_{S_{12}}$ under cSLTOs, and the cSLTOs can only access the block-diagonal elements for free-entropy extraction. That is why the only accessible free-entropy in the one-shot finite-size regime is the one corresponding to the dephased state of the original one.

Therefore, there is a free-entropy locking in the presence of such superposition as the free-entropy stored in the superposition cannot be accessed. Note, in presence of quantum correlation, e.g., entanglement, such superposition is inevitably present in the state, and there would be free-entropy locking. However, in the asymptotic regime, where the number of particles in the system becomes considerably large, this free-entropy can be unlocked and fully accessed via cSLTOs (see below). As a result, one can fully extract free-entropy from the quantum correlations present in the system in the asymptotic regime.

A.9 Second laws for the non-block-diagonal states

We have already mentioned that the second laws derived in the Theorem 13 provide the necessary and sufficient conditions for the transformation between states that are block-diagonal in the eigenbases of the Hamiltonian $H_{S_{12}}$. For the states that are not block-diagonal, the second laws become only the necessary conditions. These necessary conditions can be further supplemented by a monotonic measure of the time-translation asymmetry. For a quantum state $\rho_{S_{12}}$ with the Hamiltonian $H_{S_{12}}$, the asymmetry is quantified as

$$A_\alpha(\rho_{S_{12}}, H_{S_{12}}) = D_\alpha^q\left(\rho_{S_{12}} \parallel P_{S_{12}}(\rho_{S_{12}})\right) \tag{A.95}$$

where the $P_{S_{12}}(\rho_{S_{12}})$ is the dephased state in the energy eignebases, given in Eq. (A.26), and the quantum Rényi α-relative entropy is defined as

$$D_\alpha^q(\rho \parallel \sigma) = \begin{cases} \frac{1}{\alpha-1}\log \mathrm{Tr}\left(\rho^\alpha \sigma^{1-\alpha}\right), & \alpha \in [0,\ 1) \\ \frac{1}{\alpha-1}\log \mathrm{Tr}\left(\left[\sigma^{\frac{1-\alpha}{2\alpha}}\ \rho\ \sigma^{\frac{1-\alpha}{2\alpha}}\right]^\alpha\right), & \alpha > 0. \end{cases} \tag{A.96}$$

Note, in the limit $\alpha \to 1$, the quantum α-relative entropy converges to the well known von Neumann relative entropy $D_1^q(\rho \parallel \sigma) = \mathrm{Tr}\left(\rho \log \rho - \rho \log \sigma\right)$.

Similar to the state transformation in the presence of a single bath [208, 210], we also supplement the necessary condition for state transformation in presence of two baths via cSLTOs, in addition to the second laws for the diagonal states. Consider a transformation $(\rho_{S_{12}}, H_{S_{12}}) \to (\sigma'_{S_{12}}, H'_{S_{12}})$ via a cSLTO, where the states may have superposition in the energy eigenbases. Then, the necessary conditions for the transformation are

$$A_\alpha(\rho_{S_{12}}, H_{S_{12}}) \geqslant A_\alpha(\sigma'_{S_{12}}, H'_{S_{12}}),\ \ \forall \alpha \geqslant 0, \tag{A.97}$$

where the amount quantum asymmetry monotonically decreases under cSLTOs.

A.10 Asymptotic equipartition

The framework developed for quantum heat engines working in the one-shot finite-size regime can reproduce the know results of

thermodynamics for the engines operating in the asymptotic regime. It is well known that all the Rényi α-relative entropies converge to von Neuman relative entropy in the asymptotic regime (or i.i.d. regime), that is

$$\lim_{N\to\infty}\frac{1}{N}D_\alpha(\rho^{\otimes N}\parallel\sigma^{\otimes N})=D_1(\rho\parallel\sigma)=\mathrm{Tr}\,(\rho\log\rho-\rho\log\sigma),$$

for all α. For that reason, the α-free-entropies reduce to the Helmholtz free-entropy for all α, as

$$\lim_{N\to\infty}\frac{1}{N}S_\alpha\left(\rho_{S_{12}}^{\otimes N},\,(\gamma_{S_1}\otimes\gamma_{S_2})^{\otimes N}\right)=S_1(\rho_{S_{12}},\,\gamma_{S_1}\otimes\gamma_{S_2}).\tag{A.98}$$

Therefore, in the asymptotic regime, there is only one free-entropy and that is the Helmholtz free-entropy. Consider a transformation in the asymptotic regime via a cSLTO, where the individual system transformations as

$$(\rho_{S_{12}},H_{S_{12}})\to(\sigma'_{S_{12}},H'_{S_{12}}).\tag{A.99}$$

The many second laws in the one-shot finite-size regime converge to a single second law providing necessary and sufficient condition for the engine transformation in the asymptotic regime, that is

$$S_1(\rho_{S_{12}},\,\gamma_{S_1}\otimes\gamma_{S_2})\geqslant S_1(\sigma'_{S_{12}},\,\gamma'_{S_1}\otimes\gamma'_{S_2}).\tag{A.100}$$

The amount of extractable free-entropy or the free-entropy distance per copy of the system, given the initial and the final states, is

$$\begin{aligned}S_d(\rho_{S_{12}}\to\sigma'_{S_{12}})&=S_1(\rho_{S_{12}},\,\gamma_{S_1}\otimes\gamma_{S_2})-S_1(\sigma'_{S_{12}},\,\gamma'_{S_1}\otimes\gamma'_{S_2})\\&=\Delta S-\beta_1\Delta E_{S_1}-\beta_2\Delta E_{S_2},\end{aligned}\tag{A.101}$$

where $\Delta S=S(\rho_{S_{12}})-S(\sigma'_{S_{12}})$ the change in the von Neumann entropy. $\Delta E_{S_1}=\mathrm{Tr}\,\rho_{S_{12}}H_{S_1}-\mathrm{Tr}\,\sigma'_{S_{12}}H'_{S_1}$ is the change in average energy of the subsystem S_1, and similarly, the ΔE_{S_2} is for S_2. Note, for the reverse transformation $(\sigma'_{S_{12}},H'_{S_{12}})\to(\rho_{S_{12}},H_{S_{12}})$, the free-entropy cost per copy of the system is exactly equal to the extractable free-entropy in the forward process, i.e.,

$$S_d(\rho_{S_{12}}\to\sigma'_{S_{12}})=S_d(\rho_{S_{12}}\leftarrow\sigma'_{S_{12}}),\tag{A.102}$$

As a consequence, the thermodynamic reversibility is recovered in the asymptotic regime.

We recall that there is a free-entropy locking in the one-shot finite-size regime for the quantum states that have quantum superposition in the energy eigenbases, i.e., for $[\rho_{S_{12}}, H_{S_{12}}] \neq 0$. However, in the asymptotic limit, where the number of systems $N \to \infty$, all states become symmetric with respect to the Hamiltonian on average, and this is because of the fact that

$$\lim_{N\to\infty} \frac{1}{N} \left[\rho_{S_{12}}^{\otimes N}, \sum_{x=0}^{N-1} \mathbb{I}^{\otimes x} \otimes H_{S_{12}} \otimes \mathbb{I}^{\otimes(N-x-1)} \right] = 0, \ \ \forall\, \rho_{S_{12}}.$$

So, an arbitrary state can be written in the block-diagonal form on average in the asymptotic regime. It means that a state which is non-block-diagonal in single-copy level becomes block-diagonal (on average) in the energy eigenbases in the asymptotic regime. Consequently, the locked free-entropy due to the presence of quantum superpositions and correlations in a state can be accessed and extracted.

Let us now turn to the heat engines and show how the framework presented above reproduces the traditional thermodynamics and its laws. One may recover the statements of the second law in terms of heat, where the heat Q is defined as $Q = \Delta E - W$. Here ΔE is the change in the internal energy in the system and W is the work done by the system. Consider an engine transformation where bipartite system S_{12} is semi-locally interacting with the baths B_1 and B_2 via semi-local thermal operation. The global operation respect strict conservation of total weighted-energy, i.e., $\beta_1 \Delta E_1 + \beta_2 \Delta E_2 = 0$, where ΔE_1 and ΔE_2 is the change in energies of the B_1S_1 and B_2S_2 composites respectively. Then, the total weighted-energy conservation and Eq. (A.89) together lead to

$$\beta_1 Q_1 + \beta_2 Q_2 \leqslant 0, \tag{A.103}$$

where $Q_{1/2} = \Delta E_{1/2} - W_{1/2}$. The expression above is the Clausius inequality and mathematically captures all the statements of the second law in terms of heat. For instance, in the asymptotic regime where the above definition of heat is applicable, we recover the traditional form of Carnot efficiency as $\eta = \frac{W_\infty}{Q_1} \leqslant \frac{Q_1+Q_2}{Q_1} \leqslant 1 - \frac{\beta_1}{\beta_2}$, where the

extracted work is given by $W_\infty \leqslant Q_1 + Q_2$ and equality only holds for the reversible engine operations.

In the asymptotic regime, the role of correlations in driving "anomalous" heat flow from a cold to a hot bath can also be understood. For example, consider the situation where engine operation leads to a transformation $(\rho_{S_{12}}, H_{S_{12}}) \rightarrow (\rho_{S_1} \otimes \rho_{S_2}, H_{S_{12}})$ which exploits the correlation between the subsystems S_1 and S_2. Here $\rho_{S_1} = \mathrm{Tr}_{S_2}\rho_{S_{12}}$ and $\rho_{S_2} = \mathrm{Tr}_{S_1}\rho_{S_{12}}$. As per the second law in the asymptotic regime, the transformation takes place spontaneously if and only if the free-entropy satisfy $S_1(\rho_{S_{12}}, \gamma_{S_1} \otimes \gamma_{S_2}) \geqslant S_1(\rho_{S_1} \otimes \rho_{S_2}, \gamma_{S_1} \otimes \gamma_{S_2})$. The extractable free entropy from this process is

$$\mathcal{I}(S_1 : S_2) \geqslant \beta_1 W_1 + \beta_2 W_2 \geqslant 0. \tag{A.104}$$

where $\mathcal{I}(S_1 : S_2) = S(\rho_{S_1}) + S(\rho_{S_2}) - S(\rho_{S_{12}})$ is the mutual information quantifying the correlation present in the system S_{12}. The $W^{ext} = W_1 + W_2 \geqslant 0$ is the extractable work. This stored work in correlation is responsible for the spontaneous "anomalous" heat flow from the cold to the hot bath, which is nothing but a process that happens in the case of refrigeration.

A.11 Reversible Engine Operation in a One-step Cycle

Here we reconsider the reversible engine operation, given in the main text (see Eq. (2.21)), that yields maximum power with Carnot efficiency. We have assumed a bipartite working system S_{12} with the Hamiltonian $H_{S_{12}} = H_{S_1} + H_{S_2}$ where $H_{S_1} = a|1\rangle\langle 1|_{S_1}$ and $H_{S_2} = a|1\rangle\langle 1|_{S_2}$. We have also assumed a bipartite battery $S_{W_{12}}$ with the Hamiltonian $H_{S_{W_{12}}} = H_{S_{W_1}} + H_{S_{W_2}}$, where $H_{S_{W_1}} = E_{W_1}|1\rangle\langle 1|_{S_{W_1}}$ and $H_{S_{W_2}} = E_{W_2}|1\rangle\langle 1|_{S_{W_2}}$. The one-step cycle is executed by implementing a global unitary (U) operation on the baths-system-battery composite leading to the transformation

$$\gamma_{B_1} \otimes \gamma_{B_2} \otimes \rho_{S_{12}} \otimes \rho^i_{S_{W_{12}}} \rightarrow \sigma_{B_1B_2} \otimes \sigma_{S_{12}} \otimes \rho^f_{S_{W_{12}}}, \tag{A.105}$$

where $\rho_{S_{12}} = |0\rangle\langle 0|_{S_1} \otimes |1\rangle\langle 1|_{S_2}$ and $\sigma_{S_{12}} = |1\rangle\langle 1|_{S_1} \otimes |0\rangle\langle 0|_{S_2}$ are the initial and final states of the working system S_{12}, and $\rho^i_{S_{W_{12}}} =$

$|0\rangle\langle 0|_{S_{W_1}} \otimes |0\rangle\langle 0|_{S_{W_2}}$ and $\rho^f_{S_{W_{12}}} = |1\rangle\langle 1|_{S_{W_1}} \otimes |1\rangle\langle 1|_{S_{W_2}}$ are the initial and final states of the battery $S_{W_{12}}$. Recall, the global unitary U respects strict conservation of total energy and total weighted-energy. Therefore, we can study the transformation in each total energy block separately. Consider a block of total energy $E_1 + E_2$, where $E_1 = E_{S_1} + E_{B_1}$ is the sum of energies belonging to S_1 and B_1, and similarly for $E_2 = E_{S_2} + E_{B_2}$. In this total energy block, the transformation becomes

$$[\gamma_{B_1} \otimes \gamma_{B_2} \otimes \rho_{S_{12}}]_{E_1+E_2} \otimes \rho^i_{S_{W_{12}}} \to [\sigma_{B_1B_2} \otimes \sigma_{S_{12}}]_{E'_1+E'_2} \otimes \rho^f_{S_{W_{12}}}, \tag{A.106}$$

where $E'_1 = E'_{S_1} + E'_{B_1}$ and $E'_2 = E'_{S_2} + E'_{B_2}$. The strict conservation of the total weighted-energy and the total energy ensure that

$$\beta_1 E_1 + \beta_2 E_2 = \beta_1(E'_1 + E_{W_1}) + \beta_2(E'_2 + E_{W_2}), \tag{A.107}$$

$$E_1 + E_2 = E'_1 + E'_2 + E_{W_1} + E_{W_2}, \tag{A.108}$$

where $E_1 = E_{B_1}$, $E_2 = E_{B_2} + a$, $E'_1 = E'_{B_1} + a$, and $E'_2 = E'_{B_2}$. Here we have assumed $\beta_1 < \beta_2$.

Note, similar transformations will follow in the other total weighted-energy blocks with identical initial and final battery states. The reduced transformation on the system S_{12}, $\rho_{S_{12}} \to \sigma_{S_{12}}$ is reversible because all α-free-entropies for pure system and battery states considered here are α independent [261]. As a consequence, free-entropy distances satisfy $S_d(\rho_{S_{12}} \to \sigma_{S_{12}}) = S_d(\rho_{S_{12}} \leftarrow \sigma_{S_{12}})$, where

$$S_d(\rho_{S_{12}} \to \sigma_{S_{12}}) = \beta_2 a - \beta_1 a = \beta_1 E_{W_1} + \beta_2 E_{W_2} > 0. \tag{A.109}$$

This relation guarantees that there is strict conservation of weighted-energy of the working system and the battery together. Therefore, conservation of total weighted-energy (A.107) is reduced down to the strict conservation of the weighted-energy of the baths only, i.e.

$$\beta_1(E_{B_1} - E'_{B_1}) + \beta_2(E_{B_2} - E'_{B_2}) = \beta_1 Q_1 + \beta_2 Q_2 = 0, \tag{A.110}$$

where we have identified the heat as the change in energy of the bath B_1 given by $Q_1 = E_{B_1} - E'_{B_1}$ and similarly $Q_2 = E_{B_2} - E'_{B_2}$ for bath B_2. This is true for all energy blocks. The Eq. (A.110) represents the *Clausius equality* for the cyclic process. The other total energy blocks

will result in identical Clausius equality. The net extracted work in each (one-step) engine cycle is given by

$$W_{ext} = E_{W_1} + E_{W_2} = Q_1 + Q_2 > 0, \tag{A.111}$$

Here we have used the strict total energy conservation (A.108). It is clear from Eqs. (A.110) and (A.111) that the heat-to-work conversion is $\eta_C = \frac{W_{ext}}{Q_1} = 1 - \frac{\beta_1}{\beta_2}$, which is exactly the Carnot efficiency. Nevertheless for reversible engine transformation, the global unitary evolution strictly ensures total energy conservation of $B_1B_2S_{12}S_{W_{12}}$ and weighted-energy conservation of B_1B_2, and that are mathematically expressed by the commutation relations $[U,\ H_{B_1} + H_{B_2} + H_S] = 0$ and $[U,\ \beta_1 H_{B_1} + \beta_2 H_{B_2}] = 0$ respectively, where $H_S = H_{S_1} + H_{S_2} + H_{S_{W_1}} + H_{S_{W_2}}$ is the Hamiltonian of the system $S = S_{12}S_{W_{12}}$.

A.12 Conservation of weighted-energy implies conservation of entropy

To understand the relationship between the conservation of entropy and the conservation of weighted-energy, we analyze the engine process in terms of the transformations happening in micro-canonical ensembles. The baths are assumed to be considerably large compared to the systems and the batteries. Since the global unitary implementation of the SLTOs strictly satisfy total energy conservation, we may concentrate on the transformation happening in each total energy block separately. For instance, consider the transformation (A.106). This respects the total energy conservation, as given in Eq. (A.108). Again, the overall process occurs unitarily in isolation, so total entropy must be strictly conserved. The batteries only absorb or release work, and, by definition, they cannot exchange entropy with the rest of the system. Thus the entropy of system-bath composite ($B_1S_1S_2B_2$) must have to be conserved. Given the initial total energy $E_1 + E_2$, the strict entropy conservation implies the conservation of degeneracy, i.e.,

$$\begin{aligned} g_B(E_1 + E_2) &= g_B(E_1' + E_2') \\ &= g_B(E_1 + E_2) e^{\beta_1(E_1' - E_1) + \beta_1(E_2' - E_2)}. \end{aligned} \tag{A.112}$$

Thus, the following must have to be satisfied $\beta_1(E_1' - E_1) + \beta_1(E_2' - E_2) = 0$. Here, $E_1 = E_{B_1} + E_{S_1}$ and $E_2 = E_{B_2} + E_{S_2}$, and similarly for E_1' and E_2'. Thus, the above condition is reduced to

$$\beta_1 \left(\Delta E_{B_1} + \Delta E_{S_1}\right) + \beta_2 \left(\Delta E_{B_2} + \Delta E_{S_2}\right) = 0, \tag{A.113}$$

where $\Delta E_x = E_x' - E_x$ is the change in energy for the given total energy block. This is nothing but the condition for strict weighted-energy conservation, as ensured by the commutation relation (A.10).

A.13 Intensity-dependent Hamiltonian (2.32)

This section aims to show how the interaction Hamiltonian (2.32) can be realized with designed cavities or ion traps. We will focus here on the case of one cavity interacting with a two-level atom. Generalization to three-level systems and two different cavities coupled to the two different transitions is straightforward.

So, the starting point is a cavity (or trap) with a slight anharmonicity. That is described by the Hamiltonian of a harmonic oscillator, with frequency ω and a small controllable anharmonicity $V\left(x/x_0\right)$,

$$H_{\text{cav}} = \frac{p^2}{2m} + \frac{m\omega^2 x^2}{2} + V\left(x/x_0\right) = \hbar\omega\, a^\dagger a + V\left(\frac{a^\dagger + a}{\sqrt{2}}\right). \tag{A.114}$$

where $x_0 = \sqrt{\frac{\hbar}{m\omega}}$. Assuming that ω is much larger than any other relevant frequency, it makes sense to go to the interaction picture with respect to the harmonic part of the Hamiltonian, and apply rotating wave approximation, i.e., neglect all rapidly oscillating terms and leave only diagonal terms in the Fock basis. The end result is

$$H_{\text{cav,I}} = f(N), \tag{A.115}$$

where $N = a^\dagger a$ and $f(n) = \langle n|V(x)|n\rangle$ with $N|n\rangle = n|n\rangle$.

Similarly, we assume that atom-cavity coupling originally has a general form

$$H_{\text{c}} = \hbar g b(x/x_0)(\sigma^\dagger + \sigma), \tag{A.116}$$

where $b(x/x_0)$ is the cavity mode function, which we take to be odd, i.e. $b(-y) = -b(y)$. Assuming that the atom is close to the bare

cavity resonance and, performing the same steps as before, we end up with the interaction Hamiltonian

$$H_{c,I} = \hbar g(\theta(N)\sigma^{\dagger}a + h.c.), \tag{A.117}$$

where $\langle n-1|b(x/x_0)|n\rangle = \theta(n-1)\sqrt{n}$.

The intensity-dependent functions $f(N)$ and $\theta(N)$ are related to the original functions $V(x/x_0)$ and $b(x/x_0)$. For general $f(N)$ and $\theta(N)$, one needs to design the original functions. This can be done using Monte Carlo (MC) optimization procedures. To this aim one defines a cost function

$$C[V,b] = ||f_{\text{act}}(\cdot) - f_{\text{tar}}(\cdot)|| + ||\theta_{\text{act}}(\cdot) - \theta_{\text{tar}}(\cdot)||, \tag{A.118}$$

where $f, \theta_{\text{act,tar}}$ are the actual and target forms of the functions $f(\cdot)$ and $\theta(\cdot)$, and $||\cdot||$ denotes any norm in the space of the functions f, θ. Judging from Eq. (2.33) it can be L^2-norm for $f(\cdot)$ and L^q-norm with $q > 2$ for $\theta(\cdot)$. Now the MC procedure runs as follows: i) we choose actual form of $V_{\text{act}}(\cdot)$ and $b_{\text{act}}(\cdot)$; ii) we calculate $f_{\text{act}}(\cdot)$, $\theta_{\text{act}}(\cdot)$ and $C[V_{\text{act}}, b_{\text{act}}]$; iii) we modify slightly $V_{\text{act}}(\cdot)$ and b_{act} and calculate the new value of $C[V_{\text{act}}, b_{\text{act}}]$; iv) we accept the modification, if the new value of the error function is smaller than the previous one; v) we go to iii) and repeat this steps until convergence is achieved. MC optimization maybe modifies to allow small errors, if we treat the cost functions like energy and minimize the corresponding free energy at some arbitrary auxiliary temperature $\mathcal{T}$.

The question of the convergence of the MC procedure, as well as the sensitivity and the role of errors in the realization of our quantum engine is very interesting but clearly goes beyond the scope of present work. We will study it in a future publication.

A.14 Effective Hamiltonian of the quantum optics based quantum heat engine

We start by considering that our system S is described by the Hamiltonian of a Λ-system and that each of the two transitions is coupled to a different bosonic mode. The Hamiltonian is divided into two parts $H = H_0 + H_1$, with

$$H_0 = \omega_1 N_1 + \omega_2 N_2 + E_1|1\rangle\langle 1|_S + E_2|2\rangle\langle 2|_S + E_3|3\rangle\langle 3|_S, \tag{A.119}$$

$$H_1 = f_1(N_1) + f_2(N_2) + g_1\theta_1(N_1)(\hat{a}_1\sigma_{31} + \text{h.c.}) + g_2\theta_2(N_2)(\hat{a}_2\sigma_{32} + \text{h.c.}). \tag{A.120}$$

Here $\sigma_{ij} = |i\rangle\langle j|_S$ is the transition operator, and $N_k = a_k^\dagger a_k$ the number operator corresponding to the bath B_k. The system and bath energies are given by E_i and ω_k ($\hbar = 1$). The terms $f_k(N_k)$ represent intensity-dependent energy shifts of the baths, whereas $g_k(N_k)$ also takes into account the intensity-dependence of the dipole interaction between the system and the baths. We now set $E_1 = 0$ and move to the interaction picture with respect to $H_0' = \omega_1 N_1 + \omega_2 N_2 + E_2|2\rangle\langle 2|_S + \omega_1|3\rangle\langle 3|_S$, imposing the resonant condition $\omega_1 = \omega_2 + E_2$. This gives the interaction picture Hamiltonian

$$H_I = \Delta|3\rangle\langle 3| + f_1(N_1) + f_2(N_2) + g_1\theta_1(N_1)(\hat{a}_1\sigma_{31} + \text{h.c.}) + g_2\theta_2(N_2)(\hat{a}_2\sigma_{32} + \text{h.c.}), \tag{A.121}$$

with $\Delta = E_3 - \omega_1$. We express our quantum state in the interaction picture as:

$$|\Psi\rangle = |\tilde{\alpha}\rangle_B|1\rangle_S + |\tilde{\beta}\rangle_B|2\rangle_S + |\tilde{\gamma}\rangle_B|3\rangle_S, \tag{A.122}$$

where $|\tilde{\alpha}\rangle_B$, $|\tilde{\beta}\rangle_B$, and $|\tilde{\gamma}\rangle_B$ are unnormalized states of the B_1B_2 composite. This leads to the following form of the Schrödinger equation in components

$$i\frac{\mathrm{d}}{\mathrm{dt}}|\tilde{\alpha}\rangle_B = \left[f_1(N_1) + f_2(N_2)\right]|\tilde{\alpha}\rangle_B + g_1\theta_1(N_1)\hat{a}_1^\dagger|\tilde{\gamma}\rangle_B, \tag{A.123}$$

$$i\frac{\mathrm{d}}{\mathrm{dt}}|\tilde{\beta}\rangle_B = \left[f_1(N_1) + f_2(N_2)\right]|\tilde{\beta}\rangle_B + g_2\theta_2(N_2)\hat{a}_2^\dagger|\tilde{\gamma}\rangle_B, \tag{A.124}$$

$$i\frac{\mathrm{d}}{\mathrm{dt}}|\tilde{\gamma}\rangle_B = \left[f_1(N_1) + f_2(N_2) + \Delta\right]|\tilde{\gamma}\rangle_B + g_2\theta_2(N_2)\hat{a}_2|\tilde{\beta}\rangle_B + g_1\theta_1(N_1)\hat{a}_1|\tilde{\alpha}\rangle_B. \tag{A.125}$$

Now we consider a large detuning , i.e., $\left\|\frac{\mathrm{d}}{\mathrm{dt}}|\tilde{\gamma}\rangle_B\right\| \simeq 0$, and $\Delta \gg \langle f_1(N_1) + f_2(N_2)\rangle$, which allows us to express

$$|\tilde{\gamma}\rangle \simeq -\frac{1}{\Delta}\left(g_1\theta_1(N_1)\hat{a}_1|\tilde{\alpha}\rangle_B + g_2\theta_2(N_2)\hat{a}_2|\tilde{\beta}\rangle_B\right). \tag{A.126}$$

Introducing this result in the previous equations leads to

$$i\frac{\mathrm{d}}{\mathrm{dt}}|\tilde{\alpha}\rangle_B = \left[f_1(N_1) + f_2(N_2) - \frac{g_1^2}{\Delta}\theta_1^2(N_1)\right]|\tilde{\alpha}\rangle_B - \frac{g_1 g_2}{\Delta}\theta_1(N_1)\hat{a}_1^\dagger\hat{a}_2\theta_2(N_2)|\tilde{\beta}\rangle_B, \tag{A.127}$$

$$i\frac{\mathrm{d}}{\mathrm{dt}}|\tilde{\beta}\rangle_B = \left[f_1(N_1) + f_2(N_2) - \frac{g_2^2}{\Delta}\theta_2^2(N_2)\right]|\tilde{\beta}\rangle_B - \frac{g_1 g_2}{\Delta}\theta_2(N_2)\hat{a}_2^\dagger\hat{a}_1\theta_1(N_1)|\tilde{\alpha}\rangle_B. \tag{A.128}$$

The latter are the same equations of motion generated by an effective interacting Hamiltonian given by

$$H'_{\mathrm{eff}} = f_1(N_1) + f_2(N_2) - \frac{g_1^2}{\Delta}\theta_1^2(N_1) - \frac{g_2^2}{\Delta}\theta_2^2(N_2) - \frac{g_1 g_2}{\Delta}(\theta_1(N_1)\hat{a}_1^\dagger\hat{a}_2\theta_2(N_2)\sigma_{21} + \mathrm{h.c.}). \tag{A.129}$$

For suitable functions that satisfy

$$f_k(N_k) = \frac{g_k^2}{\Delta}\theta_k^2(N_k), \tag{A.130}$$

we obtain the final effective Hamiltonian

$$H_{\mathrm{eff}} = -\frac{g_1 g_2}{\Delta}\theta_1(N_1)\hat{a}_1^\dagger\hat{a}_2\theta_2(N_2)\sigma_{21} + \mathrm{h.c.}. \tag{A.131}$$

Appendix B

Appendix: Synthetic negative temperature

Below, we consider steady-state thermodynamics, where the working system is weakly interacting with two baths and driven by a time-dependent Hamiltonian. In particular, when the time-dependent Hamiltonian has simple periodic time dependence, there exists a rotating frame in which the overall dynamics become time-independent. In that case, thermodynamic quantities like heat, work, entropy, etc. can be consistently defined.

B.1 Rotating frame and steady-state thermodynamics

Let us consider the setup discussed in Section 3.3 of the main text. The Hamiltonian of the working systems are

$$
\begin{aligned}
&H_L = (E_H - E_C)|2\rangle\langle 2| + E_H|3\rangle\langle 3|, \\
&H_W = E_W|2\rangle\langle 2|, \\
&H_{in}^E(t) = \delta\left(|11\rangle\langle 22|\ e^{i\omega t} + |22\rangle\langle 11|\, e^{-i\omega t}\right), \\
&H_T^E(t) = H_L + H_W + H_{in}^E(t),
\end{aligned}
$$

where $E_W = E_H - E_C$. The Hamiltonian H_L corresponds to a qutrit L. It weakly interacts with a hot (H) and a cold (C) bath at inverse temperatures β_H and β_C (as described in Section 3.3 of the main text) to synthesize a bath with negative inverse temperature β_{LS}. The qubit

W, with Hamiltonian H_W, weakly interacts with a bath with positive inverse temperature β_W. The L and W interact between them with a time-dependent interaction Hamiltonian given by $H_{in}^E(t)$. After having all these interactions, the overall dynamics of the composite LW is

$$\frac{\partial \rho_{LW}(t)}{\partial t} = i[\rho_{LW}(t), H_T^E(t)] + \mathcal{L}_L(\rho_{LW}(t)) + \mathcal{L}_W(\rho_{LW}(t)), \tag{B.1}$$

for a state ρ_{LW}, where $\mathcal{L}_L(\cdot) = \mathcal{L}_{LH}(\cdot) + \mathcal{L}_{LC}(\cdot)$ is the Lindbld super-operator (LOS) representing the dissipative dynamics due to baths H and C, and $\mathcal{L}_W(\cdot)$ is the LOS for the bath with inverse temperature β_W. For this dynamics, the heat flux and power are defined as [270, 273]

$$\dot{Q} = \mathrm{Tr}\left[\frac{\partial \rho_{LW}(t)}{\partial t}\, H_T^E(t)\right], \tag{B.2}$$

$$P = \mathrm{Tr}\left[\rho_{LW}\, \frac{\partial H_T^E(t)}{\partial t}\right]. \tag{B.3}$$

Note the heat flux $\dot{Q}$ and the power P may have time dependence.

For time-dependent Hamiltonians, the dynamics generally never leads to a steady state. However, for a periodic time-dependence, as in $H_{in}^E(t)$, there is a rotating frame in which the Hamiltonian can be made time-independent. For that, a counter-rotation is applied on the laboratory frame by $U = e^{iH_R t}$ with $[H_R, H_0]$, where $H_0 = H_L + H_W$. In the rotating frame, an operator A in the laboratory frame transforms as $A \to (A)_R = UAU^\dagger$. Further, there exists a Hamiltonian H_R for which the interaction Hamiltonian reduces to a time-independent one, given by $V_{in} = UH_{in}^E(t)U^\dagger$. Accordingly, the overall Hamiltonian becomes time-independent, and it is $\bar{H}_T^E = H_0 - H_R + V_{in}$. In this rotating frame, the overall dynamics is recast as

$$\frac{\partial \rho_{LW}^R(t)}{\partial t} = \mathcal{L}_U(\rho_{LW}^R) + \mathcal{L}_L(\rho_{LW}^R) + \mathcal{L}_W(\rho_{LW}^R), \tag{B.4}$$

for a state ρ_{LW}, with $\rho_{LW}^R = U\rho_{LW}U^\dagger$. Here we denote $\mathcal{L}_U(\rho_{LW}^R) = i[\rho_{LW}^R, \bar{H}_T^E]$ which is the unitary controbution to the dynamics. This dynamics can lead to a steady state, say σ_{LW}^R. It can be easily checked that the LOSs remain unchanged in this rotating frame. Given that

$\mathrm{Tr}[AB] = \mathrm{Tr}[(A)_R(B)_R]$ for two arbitrary operators A and B, we may re-express the heat flux and power as [270]

$$\dot{Q} = \mathrm{Tr}\left[\left(\frac{\partial \rho_{LW}(t)}{\partial t}\right)_R \left(H_T^E(t)\right)_R\right] = \mathrm{Tr}\left[\mathcal{L}(\rho_{LW}^R)\, H_0\right], \tag{B.5}$$

where $\mathcal{L}(\rho_{LW}^R) = \mathcal{L}_L(\rho_{LW}^R) + \mathcal{L}_W(\rho_{LW}^R)$, and the power as

$$P = \mathrm{Tr}\left[(\rho_{LW})_R \left(\frac{\partial H_T^E(t)}{\partial t}\right)_R\right] = -i\,\mathrm{Tr}\left[\rho_{LW}^R\, [H_0, V_{in}]\right], \tag{B.6}$$

where $[A, B] = AB - BA$. The heat flux $\dot{Q}$ can be divided into two parts. One contribution comes from interaction of L with baths H and C, i.e., $\dot{Q}_L = \mathrm{Tr}\left[\mathcal{L}_L(\rho_{LW}^R)\, H_0\right]$ and the other due to interaction between W with its bath, i.e., $\dot{Q}_W = \mathrm{Tr}\left[\mathcal{L}_W(\rho_{LW}^R)\, H_0\right]$.

Now we study the entropy flux through LW. Note the rate of change in von Neumann entropy is given by

$$\begin{aligned}\dot{S} &= -\mathrm{Tr}\left[\frac{\partial \rho_{LW}(t)}{\partial t}\log \rho_{LW}(t)\right] \\ &= -\mathrm{Tr}\left[\left(\frac{\partial \rho_{LW}(t)}{\partial t}\right)_R \log\left(\rho_{LW}(t)\right)_R\right].\end{aligned}$$

In the rotating frame and at steady-state, it reduces to

$$\dot{S} = -\mathrm{Tr}\left[\frac{\partial \sigma_{LW}^R}{\partial t}\log \sigma_{LW}^R\right] = 0.$$

The rate of change in entropy vanishes because the state does not change over time. Nevertheless, there still can be a non-vanishing flux of entropy passing through L and W. Given that unitary dynamics does not contribute to the entropy flux,
i.e., $-\mathrm{Tr}[\mathcal{L}_U(\rho_{LW}^R)\log \sigma_{LW}^R] = 0$, we can calculate the entropy flux through L and W respectively as

$$\dot{S}_L = -\mathrm{Tr}[\mathcal{L}_L(\rho_{LW}^R)\log \sigma_{LW}^R], \tag{B.7}$$

$$\dot{S}_W = -\mathrm{Tr}[\mathcal{L}_W(\rho_{LW}^R)\log \sigma_{LW}^R], \tag{B.8}$$

where $\dot{S}_L + \dot{S}_R = 0$.

B.2 Thermodynamics analysis with original baths

To check the thermodynamic consistency of the results discussed in Section 3.3, we also analyze the engine from the perspective of the original baths with inverse temperatures β_H, β_C, and β_W. We have seen in the main text that heat fluxes from the baths H and C are $\dot{Q}_{LH} > 0$, $\dot{Q}_{LC} < 0$ respectively, and $\dot{Q}_W > 0$. The total heat flux that is entering the engine is $\dot{Q}_I = \dot{Q}_{LH} + \dot{Q}_W$. By using the first law $\dot{Q}_{LH} + \dot{Q}_{LC} + \dot{Q}_W + P = 0$ and the Clausius inequality in differential form $\beta_H \dot{Q}_{LH} + \beta_C \dot{Q}_{LC} + \beta_W \dot{Q}_W \leq 0$, we can drive the engine efficiency, i.e.,

$$\frac{-P}{\dot{Q}_I} \leq 1 - \frac{\beta_H \dot{Q}_H + \beta_W \dot{Q}_W}{\beta_C \dot{Q}_H + \beta_C \dot{Q}_W} = \eta_{Car}.$$

The upper bound is the Carnot efficiency and is always less than unity. In fact, for $\beta_W = \beta_H$, the Carnot bound results in the traditional bound, $\eta_{Car} = 1 - \beta_H/\beta_C$. For $\beta_W = \beta_C$, the bound reduces to $\eta_{Car} = (1 - \beta_H/\beta_C)\dot{Q}_H/\dot{Q}_I$.

Appendix C

Density matrix renormalization group (DMRG) method

The Density Matrix Renormalization Group (DMRG) is a computational methodology of significant potency that has been devised for the investigation of quantum systems that are one-dimensional in nature. The DMRG methodology is founded on the principle of partitioning the system into two distinct halves and subsequently optimizing the density matrix for each of these halves independently. The process of optimization entails a methodical reduction of the Hilbert space of the system by retaining solely the most notable states, followed by conducting computations on this condensed space. The aforementioned technique is subsequently employed in a repetitive manner to the residual degrees of freedom until the intended degree of precision is attained.

The DMRG methodology is heavily reliant on the fundamental principle of renormalization. The concept of renormalization pertains to the removal of high-energy degrees of freedom from a given system in order to facilitate the computational process. Within the framework of DMRG, the process of eliminating the high-energy degrees of freedom involves a systematic truncation of the Hilbert space of the system, whereby only the most pertinent states are retained. The parameter referred to as the bond dimension is commonly used to determine the quantity of states that are preserved, thereby regulating the magnitude of the truncated Hilbert space.

DMRG has been effectively implemented in various physical systems, including spin chains, lattice models, and quantum field theo-

ries. The DMRG method exhibits a notable advantage in analyzing systems characterized by pronounced correlations, a scenario where conventional techniques prove inadequate owing to the exponential expansion of the Hilbert space. The application of DMRG has been observed in the examination of intricate materials, including high-temperature superconductors. This has resulted in novel revelations regarding the conduct of quantum matter.

C.1 Structure of the DMRG algorithm

As can be seen in Fig. C.1, we break up the superblock into two distinct blocks: the environment block, which is represented by the symbol $|j\rangle$, and the system block, which is denoted by the symbol $|i\rangle$.

$$|\Phi\rangle = \sum_{i,j} \Phi_{i,j} |i\rangle |j\rangle \tag{C.1}$$

It has been assumed that $\langle \Phi \mid \Phi \rangle = 1$. Now, we trace out the environment part, the reduced density matrix would be

$$Tr_E[|\Phi\rangle\langle\Phi|] = \hat{\sigma}_{ii'} = \sum_j \Phi_{ij} \Phi^*_{i'j} |i\rangle\langle i'| \tag{C.2}$$

The expectation value of an operator associated with the system can be written

$$Tr[\hat{\sigma}_{ii'}\hat{O}] = \sum_\alpha w_\alpha \left\langle u^\alpha | \hat{O} | u^\alpha \right\rangle \tag{C.3}$$

where w_α is the non-negative eigenvalue of eigenvector $|u^\alpha\rangle$ of the system's density matrix. We have $\sum_\alpha w_\alpha = 1$ because of $Tr[\hat{\sigma}_{ii'}] = 1$ Since $\mathrm{Tr}\,\hat{\sigma} = 1$. Now we only consider the states having noticeable ω_α value, and the rest would be eliminated. That leads to reduce dimensions of Hilbert space, but we have to compromise with little error in the expected value of the system operator.

$$\langle \Phi | \hat{O} | \Phi \rangle_{\text{approx}} = \sum_{\alpha=1}^{m} w_\alpha \left\langle u^\alpha | \hat{O} | u^\alpha \right\rangle \tag{C.4}$$

here m indicated those $\omega_m \neq 0$ values with high weight. Now,

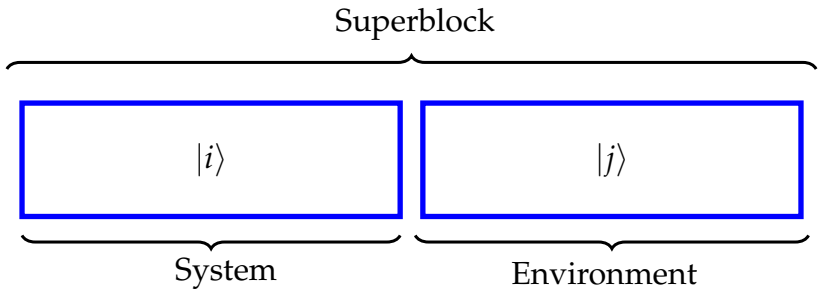

Figure C.1: The superblock is divided into system and environment blocks.

look at the ground state after the approximation. After the desired approximation we can write:

$$|\Phi\rangle \approx \left|\Phi'\right\rangle = \sum_{j}\sum_{\alpha=1}^{m} a_{\alpha,j}\,|u^{\alpha}\rangle\,|j\rangle \tag{C.5}$$

We can express the system block states, $|u^{\alpha}\rangle = \sum_i u_i^{\alpha}|i\rangle, \quad \alpha = 1, \cdots, m$. The error that we have to compromise with

$$\mathcal{S}_m = \left||\Phi\rangle - \left|\Phi'\right\rangle\right|^2 \tag{C.6}$$

In general, we can write

$$\left|\Phi'\right\rangle = \sum_{\alpha} a_{\alpha}\,|u^{\alpha}\rangle\,|v^{\alpha}\rangle\,, \tag{C.7}$$

where $v_j^{\alpha} = \langle j \mid v^{\alpha}\rangle = N_{\alpha}a_{\alpha,j}$, with N_{α} chosen to set $\sum_j \left|v_j^{\alpha}\right|^2 = 1$. The error $\mathcal{S}_m$ would be expressed as

$$\mathcal{S}_m = \sum_{ij}\left(\Phi_{ij} - \sum_{\alpha=1}^{m} a_{\alpha}u_i^{\alpha}v_j^{\alpha}\right)^2, \tag{C.8}$$

We have the opportunity to minimize $\mathcal{S}_m$ by exploring all possible combinations of u^{α}, v^{α}, and a_{α} with the given number of m. One can determine the solution by using the singular value decomposition of the rectangular matrix Φ

$$\Phi = UDV^T, \tag{C.9}$$

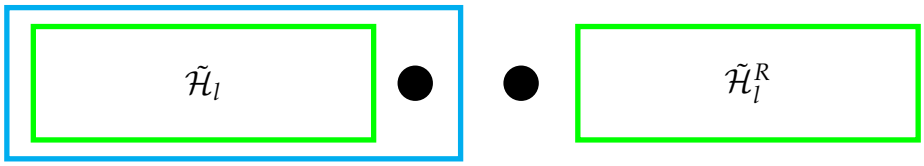

Figure C.2: Superblock configuration, $\tilde{\mathcal{H}}_l$ and $\tilde{\mathcal{H}}_l^R$ are the Hamiltonians of system and environment, respectively.

The given expression involves a $\ell \times \ \ell$ orthogonal matrix U and a $\ell \times J$ column-orthogonal matrix V, where j ranges from 1 to J. It is assumed that J is greater than or equal to ℓ. The singular values of Φ are contained in the diagonal matrix D. The elements situated on the diagonal of matrix D are denoted by a_α. The columns of matrices U and V that correspond to these diagonal elements are represented by u^α and v^α, respectively. So, one can write from the Eq. (C.1)

$$\sigma = UD^2U^T. \tag{C.10}$$

The w_α values represent the eigenvalues of σ, which are equivalent to the square of a_α. The u^α values correspond to the eigenstates of σ that possess the highest eigenvalues. The variable w_α denotes the likelihood of the block existing in the state u^α, subject to the constraint that the summation of all w_α values is equal to a certain quantity. The variable w_α denotes the likelihood of the block existing in the state u^α, subject to the constraint that u^α, with $\sum_\alpha w_\alpha$

The truncated weight would be

$$D_m = \sum_{\alpha=m+1}^{m_{\max}} w_\alpha = 1 - \sum_{\alpha=1}^{m} w_\alpha, \tag{C.11}$$

where m_{max} denotes the dimensionality of the density matrix.There exists a measure, denoted as D_m, which exhibits a strong correlation with the error in the ground-state energy. The discarded weight D_m is often used to measure the error. It is possible to compute the ground-state energy and the discarded weight for various values of m and perform an extrapolation as m approaches infinity. This methodology offers a dependable approximation of the discrepancy in the energy of the ground-state energy [357, 358].

C.1.1 The infinite-size algorithm

Starting with the procedure for infinite systems, the DMRG approach gradually increases the system's size in physical space until it achieves the target size while keeping the maximum dimension of the superblock Hamiltonian constant. Using a reflection of the system block, the environment block is built. The superblock's layout is shown in Fig C.2. The Hamiltonian of the system block with reduced basis is $\mathcal{H}_l$. We get the environment block with the Hamiltonian $\mathcal{H}_l^R$, which is obtained by the reflection of $\mathcal{H}_l$.

So, if the system is symmetrical in reflection, here's (Fig C.3) how the algorithm can be put together:

1. Create a superblock consisting of L sites, making sure it's small enough to allow for exact diagonalization.

2. Then, diagonalize the Hamiltonian of the superblock, denoted by $\mathcal{H}L^{\mathrm{SB}}$, using techniques such as the Lanczos algorithm or the more sophisticated Lanczos-Davidson algorithm [359,360]. This process will yield the ground-state eigenvalue, E_0, and the corresponding eigenvector, $|\Phi_0\rangle$.

3. Construct the reduced density matrix, denoted as $\rho_{ii'}$, for a new system block containing l' sites derived from the state $|\Phi\rangle$, by applying Eq (C.2). In this case, l' is equal to l, which is given by $(L/2) - 1$.

4. Perform the diagonalization of the reduced density matrix $\rho_{ii'}$ to acquire its m eigenvectors, denoted as $u_1, \cdots, u_m$, which correspond to the largest eigenvalues.

5. Create the Hamiltonian $\mathcal{H}_{l+1}$ and other operators O_{l+1} for the new system block, then transform them into the eigenbasis of the reduced density matrix by calculating $\tilde{\mathcal{H}}_{l+1} = R_L^\dagger \mathcal{H}_{l+1} R_L$ and $\tilde{O}_{l+1} = R_L^\dagger O_{l+1} R_L$. Here, the transformation matrix R_L consists of the m eigenvectors, represented as $R_L = (u_1, \cdots, u_m)$.

6. Form a new superblock Hamiltonian, denoted as $\mathcal{H}^{\mathrm{SB}}_{L+2}$, by combining the transformed Hamiltonian $\tilde{\mathcal{H}}_{l+1}$, two individual sites, and the right-side transformed Hamiltonian $\tilde{\mathcal{H}}^{\mathrm{R}}_{l+1}$.

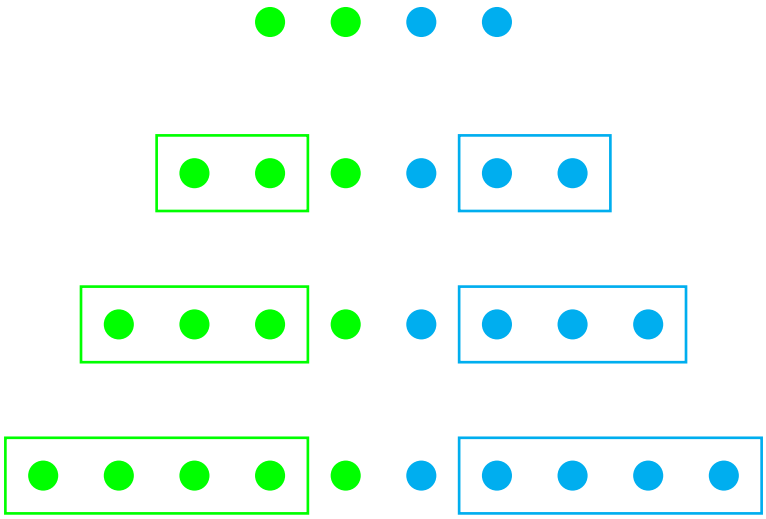

Figure C.3: The process of the infinite system algorithm

7. Repeat the process starting from step 2, but now replace L with $L + 2$.

8. Keep repeating steps 2 - 6 until the algorithm converges!

The size of the superblock expands by two sites during each stage, as illustrated in Fig. C.3. The iterations persist until a satisfactory approximation of the infinite system is achieved.

C.1.2 The finite-size algorithm

White [357, 361] introduced the finite system algorithm as a method to precisely determine the characteristics of systems with finite dimensions, which complements the infinite system algorithm. The first phase of the method is similar to the infinite system variation, but we cease increasing both blocks once the algorithm converges on a new superblock length L. At this point, one might stop and utilize the existing building pieces as a stand-in for the finite system. But experience shows that the approach usually ends up producing unsatisfactory results. Specifically, this is because, in the first stages of the infinite system method, the environment block is too tiny to effectively reflect the embedding in the final system, resulting in significant environmental errors. To address this, White developed

a strategy for sweeping across the finite system. During these sweeps, one continues with the renormalization processes, but rather than increasing both blocks; one block is enlarged at the cost of the other in order to maintain the same size for the superblock. Currently, the scenario has undergone a reversal and the expansion process occurs in the converse direction. Each iteration of the process encompasses a complete cycle of growth and shrinkage for both blocks, updating each block once for every size. If the system has reflection symmetry, then it is feasible to use the reflection of the left block at a certain magnitude to represent the right block at the same magnitude. In this particular scenario, the growth of the environment block may be replaced with the growth of the system block by simply resetting the size of the system block to 1 and continuing with the development of that block.

These sweeps' rationale is to enhance the inclusivity of various block sizes by enabling their integration into the final system. On the other hand, the effectiveness of the embedding process is anticipated to increase as representations of the building blocks grow more accurate. Sweeping the system frequently reduces environmental mistakes and brings the overall error close to the truncation error, thus eliminating it. As a result, we are able to realistically reduce the overall error to below the truncation error level.

The following (Fig C.4) is the procedure for the finite-system algorithm:

1. Execute the infinite-system algorithm until the superblock attains the size L. Preserve the $\tilde{\mathcal{H}}_l$ values and the necessary operators for connecting the blocks during each iteration.

2. Repeats steps 3-5 of the infinite-system algorithm to get $\tilde{\mathcal{H}}_{l+1}$, although here, $l \neq l'$.

3. Create further a superblock of length L by combining $\tilde{\mathcal{H}}_{l+1}$ two single sites and $\tilde{\mathcal{H}}_{l'-1}$.

4. Repeat steps 2 and 3 until reaching the final location of the environment length archives $l' = 1$. This segment of the algorithm is referred to as the left-to-right zipping phase.

5. Execute iterations 3-to-5 of the infinite-system algorithm with the objective of constructing the environment and preserving

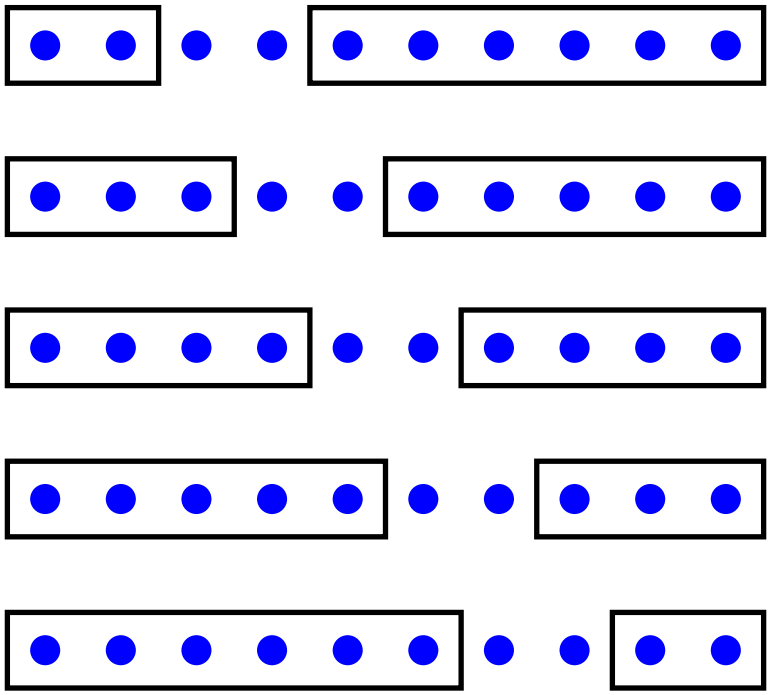

Figure C.4: Finite system algorithm

the value of the corresponding Hamiltonian $\tilde{\mathcal{H}}^{R}_{l'-1}$ in every iteration.

6. Similarly, create a superblock of size$L$ by combining $\tilde{\mathcal{H}}_{l-1}$, two individual sites, and $\tilde{\mathcal{H}}_{l'+1}$.

7. Continue performing steps 5 and 6 until $l = 1$. his segment of the algorithm is referred to as the right-to-left zipping phase.

8. Repetition will continue from step 1 until the algorithm converges.

C.2 Elements of DMRG within tensor network approach

Tensor Network techniques offer a generic framework for the study of many-body systems in any dimension. The fundamental concept underlying Tensor Networks is to represent the wavefunction of the

many-body system as a network of tensors, with each tensor standing in for a local degree of freedom of the system. This is the fundamental principle behind Tensor Networks.

When tensor network approaches are used with DMRG, the result is a powerful and versatile tool for investigating quantum systems that is both accurate and interpretable. It enables the accurate depiction of big, complicated systems with a large number of degrees of freedom, and it achieves a high level of accuracy in predictions, making it a suitable tool for the study of highly coupled systems. This method may be used for a broad variety of quantum systems, such as those that exhibit a variety of interactions, symmetries, and boundary conditions. The wave function is easily interpretable when seen through the lens of the tensor network, which makes it simple to draw conclusions about the physical world based on the outcomes of TN-DMRG with Tensor Network computations.

C.2.1 Matrix Product State

An MPS is a shorthand term for an ansatz that represents a many-body wave function. Consider a many-body quantum system, which consists of N coupled systems, each of which is formed of d dimensional states. The dimension of the Hilbert space would be d^N and the basis vectors are expressed as $|S_1\rangle \otimes |S_2\rangle \otimes |S_3\rangle \otimes ..... \otimes |S_N\rangle$. We can write the general form of the wave function

$$|\Phi\rangle = \sum_{S_1 S_2 S_3 \ldots S_N} \Phi_{S_1 S_2 S_3 \ldots S_N} |S_1\rangle |S_2\rangle |S_3\rangle \ldots |S_N\rangle \tag{C.12}$$

Each sub-system's unique index combinability is a multiplicative factor that has the potential to increase the total number of basis states. As a basic principle of quantum mechanics, the fact that the size of the Hilbert space grows exponentially with the size of the system is very different from the way the size of the state space grows linearly in classical mechanics. We can express (C.12) diagrammatically,

An MPS is represented as a collection of three-index tensors $A^{S_i}_{\alpha_i,\alpha_{i+1}}$, where S_i is the physical index representing the local basis at site i, and α_i and α_{i+1} are auxiliary indices (also known as bond indices) for a one-dimensional system.

$$|\Phi\rangle = \sum_{\substack{\sigma_1\sigma_2\sigma_3\ldots\sigma_N \\ \alpha_1\alpha_2\alpha_3\ldots\alpha_{N-1}}} A^{S_1}_{1\alpha_1} A^{S_2}_{\alpha_1\alpha_2} A^{S_3}_{\alpha_2\alpha_3} \ldots A^{S_N}_{\alpha_{N-1}1} |S_1\rangle |S_2\rangle |S_3\rangle \ldots |S_N\rangle \tag{C.13}$$

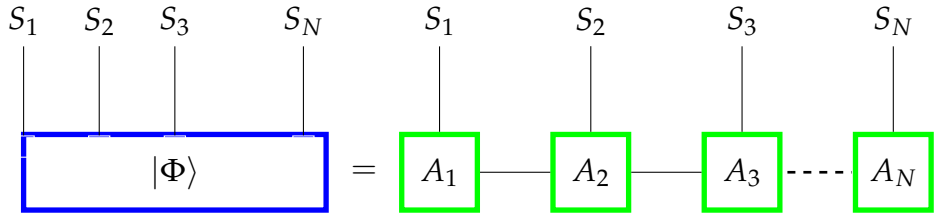

Figure C.5: Matrix product state

C.2.2 Matrix-Product Operators

In a way comparable to that of the matrix product state, one can define the Matrix Product operator (MPO). Every site of MPO is connected with two legs with different indices in Fig C.6.

$$\hat{O} = \sum_{\substack{S'_1S'_2\ldots S'_N \\ S_1S_2\ldots S_N}} O^{S'_1}_{S_1} O^{S'_2}_{S_2} \ldots O^{S'_N}_{S_N} |S_1\rangle |S_2\rangle |S_3\rangle \ldots |S_N\rangle \langle S'_1| \langle S'_2| \langle S'_3| \ldots \langle S'_N| \tag{C.14}$$

The expectation value of an operator can be express like the Fig. C.2.2.

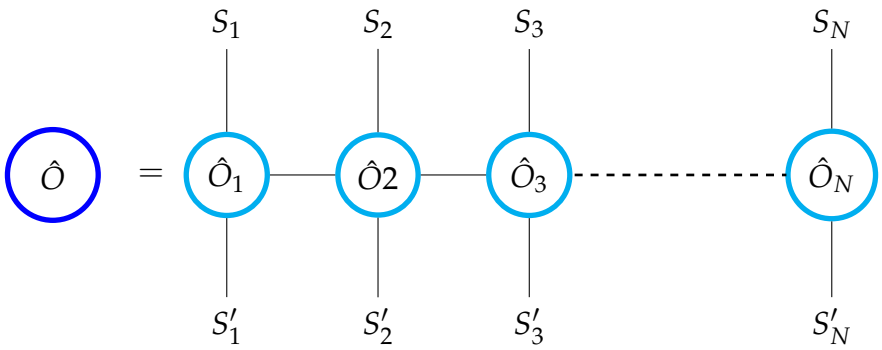

Figure C.6: Matrix product operator

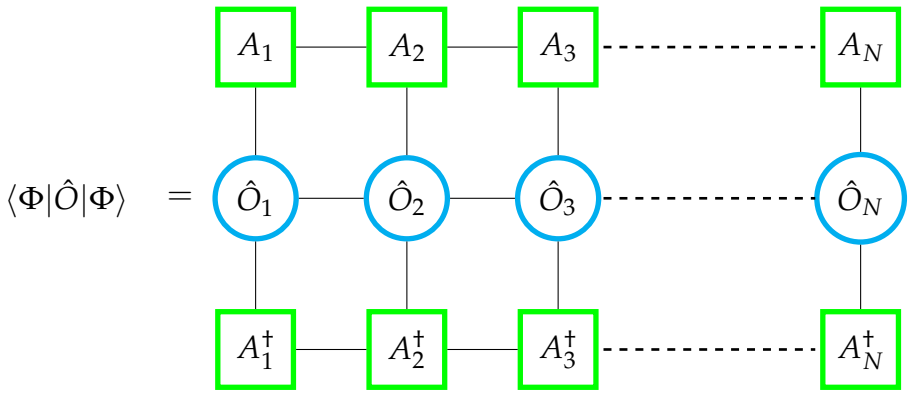

Figure C.7: The expectation value of the operator O.

C.2.3 DMRG algorithm

The DMRG approach leverages Matrix Product States (MPS) to encode quantum states, allowing for good accuracy while keeping a computationally viable cost. Here we learn the Density Matrix Renormalization Group (DMRG) approach using matrix product states.

Here, we provide a step-by-step procedure of the DMRG method through MPS.

1. **Hamiltonian representation:** To begin, one needs to express the Hamiltonian of the quantum system in terms of the local interactions.

2. **Initialize MPS:** The tensors must be set to random values or

a known beginning state before the operation can begin on an MPS. In order to prevent biases in the tensor network representation, it is usual practice to assign random values to the tensors from the beginning. A different option is to initialize the tensors with a ground state or product state of a simpler system.

3. **Create a tensor for the environment:** The environment tensors are constructed using a combination of the Hamiltonian and the MPS tensors for the neighboring sites. Update the environment tensors as we move through the system during the sweep procedure.

4. **Sweep operation:** In a tensor network, optimizing the tensor at each site requires a series of iterative sweeps. An optimization sweep involves iteratively reversing the direction of the tensor optimization from left to right and back again. This step is critical for developing a tensor network representation that is both effective and precise. There are two main processes involved in every sweep: optimization and gauge transformation. The optimization process seeks for the tensor that provides the most overall satisfaction across all sites. Conversely, the goal of the gauge transformation is to reduce inefficient redundancy in the tensor network. In order to eliminate the gauge degrees of freedom, a local unitary transformation is applied to the MPS tensors, a process known as gauge transformation. It is necessary to repeat the sweeps until the energy or MPS tensors converge in order to optimize the tensors in the system. When the difference between the most recent and earlier tensors falls below a certain threshold, we say that the tensor network has converged.

   The sweep operation comprises two essential steps: optimization and gauge transformation.

   - **Optimization:** The optimization process involves the following steps to update the MPS tensor for the current site and minimize the energy of the local Hamiltonian at this site:

     (a) Form an effective Hamiltonian for the current site by combining the local Hamiltonian with the environment tensors. This effective Hamiltonian describes the

interaction of the current site with the rest of the system. The environment tensors represent the tensors of all other sites in the system, excluding the current site.

(b) Compute the reduced density matrix for the current site by tracing out the rest of the system. This density matrix describes the probability of finding the current site in a particular state while averaging over the states of the other sites in the system. Using the MPS representation, one can perform this operation efficiently, which is essential for large systems.

(c) Obtain a collection of eigenvalues and eigenvectors by solving an eigenvalue problem for the effective Hamiltonian. The energy state of the current site that is most stable is that with the lowest eigenvalue (ground state). Then, one can make sure that the tensor network representation appropriately depicts the system's ground state by updating the MPS tensor for the current site with the relevant eigenvector.

In general, the optimization procedure is an essential part of the tensor network approaches, since it is the step that guarantees the MPS tensor at each site is updated properly and effectively. One may acquire an accurate representation of the system's ground state and the attributes it has by decreasing the energy of the local Hamiltonian at each site.

- **Gauge transformation:** The process of updating the MPS tensor for the current site in a tensor network involves the following steps in detail:

(a) For the current site, do a singular value decomposition (SVD) (in Fig C.2.3) on the updated MPS tensor. In this stage, the tensor is divided into a set of singular values and the left and right singular vectors that go with them. The SVD is an important stage in tensor network approaches because it makes it possible to manipulate the tensor network effectively.

(b) Keep only the most significant singular values in the SVD, as determined by a threshold or a predefined maximum number of states. This truncation phase

is required to guarantee that the MPS remains manageable in size, especially for large systems. By discarding the less significant singular values, the storage requirements of the tensor network can be drastically reduced.

(c) Using the truncated SVD, update the MPS tensors for the current site and the next (or prior, depending on the sweep direction). In this stage, the left and right singular vectors are combined with the reduced singular values to generate new tensors. These revised tensors offer a more accurate and compact representation of a tensor network.

(d) Update the environment tensors for the next (or prior) site as needed. The environment tensors are the tensors of all other sites in the system that are not current or updated. One may guarantee that the tensor network stays consistent and correct by updating these tensors depending on the reduced SVD.

Overall, updating the MPS tensor for the current site in a tensor network comprises a number of essential stages, including SVD, truncation, and updates to the MPS and environment tensors. By carefully following these methods, one may generate an efficient and accurate tensor network representation.

The optimization step involves finding the best possible tensor that satisfies the optimization criteria at each site. In contrast, the gauge transformation step aims to remove the unwanted redundancy in the tensor network, making it more compact and efficient.

It is crucial to repeat the sweeps until the energy or MPS tensors converge, as this guarantees the accuracy of the tensor network representation. Convergence refers to the point where the difference between the current and the previous tensors is below a predefined threshold, indicating that the tensor network has stabilized.

We consider only four physical sites in Fig. C.9 for simplicity. We can do SVD from the left side, which leads to the left canonical form

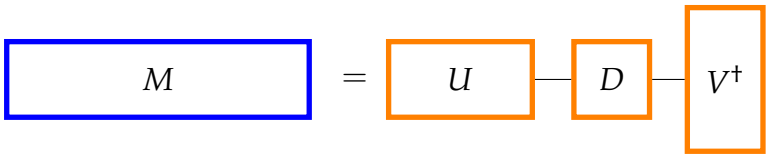

Figure C.8: Singular value decomposition of M.

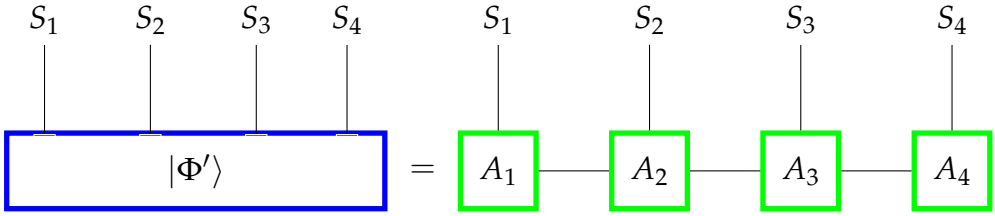

Figure C.9: Caption

shown in Fig. C.10. Similarly, one can do SVD from the right sides, which leads to the right canonical form Fig. C.11. Although in DMRG, it would be conventions take a combination of left and right canonical form which results in a mixed canonical form (in Fig. C.12).

We draw a diagram of matrix product operator for Hamiltonian in Fig. C.13. Using the mixed canonical form and writing down the Hamiltonian on the local MPS (in Fig. C.16) we can solve the Schrödinger equation as an eigen value problem.

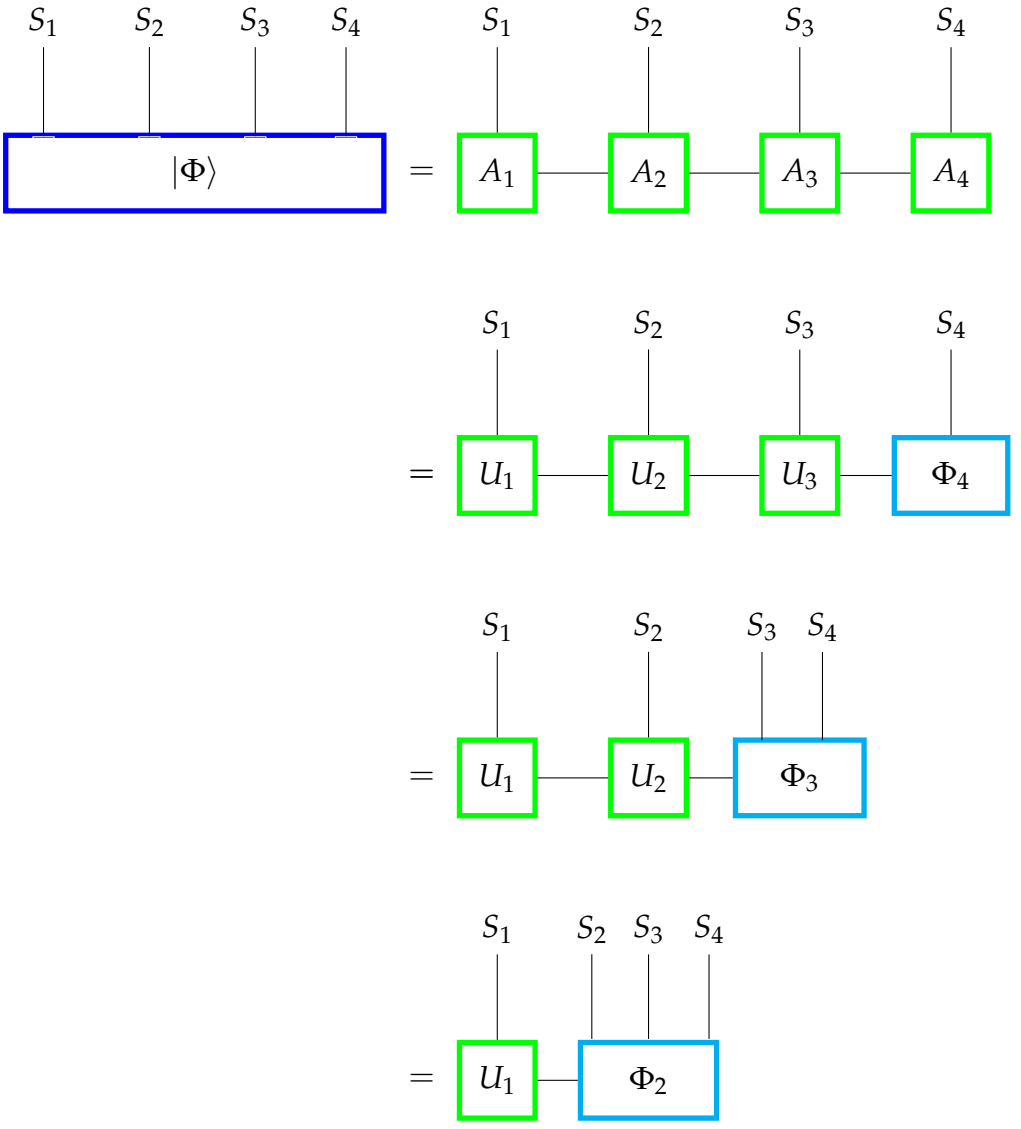

Figure C.10: Left-canonical form

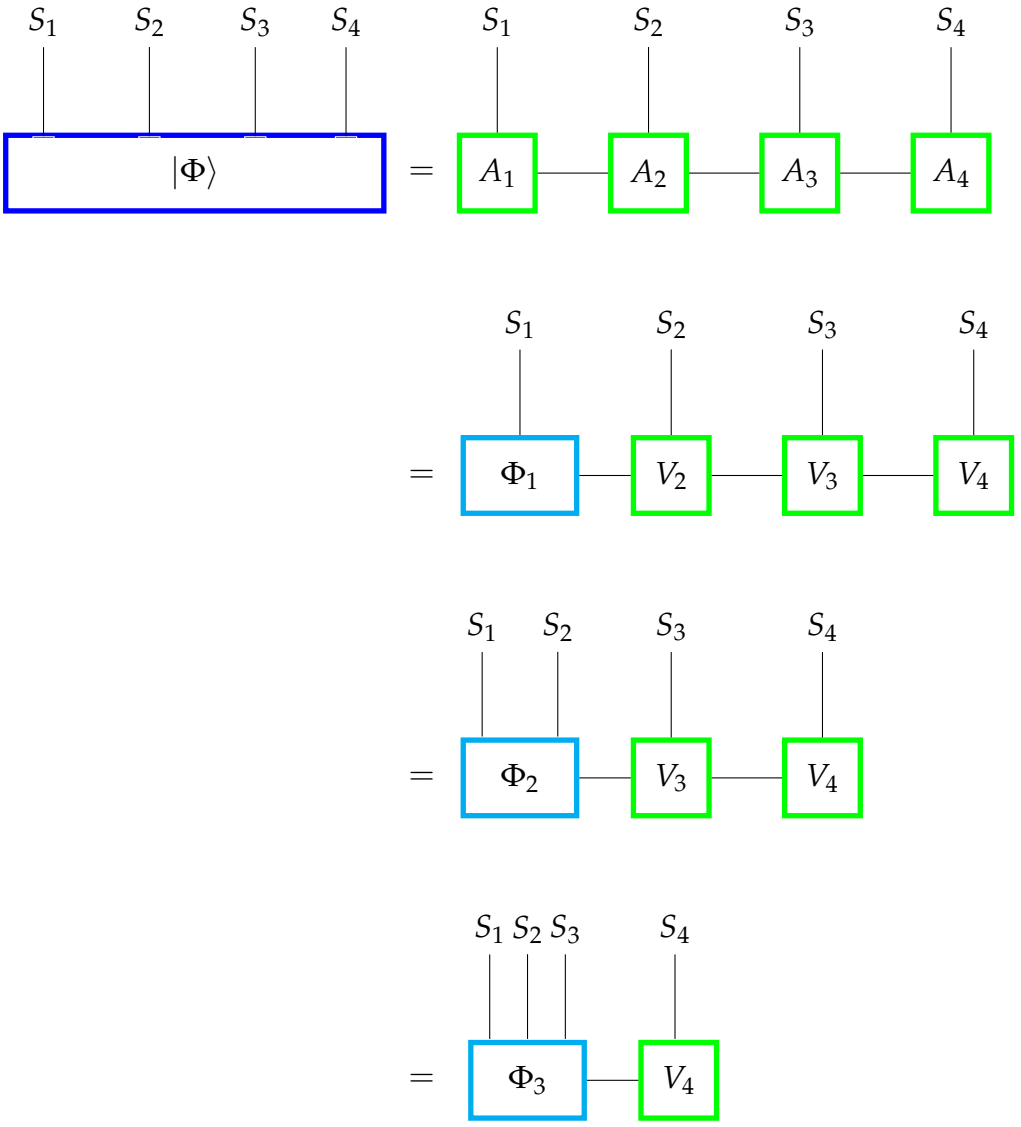

Figure C.11: Right-canonical form

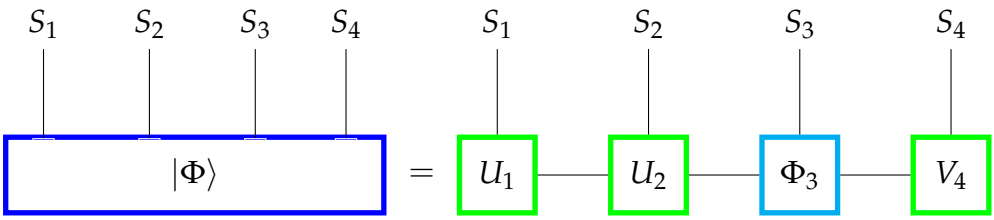

Figure C.12: Mixed-canonical form; the most convenient form for DMRG

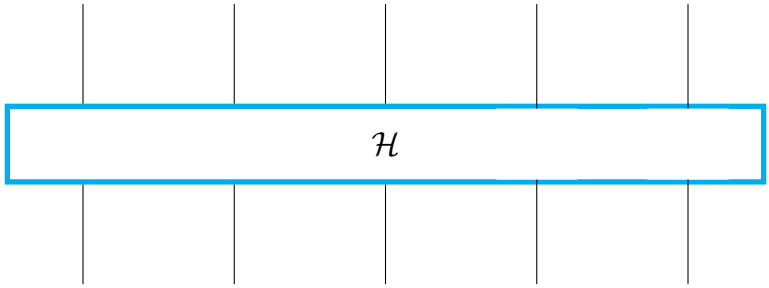

Figure C.13: Hamiltonian

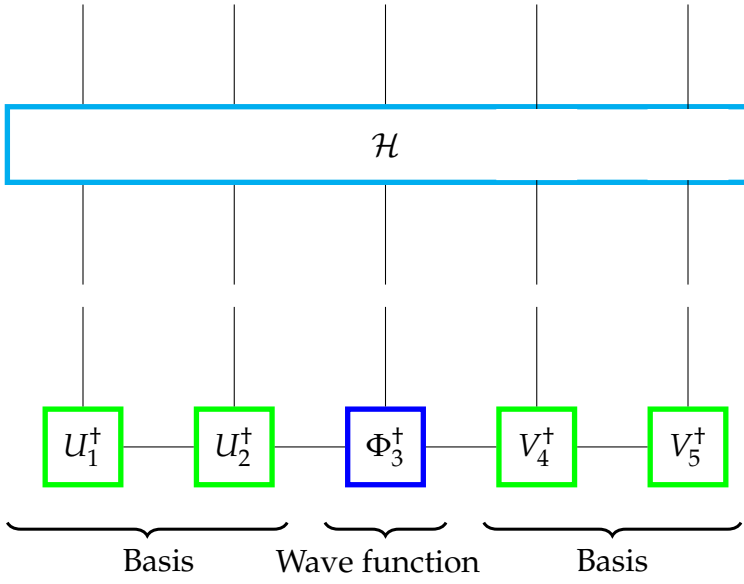

Figure C.14: Utilize mixed canonical form

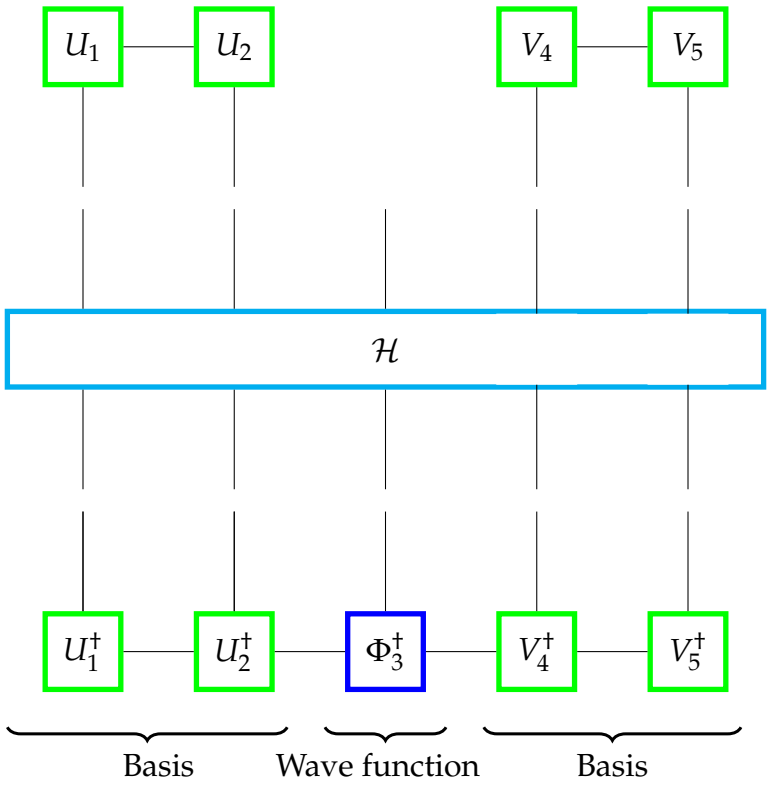

Figure C.15: Hamiltonian is projected into local MPS basis

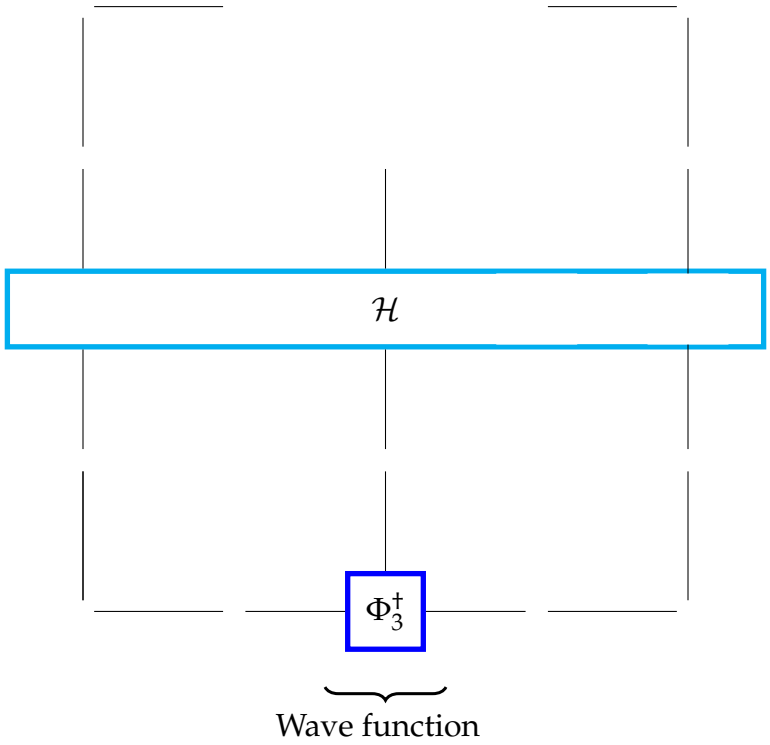

Figure C.16: The Hamiltonian only acting on local MPS $\Phi_3^\dagger$ to solve the Schrödinger equation as an eigen value problem.

Bibliography

[1] Michael A. Nielsen and Isaac L. Chuang. *Quantum Computation and Quantum Information: 10th Anniversary Edition*. Cambridge University Press, USA, 10th edition, 2011.

[2] Markus Arndt and Klaus Hornberger. Testing the limits of quantum mechanical superpositions. *Nature Physics*, 10(4):271–277, April 2014.

[3] Andreas Winter and Dong Yang. Operational resource theory of coherence. *Physical Review Letters*, 116(12), March 2016.

[4] William Marshall, Christoph Simon, Roger Penrose, and Dik Bouwmeester. Towards quantum superpositions of a mirror. *Physical Review Letters*, 91(13), September 2003.

[5] Jun John Sakurai. *Modern quantum mechanics; rev. ed.* Addison-Wesley, Reading, MA, 1994.

[6] Anatole Kenfack and Karol yczkowski. Negativity of the wigner function as an indicator of non-classicality. *Journal of Optics B: Quantum and Semiclassical Optics*, 6(10):396–404, August 2004.

[7] V. V. Dodonov, O. V. Man'ko, V. I. Man'ko, and A. Wünsche. Hilbert-schmidt distance and non-classicality of states in quantum optics. *Journal of Modern Optics*, 47(4):633–654, March 2000.

[8] A Smirne, D Egloff, M G Díaz, M B Plenio, and S F Huelga. Coherence and non-classicality of quantum markov processes. *Quantum Science and Technology*, 4(1):01LT01, November 2018.

[9] Nicolas Laflorencie. Quantum entanglement in condensed matter systems. *Physics Reports*, 646:1–59, August 2016.

[10] Ryszard Horodecki, Paweł Horodecki, Michał Horodecki, and Karol Horodecki. Quantum entanglement. *Reviews of Modern Physics*, 81(2):865–942, June 2009.

[11] Manuel Erhard, Mario Krenn, and Anton Zeilinger. Advances in high-dimensional quantum entanglement. *Nature Reviews Physics*, 2(7):365–381, June 2020.

[12] Sandu Popescu, Anthony J. Short, and Andreas Winter. Entanglement and the foundations of statistical mechanics. *Nature Physics*, 2(11):754–758, October 2006.

[13] M. D. Reid, P. D. Drummond, W. P. Bowen, E. G. Cavalcanti, P. K. Lam, H. A. Bachor, U. L. Andersen, and G. Leuchs. Colloquium: The einstein-podolsky-rosen paradox: From concepts to applications. *Reviews of Modern Physics*, 81(4):1727–1751, December 2009.

[14] Nicolas Brunner, Daniel Cavalcanti, Stefano Pironio, Valerio Scarani, and Stephanie Wehner. Bell nonlocality. *Reviews of Modern Physics*, 86(2):419–478, April 2014.

[15] J. Tura, R. Augusiak, A. B. Sainz, T. Vértesi, M. Lewenstein, and A. Acín. Detecting nonlocality in many-body quantum states. *Science*, 344(6189):1256–1258, June 2014.

[16] Harry Buhrman, Richard Cleve, Serge Massar, and Ronald de Wolf. Nonlocality and communication complexity. *Reviews of Modern Physics*, 82(1):665–698, March 2010.

[17] Antonio Acín, Tobias Fritz, Anthony Leverrier, and Ana Belén Sainz. A combinatorial approach to nonlocality and contextuality. *Communications in Mathematical Physics*, 334(2):533–628, January 2015.

[18] Jonathan P. Dowling and Gerard J. Milburn. Quantum technology: the second quantum revolution. *Philosophical Transactions of the Royal Society of London. Series A: Mathematical, Physical and Engineering Sciences*, 361(1809):1655–1674, June 2003.

[19] Antonio Acín, Immanuel Bloch, Harry Buhrman, Tommaso Calarco, Christopher Eichler, Jens Eisert, Daniel Esteve, Nicolas Gisin, Steffen J Glaser, Fedor Jelezko, Stefan Kuhr, Maciej

Lewenstein, Max F Riedel, Piet O Schmidt, Rob Thew, Andreas Wallraff, Ian Walmsley, and Frank K Wilhelm. The quantum technologies roadmap: a european community view. *New Journal of Physics*, 20(8):080201, August 2018.

[20] Claude Cohen-Tannoudji, Bernard Diu, and Franck Laloë. *Quantum mechanics; 1st ed.* Wiley, New York, NY, 1977. Trans. of : Mécanique quantique. Paris : Hermann, 1973.

[21] Marin Bukov, Luca D'Alessio, and Anatoli Polkovnikov. Universal high-frequency behavior of periodically driven systems: from dynamical stabilization to floquet engineering. *Advances in Physics*, 64(2):139–226, March 2015.

[22] Utso Bhattacharya, Sayak Dasgupta, and Amit Dutta. Dynamical merging of dirac points in the periodically driven kitaev honeycomb model. *The European Physical Journal B*, 89(10), October 2016.

[23] Utso Bhattacharya and Amit Dutta. Topological footprints of the kitaev chain with long-range superconducting pairings at a finite temperature. *Physical Review B*, 97(21), June 2018.

[24] Marin Bukov, Sarang Gopalakrishnan, Michael Knap, and Eugene Demler. Prethermal floquet steady states and instabilities in the periodically driven, weakly interacting bose-hubbard model. *Physical Review Letters*, 115(20), November 2015.

[25] Utso Bhattacharya, Somnath Maity, Amit Dutta, and Diptiman Sen. Critical phase boundaries of static and periodically kicked long-range kitaev chain. *Journal of Physics: Condensed Matter*, 31(17):174003, March 2019.

[26] Somnath Maity, Utso Bhattacharya, Amit Dutta, and Diptiman Sen. Fibonacci steady states in a driven integrable quantum system. *Physical Review B*, 99(2), January 2019.

[27] M. Nuske, L. Broers, B. Schulte, G. Jotzu, S. A. Sato, A. Cavalleri, A. Rubio, J. W. McIver, and L. Mathey. Floquet dynamics in light-driven solids. *Physical Review Research*, 2(4), December 2020.

[28] Utso Bhattacharya, Swati Chaudhary, Tobias Grass, Allan S. Johnson, Simon Wall, and Maciej Lewenstein. Fermionic chern insulator from twisted light with linear polarization. *Physical Review B*, 105(8), February 2022.

[29] YiJing Yan and RuiXue Xu. Quantum mechanics of dissipative system. *Annual Review of Physical Chemistry*, 56(1):187–219, May 2005.

[30] H. P. Breuer and F. Petruccione. Great Clarendon Street, 2009.

[31] Brian Skinner, Jonathan Ruhman, and Adam Nahum. Measurement-induced phase transitions in the dynamics of entanglement. *Physical Review X*, 9(3), July 2019.

[32] Davide Rossini and Ettore Vicari. Measurement-induced dynamics of many-body systems at quantum criticality. *Physical Review B*, 102(3), July 2020.

[33] Piotr Sierant, Giuliano Chiriacò, Federica M. Surace, Shraddha Sharma, Xhek Turkeshi, Marcello Dalmonte, Rosario Fazio, and Guido Pagano. Dissipative floquet dynamics: from steady state to measurement induced criticality in trapped-ion chains. *Quantum*, 6:638, February 2022.

[34] Sima Pouyandeh, Farhad Shahbazi, and Abolfazl Bayat. Measurement-induced dynamics for spin-chain quantum communication and its application for optical lattices. *Physical Review A*, 90(1), July 2014.

[35] Romain Geneaux, Hugo J. B. Marroux, Alexander Guggenmos, Daniel M. Neumark, and Stephen R. Leone. Transient absorption spectroscopy using high harmonic generation: a review of ultrafast x-ray dynamics in molecules and solids. *Philosophical Transactions of the Royal Society A: Mathematical, Physical and Engineering Sciences*, 377(2145):20170463, April 2019.

[36] Carsten Winterfeldt, Christian Spielmann, and Gustav Gerber. Colloquium: Optimal control of high-harmonic generation. *Reviews of Modern Physics*, 80(1):117–140, January 2008.

[37] T. Shaaran, M.F. Ciappina, and M. Lewenstein. Estimating the plasmonic field enhancement using high-order harmonic generation: the role of the field inhomogeneity. *Journal of Modern Optics*, 59(19):1634–1639, November 2012.

[38] M F Ciappina, J A Pérez-Hernández, A S Landsman, W A Okell, S Zherebtsov, B Förg, J Schötz, L Seiffert, T Fennel, T Shaaran, T Zimmermann, A Chacón, R Guichard, A Zaïr, J W G Tisch, J P Marangos, T Witting, A Braun, S A Maier, L Roso, M Krüger, P Hommelhoff, M F Kling, F Krausz, and M Lewenstein. Attosecond physics at the nanoscale. *Reports on Progress in Physics*, 80(5):054401, March 2017.

[39] M. Lewenstein, N. Baldelli, U. Bhattacharya, J. Biegert, M. F. Ciappina, U. Elu, T. Grass, P. T. Grochowski, A. Johnson, Th. Lamprou, A. S. Maxwell, A. Ordóñez, E. Pisanty, J. Rivera-Dean, P. Stammer, I. Tyulnev, and P. Tzallas. Attosecond physics and quantum information science, 2022.

[40] Kasra Amini, Jens Biegert, Francesca Calegari, Alexis Chacón, Marcelo F Ciappina, Alexandre Dauphin, Dmitry K Efimov, Carla Figueira de Morisson Faria, Krzysztof Giergiel, Piotr Gniewek, Alexandra S Landsman, Michał Lesiuk, Michał Mandrysz, Andrew S Maxwell, Robert Moszyński, Lisa Ortmann, Jose Antonio Pérez-Hernández, Antonio Picón, Emilio Pisanty, Jakub Prauzner-Bechcicki, Krzysztof Sacha, Noslen Suárez, Amelle Zaïr, Jakub Zakrzewski, and Maciej Lewenstein. Symphony on strong field approximation. *Reports on Progress in Physics*, 82(11):116001, October 2019.

[41] Maciej Lewenstein and Anne L'Huillier. Principles of single atom physics: High-order harmonic generation, above-threshold ionization and non-sequential ionization. In *Strong Field Laser Physics*, pages 147–183. Springer New York, 2008.

[42] Utso Bhattacharya, Joanna Hutchinson, and Amit Dutta. Quenching in chern insulators with satellite dirac points: The fate of edge states. *Physical Review B*, 95(14), April 2017.

[43] Sougata Mardanya, Utso Bhattacharya, Amit Agarwal, and Amit Dutta. Dynamics of edge currents in a linearly quenched haldane model. *Physical Review B*, 97(11), March 2018.

[44] José P. Palao and Ronnie Kosloff. Quantum computing by an optimal control algorithm for unitary transformations. *Physical Review Letters*, 89(18), October 2002.

[45] Qing Liu, Thomas J. Elliott, Felix C. Binder, Carlo Di Franco, and Mile Gu. Optimal stochastic modeling with unitary quantum dynamics. *Physical Review A*, 99(6), June 2019.

[46] Aditi Mitra. Quantum quench dynamics. *Annual Review of Condensed Matter Physics*, 9(1):245–259, March 2018.

[47] Titas Chanda, Jakub Zakrzewski, Maciej Lewenstein, and Luca Tagliacozzo. Confinement and lack of thermalization after quenches in the bosonic schwinger model. *Physical Review Letters*, 124(18), May 2020.

[48] Guanru Feng, Franklin H. Cho, Hemant Katiyar, Jun Li, Dawei Lu, Jonathan Baugh, and Raymond Laflamme. Gradient-based closed-loop quantum optimal control in a solid-state two-qubit system. *Physical Review A*, 98(5), November 2018.

[49] Valentin Kasper, Torsten V. Zache, Fred Jendrzejewski, Maciej Lewenstein, and Erez Zohar. Non-abelian gauge invariance from dynamical decoupling. *Physical Review D*, 107(1), January 2023.

[50] P. Hauke, R. J. Sewell, M. W. Mitchell, and M. Lewenstein. Quantum control of spin correlations in ultracold lattice gases. *Physical Review A*, 87(2), February 2013.

[51] Jesper Hasseriis Mohr Jensen, Frederik Skovbo Møller, Jens Jakob Sørensen, and Jacob Friis Sherson. Achieving fast high-fidelity optimal control of many-body quantum dynamics. *Physical Review A*, 104(5), November 2021.

[52] Philipp Hauke, Helmut G Katzgraber, Wolfgang Lechner, Hidetoshi Nishimori, and William D Oliver. Perspectives of quantum annealing: methods and implementations. *Reports on Progress in Physics*, 83(5):054401, May 2020.

[53] Giuseppe E Santoro and Erio Tosatti. Optimization using quantum mechanics: quantum annealing through adiabatic evolution. *Journal of Physics A: Mathematical and General*, 39(36):R393–R431, August 2006.

[54] Tobias Graß. Quantum annealing with longitudinal bias fields. *Physical Review Letters*, 123(12), September 2019.

[55] Yuki Bando, Yuki Susa, Hiroki Oshiyama, Naokazu Shibata, Masayuki Ohzeki, Fernando Javier Gómez-Ruiz, Daniel A. Lidar, Sei Suzuki, Adolfo del Campo, and Hidetoshi Nishimori. Probing the universality of topological defect formation in a quantum annealer: Kibble-zurek mechanism and beyond. *Physical Review Research*, 2(3), September 2020.

[56] Tobias Grass. Quantum annealing sampling with a bias field. *Physical Review Applied*, 18(4), October 2022.

[57] Felix Binder, Luis A. Correa, Christian Gogolin, Janet Anders, and Gerardo Adesso, editors. *Thermodynamics in the Quantum Regime*. Springer International Publishing, 2018.

[58] Raam Uzdin and Saar Rahav. Global passivity in microscopic thermodynamics. *Physical Review X*, 8(2), June 2018.

[59] Manabendra Nath Bera, Arnau Riera, Maciej Lewenstein, Zahra Baghali Khanian, and Andreas Winter. Thermodynamics as a Consequence of Information Conservation. *Quantum*, 3:121, February 2019.

[60] Raam Uzdin and Saar Rahav. Passivity deformation approach for the thermodynamics of isolated quantum setups. *PRX Quantum*, 2(1), March 2021.

[61] Fernando G. S. L. Brandão, Michał Horodecki, Jonathan Oppenheim, Joseph M. Renes, and Robert W. Spekkens. Resource theory of quantum states out of thermal equilibrium. *Physical Review Letters*, 111(25), December 2013.

[62] Michał Horodecki and Jonathan Oppenheim. Fundamental limitations for quantum and nanoscale thermodynamics. *Nature Communications*, 4(1), June 2013.

[63] Gilad Gour, Markus P. Müller, Varun Narasimhachar, Robert W. Spekkens, and Nicole Yunger Halpern. The resource theory of informational nonequilibrium in thermodynamics. *Physics Reports*, 583:1–58, July 2015.

[64] Fernando Brandão, Michał Horodecki, Nelly Ng, Jonathan Oppenheim, and Stephanie Wehner. The second laws of quantum thermodynamics. *Proceedings of the National Academy of Sciences*, 112(11):3275–3279, February 2015.

[65] Matteo Lostaglio, David Jennings, and Terry Rudolph. Description of quantum coherence in thermodynamic processes requires constraints beyond free energy. *Nature Communications*, 6(1), March 2015.

[66] Nelly Huei Ying Ng and Mischa Prebin Woods. Resource theory of quantum thermodynamics: Thermal operations and second laws. In *Fundamental Theories of Physics*, pages 625–650. Springer International Publishing, 2018.

[67] Matteo Lostaglio. An introductory review of the resource theory approach to thermodynamics. *Reports on Progress in Physics*, 82(11):114001, October 2019.

[68] Mohit Lal Bera, Maciej Lewenstein, and Manabendra Nath Bera. Attaining carnot efficiency with quantum and nanoscale heat engines. *npj Quantum Information*, 7(1), February 2021.

[69] Patrick Pietzonka and Udo Seifert. Universal trade-off between power, efficiency, and constancy in steady-state heat engines. *Phys. Rev. Lett.*, 120:190602, May 2018.

[70] Heinz-Peter Breuer and Francesco Petruccione. *The Theory of Open Quantum Systems*. Oxford University PressOxford, January 2007.

[71] Howard Carmichael. *An Open Systems Approach to Quantum Optics*. Springer Berlin Heidelberg, 1993.

[72] Robert Zwanzig. *Nonequilibrium statistical mechanics*. Oxford university press, 2001.

[73] Ulrich Weiss. *Quantum Dissipative Systems*. World scientific, November 2011.

[74] Michael A Nielsen and Isaac Chuang. Quantum computation and quantum information, 2002.

[75] Massimiliano Esposito, Upendra Harbola, and Shaul Mukamel. Nonequilibrium fluctuations, fluctuation theorems, and counting statistics in quantum systems. *Reviews of Modern Physics*, 81(4):1665–1702, December 2009.

[76] Matteo Ippoliti, Tibor Rakovszky, and Vedika Khemani. Fractal, logarithmic, and volume-law entangled nonthermal steady states via spacetime duality. *Physical Review X*, 12(1), March 2022.

[77] G. Dagvadorj, J. M. Fellows, S. Matyjaśkiewicz, F. M. Marchetti, I. Carusotto, and M. H. Szymańska. Nonequilibrium phase transition in a two-dimensional driven open quantum system. *Physical Review X*, 5(4), November 2015.

[78] Daniel Hurowitz, Saar Rahav, and Doron Cohen. The nonequilibrium steady state of sparse systems with non-trivial topology. *EPL (Europhysics Letters)*, 98(2):20002, April 2012.

[79] Jacek Dziarmaga. Dynamics of a quantum phase transition and relaxation to a steady state. *Advances in Physics*, 59(6):1063–1189, September 2010.

[80] Mona H. Kalthoff, Dante M. Kennes, Andrew J. Millis, and Michael A. Sentef. Nonequilibrium phase transition in a driven-dissipative quantum antiferromagnet. *Phys. Rev. Res.*, 4:023115, May 2022.

[81] Michael J. Kastoryano and Mark S. Rudner. Topological transport in the steady state of a quantum particle with dissipation. *Physical Review B*, 99(12), March 2019.

[82] L. Hartmann, W. Dür, and H.-J. Briegel. Steady-state entanglement in open and noisy quantum systems. *Physical Review A*, 74(5), nov 2006.

[83] Y. Lin, J. P. Gaebler, F. Reiter, T. R. Tan, R. Bowler, A. S. Sørensen, D. Leibfried, and D. J. Wineland. Dissipative production of a maximally entangled steady state of two quantum bits. *Nature*, 504(7480):415–418, November 2013.

[84] Mihai Macovei, Jörg Evers, and Christoph H. Keitel. Phase control of collective quantum dynamics. *Physical Review Letters*, 91(23), December 2003.

[85] Karthik I. Seetharam, Charles-Edouard Bardyn, Netanel H. Lindner, Mark S. Rudner, and Gil Refael. Steady states of interacting floquet insulators. *Physical Review B*, 99(1), January 2019.

[86] Tatsuhiko N. Ikeda and Masahiro Sato. General description for nonequilibrium steady states in periodically driven dissipative quantum systems. *Science Advances*, 6(27), July 2020.

[87] Frank Verstraete, Michael M. Wolf, and J. Ignacio Cirac. Quantum computation and quantum-state engineering driven by dissipation. *Nature Physics*, 5(9):633–636, July 2009.

[88] Paolo Zanardi and Lorenzo Campos Venuti. Coherent quantum dynamics in steady-state manifolds of strongly dissipative systems. *Physical Review Letters*, 113(24), December 2014.

[89] E. M. Purcell and R. V. Pound. A nuclear spin system at negative temperature. *Physical Review*, 81(2):279–280, January 1951.

[90] Norman F. Ramsey. Thermodynamics and statistical mechanics at negative absolute temperatures. *Phys. Rev.*, 103:20–28, Jul 1956.

[91] Hans-Georg Schöpf. Zur thermodynamik negativer absoluter temperaturen. *Annalen der Physik*, 464(3-4):107–123, 1962.

[92] R. J. Tykodi. Negative kelvin temperatures: Some anomalies and a speculation. *American Journal of Physics*, 43(3):271–273, March 1975.

[93] André-Marie Tremblay. Comment on "negative kelvin temperatures: Some anomalies and a speculation". *American Journal of Physics*, 44(10):994–995, October 1976.

[94] R. J. Tykodi. Quasi-carnot cycles, negative kelvin temperatures, and the laws of thermodynamics. *American Journal of Physics*, 46(4):354–359, April 1978.

[95] A. P. Mosk. Atomic gases at negative kinetic temperature. *Physical Review Letters*, 95(4), July 2005.

[96] Akos Rapp, Stephan Mandt, and Achim Rosch. Equilibration rates and negative absolute temperatures for ultracold atoms in optical lattices. *Physical Review Letters*, 105(22), November 2010.

[97] S. Braun, J. P. Ronzheimer, M. Schreiber, S. S. Hodgman, T. Rom, I. Bloch, and U. Schneider. Negative absolute temperature for motional degrees of freedom. *Science*, 339(6115):52–55, January 2013.

[98] Lincoln D. Carr. Negative temperatures? *Science*, 339(6115):42–43, January 2013.

[99] Jörn Dunkel and Stefan Hilbert. Consistent thermostatistics forbids negative absolute temperatures. *Nature Physics*, 10(1):67–72, December 2013.

[100] Stefan Hilbert, Peter Hänggi, and Jörn Dunkel. Thermodynamic laws in isolated systems. *Physical Review E*, 90(6), December 2014.

[101] Peter Hänggi, Stefan Hilbert, and Jörn Dunkel. Meaning of temperature in different thermostatistical ensembles. *Philosophical Transactions of the Royal Society A: Mathematical, Physical and Engineering Sciences*, 374(2064):20150039, March 2016.

[102] Luca Cerino, Andrea Puglisi, and Angelo Vulpiani. A consistent description of fluctuations requires negative temperatures. *Journal of Statistical Mechanics: Theory and Experiment*, 2015(12):P12002, December 2015.

[103] Pierfrancesco Buonsante, Roberto Franzosi, and Augusto Smerzi. On the dispute between boltzmann and gibbs entropy. *Annals of Physics*, 375:414–434, December 2016.

[104] J. Poulter. In defense of negative temperature. *Physical Review E*, 93(3), March 2016.

[105] Eitan Abraham and Oliver Penrose. Physics of negative absolute temperatures. *Physical Review E*, 95(1), January 2017.

[106] Robert H Swendsen. Thermodynamics of finite systems: a key issues review. *Reports on Progress in Physics*, 81(7):072001, June 2018.

[107] Jian-Sheng Wang. Critique of the gibbs volume entropy and its implication, 2015.

[108] Robert H. Swendsen and Jian-Sheng Wang. Negative temperatures and the definition of entropy. *Physica A: Statistical Mechanics and its Applications*, 453:24–34, July 2016.

[109] J. E. Geusic, E. O. Schulz-DuBios, and H. E. D. Scovil. Quantum equivalent of the carnot cycle. *Phys. Rev.*, 156:343–351, Apr 1967.

[110] P T Landsberg. Heat engines and heat pumps at positive and negative absolute temperatures. *Journal of Physics A: Mathematical and General*, 10(10):1773–1770, October 1977.

[111] T Nakagomi. Mathematical formulation of the heat-engine theory of thermodynamics including negative absolute temperatures. *Journal of Physics A: Mathematical and General*, 13(1):291–299, January 1980.

[112] J Dunning-Davies. Negative absolute temperatures and carnot cycles. *Journal of Physics A: Mathematical and General*, 9(4):605–609, April 1976.

[113] J. Dunning-Davies. Remarks on negative absolute temperatures and carnot cycles. *American Journal of Physics*, 46(5):583–585, May 1978.

[114] P T Landsberg, R J Tykodi, and A M Tremblay. Systematics of carnot cycles at positive and negative kelvin temperatures. *Journal of Physics A: Mathematical and General*, 13(3):1063–1074, March 1980.

[115] Jing-Yi Xi and Hai-Tao Quan. Quantum heat engine and negative boltzmann temperature. *Communications in Theoretical Physics*, 68(3):347, September 2017.

[116] Rogério J. de Assis, Taysa M. de Mendonça, Celso J. Villas-Boas, Alexandre M. de Souza, Roberto S. Sarthour, Ivan S. Oliveira, and Norton G. de Almeida. Efficiency of a quantum otto heat engine operating under a reservoir at effective negative temperatures. *Physical Review Letters*, 122(24), June 2019.

[117] Gabriella G Damas, Rogério J de Assis, and Norton G de Almeida. Negative temperature is cool for cooling. *arXiv preprint arXiv:2204.09479*, 2022.

[118] M. Lewenstein, Ph. Balcou, M. Yu. Ivanov, Anne L'Huillier, and P. B. Corkum. Theory of high-harmonic generation by low-frequency laser fields. *Physical Review A*, 49(3):2117–2132, March 1994.

[119] Shambhu Ghimire, Anthony D. DiChiara, Emily Sistrunk, Pierre Agostini, Louis F. DiMauro, and David A. Reis. Observation of high-order harmonic generation in a bulk crystal. *Nature Physics*, 7(2):138–141, December 2010.

[120] P. B. Corkum. Plasma perspective on strong field multiphoton ionization. *Physical Review Letters*, 71(13):1994–1997, September 1993.

[121] D. N. Fittinghoff, P. R. Bolton, B. Chang, and K. C. Kulander. Observation of nonsequential double ionization of helium with optical tunneling. *Physical Review Letters*, 69(18):2642–2645, November 1992.

[122] Luis Plaja, Luis Roso, Kazimierz Rzaazewski, and Maciej Lewenstein. Generation of a train of attosecond pulses in the reflected field from a laser-plasma interaction. In *AIP Conference Proceedings*. AIP, 1998.

[123] Giampaolo Pitruzzello. A bright future for attosecond physics. *Nature Photonics*, 16(8):550–552, July 2022.

[124] Randy A. Bartels, Ariel Paul, Hans Green, Henry C. Kapteyn, Margaret M. Murnane, Sterling Backus, Ivan P. Christov, Yanwei Liu, David Attwood, and Chris Jacobsen. Generation of spatially coherent light at extreme ultraviolet wavelengths. *Science*, 297(5580):376–378, July 2002.

[125] N. H. Burnett, H. A. Baldis, M. C. Richardson, and G. D. Enright. Harmonic generation in CO2 laser target interaction. *Applied Physics Letters*, 31(3):172–174, August 1977.

[126] A. McPherson, G. Gibson, H. Jara, U. Johann, T. S. Luk, I. A. McIntyre, K. Boyer, and C. K. Rhodes. Studies of multiphoton production of vacuum-ultraviolet radiation in the rare gases. *Journal of the Optical Society of America B*, 4(4):595, April 1987.

[127] M Ferray, A L'Huillier, X F Li, L A Lompre, G Mainfray, and C Manus. Multiple-harmonic conversion of 1064 nm radiation in rare gases. *Journal of Physics B: Atomic, Molecular and Optical Physics*, 21(3):L31–L35, February 1988.

[128] M. Lewenstein, M. F. Ciappina, E. Pisanty, J. Rivera-Dean, P. Stammer, Th. Lamprou, and P. Tzallas. Generation of optical schrödinger cat states in intense laser–matter interactions. *Nature Physics*, 17(10):1104–1108, August 2021.

[129] O. Schubert, M. Hohenleutner, F. Langer, B. Urbanek, C. Lange, U. Huttner, D. Golde, T. Meier, M. Kira, S. W. Koch, and R. Huber. Sub-cycle control of terahertz high-harmonic generation by dynamical bloch oscillations. *Nature Photonics*, 8(2):119–123, January 2014.

[130] C. R. McDonald, G. Vampa, P. B. Corkum, and T. Brabec. Interband bloch oscillation mechanism for high-harmonic generation in semiconductor crystals. *Physical Review A*, 92(3), September 2015.

[131] Shambhu Ghimire, Anthony D. DiChiara, Emily Sistrunk, Georges Ndabashimiye, Urszula B. Szafruga, Anis Mohammad, Pierre Agostini, Louis F. DiMauro, and David A. Reis. Generation and propagation of high-order harmonics in crystals. *Physical Review A*, 85(4), April 2012.

[132] G. Vampa, C. R. McDonald, G. Orlando, D. D. Klug, P. B. Corkum, and T. Brabec. Theoretical analysis of high-harmonic generation in solids. *Physical Review Letters*, 113(7), August 2014.

[133] G. Vampa, T. J. Hammond, N. Thiré, B. E. Schmidt, F. Légaré, C. R. McDonald, T. Brabec, and P. B. Corkum. Linking high harmonics from gases and solids. *Nature*, 522(7557):462–464, June 2015.

[134] D. Golde, T. Meier, and S. W. Koch. High harmonics generated in semiconductor nanostructures by the coupled dynamics of optical inter- and intraband excitations. *Physical Review B*, 77(7), February 2008.

[135] Georges Ndabashimiye, Shambhu Ghimire, Mengxi Wu, Dana A. Browne, Kenneth J. Schafer, Mette B. Gaarde, and David A. Reis. Solid-state harmonics beyond the atomic limit. *Nature*, 534(7608):520–523, June 2016.

[136] Mina R. Bionta, Elissa Haddad, Adrien Leblanc, Vincent Gruson, Philippe Lassonde, Heide Ibrahim, Jérémie Chaillou, Nicolas Émond, Martin R. Otto, Álvaro Jiménez-Galán, Rui E. F. Silva, Misha Ivanov, Bradley J. Siwick, Mohamed Chaker, and François Légaré. Tracking ultrafast solid-state dynamics using high harmonic spectroscopy. *Physical Review Research*, 3(2), June 2021.

[137] Xiao-Liang Qi and Shou-Cheng Zhang. Topological insulators and superconductors. *Reviews of Modern Physics*, 83(4):1057–1110, October 2011.

[138] Da-Wei Wang, Chao Song, Wei Feng, Han Cai, Da Xu, Hui Deng, Hekang Li, Dongning Zheng, Xiaobo Zhu, H. Wang, Shi-Yao Zhu, and Marlan O. Scully. Synthesis of antisymmetric spin exchange interaction and chiral spin clusters in superconducting circuits. *Nature Physics*, 15(4):382–386, January 2019.

[139] Xiaoxiao Wu, Haiyan Fan, Tuo Liu, Zhongming Gu, Ruo-Yang Zhang, Jie Zhu, and Xiang Zhang. Topological phononics arising from fluid-solid interactions. *Nature Communications*, 13(1), October 2022.

[140] Alexander B. Khanikaev, S. Hossein Mousavi, Wang-Kong Tse, Mehdi Kargarian, Allan H. MacDonald, and Gennady Shvets. Photonic topological insulators. *Nature Materials*, 12(3):233–239, December 2012.

[141] Bo Wang, Tian Chen, and Xiangdong Zhang. Experimental observation of topologically protected bound states with vanishing chern numbers in a two-dimensional quantum walk. *Physical Review Letters*, 121(10), September 2018.

[142] Chao Chen, Xing Ding, Jian Qin, Yu He, Yi-Han Luo, Ming-Cheng Chen, Chang Liu, Xi-Lin Wang, Wei-Jun Zhang, Hao Li, Li-Xing You, Zhen Wang, Da-Wei Wang, Barry C. Sanders, Chao-Yang Lu, and Jian-Wei Pan. Observation of topologically protected edge states in a photonic two-dimensional quantum walk. *Physical Review Letters*, 121(10), September 2018.

[143] Zhaoyang Zhang, Rong Wang, Yiqi Zhang, Yaroslav V. Kartashov, Feng Li, Hua Zhong, Hua Guan, Kelin Gao, Fuli Li, Yanpeng Zhang, and Min Xiao. Observation of edge solitons in photonic graphene. *Nature Communications*, 11(1), April 2020.

[144] Nikhil Parappurath, Filippo Alpeggiani, L. Kuipers, and Ewold Verhagen. Direct observation of topological edge states in silicon photonic crystals: Spin, dispersion, and chiral routing. *Science Advances*, 6(10), March 2020.

[145] M. Hafezi, S. Mittal, J. Fan, A. Migdall, and J. M. Taylor. Imaging topological edge states in silicon photonics. *Nature Photonics*, 7(12):1001–1005, October 2013.

[146] Nikita A. Olekhno, Egor I. Kretov, Andrei A. Stepanenko, Polina A. Ivanova, Vitaly V. Yaroshenko, Ekaterina M. Puhtina, Dmitry S. Filonov, Barbara Cappello, Ladislau Matekovits, and Maxim A. Gorlach. Topological edge states of interacting photon pairs emulated in a topolectrical circuit. *Nature Communications*, 11(1), March 2020.

[147] Zhifeng Zhang, Mohammad Hosain Teimourpour, Jake Arkinstall, Mingsen Pan, Pei Miao, Henning Schomerus, Ramy El-Ganainy, and Liang Feng. Experimental realization of multiple

topological edge states in a 1d photonic lattice. *Laser and Photonics Reviews*, 13(2):1800202, January 2019.

[148] Yaakov Lumer, Mikael C. Rechtsman, Yonatan Plotnik, and Mordechai Segev. Instability of bosonic topological edge states in the presence of interactions. *Physical Review A*, 94(2), August 2016.

[149] Tun Cao, Linhan Fang, Ying Cao, Nan Li, Zhiyou Fan, and Zhiguo Tao. Dynamically reconfigurable topological edge state in phase change photonic crystals. *Science Bulletin*, 64(12):814–822, June 2019.

[150] P. St-Jean, V. Goblot, E. Galopin, A. Lemaître, T. Ozawa, L. Le Gratiet, I. Sagnes, J. Bloch, and A. Amo. Lasing in topological edge states of a one-dimensional lattice. *Nature Photonics*, 11(10):651–656, September 2017.

[151] Peiheng Zhou, Gui-Geng Liu, Yihao Yang, Yuan-Hang Hu, Sulin Ma, Haoran Xue, Qiang Wang, Longjiang Deng, and Baile Zhang. Observation of photonic antichiral edge states. *Physical Review Letters*, 125(26), December 2020.

[152] F. Alpeggiani and L. Kuipers. Topological edge states in bichromatic photonic crystals. *Optica*, 6(1):96, January 2019.

[153] Sebabrata Mukherjee, Alexander Spracklen, Manuel Valiente, Erika Andersson, Patrik Öhberg, Nathan Goldman, and Robert R. Thomson. Experimental observation of anomalous topological edge modes in a slowly driven photonic lattice. *Nature Communications*, 8(1), January 2017.

[154] Yuhao Kang, Xiang Ni, Xiaojun Cheng, Alexander B. Khanikaev, and Azriel Z. Genack. Pseudo-spin–valley coupled edge states in a photonic topological insulator. *Nature Communications*, 9(1), August 2018.

[155] Daria Smirnova, Sergey Kruk, Daniel Leykam, Elizaveta Melik-Gaykazyan, Duk-Yong Choi, and Yuri Kivshar. Third-harmonic generation in photonic topological metasurfaces. *Physical Review Letters*, 123(10), September 2019.

[156] Tzuhsuan Ma and Gennady Shvets. Scattering-free edge states between heterogeneous photonic topological insulators. *Physical Review B*, 95(16), April 2017.

[157] Wei Nie and Yu xi Liu. Bandgap-assisted quantum control of topological edge states in a cavity. *Physical Review Research*, 2(1), March 2020.

[158] M. Milićević, T. Ozawa, G. Montambaux, I. Carusotto, E. Galopin, A. Lemaître, L. Le Gratiet, I. Sagnes, J. Bloch, and A. Amo. Orbital edge states in a photonic honeycomb lattice. *Physical Review Letters*, 118(10), March 2017.

[159] Yu-Xin Wang and Aashish A. Clerk. Intrinsic and induced quantum quenches for enhancing qubit-based quantum noise spectroscopy. *Nature Communications*, 12(1), November 2021.

[160] Shiwei Tang, Yikai Xu, Fei Ding, and Feng Liu. Continuously tunable topological defects and topological edge states in dielectric photonic crystals. *Physical Review B*, 107(4), January 2023.

[161] S. K. Kanungo, J. D. Whalen, Y. Lu, M. Yuan, S. Dasgupta, F. B. Dunning, K. R. A. Hazzard, and T. C. Killian. Realizing topological edge states with rydberg-atom synthetic dimensions. *Nature Communications*, 13(1), February 2022.

[162] L. Xiao, X. Zhan, Z. H. Bian, K. K. Wang, X. Zhang, X. P. Wang, J. Li, K. Mochizuki, D. Kim, N. Kawakami, W. Yi, H. Obuse, B. C. Sanders, and P. Xue. Observation of topological edge states in parity–time-symmetric quantum walks. *Nature Physics*, 13(11):1117–1123, July 2017.

[163] G. Pelegrí, A. M. Marques, R. G. Dias, A. J. Daley, J. Mompart, and V. Ahufinger. Topological edge states and aharanov-bohm caging with ultracold atoms carrying orbital angular momentum. *Physical Review A*, 99(2), February 2019.

[164] Nathan Goldman, Jean Dalibard, Alexandre Dauphin, Fabrice Gerbier, Maciej Lewenstein, Peter Zoller, and Ian B. Spielman. Direct imaging of topological edge states in cold-atom systems.

Proceedings of the National Academy of Sciences, 110(17):6736–6741, April 2013.

[165] Martin Leder, Christopher Grossert, Lukas Sitta, Maximilian Genske, Achim Rosch, and Martin Weitz. Real-space imaging of a topologically protected edge state with ultracold atoms in an amplitude-chirped optical lattice. *Nature Communications*, 7(1), October 2016.

[166] Chao Hang, Dmitry A. Zezyulin, Guoxiang Huang, and Vladimir V. Konotop. Nonlinear topological edge states in a non-hermitian array of optical waveguides embedded in an atomic gas. *Physical Review A*, 103(4), April 2021.

[167] Entong Zhao, Chengdong He, and Gyu-Boong Jo. "designing synthetic topological matter with atoms and lights". *Light: Science and Applications*, 11(1), February 2022.

[168] Cheng He, Xu Ni, Hao Ge, Xiao-Chen Sun, Yan-Bin Chen, Ming-Hui Lu, Xiao-Ping Liu, and Yan-Feng Chen. Acoustic topological insulator and robust one-way sound transport. *Nature Physics*, 12(12):1124–1129, aug 2016.

[169] Xiang Ni, Kai Chen, Matthew Weiner, David J. Apigo, Camelia Prodan, Andrea Alù, Emil Prodan, and Alexander B. Khanikaev. Observation of hofstadter butterfly and topological edge states in reconfigurable quasi-periodic acoustic crystals. *Communications Physics*, 2(1), June 2019.

[170] He Gao, Haoran Xue, Qiang Wang, Zhongming Gu, Tuo Liu, Jie Zhu, and Baile Zhang. Observation of topological edge states induced solely by non-hermiticity in an acoustic crystal. *Physical Review B*, 101(18), May 2020.

[171] Weiwei Zhu, Xinsheng Fang, Dongting Li, Yong Sun, Yong Li, Yun Jing, and Hong Chen. Simultaneous observation of a topological edge state and exceptional point in an open and non-hermitian acoustic system. *Physical Review Letters*, 121(12), September 2018.

[172] Ze-Guo Chen, Changqing Xu, Rasha Al Jahdali, Jun Mei, and Ying Wu. Corner states in a second-order acoustic topological insulator as bound states in the continuum. *Phys. Rev. B*, 100:075120, Aug 2019.

[173] Xiang Ni, Maxim A Gorlach, Andrea Alu, and Alexander B Khanikaev. Topological edge states in acoustic kagome lattices. *New Journal of Physics*, 19(5):055002, may 2017.

[174] Marc-Antoine Lemonde, Vittorio Peano, Peter Rabl, and Dimitris G Angelakis. Quantum state transfer via acoustic edge states in a 2d optomechanical array. *New Journal of Physics*, 21(11):113030, nov 2019.

[175] Amir Darabi and Michael J. Leamy. Tunable nonlinear topological insulator for acoustic waves. *Physical Review Applied*, 12(4), oct 2019.

[176] Xinhua Wen, Chunyin Qiu, Yajuan Qi, Liping Ye, Manzhu Ke, Fan Zhang, and Zhengyou Liu. Acoustic landau quantization and quantum-hall-like edge states. *Nature Physics*, 15(4):352–356, mar 2019.

[177] Guancong Ma, Meng Xiao, and C. T. Chan. Topological phases in acoustic and mechanical systems. *Nature Reviews Physics*, 1(4):281–294, March 2019.

[178] Haoran Xue, Yahui Yang, Fei Gao, Yidong Chong, and Baile Zhang. Acoustic higher-order topological insulator on a kagome lattice. *Nature Materials*, 18(2):108–112, December 2018.

[179] Matthew Weiner, Xiang Ni, Mengyao Li, Andrea Alù, and Alexander B. Khanikaev. Demonstration of a third-order hierarchy of topological states in a three-dimensional acoustic metamaterial. *Science Advances*, 6(13), mar 2020.

[180] Xiang Ni, Mengyao Li, Matthew Weiner, Andrea Alù, and Alexander B. Khanikaev. Demonstration of a quantized acoustic octupole topological insulator. *Nature Communications*, 11(1), apr 2020.

[181] Li Zhang, Yihao Yang, Yong Ge, Yi-Jun Guan, Qiaolu Chen, Qinghui Yan, Fujia Chen, Rui Xi, Yuanzhen Li, Ding Jia, Shou-Qi Yuan, Hong-Xiang Sun, Hongsheng Chen, and Baile Zhang. Acoustic non-hermitian skin effect from twisted winding topology. *Nature Communications*, 12(1), nov 2021.

[182] Zhong-Ke Ding, Yu-Jia Zeng, Hui Pan, Nannan Luo, Jiang Zeng, Li-Ming Tang, and Ke-Qiu Chen. Edge states of topological acoustic phonons in graphene zigzag nanoribbons. *Physical Review B*, 106(12), sep 2022.

[183] Haoran Xue, Yihao Yang, and Baile Zhang. Topological acoustics. *Nature Reviews Materials*, 7(12):974–990, August 2022.

[184] Joel E. Moore. The birth of topological insulators. *Nature*, 464(7286):194–198, March 2010.

[185] M. Z. Hasan and C. L. Kane. Colloquium: Topological insulators. *Reviews of Modern Physics*, 82(4):3045–3067, November 2010.

[186] Miguel A. Bandres, Steffen Wittek, Gal Harari, Midya Parto, Jinhan Ren, Mordechai Segev, Demetrios N. Christodoulides, and Mercedeh Khajavikhan. Topological insulator laser: Experiments. *Science*, 359(6381), March 2018.

[187] Yoshinori Tokura, Kenji Yasuda, and Atsushi Tsukazaki. Magnetic topological insulators. *Nature Reviews Physics*, 1(2):126–143, January 2019.

[188] Masatoshi Sato and Yoichi Ando. Topological superconductors: a review. *Reports on Progress in Physics*, 80(7):076501, May 2017.

[189] Zhiwang Zhang, Ye Tian, Ying Cheng, Qi Wei, Xiaojun Liu, and Johan Christensen. Topological acoustic delay line. *Physical Review Applied*, 9(3), mar 2018.

[190] S. M. Frolov, M. J. Manfra, and J. D. Sau. Topological superconductivity in hybrid devices. *Nature Physics*, 16(7):718–724, July 2020.

[191] Ayelet J. Uzan, Hadas Soifer, Oren Pedatzur, Alex Clergerie, Sylvain Larroque, Barry D. Bruner, Bernard Pons, Misha Ivanov, Olga Smirnova, and Nirit Dudovich. Spatial molecular interferometry via multidimensional high-harmonic spectroscopy. *Nature Photonics*, 14(3):188–194, February 2020.

[192] Alexis Chacón, Dasol Kim, Wei Zhu, Shane P. Kelly, Alexandre Dauphin, Emilio Pisanty, Andrew S. Maxwell, Antonio Picón, Marcelo F. Ciappina, Dong Eon Kim, Christopher Ticknor, Avadh Saxena, and Maciej Lewenstein. Circular dichroism in higher-order harmonic generation: Heralding topological phases and transitions in chern insulators. *Physical Review B*, 102(13), October 2020.

[193] Eleftherios Goulielmakis and Thomas Brabec. High harmonic generation in condensed matter. *Nature Photonics*, 16(6):411–421, May 2022.

[194] Javier Rivera-Dean, Philipp Stammer, Andrew S. Maxwell, Theocharis Lamprou, Andrés F. Ordóñez, Emilio Pisanty, Paraskevas Tzallas, Maciej Lewenstein, and Marcelo F. Ciappina. Quantum optical analysis of high-harmonic generation in solids within a wannier-bloch picture, 2022.

[195] Christoph Jürß and Dieter Bauer. High-harmonic generation in su-schrieffer-heeger chains. *Physical Review B*, 99(19), May 2019.

[196] Sadi Carnot. *Réflexions sur la puissance motrice de feu et sur les machines propres à développer cette puissance*. Bachelier, Paris, 1824.

[197] Herbert B Callen. *Thermodynamics and an introduction to thermostatistics; 2nd ed.* Wiley, New York, NY, 1985.

[198] Michal Horodecki and Jonathan Oppenheim. Fundamental limitations for quantum and nanoscale thermodynamics. *Nature Communications*, 4:2059, 2013.

[199] Fernando G. S. L. Brandao, Michal Horodecki, Nelly Ng, Jonathan Oppenheim, and Stephanie Wehner. The second laws

of quantum thermodynamics. *Proc. Natl. Acad. Sci.*, 112:3275–3279, 2015.

[200] J. Gemmer, M. Michel, and G. Mahler. *Lecture Notes in Physics: Quantum thermodynamics*, volume 748. Berlin, Heidelberg: Springer, 2009.

[201] Felix Binder, Luis A. Correa, Christian Gogolin, Janet Anders, and Gerardo Adesso. *Thermodynamics in the Quantum Regime*, volume 195. Springer International Publishing, 2018.

[202] C. Jarzynski. Nonequilibrium equality for free energy differences. *Phys. Rev. Lett.*, 78:2690–2693, Apr 1997.

[203] Gavin E. Crooks. Entropy production fluctuation theorem and the nonequilibrium work relation for free energy differences. *Phys. Rev. E*, 60:2721–2726, Sep 1999.

[204] Michele Campisi, Peter Hänggi, and Peter Talkner. Colloquium: Quantum fluctuation relations: Foundations and applications. *Rev. Mod. Phys.*, 83:771–791, Jul 2011.

[205] Fernando G. S. L. Brandao, Michal Horodecki, Jonathan Oppenheim, Joseph M. Renes, and Robert W. Spekkens. Resource theory of quantum states out of thermal equilibrium. *Physical Review Letters*, 111:250404, Dec 2013.

[206] Paul Skrzypczyk, Anthony J. Short, and Sandu Popescu. Work extraction and thermodynamics for individual quantum systems. *Nature Communications*, 5:4185, 2014.

[207] Johan Aberg. Truly work-like work extraction via a single-shot analysis. *Nature Communications*, 4:1925, 2013.

[208] Matteo Lostaglio, Kamil Korzekwa, David Jennings, and Terry Rudolph. Quantum coherence, time-translation symmetry, and thermodynamics. *Physical Review X*, 5:021001, Apr 2015.

[209] Piotr Ćwikliński, Michał Studziński, Michał Horodecki, and Jonathan Oppenheim. Limitations on the evolution of quantum coherences: Towards fully quantum second laws of thermodynamics. *Physical Review Letters*, 115:210403, Nov 2015.

[210] Matteo Lostaglio, David Jennings, and Terry Rudolph. Description of quantum coherence in thermodynamic processes requires constraints beyond free energy. *Nature Communications*, 6:6383, 2015.

[211] Manabendra Nath Bera, Arnau Riera, Maciej Lewenstein, and Andreas Winter. Generalized laws of thermodynamics in the presence of correlations. *Nature Communications*, 8:2180, 2017.

[212] Manabendra Nath Bera, Arnau Riera, Maciej Lewenstein, Zahra Baghali Khanian, and Andreas Winter. Thermodynamics as a Consequence of Information Conservation. *Quantum*, 3:121, February 2019.

[213] Carlo Sparaciari, Jonathan Oppenheim, and Tobias Fritz. Resource theory for work and heat. *Phys. Rev. A*, 96:052112, Nov 2017.

[214] Raam Uzdin and Saar Rahav. Global passivity in microscopic thermodynamics. *Phys. Rev. X*, 8:021064, Jun 2018.

[215] Markus P. Müller. Correlating thermal machines and the second law at the nanoscale. *Phys. Rev. X*, 8:041051, Dec 2018.

[216] Gilad Gour, David Jennings, Francesco Buscemi, and Iman Duan, Runyao Marvian. Quantum majorization and a complete set of entropic conditions for quantum thermodynamics. *Nature Communications*, 9:5352, 2018.

[217] Álvaro M. Alhambra, Lluis Masanes, Jonathan Oppenheim, and Christopher Perry. Fluctuating work: From quantum thermodynamical identities to a second law equality. *Phys. Rev. X*, 6:041017, Oct 2016.

[218] Johan Åberg. Fully quantum fluctuation theorems. *Phys. Rev. X*, 8:011019, Feb 2018.

[219] G. Guarnieri, N. H. Y. Ng, K. Modi, J. Eisert, M. Paternostro, and J. Goold. Quantum work statistics and resource theories: Bridging the gap through rényi divergences. *Phys. Rev. E*, 99:050101(R), May 2019.

[220] R Alicki. The quantum open system as a model of the heat engine. *Journal of Physics A: Mathematical and General*, 12(5):L103–L107, may 1979.

[221] Tien D. Kieu. The second law, maxwell's demon, and work derivable from quantum heat engines. *Phys. Rev. Lett.*, 93:140403, Sep 2004.

[222] Gatien Verley, Massimiliano Esposito, Tim Willaert, and Christian Van den Broeck. The unlikely carnot efficiency. *Nature Communications*, 5:4721, 2014.

[223] J. Roßnagel, O. Abah, F. Schmidt-Kaler, K. Singer, and E. Lutz. Nanoscale heat engine beyond the carnot limit. *Phys. Rev. Lett.*, 112:030602, Jan 2014.

[224] Raam Uzdin, Amikam Levy, and Ronnie Kosloff. Equivalence of quantum heat machines, and quantum-thermodynamic signatures. *Phys. Rev. X*, 5:031044, Sep 2015.

[225] Hiroyasu Tajima and Masahito Hayashi. Finite-size effect on optimal efficiency of heat engines. *Phys. Rev. E*, 96:012128, Jul 2017.

[226] Nelly Huei Ying Ng, Mischa Prebin Woods, and Stephanie Wehner. Surpassing the carnot efficiency by extracting imperfect work. *New Journal of Physics*, 19(11):113005, nov 2017.

[227] Kosuke Ito and Masahito Hayashi. Optimal performance of generalized heat engines with finite-size baths of arbitrary multiple conserved quantities beyond independent-and-identical-distribution scaling. *Phys. Rev. E*, 97:012129, Jan 2018.

[228] Mischa P. Woods, Ralph Silva, and Jonathan Oppenheim. Autonomous quantum machines and finite-sized clocks. *Annales Henri Poincaré*, 20(1):125–218, Jan 2019.

[229] Mischa P. Woods, Nelly Huei Ying Ng, and Stephanie Wehner. The maximum efficiency of nano heat engines depends on more than temperature. *Quantum*, 3:177, August 2019.

[230] F. L. Curzon and B. Ahlborn. Efficiency of a carnot engine at maximum power output. *American Journal of Physics*, 43(1):22–24, 1975.

[231] R. S. Berry, V. Kazakov, S. Sieniutycz, Z. Szwast, and A. M. Tsirlin. *Thermodynamic Optimization of Finite-Time Processes*. Wiley, 2000.

[232] P. Salamon, J. D. Nulton, G. Siragusa, T. R. Andersen, and A. Limon. Principles of control thermodynamics. *Energy*, 26(3):307 – 319, 2001.

[233] Zahra Baghali Khanian, Manabendra Nath Bera, Arnau Riera, Maciej Lewenstein, and Andreas Winter. Resource theory of heat and work with non-commuting charges: yet another new foundation of thermodynamics. *arXiv:2011.08020*, 2020.

[234] Ronnie Kosloff and Amikam Levy. Quantum heat engines and refrigerators: Continuous devices. *Annu. Rev. Phys. Chem.*, 65(1):365–393, 2014.

[235] Jan Klaers, Stefan Faelt, Atac Imamoglu, and Emre Togan. Squeezed thermal reservoirs as a resource for a nanomechanical engine beyond the carnot limit. *Phys. Rev. X*, 7:031044, Sep 2017.

[236] J. Roßnagel, O. Abah, F. Schmidt-Kaler, K. Singer, and E. Lutz. Nanoscale heat engine beyond the carnot limit. *Phys. Rev. Lett.*, 112:030602, Jan 2014.

[237] Ken Funo and Masahito Ueda. Work fluctuation-dissipation trade-off in heat engines. *Phys. Rev. Lett.*, 115:260601, Dec 2015.

[238] Mischa P. Woods, Nelly Huei Ying Ng, and Stephanie Wehner. The maximum efficiency of nano heat engines depends on more than temperature. *Quantum*, 3:177, August 2019.

[239] Sreekanth K. Manikandan, Lennart Dabelow, Ralf Eichhorn, and Supriya Krishnamurthy. Efficiency fluctuations in microscopic machines. *Phys. Rev. Lett.*, 122:140601, Apr 2019.

[240] Massimiliano Esposito, Ryoichi Kawai, Katja Lindenberg, and Christian Van den Broeck. Quantum-dot carnot engine at maximum power. *Phys. Rev. E*, 81:041106, Apr 2010.

[241] Marlan O. Scully, Kimberly R. Chapin, Konstantin E. Dorfman, Moochan Barnabas Kim, and Anatoly Svidzinsky. Quantum heat engine power can be increased by noise-induced coherence. *Proc. Natl. Acad. Sci.*, 108(37):15097–15100, 2011.

[242] Michele Campisi and Rosario Fazio. The power of a critical heat engine. *Nat. Commun.*, 7:11895, 2016.

[243] Viktor Holubec and Artem Ryabov. Maximum efficiency of low-dissipation heat engines at arbitrary power. *Journal of Statistical Mechanics: Theory and Experiment*, 2016(7):073204, jul 2016.

[244] Kay Brandner, Michael Bauer, and Udo Seifert. Universal coherence-induced power losses of quantum heat engines in linear response. *Phys. Rev. Lett.*, 119:170602, Oct 2017.

[245] Tobias Denzler and Eric Lutz. Power fluctuations in a finite-time quantum carnot engine. *arXiv:2007.01034*, 2020.

[246] O. Abah, J. Roßnagel, G. Jacob, S. Deffner, F. Schmidt-Kaler, K. Singer, and E. Lutz. Single-ion heat engine at maximum power. *Phys. Rev. Lett.*, 109:203006, Nov 2012.

[247] Massimiliano Esposito, Ryoichi Kawai, Katja Lindenberg, and Christian Van den Broeck. Efficiency at maximum power of low-dissipation carnot engines. *Phys. Rev. Lett.*, 105:150603, Oct 2010.

[248] Juncheng Guo, Junyi Wang, Yuan Wang, and Jincan Chen. Universal efficiency bounds of weak-dissipative thermodynamic cycles at the maximum power output. *Phys. Rev. E*, 87:012133, Jan 2013.

[249] Yu-Han Ma, Dazhi Xu, Hui Dong, and Chang-Pu Sun. Universal constraint for efficiency and power of a low-dissipation heat engine. *Phys. Rev. E*, 98:042112, Oct 2018.

[250] Viktor Holubec and Artem Ryabov. Cycling tames power fluctuations near optimum efficiency. *Phys. Rev. Lett.*, 121:120601, Sep 2018.

[251] Konstantin E. Dorfman, Dazhi Xu, and Jianshu Cao. Efficiency at maximum power of a laser quantum heat engine enhanced by noise-induced coherence. *Phys. Rev. E*, 97:042120, Apr 2018.

[252] Paolo Abiuso and Martí Perarnau-Llobet. Optimal cycles for low-dissipation heat engines. *Phys. Rev. Lett.*, 124:110606, Mar 2020.

[253] Kay Brandner and Keiji Saito. Thermodynamic geometry of microscopic heat engines. *Phys. Rev. Lett.*, 124:040602, Jan 2020.

[254] Harry J. D. Miller and Mohammad Mehboudi. Geometry of work fluctuations versus efficiency in microscopic thermal machines. *Phys. Rev. Lett.*, 125:260602, Dec 2020.

[255] Varinder Singh. Optimal operation of a three-level quantum heat engine and universal nature of efficiency. *Phys. Rev. Research*, 2:043187, Nov 2020.

[256] Giuliano Benenti, Giulio Casati, and Jiao Wang. Power, efficiency, and fluctuations in steady-state heat engines. *Phys. Rev. E*, 102:040103, Oct 2020.

[257] Johannes Roßnagel, Samuel T. Dawkins, Karl N. Tolazzi, Obinna Abah, Eric Lutz, Ferdinand Schmidt-Kaler, and Kilian Singer. A single-atom heat engine. *Science*, 352(6283):325–329, 2016.

[258] Sushant Saryal and Bijay Kumar Agarwalla. Bounds on fluctuations for finite-time quantum otto cycle. *arXiv:2104.12173*, 2021.

[259] Sushant Saryal, Matthew Gerry, Ilia Khait, Dvira Segal, and Bijay Kumar Agarwalla. Universal bounds on fluctuations in continuous thermal machines. *arXiv:2103.13513*, 2021.

[260] Quentin Bouton, Jens Nettersheim, Sabrina Burgardt, Daniel Adam, Eric Lutz, and Artur Widera. A quantum heat engine

driven by atomic collisions. *Nature Communications*, 12(1), April 2021.

[261] Mohit Lal Bera, Maciej Lewenstein, and Manabendra Nath Bera. Attaining Carnot efficiency with quantum and nanoscale heat engines. *npj Quantum Information*, 7:31, 2021.

[262] J. Anandan and Y. Aharonov. Geometry of quantum evolution. *Phys. Rev. Lett.*, 65:1697–1700, Oct 1990.

[263] Christopher C. Gerry and J. H. Eberly. Dynamics of a raman coupled model interacting with two quantized cavity fields. *Phys. Rev. A*, 42:6805–6815, Dec 1990.

[264] Ying Wu. Effective raman theory for a three-level atom in the Λ configuration. *Phys. Rev. A*, 54:1586–1592, Aug 1996.

[265] Andrew D Greentree, Jens Koch, and Jonas Larson. Fifty years of jaynes–cummings physics. *J. Phys. B: At. Mol. Opt. Phys.*, 46(22):220201, nov 2013.

[266] H. E. D. Scovil and E. O. Schulz-DuBois. Three-level masers as heat engines. *Phys. Rev. Lett.*, 2:262–263, Mar 1959.

[267] Arnab Ghosh, David Gelbwaser-Klimovsky, Wolfgang Niedenzu, Alexander I. Lvovsky, Igor Mazets, Marlan O. Scully, and Gershon Kurizki. Two-level masers as heat-to-work converters. *Proc. Natl. Acad. Sci.*, 115(40):9941–9944, 2018.

[268] Henning Struchtrup. Work storage in states of apparent negative thermodynamic temperature. *Physical Review Letters*, 120(25), June 2018.

[269] Jens Nettersheim, Sabrina Burgardt, Quentin Bouton, Daniel Adam, Eric Lutz, and Artur Widera. Power of a quasispin quantum otto engine at negative effective spin temperature. *PRX Quantum*, 3(4), December 2022.

[270] E. Boukobza and D. J. Tannor. Thermodynamics of bipartite systems: Application to light-matter interactions. *Physical Review A*, 74(6), December 2006.

[271] E. Boukobza and D. J. Tannor. Thermodynamic analysis of quantum light amplification. *Physical Review A*, 74(6), December 2006.

[272] E. Boukobza and D. J. Tannor. Three-level systems as amplifiers and attenuators: A thermodynamic analysis. *Physical Review Letters*, 98(24), June 2007.

[273] R Alicki. The quantum open system as a model of the heat engine. *Journal of Physics A: Mathematical and General*, 12(5):L103–L107, May 1979.

[274] Ronnie Kosloff and Amikam Levy. Quantum heat engines and refrigerators: Continuous devices. *Annual Review of Physical Chemistry*, 65(1):365–393, April 2014.

[275] Shunsuke A. Sato, Hideki Hirori, Yasuyuki Sanari, Yoshihiko Kanemitsu, and Angel Rubio. High-order harmonic generation in graphene: Nonlinear coupling of intraband and interband transitions. *Physical Review B*, 103(4), January 2021.

[276] Rui-Xin Zuo, Xiao-Hong Song, Xi-Wang Liu, Shi-Dong Yang, and Wei-Feng Yang. Influence of intraband motion on the interband excitation and high harmonic generation. *Chinese Physics B*, 28(9):094208, September 2019.

[277] Takuya Higuchi, Mark I. Stockman, and Peter Hommelhoff. Strong-field perspective on high-harmonic radiation from bulk solids. *Physical Review Letters*, 113(21), November 2014.

[278] Seunghwoi Han, Lisa Ortmann, Hyunwoong Kim, Yong Woo Kim, Takashi Oka, Alexis Chacon, Brent Doran, Marcelo Ciappina, Maciej Lewenstein, Seung-Woo Kim, Seungchul Kim, and Alexandra S. Landsman. Extraction of higher-order nonlinear electronic response in solids using high harmonic generation. *Nature Communications*, 10(1), July 2019.

[279] Naotaka Yoshikawa, Kohei Nagai, Kento Uchida, Yuhei Takaguchi, Shogo Sasaki, Yasumitsu Miyata, and Koichiro Tanaka. Interband resonant high-harmonic generation by valley polarized electron-hole pairs. *Nature Communications*, 10(1), August 2019.

[280] Shambhu Ghimire and David A. Reis. High-harmonic generation from solids. *Nature Physics*, 15(1):10–16, November 2018.

[281] K. J. Schafer, Baorui Yang, L. F. DiMauro, and K. C. Kulander. Above threshold ionization beyond the high harmonic cutoff. *Physical Review Letters*, 70(11):1599–1602, March 1993.

[282] M. Garg, M. Zhan, T. T. Luu, H. Lakhotia, T. Klostermann, A. Guggenmos, and E. Goulielmakis. Multi-petahertz electronic metrology. *Nature*, 538(7625):359–363, October 2016.

[283] Neil W. Ashcroft and N. David Mermin. *Solid state physics*. Holt, Rinehart and Winston, New York, 1976.

[284] Mengxi Wu, Shambhu Ghimire, David A. Reis, Kenneth J. Schafer, and Mette B. Gaarde. High-harmonic generation from bloch electrons in solids. *Physical Review A*, 91(4), April 2015.

[285] J Lloyd-Hughes, P M Oppeneer, T Pereira dos Santos, A Schleife, S Meng, M A Sentef, M Ruggenthaler, A Rubio, I Radu, M Murnane, X Shi, H Kapteyn, B Stadtmüller, K M Dani, F H da Jornada, E Prinz, M Aeschlimann, R L Milot, M Burdanova, J Boland, T Cocker, and F Hegmann. The 2021 ultrafast spectroscopic probes of condensed matter roadmap. *Journal of Physics: Condensed Matter*, 33(35):353001, July 2021.

[286] Tao Jiang, Vasily Kravtsov, Mikhail Tokman, Alexey Belyanin, and Markus B. Raschke. Ultrafast coherent nonlinear nanooptics and nanoimaging of graphene. *Nature Nanotechnology*, 14(9):838–843, August 2019.

[287] Max Gulde, Simon Schweda, Gero Storeck, Manisankar Maiti, Hak Ki Yu, Alec M. Wodtke, Sascha Schäfer, and Claus Ropers. Ultrafast low-energy electron diffraction in transmission resolves polymer/graphene superstructure dynamics. *Science*, 345(6193):200–204, July 2014.

[288] M. Hohenleutner, F. Langer, O. Schubert, M. Knorr, U. Huttner, S. W. Koch, M. Kira, and R. Huber. Real-time observation of interfering crystal electrons in high-harmonic generation. *Nature*, 523(7562):572–575, July 2015.

[289] Nicolas Tancogne-Dejean, Michael A. Sentef, and Angel Rubio. Ultrafast modification of hubbard u in a strongly correlated material:*ab initio* high-harmonic generation in NiO. *Physical Review Letters*, 121(9), August 2018.

[290] Philipp Stammer, Javier Rivera-Dean, Andrew Maxwell, Theocharis Lamprou, Andrés Ordóñez, Marcelo F. Ciappina, Paraskevas Tzallas, and Maciej Lewenstein. Quantum electrodynamics of intense laser-matter interactions: A tool for quantum state engineering. *PRX Quantum*, 4(1), January 2023.

[291] Ferenc Krausz and Misha Ivanov. Attosecond physics. *Rev. Mod. Phys.*, 81:163–234, Feb 2009.

[292] Shambhu Ghimire, Georges Ndabashimiye, Anthony D DiChiara, Emily Sistrunk, Mark I Stockman, Pierre Agostini, Louis F DiMauro, and David A Reis. Strong-field and attosecond physics in solids. *Journal of Physics B: Atomic, Molecular and Optical Physics*, 47(20):204030, October 2014.

[293] Ofer Neufeld, David Ayuso, Piero Decleva, Misha Y. Ivanov, Olga Smirnova, and Oren Cohen. Ultrasensitive chiral spectroscopy by dynamical symmetry breaking in high harmonic generation. *Physical Review X*, 9(3), July 2019.

[294] Thomas A. A. Oliver. Recent advances in multidimensional ultrafast spectroscopy. *Royal Society Open Science*, 5(1):171425, January 2018.

[295] Natalie L. Gruenke, M. Fernanda Cardinal, Michael O. McAnally, Renee R. Frontiera, George C. Schatz, and Richard P. Van Duyne. Ultrafast and nonlinear surface-enhanced raman spectroscopy. *Chemical Society Reviews*, 45(8):2263–2290, 2016.

[296] F. H. M. Faisal and J. Z. Kamiński. Floquet-bloch theory of high-harmonic generation in periodic structures. *Physical Review A*, 56(1):748–762, July 1997.

[297] Jordi Alcalà, Utso Bhattacharya, Jens Biegert, Marcelo Ciappina, Ugaitz Elu, Tobias Graß, Piotr T. Grochowski, Maciej Lewenstein, Anna Palau, Themistoklis P. H. Sidiropoulos, Tobias Steinle, and Igor Tyulnev. High-harmonic spectroscopy of

quantum phase transitions in a high-tc superconductor. *Proceedings of the National Academy of Sciences*, 119(40), September 2022.

[298] Margherita Maiuri, Marco Garavelli, and Giulio Cerullo. Ultrafast spectroscopy: State of the art and open challenges. *Journal of the American Chemical Society*, 142(1):3–15, December 2019.

[299] Sergey Zayko, Ofer Kfir, Michael Heigl, Michael Lohmann, Murat Sivis, Manfred Albrecht, and Claus Ropers. Ultrafast high-harmonic nanoscopy of magnetization dynamics. *Nature Communications*, 12(1), November 2021.

[300] Mara Strungaru, Mathias Augustin, and Elton J. G. Santos. Ultrafast laser-driven topological spin textures on a 2d magnet. *npj Computational Materials*, 8(1), August 2022.

[301] Yang Yang, Richard B. Wilson, Jon Gorchon, Charles-Henri Lambert, Sayeef Salahuddin, and Jeffrey Bokor. Ultrafast magnetization reversal by picosecond electrical pulses. *Science Advances*, 3(11), November 2017.

[302] Alfred Zong, Bailey R. Nebgen, Sheng-Chih Lin, Jacob A. Spies, and Michael Zuerch. Emerging ultrafast techniques for studying quantum materials. *Nature Reviews Materials*, February 2023.

[303] Murat Sivis, Marco Taucer, Giulio Vampa, Kyle Johnston, André Staudte, Andrei Yu. Naumov, D. M. Villeneuve, Claus Ropers, and P. B. Corkum. Tailored semiconductors for high-harmonic optoelectronics. *Science*, 357(6348):303–306, July 2017.

[304] B. Frietsch, A. Donges, R. Carley, M. Teichmann, J. Bowlan, K. Döbrich, K. Carva, D. Legut, P. M. Oppeneer, U. Nowak, and M. Weinelt. The role of ultrafast magnon generation in the magnetization dynamics of rare-earth metals. *Science Advances*, 6(39), September 2020.

[305] Hiroyuki Nishidome, Kohei Nagai, Kento Uchida, Yota Ichinose, Yohei Yomogida, Yasumitsu Miyata, Koichiro Tanaka, and Kazuhiro Yanagi. Control of high-harmonic generation

by tuning the electronic structure and carrier injection. *Nano Letters*, 20(8):6215–6221, July 2020.

[306] W. Becker, A. Lohr, M. Kleber, and M. Lewenstein. A unified theory of high-harmonic generation: Application to polarization properties of the harmonics. *Physical Review A*, 56(1):645–656, July 1997.

[307] Óscar Zurrón, Antonio Picón, and Luis Plaja. Theory of high-order harmonic generation for gapless graphene. *New Journal of Physics*, 20(5):053033, May 2018.

[308] Jongkyoon Park, Amutha Subramani, Seungchul Kim, and Marcelo F. Ciappina. Recent trends in high-order harmonic generation in solids. *Advances in Physics: X*, 7(1), December 2021.

[309] János K Asbóth, László Oroszlány, and András Pályi. A short course on topological insulators. *Lecture notes in physics*, 919:166, 2016.

[310] Oscar Viyuela, A Rivas, Simone Gasparinetti, Andreas Wallraff, Stefan Filipp, and Miguel A Martín-Delgado. Observation of topological uhlmann phases with superconducting qubits. *npj Quantum Information*, 4(1):10, 2018.

[311] Marcos Atala, Monika Aidelsburger, Julio T Barreiro, Dmitry Abanin, Takuya Kitagawa, Eugene Demler, and Immanuel Bloch. Direct measurement of the zak phase in topological bloch bands. *Nature Physics*, 9(12):795–800, 2013.

[312] Mikael C Rechtsman, Julia M Zeuner, Yonatan Plotnik, Yaakov Lumer, Daniel Podolsky, Felix Dreisow, Stefan Nolte, Mordechai Segev, and Alexander Szameit. Photonic floquet topological insulators. *Nature*, 496(7444):196–200, 2013.

[313] Simon Stützer, Yonatan Plotnik, Yaakov Lumer, Paraj Titum, Netanel H Lindner, Mordechai Segev, Mikael C Rechtsman, and Alexander Szameit. Photonic topological anderson insulators. *Nature*, 560(7719):461–465, 2018.

[314] Jia Ningyuan, Clai Owens, Ariel Sommer, David Schuster, and Jonathan Simon. Time- and site-resolved dynamics in a topological circuit. *Phys. Rev. X*, 5:021031, Jun 2015.

[315] A.Yu. Kitaev. Fault-tolerant quantum computation by anyons. *Annals of Physics*, 303(1):2–30, 2003.

[316] Stephan Plugge, Asbjørn Rasmussen, Reinhold Egger, and Karsten Flensberg. Majorana box qubits. *New Journal of Physics*, 19(1):012001, jan 2017.

[317] Linhu Li, Chao Yang, and Shu Chen. Winding numbers of phase transition points for one-dimensional topological systems. *Europhysics Letters*, 112(1):10004, oct 2015.

[318] Linhu Li, Zhihao Xu, and Shu Chen. Topological phases of generalized su-schrieffer-heeger models. *Phys. Rev. B*, 89:085111, Feb 2014.

[319] Mirko Cinchetti. Topology communicates. *Nature nanotechnology*, 9(12):965–966, 2014.

[320] Naoto Nagaosa and Yoshinori Tokura. Topological properties and dynamics of magnetic skyrmions. *Nature nanotechnology*, 8(12):899–911, 2013.

[321] W. P. Su, J. R. Schrieffer, and A. J. Heeger. Solitons in polyacetylene. *Phys. Rev. Lett.*, 42:1698–1701, Jun 1979.

[322] H. W. Streitwolf. Physical properties of polyacetylene. *physica status solidi (b)*, 127(1):11–54, 1985.

[323] Beatriz Pérez-González, Miguel Bello, Álvaro Gómez-León, and Gloria Platero. Ssh model with long-range hoppings: topology, driving and disorder, 2018.

[324] Francesca Calegari, Giuseppe Sansone, Salvatore Stagira, Caterina Vozzi, and Mauro Nisoli. Advances in attosecond science. *Journal of Physics B: Atomic, Molecular and Optical Physics*, 49(6):062001, feb 2016.

[325] Hamed Koochaki Kelardeh, Vadym Apalkov, and Mark I. Stockman. Graphene superlattices in strong circularly polarized fields: Chirality, berry phase, and attosecond dynamics. *Phys. Rev. B*, 96:075409, Aug 2017.

[326] Dieter Bauer and Kenneth K. Hansen. High-harmonic generation in solids with and without topological edge states. *Phys. Rev. Lett.*, 120:177401, Apr 2018.

[327] Christoph Jürß and Dieter Bauer. High-harmonic generation in su-schrieffer-heeger chains. *Phys. Rev. B*, 99:195428, May 2019.

[328] REF Silva, Á Jiménez-Galán, B Amorim, O Smirnova, and M Ivanov. Topological strong-field physics on sub-laser-cycle timescale. *Nature Photonics*, 13(12):849–854, 2019.

[329] Alexis Chacón, Dasol Kim, Wei Zhu, Shane P. Kelly, Alexandre Dauphin, Emilio Pisanty, Andrew S. Maxwell, Antonio Picón, Marcelo F. Ciappina, Dong Eon Kim, Christopher Ticknor, Avadh Saxena, and Maciej Lewenstein. Circular dichroism in higher-order harmonic generation: Heralding topological phases and transitions in chern insulators. *Phys. Rev. B*, 102:134115, Oct 2020.

[330] Helena Drüeke and Dieter Bauer. Robustness of topologically sensitive harmonic generation in laser-driven linear chains. *Phys. Rev. A*, 99:053402, May 2019.

[331] Tatsuhiko N. Ikeda, Koki Chinzei, and Hirokazu Tsunetsugu. Floquet-theoretical formulation and analysis of high-order harmonic generation in solids. *Phys. Rev. A*, 98:063426, Dec 2018.

[332] Adhip Pattanayak, Sumiran Pujari, and Gopal Dixit. Role of majorana fermions in high-harmonic generation from kitaev chain. *Scientific Reports*, 12(1):6722, Apr 2022.

[333] Niccolò Baldelli, Utso Bhattacharya, Daniel González-Cuadra, Maciej Lewenstein, and Tobias Graß. Detecting majorana zero modes via strong field dynamics. *ACS Omega*, 7(50):47424–47430, December 2022.

[334] Tran Trung Luu and Hans Jakob Wörner. Measurement of the berry curvature of solids using high-harmonic spectroscopy. *Nature communications*, 9(1):916, 2018.

[335] J Reimann, Stefan Schlauderer, CP Schmid, Fabian Langer, Sebastian Baierl, KA Kokh, OE Tereshchenko, A Kimura, Christoph Lange, Jens Güdde, et al. Subcycle observation of lightwave-driven dirac currents in a topological surface band. *Nature*, 562(7727):396–400, 2018.

[336] Beatriz Pérez-González, Miguel Bello, Álvaro Gómez-León, and Gloria Platero. Interplay between long-range hopping and disorder in topological systems. *Phys. Rev. B*, 99:035146, Jan 2019.

[337] Eric J. Meier, Fangzhao Alex An, and Bryce Gadway. Observation of the topological soliton state in the su–schrieffer–heeger model. *Nature Communications*, 7(1), December 2016.

[338] Vincent Lienhard, Sylvain de Léséleuc, Pascal Scholl, Daniel Barredo, Thierry Lahaye, and Antoine Browaeys. Experimental realization of a bosonic version of the su-schrieffer-heeger (SSH) model with rydberg atoms. In *Quantum Information and Measurement (QIM) V: Quantum Technologies*. OSA, 2019.

[339] Luke Thatcher, Parker Fairfield, Lázaro Merlo-Ramírez, and Juan M Merlo. Experimental observation of topological phase transitions in a mechanical 1d-SSH model. *Physica Scripta*, 97(3):035702, February 2022.

[340] Tatiana G. Rappoport, Yuliy V. Bludov, Frank H. L. Koppens, and Nuno M. R. Peres. Topological graphene plasmons in a plasmonic realization of the su–schrieffer–heeger model. *ACS Photonics*, 8(6):1817–1823, May 2021.

[341] A. D. Bandrauk, S. Chelkowski, D. J. Diestler, J. Manz, and K.-J. Yuan. Quantum simulation of high-order harmonic spectra of the hydrogen atom. *Phys. Rev. A*, 79:023403, Feb 2009.

[342] Jan Conrad Baggesen and Lars Bojer Madsen. On the dipole, velocity and acceleration forms in high-order harmonic generation from a single atom or molecule. *Journal of Physics B: Atomic, Molecular and Optical Physics*, 44(11):115601, may 2011.

[343] Bala Sundaram and Peter W. Milonni. High-order harmonic generation: Simplified model and relevance of single-atom theories to experiment. *Phys. Rev. A*, 41:6571–6573, Jun 1990.

[344] Jordi Alcalà, Utso Bhattacharya, Jens Biegert, Marcelo Ciappina, Ugaitz Elu, Tobias Graß, Piotr T. Grochowski, Maciej Lewenstein, Anna Palau, Themistoklis P. H. Sidiropoulos, Tobias Steinle, and Igor Tyulnev. High-harmonic spectroscopy of quantum phase transitions in a high-tc superconductor. *Proceedings of the National Academy of Sciences*, 119(40):e2207766119, 2022.

[345] Serge Aubry and Gilles André. Analyticity breaking and anderson localization in incommensurate lattices. 1980.

[346] Y. Lahini, R. Pugatch, F. Pozzi, M. Sorel, R. Morandotti, N. Davidson, and Y. Silberberg. Observation of a localization transition in quasiperiodic photonic lattices. *Physical Review Letters*, 103(1), June 2009.

[347] Yaacov E. Kraus, Yoav Lahini, Zohar Ringel, Mor Verbin, and Oded Zilberberg. Topological states and adiabatic pumping in quasicrystals. *Physical Review Letters*, 109(10), September 2012.

[348] Henrik P. Lüschen, Sebastian Scherg, Thomas Kohlert, Michael Schreiber, Pranjal Bordia, Xiao Li, S. Das Sarma, and Immanuel Bloch. Single-particle mobility edge in a one-dimensional quasiperiodic optical lattice. *Physical Review Letters*, 120(16), April 2018.

[349] Sergi Julià Farré. Controlling interactions in quantum materials: from a microscopic description to quantum simulation. 2022.

[350] Pinaki Sengupta, Anders W. Sandvik, and David K. Campbell. Bond-order-wave phase and quantum phase transitions in the one-dimensional extended hubbard model. *Physical Review B*, 65(15), April 2002.

[351] Peter Schmitteckert and Ralph Werner. Charge-density-wave instabilities driven by multiple umklapp scattering. *Physical Review B*, 69(19), May 2004.

[352] Tapan Mishra, Juan Carrasquilla, and Marcos Rigol. Phase diagram of the half-filled one-dimensional t-v-v'. *Physical Review B*, 84(11), September 2011.

[353] M. Di Dio, L. Barbiero, A. Recati, and M. Dalmonte. Spontaneous peierls dimerization and emergent bond order in one-dimensional dipolar gases. *Physical Review A*, 90(6), December 2014.

[354] Sergi Julià-Farré, Daniel González-Cuadra, Alexander Patscheider, Manfred J. Mark, Francesca Ferlaino, Maciej Lewenstein, Luca Barbiero, and Alexandre Dauphin. Revealing the topological nature of the bond order wave in a strongly correlated quantum system. *Physical Review Research*, 4(3), July 2022.

[355] Albert W. Marshall, Ingram Olkin, and Barry C. Arnold. *Inequalities: Theory of Majorization and its Applications*. Springer, second edition, 2011.

[356] Michal Horodecki and Jonathon Oppenheim. (quantumness in the context of) resource theories. *International Journal of Modern Physics B*, 27(01n03):1345019, 2013.

[357] Steven R. White. Density matrix formulation for quantum renormalization groups. *Physical Review Letters*, 69(19):2863–2866, November 1992.

[358] Eric Jeckelmann. Mott-peierls transition in the extended peierls-hubbard model. *Physical Review B*, 57(19):11838, 1998.

[359] Ernest R. Davidson. The iterative calculation of a few of the lowest eigenvalues and corresponding eigenvectors of large real-symmetric matrices. *Journal of Computational Physics*, 17(1):87–94, January 1975.

[360] Ernest R. Davidson and William J. Thompson. Monster matrices: Their eigenvalues and eigenvectors. *Computers in Physics*, 7(5):519, 1993.

[361] Steven R. White. Density-matrix algorithms for quantum renormalization groups. *Physical Review B*, 48(14):10345–10356, October 1993.